Heterogeneous Photoelectrochemistry and Photocatalysis of TiO$_2$-based Nanomaterials

-Towards photocatalytic CO$_2$ reduction-

DISSERTATION

zur Erlangung des Grades Dr. rer. nat.
der Fakultät für Chemie und Biochemie
der Ruhr-Universität Bochum.

vorgelegt von
Bastian Timo Mei
aus Hagen

Diese vorliegende Arbeit wurde im Zeitraum vom August 2009 bis zum Januar 2013 am Lehrstuhl für Technische Chemie der Ruhr-Universität Bochum angefertigt.

Danksagung

Zunächst möchte ich mich bei Herrn Prof. Dr. Martin Muhler für die Möglichkeit bedanken diese Arbeit an seinem Lehrstuhl anzufertigen, sowie für wissenschaftliche Leitung. Außerdem danke ich ihm für die vorhandenen Freiheiten während meiner Arbeit und das mir entgegengebrachte Vertrauen.

Herrn Prof. Dr. Wolfgang Schuhmann danke ich für die Übernahme des Koreferats.

Frau Dr. Jennifer Strunk danke ich für die groartige Betreuung während meiner Arbeit, die erfolgreiche Zusammenarbeit im Rahmen des "Photocatalysts for CO_2 Reduction" Projekts und die gute Leitung des Projekts. Allen Mitgliedern danke ich für die zahlreichen fachlichen Diskussionen und die guten Ratschläge. Im Einzelnen möchte ich mich bei Dr. Freddy Oropeza für sein stätiges Interesse, bei Ahmet Becerkili für die unzähligen Synthesen und bei Anna Pougin für Ihre Hilfestellungen und Ideen bei Aufbau des Photoreaktors bedanken.

Frau Dr. Wilma Busser danke ich für die Unterstützung bei photokatalytischen Messungen und der Präparation einiger Katalysatoren. Außerdem möchte ich mich für die vielen gewinnbringenden Diskussionen bedanken.

Vielen Dank auch an Dr. Thomas Reinecke für die Durchführung der XRD-Messungen und an Frau Kirsten Keppler für die Durchführung der Elementaranalysen.

Frau Sigrid Kalender danke ich dafür, dass Sie immer ein offenes Ohr hatte und viele Tage mit Kaffee erträglich machte.

Bei Frau Susanne Buse, Frau Lina Freitag und Frau Noushin Arshadi bedanke ich mich für BET und IR Messungen.

Allen Mitarbeitern des Lehrstuhls für Technische Chemie danke ich für die freundliche Arbeitsatmosphäre und Hilfsbereitschaft während meiner Zeit am Lehrstuhl.

Dem Graduiertenkolleg des Sonderforschungsbereichs SFB 558 der Deutschen Forschungsgemeinschaft und der Research School der Ruhr-Universität Bochum danke ich für die finanzielle Unterstützung.

Ein riesiges Dankeschön geht an meine Eltern, Geschwister und Großeltern, die mich jeweils auf ihre eigene Weise während des Studiums und der Promotion unterstützt und motiviert haben. Danke, dass ich mich immer auf euch verlassen kann.

Besonders danken möchte ich meiner tollen Freundin Marie Holz, die auch in schwierigen Zeiten zu mir hält und mir dadurch viel Kraft gibt.

Zusammenfassung

Die photokatalytische Umsetzung von Kohlenstoffdioxid mit Wasser zu C1-Basischemikalien der chemischen Industrie wie z.B. Methanol oder Methan unter Nutzung des Sonnenlichtes bietet eine Möglichkeit, Erdöl oder Erdgas als primäre Energiequellen abzulösen und gleichzeitig die Kohlenstoffdioxid-Bilanz zu verbessern, indem in einem idealen Prozess CO_2 rezykliert wird. Ziel dieser Arbeit war die Durchführung systematischer Untersuchungen an Titandioxid-basierten Photokatalysatoren für die CO_2-Reduktion und der Aufbau einer geeigneten Testanlage für photokatalytische Aktivitätsmessungen in dieser Gasphasenreaktion.

In der vorliegenden Arbeit wurden, ausgehend von den Arbeiten der Gruppe um Masakazu Anpo, unterschiedliche Strukturen von auf mesoporösem Siliziumdioxid geträgerten Titandioxid-Spezies (TiO_x-Spezies) synthetisiert. Die Bestimmung der so erhaltenen TiO_x-Spezies erfolgte durch die Kombination komplementärer spektroskopischer Untersuchungsmethoden. Es konnte gezeigt werden, dass in Abhängigkeit von der Titanbeladung gezielt isolierte, oligomerisierte oder polymerisierte TiO_x-Spezies synthetisiert werden konnten. Somit wurden TiO_2-basierte Materialien hergestellt, die als Ausgangsmaterialen für die Optimierung TiO_2-basierter Photokatalysatoren reproduzierbar zur Verfügung stehen. Des Weiteren eignen sich die synthetisierten Materialien dazu, eine detaillierte Studie des Einflusses der Titandioxid-Struktur durchzuführen und somit Struktur-Aktivitäts-Beziehungen in der photokatalytischen CO_2-Reduktion zu erhalten.

Die photokatalytische Aktivität isolierter TiO_x-Spezies in der CO_2 Reduktion konnte im Rahmen dieser Arbeit bestätigt werden. Methan und höhere Alkane konnten als Produkte detektiert werden und Formaldehyd konnte durch spektroskopische Untersuchungen als Intermediat der photokatalytischen Reduktion von CO_2 identifiziert werden. Die Abscheidung von Gold-Nanopartikeln auf der Oberfläche des Photokatalysators steigerte die Hydrieraktivität des Materials, wodurch höhere Methanausbeuten erzielt wurden und die Anreicherung von stabilen Formaldehyd-Spezies auf der Oberfläche des Photokatalysators verringert wurde. Des Weiteren konnte mit Hilfe geeigneter Testreaktionen gezeigt werden, dass die photokatalytische Aktivität der Materialien mit dem Polymerisationsgrad der TiO_x-Spezies abfällt.

Die Charakterisierung der spezifischen Wechselwirkungen von CO_2 mit isolierten und polymerisierten TiO_x-Spezies mittels temperaturprogrammierter Desorption und Infrarot-Spektroskopie zeigten, dass CO_2 lediglich bei tiefen Temperaturen mit den Photokatalysatoren wechselwirkt, wodurch eine Aktivierung des CO_2 auf der Katalysatoroberfläche unter realen Reaktionsbedingungen ausgeschlossen werden kann. Es konnte jedoch gezeigt werden, dass die Wechselwirkungen von CO_2 mit dem Katalysator durch Einbringen kleiner Zinkoxid-Agglomerate verbessert wird. Systematische Untersuchungen an Zinkoxid-modifizierten TiO_x-haltigen Materialien zeigten, dass die Photonenanregung der TiO_x-Spezies die photokat-

alytische Aktivität der Materialien bestimmt. Es konnte außerdem gezeigt werden, dass das Trägermaterial Einfluss auf die photokatalytische Aktivität der TiO_x-Spezies hat und die spezifischen Wechselwirkungen zwischen TiO_x- und Zinkoxid-Spezies die Aktivität in den durchgeführten Testmessungen bestimmen. Abschließend wurde durch hochauflösende Transmissionselektronenmikroskopie-Messungen gezeigt, dass die Mobilität der TiO_x-Spezies durch die Anwesenheit von Zinkoxid verringert wird, wodurch die Abscheidung von Gold-Nanopartikeln auf den Materialien beeinflusst wird.

Im zweiten Teil der Arbeit wurde eine neuartige Syntheseroute basierend auf dem Sprühtrocknungsprozess zur Präparation dotierter TiO_2-Materialien entwickelt. Ausgehend von wässrigen Lösungen von Titan(IV)-oxidsulfat erlaubt die Sprühtrocknungsmethode, homogene Verteilungen eines Dotierelements in TiO_2 zu erhalten und durch anschließende Kalzination dotiertes TiO_2 in unterschiedlichen polymorphen Strukturen zu synthetisieren. niobdotiertes TiO_2 wurde mit Hilfe dieser Syntheseroute erfolgreich präpariert und die erhaltenen Materialien konnten erfolgreich in der photoelektrochemischen Wasserspaltung eingesetzt werden. Der Einbau geringer Konzentrationen von Niob in die Gerüstrstuktur der TiO_2 Materialien führte zur einer Erhöhung der gemessenen Photoströme um ca. 30 % im Vergleich zu undotierten TiO_2 Materialien, die über das Sprütrocknungsverfahren hergestellt wurden. Die verbesserten Eigenschaften der niobmodifizierten TiO_2-Materialien konnte auf einen verbesserten Elektronentransport in den Materialien zurückgeführt werden. Abschließend wurde außerdem gezeigt, dass die verbesserten Eigenschaften des Elektronenkollektors auch nach Modifikation der Oberfläche mit einer Polyheptazin-Hülle beibehalten werden konnten, wodurch die Materialien unter sichtbarem Licht photokatalytische Aktivität zeigen.

Die Ergebnisse dieser Arbeit zeigen somit eindrucksvoll, dass TiO_2-basierte Materialien gezielt mit verschiedenen Strukturen oder Dotierungen synthetisiert werden konnten, deren Anwendbarkeit in unterschiedlichen photokatalytischen Prozessen demonstriert wurde. Dabei wurden neue Strategien verfolgt, um die Aktivität bekannter Systeme zu verbessern und die Struktur-Wirkungs-Beziehungen der Materialien genauer zu charakterisieren.

Table of Contents

List of Figures

List of Tables

Symbols

symbol	denotion	unit
α	absorption coefficient	
d	thickness of a material	$[m]$
d(BET)	diameter determined by BET	$[nm]$
d(XRD)	diameter determined by XRD	$[nm]$
ΔG	change in Gibbs energy	$[kJ/mol]$
$\Delta \mu$	energy difference between ${}^*E_{Fn}$ and ${}^*E_{Fp}$	$[eV]$
e^-	electron	
E_f	Energy of the Fermi level	
${}^*E_{Fn}$	quasi-Fermi level of electrons	
${}^*E_{Fp}$	quasi-Fermi level of holes	
E_g	band gap energy	$[eV]$
E_O^{redox}	standard reduction potential	
f(E)	Fermi-Dirac distribution	
$F(R_\infty)$	Kubelka-Munk function	
h^+	hole in the valence band	
h	Planck constant	$[Js]$
I_0	incident light	
I	transmitted light	
λ	wavelength	$[m]$
N_A	Avogadro constant	$[mol^{-1}]$
n_{ads}	adsorbed amount of substance	$[mol]$
N(E)	density of states	
ν	frequency	$[s^{-1}]$
p	pressure	$[mbar]$
p/p_0	relative pressure	
pH	pH-value	
R	gas constant	$[J\ K^{-1}\ mol^{-1}]$
ρ	density	$[kg\ m^{-3}]$
φ	work function	$[eV]$
T	transmittance	

symbol	denotion	unit
$Ti(O^iPr)_4$	titanium tetraisopropoxide	
θ	diffraction angle	$[°]$
V	volume	$[ml]$
V_{pore}	total pore volume	$[ml\ g^{-1}]$
$Zn(acac)_2$	zinc acetylacetonate	

Abbreviations

abbreviation	denotion
AAS	**A**tomic **A**bsorption **S**pectroscopy
ANO	**A**mmonium **N**iobate (V)**O**xalate
BET	**B**runnauer-**E**mmet-**T**eller
BJH	**B**arret-**J**oyner-**H**alenda
CB	**C**onduction **B**and
DOE	**D**epartment **O**f **E**nergy
DOS	**D**ensity **O**f **S**tates
DR	**D**iffuse **R**eflectance
DTG	**D**ifferential **T**hermo**g**ravimetry
EA	**E**lemental **A**nalysis
EDX	**E**nergy **D**ispersive **X**-Ray spectroscopy
EPR	**E**lectron **P**aramagnetic **R**esonance
EXAFS	**E**xtended **X**-Ray **A**bsorption **F**ine **S**tructure
FFT	**F**ast **F**ourier **T**ransform
FID	**F**lame **I**onization **D**etector
FTIR	**F**ourier **T**ransform **I**nfra**r**ed spectroscopy
FWHM	**F**ull **W**idth at **H**alf **M**aximum
GC	**G**as **C**hromatograph
HAADF	**H**igh-**a**ngle Annular **D**ark-Field imaging
HOMO	**H**ighest **O**ccupied **M**olecular **O**rbital
ICP-OES	**I**nductively **C**oupled **P**lasma **O**ptical **E**mission **S**pectrometry
IPCC	**I**ntergovernmental **P**anel on **C**limate **C**hange
IPCE	**I**ncident **P**hoton to **C**urrent **E**fficiency
IR	**I**nfra**r**ed
ITO	**I**ndium **T**in **O**xide
IUPAC	**I**nternational **U**nion of **P**ure and **A**pplied **C**hemistry
LMCT	**L**igand to **M**etal **C**harge **T**ransfer
LUMO	**L**owest Unoccupied **M**olecular **O**rbital
MCM-48	**M**obil **C**rystalline **M**aterial-48

abbreviation	denotion
MFC	**M**ass **f**low **c**ontroller
NHE	**N**ormal **H**ydrogen **E**lectrode
PVA	**P**oly**v**inyl **A**lcohol
PVS	**P**oly**v**inyl **S**iloxane
QMS	**Q**uadrupole **M**ass **S**pectrometry
RHE	**R**eversible **H**ydrogen **E**lectrode
SBA-15	**S**anta **Ba**rbara-No.**15**
SEM	**S**canning **E**lectron **M**icroscopy
TA	**T**erephthalic **A**cid
TCD	**T**hermal **C**onductivity **D**etector
TEOS	**T**etra**e**thyl**o**rtho**s**ilicate
TEM	**T**ransmission **E**lectron **M**icroscopy
TG	**T**hermo **G**ravimetry
TGA	**T**hermal **G**ravimetric **A**nalysis
TOC	**T**otal **O**rganic **C**arbon
TPD	**T**emperature **P**rogrammed **R**eduction
UHV	**U**ltra **H**igh **V**accum
VB	**V**alence **B**and
XANES	**X**-ray **A**bsorption **N**ear **E**dge **S**tructure
XAS	**X**-ray **A**bsorption **S**pectroscopy
XPS	**X**-ray **P**hotoelectron **S**pectroscopy
XRD	**X**-**r**ay **d**iffraction

1 Introduction

During the past four decades photochemistry has been a strongly growing field of scientific interest. Certainly, the pioneering reports by Fujishima and Honda[1] on solar water splitting into hydrogen and oxygen on a TiO_2 photoelectrode in the early 1970's revealed the practical potential of photochemical processes for solar energy conversion and storage on semiconductor materials. Subsequently, the potential of photochemistry was verified for several reactions, e.g. the removal of organic pollutants from water or air,[2,3] organic synthesis,[4] and for the reduction of carbon dioxide, which was first published in 1979 by Inoue et al.[5] These examples clearly demonstrated that photocatalysis and photoelectrochemistry exhibit the possibility to convert thermodynamically stable raw materials, such as water and carbon dioxide, into valuable chemicals with the help of solar energy and a semiconductor catalyst. In a recommended definition by the International Union of Pure and Applied Chemistry (IUPAC), photocatalysis is described as the "Change in the rate of a chemical reaction or its initiation under the action of ultraviolet, visible, or infrared radiation in the presence of a substance - the photocatalyst - that absorbs light and is involved in the chemical transformation of the reaction partners".[6] In recent years the developed photocatalytic concepts have gained excessive attention as one of the most important scientific challenges nowadays is to secure the futures energy supply.[7]

The need for new energy sources can be rationalized considering that today's energy consumption is mainly covered by fossil fuels ($\sim$ 87 %),[8] which, at reasonable cost, will supply the world's energy demand for several years. However, meeting global energy consumption in a sustainable, carbon-neutral manner is desirable. For instance the USA's Department of Energy (DOE) estimated that carbon-free energy will be needed by 2050[9] and the Intergovernmental Panel on Climate Change (IPCC) showed that the global warming is mostly due to human activities and the release of green house gases, like carbon dioxide.[10] Biomass conversion will always compete with the human food supply and wind energy as well as energy from photovoltaic devices is accompanied by severe fluctuations. Therefore, energy storage systems are required, which of course is a scientific challenge by itself. However, the earth receives 5,000 times more energy from the sun than mankind uses over a year.[11,12] Thus, it is arguable that utilizing sunlight to convert energy-poor to energy-rich molecules is a promising technology. Nature already showed us by million years of successful photosynthesis that it is accomplishable.[7] In this sense replacing fossil fuels by solar chemical fuels is a goal of current research and even though it is arguable to which degree solar irradiance can be efficiently converted into usable energy-rich molecules, scientists have to explore the possibility of a partly solar energy-

driven society with a reasonably high effort. One of the likely solar fuels would be hydrogen in case it is efficiently produced from solar water splitting.[8,13] The long-term goal within this field of research can be defined as the direct hydrogenation of the green house gas carbon dioxide into high-energy carriers using water.[8] The energy required to bridge the thermodynamic gap between reactants and desired products will be supplied by radiation. Considering the conversion of CO_2 and water to methanol, for instance, 698.7 kJ/mol are needed to overcome the thermodynamic gap of this endergonic reaction[14]:

$$CO_2 + 2H_2O \xrightarrow[h\nu]{} CH_3OH + \frac{3}{2}O_2$$
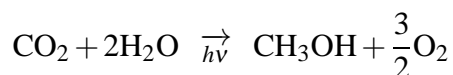
As this process basically mimics the production of polysaccharide conducted by green plants it is often referred to as "artificial photosynthesis".

Besides the photochemical process, strategies have already been developed to diminish the atmospheric CO_2 content. Numerous efforts have been put into the field of CO_2 capture and separation by high performance adsorbents. But there are also catalytic reactions, where this highly thermodynamically stable and therefore almost unreactive molecule is used in industrial relevant processes[15]:

- CO_2 is used as a reactant in the urea synthesis which is an important fertilizer,

- in the Kolbe-Schmitt process to form salicylic acid,

- cyclic organic carbonates and epoxides are synthesized from CO_2,

- and CO_2 participates in the methanol synthesis over copper catalysts:

$$CO_2 + 3H_2 \rightarrow CH_3OH + H_2O.$$
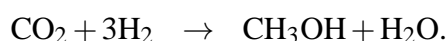
Despite these efforts it was estimated that since the industrial revolution the content of carbon dioxide in the atmosphere increased by $\sim$ 35 % to its current level of 383 ppm[16] and recent considerations claimed that at the current increase of atmospheric CO_2 the global temperature will increase of $\sim$ 6 °C before the end of the century.[17] Today, still less than 1 % of the overall emitted CO_2 is chemically converted[12] and mostly CO_2 is not recycled at all. Instead, CO_2 as a reactant is mainly provided by synthesis gas (CO, CO_2, and H_2) produced from fossil fuels. Furthermore, the hardly reactive CO_2 molecule has to be activated, e.g. by elevated temperatures facilitating an unfavorable energy balance and raising the carbon footprint. Alternatively, this work will explore the photochemical fixation of CO_2 in useful base chemicals by the help of photocatalytically active titania materials.

Titania-related materials seem to be the most promising semiconductors for many photocatalytic and photoelectrochemical applications, particularly due to its commercial availability, non-toxicity, and excellent stability against photocorrosion.[18–20] Thus, it is not remarkable that titania-based materials are frequently studied for photocatalytic CO_2 reduction and other

reactions. While the main focus of this dissertation is the study of the photocatalytic CO_2 reduction on isolated titania species incorporated in an mesoporous silica matrix, in the second part bulk TiO_2 materials are discussed. The key points and questions addressed in the first part of this dissertation are:

1. What are the requirements of a gas-phase reactor for photocatalytic CO_2 reduction? According to the requirements the gas-phase reactor should be developed allowing for trace gas analysis and reproducible CO_2 reduction experiments.

2. A reproducible synthesis procedure for isolated titania species with high titania loading and a reliable characterization routine to distinguish between isolated and polymerized titania should be developed. Synthesis and characterization should be applicable for a variety of different isolated metal oxide materials.

3. Are isolated titania species really active in the photocatalytic CO_2 reduction and what are the main products of the photocatalytic CO_2 reduction reaction on isolated titania sites? What is the effect of titania polymerization?

4. Is CO_2 interacting with isolated titania species?

5. How can materials with beneficial CO_2 adsorption properties be synthesized on the basis of a material containing isolated titania sites? Is there any relation between the CO_2 adsorption and the photocatalytic activity of the materials?

Certainly, the use of bulk TiO_2 in a photocatalytic CO_2 reduction process is preferable due to its commercial availability and due to its lower band gap, which can be even reduced by doping. However, in recent studies isolated titania appeared to be more active in comparison to bulk TiO_2.[21] Nevertheless, the thorough investigation of the CO_2 reduction mechanism on isolated and polymerized titania species may later on provide the knowledge to design highly active bulk TiO_2 materials. In this sense it is desirable to study the properties of bulk TiO_2 and the key points and questions, which were addressed in these studies are:

1. A simple and reliable synthesis method for the preparation of TiO_2 should be developed, which should offer the possibility to synthesize doped TiO_2.

2. Do the synthesized TiO_2 or doped TiO_2 materials possess exceptional properties in a well-known photocatalytic process?

3. Are there further modification possibilities, e.g. to improve the light-harvesting properties and to increase the photocatalytic activity of TiO_2?

Finally, the outline of this thesis can be summarized as follows. Chapter 2 will shortly introduce the basic concepts of semiconductor physics and their impact on photocatalysis with semiconductor materials in general and particularly on TiO_2 and isolated titania species. A short literature review on photocatalytic CO_2 reduction on isolated titania species and TiO_2 is given in chapter 3. In chapter 4 the developed gas-phase photoreactor will be described and

the calibration data will be shown. The results obtained in the studies performed with isolated titania are shown in chapter 5. The chapter is divided in three sections. First, the synthesis and the characterization results are discussed and the interaction of CO_2 is studied. A possibility to increase the CO_2 adsorption by incorporation of zinc oxide is demonstrated. In the second section the feasible photocatalytic CO_2 reduction on isolated titania species is presented and a possible intermediate of the photocatalytic CO_2 reduction on isolated titania is identified. Additionally, differences in the photocatalytic activities of gold-modified materials are discussed. The effect of zinc oxide species incorporated into the titania materials is investigated by means of photo-deposition of gold nanoparticles, the hydroxylation of terephthalic acid, and high resolution transmission electron microscopy. Corresponding to chapter 5 chapter 6 is divided into three sections dealing with a the description of a novel synthesis technique for metal doped TiO_2 materials, which were subsequently highlighted to exhibit unique properties in photo-electrochemical water oxidation and finally first results for an improved visible light harvesting of non-metal/metal co-doped TiO_2 are shown. Finally, the main results obtained within the scope of this dissertation will be summarized and an outlook will be given in chapter 7.

2 Basic Principles

2.1 Physical and Chemical Properties of Semiconductors

Semiconductors are materials with conductivity between the conductivity of conductors and insulators. The typical semiconducting properties are caused by atomic interactions, hence by the nature of the chemical bond and the resulting lattice structure of the material. At absolute zero temperature semiconductors are not conductive. The intrinsic conductivity increases, to a certain extent, with increasing temperature. Depending on the temperature the electron mobility increases and electron excitation into the conduction band is becoming favored. To describe this behavior the energy band model and the Fermi function are used.

2.1.1 The Energy Band Model

The energy band model, derived as an extension of molecular orbital theory, describes the interaction of atoms in an ideal crystal and is used to specify the conductivity of metals, semiconductors, and insulators.[22] The model mainly consists of two stacked energy bands (valence and conduction band) separated by a gap (band gap). In fact the valence band is the highest occupied band of the lattice structure. Contrary to the valence band the conduction band is the lowest unoccupied band in the ground state (T = 0 K). The separation or more precisely the size of the band gap influences the conductivity of the material. Therefore, the energy band model is a convenient way to describe the electronic and optical properties of a semiconductor.

The atom model developed by Bohr describes a single atom by discrete energy states, which can be occupied by up to two electrons. In molecular orbital theory the formation of bonding, antibonding and non-bonding orbitals due to interaction between several atoms is described.[20] These interactions are possible across several inter-atomic distances and with increasing number of interacting atoms the discrete levels are getting more and more indistinguishable, resulting in broad energy regions or bands (Fig. 2.1). The number of electrons incorporated in one of these bands is similar to twice the number of atoms involved and the band width increases with decreasing binding strength between atomic core and electron. The weekly bound electrons are easily released from the core and hence they can interact with neighboring atoms resulting in mobile electrons. In case of the valence electrons they are completely merged together and
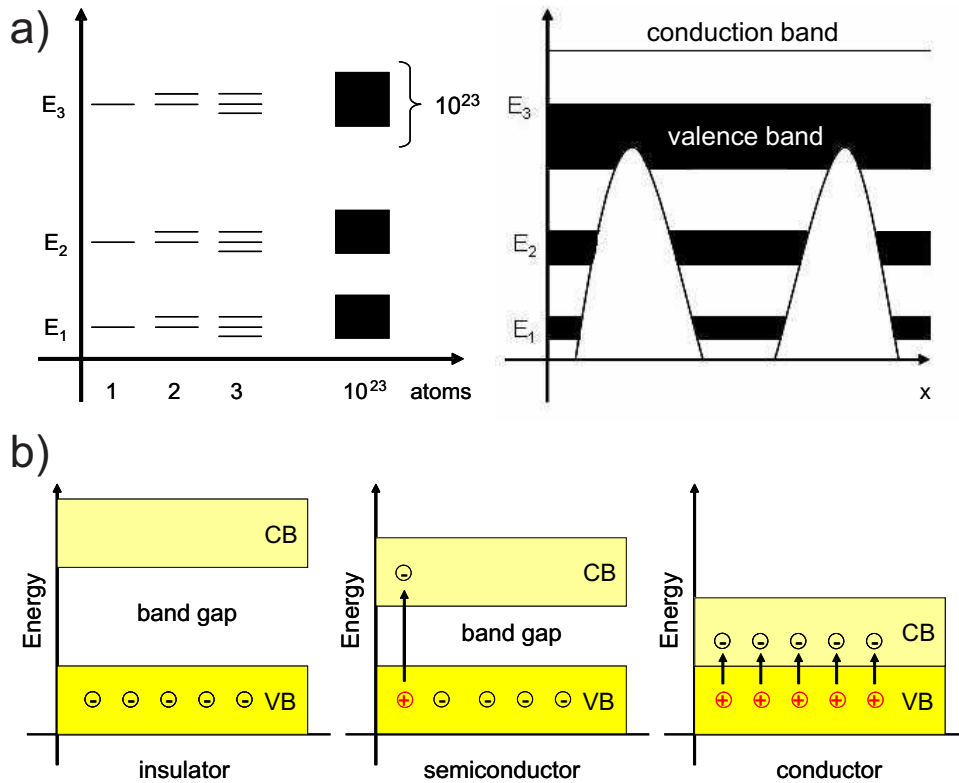
Figure 2.1: a) Schematic description of the interaction of discrete atom energy levels and the formation of energy bands. The figure was adapted from Hoffmann et al.[20] b) Available electrons in insulator, semiconductor, and metal-type materials. With increasing band gap the amount of electrons excited into the conduction band decreases.

electrons cannot be assigned to a special atom anymore (valence band). The lowest unoccupied band consisting of anti-bonding states is associated with the conduction band.

For conduction unoccupied states within the valence band or charge carriers within the conduction band are necessary. In metals the conductivity is generally realized by the overlap of the valence and the conduction band, or by a half-filled valence band (Fig. 2.1). In any case free electrons can participate in the conduction process. This is not the case in insulators or semiconductor materials. The valence bands of these materials are completely filled and a gap appears between conduction and valence band, which is rather small for semiconductors ($E_g <$ 3 eV). Hence, electrons are rigid in the valence band and have to be excited into the conduction band to participate in the conduction process (Fig. 2.2). Excitation of electrons is possible by thermal excitation and/or by the absorption of light and negative, mobile charge carriers are available within the conduction band. The latter is the primary process in photo-related mechanisms.

The thermally introduced increase in conductivity is best described by the Fermi function or Fermi-Dirac distribution f(E) and the density of states (DOS) N(E) concepts (eq. 2.1). The Fermi function gives the probability that a given energy state is completely filled and the electron electron density of states N(E) describes the available energy states. Thus, the population
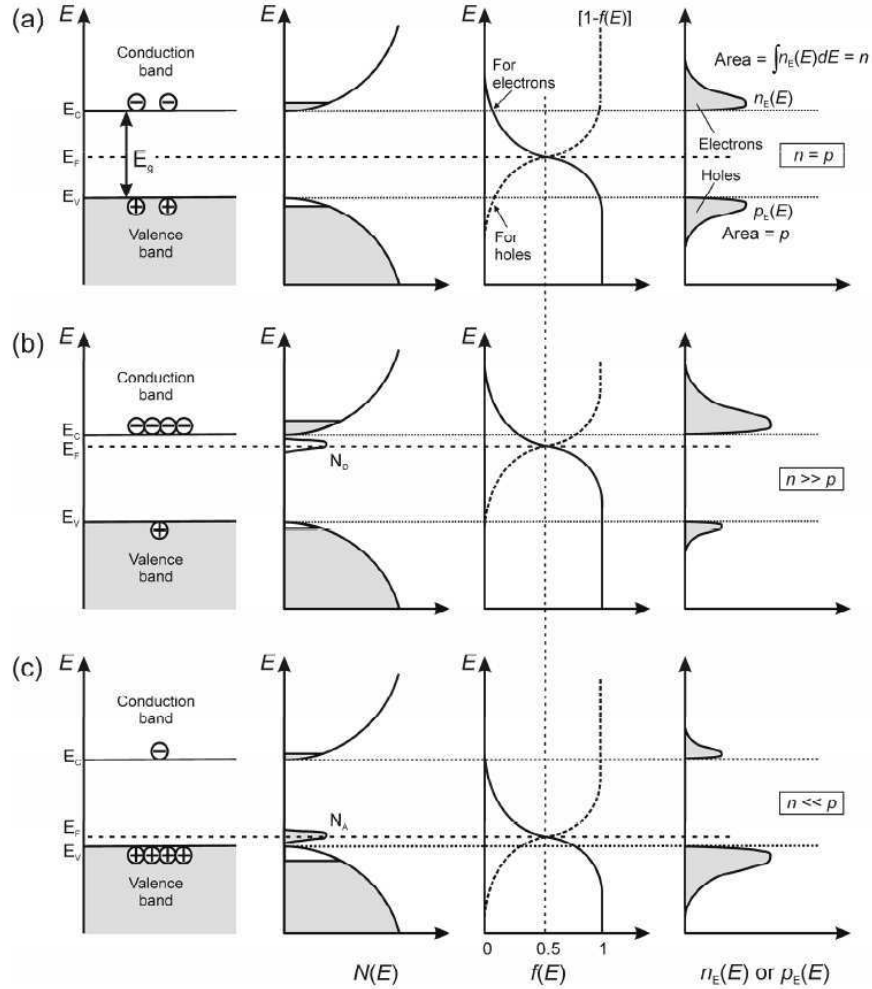
Figure 2.2: Characteristics of a) an intrinsic, b) a n-type, and c) a p-type semiconductor. The figure was adapted from *Principles of electronic materials and devices*.[23]

of an energy state is given by the product of the N(E) and f(E).

$$f(E) = \frac{1}{1 + exp\dfrac{E - E_F}{kT}}, \quad N(E)dE = A \cdot \sqrt{E}dE \tag{2.1}$$

E_F is known as the energy of the Fermi level and is associated with the highest electron level at absolute zero temperature, where no electron will have enough energy to pass through.[24] For intrinsic semiconductors the Fermi level is situated half-way between the valence and the conduction band. There are several characteristics of f(E) and DOS explaining the behavior of intrinsic semiconductor material. Inside the semiconductor's band gap the DOS is zero, so there are no electrons inside the gap although the Fermi function has a finite value. Furthermore, the Fermi function at T = 0 K is zero for the conduction band. Hence, there are no free charge carriers within the conduction band, even though the DOS has a finite value for the conduction band. The only possibility to increase the number of charge carriers within the conduction band is to increase the temperature. With higher temperature both functions have a finite value and

a conducting population can be assumed and for certain semiconductors excitation of electrons at ambient temperature is feasible.

A specific modification of intrinsic semiconductors is possible by introducing impurities into the lattice structure of the material by impurity doping. Due to the impurity atoms new energy levels are produced, which are mostly inside the band gap near the valence or the conduction band. Therefore, the energy difference is getting smaller, electron excitation is getting easier and the material is more conductive at lower temperature. Doped semiconductors are also called extrinsic semiconductor. Extrinsic semiconductors are divided into two groups depending on the nature of chemical impurity. Electron donating impurity atoms provide a single-occupied energy level close to the conduction band. Less energy is required to excite these electrons to the conduction band, and therefore, negative charges are the majority carriers of electric currents in these n-type doped materials. In n-type semiconductors the Fermi level discussed above is shifted towards higher energies and it is located between the donor states and the conduction band.[24] Analogous to n-type doping positive charges, so-called holes can be introduced by doping with an acceptor atom (p-type doping). Due to one electron deficiency, an empty energy state is created close to the valence band. These states can easily be occupied by valence band electrons and new positive charge carriers are the majority carriers of electric currents. In this case the Fermi level is shifted to lower energies and is situated between the valence band and the new empty states (Fig. 2.2). Among many semiconducting materials titanium dioxide (TiO_2) is one of the best-known semiconductors exhibiting n-type character which is used for numerous purposes.[18,19]

2.1.2 Optical Properties of Semiconductors

The ability of a semiconductor to absorb UV or visible light is basically determined by the separation of the valence (VB) and conduction band (CB).[25,26] Upon illumination of a semiconductor with light possessing energy greater than the difference of energy between the VB and the CB an electron can be excited from the VB to the CB. Based on the relative position of the valence band apex and the energy valleys of the CB in the energy/momentum k-space the excitation of an electron can be classified as direct or indirect excitation (Fig. 2.3). For indirect excitation in an so-called indirect semiconductor an additional momentum is necessary, e.g. a phonon. The difference of the mechanisms can be illustrated best by having a closer look at the real band structure in the momentum k-space. Valence bands as well as conduction bands are described by different trajectories possessing extreme values. The highest probability for the excitation of an electron is from the VB maximum to CB minimum. In case of an equal momentum of VB maximum and CB minimum electrons are directly excited in a one-step process. These materials are semiconductors with direct allowed optical transition. Otherwise, an extra momentum is necessary for electron excitation. In that case minimum and maximum appear at two different momentums (Fig. 2.3) and excitation occurs in a two-step process. The

probability of an electron excitation is typically lower for an indirect transition, which can be measured in terms of the absorption coefficient α.
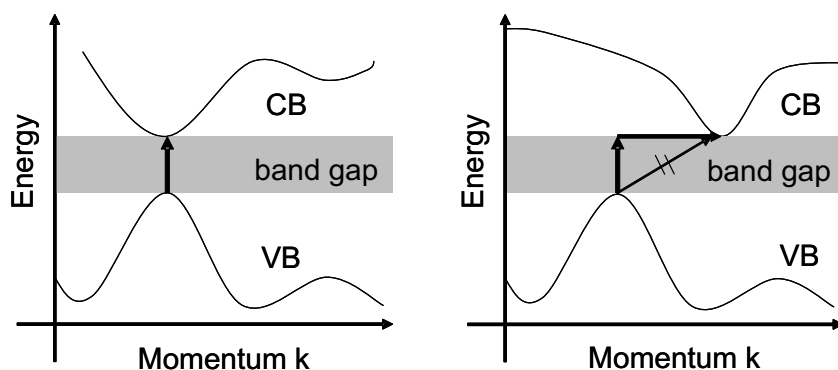
Figure 2.3: Scheme of an allowed direct (left) and an allowed indirect (right) optical transition.

The absorption coefficient α is directly accessible by the absorption spectrum of a material as a consequence of the Lambert-Beer law (eq. 2.2). Based on the Lambert-Beer law α can be determined by the logarithm of the intensity of the incident light I_0 and the transmitted light I and the thickness of a material d.[27]

$$ln\frac{I}{I_0} = lnT = -\alpha d = A \tag{2.2}$$

The basic principle of these measurements is to describe the attenuation of transmitted light intensity. Here, the loss of intensity is due to electron excitation. Since the excitation process is possible in atoms, molecules, and solids (interband transition) information about bulk and surfaces properties of a catalyst sample as well as of adsorbed species can be obtained (Tab. 2.1).[27,28]

Table 2.1: Wavenumber ranges of different excitation processes.

Bulk and surface	Wavenumber range	Adsorbed species	Wavenumber range
Band gap	UV 30,000 - 50,000 cm^{-1}	Transition metal ions	NIR, UV-Vis 5,000 - 50,000 cm^{-1}
Defects	UV 30,000 - 50,000 cm^{-1}	Molecules with chromophoric groups	UV-Vis 14,000 - 50,000 cm^{-1}
Transition metal ions	NIR, UV-Vis 5,000 - 50,000 cm^{-1}	Vibrational overtone and combination bands	NIR 5,000 - 14,000 cm^{-1}

However, the absorption spectrum of a semiconductor powder is not easily accessible and diffuse reflectance data are usually recorded. The interpretation of diffuse reflectance spectra is

based on the Kubelka and Munk theory, which relates α and the reflection behavior of a powder material.[27] The Kubelka-Munk function $F(R_\infty)$ is given by eq. 2.3.

$$F(R_\infty) = \frac{(1 - R_\infty)^2}{2R_\infty} \tag{2.3}$$

Assuming a wavelength-independent scattering $F(R_\infty)$ is proportional to α and the band gap energy of a powder material is accessible by the Tauc equation (eq. 2.4).

$$\alpha = A\frac{(h\nu - E_g)^n}{h\nu} \tag{2.4}$$

Here, A is a constant, $h\nu$ is the energy of light, E_g is the band gap energy, and n (= 0.5, 1.5, 2 and 3) is a factor, which depends on the nature of the optical transition of the material.

2.2 Heterogeneous Photocatalysis on Semiconductor Particles

The principles of heterogeneous photocatalysis on small semiconductor particles is explained best by the schematic representation of a small particle as depicted in Fig. 2.4top.

The key steps of the photocatalytic process are 1) the absorption of light, 2) the migration of electrons and holes to the particle surface, where they are trapped at reactive surface sites and the subsequently occurring 3) and 4) simultaneous redox reactions. The photo-exited trapped electron reduces an acceptor species A to a primary product $A^{\cdot-}$ (process 3) and the hole oxidizes a donor species $D^{\cdot+}$ (process 4). Thus, photocatalytic reactions, e.g. overall water splitting, can only occur if the redox potential of the photo-excited electron is more negative than the standard redox potential of protons and the redox potential of the photo-generated hole is more positive than the standard redox potential of H_2O in the oxygen evolution reaction.[26] In a simplified picture the bottom of the CB and the top of the VB have to enclose the redox potentials of the specific redox reactions. In Fig. 2.4middle the position of the band edges in an aqueous solution at pH 1 are shown in relation to the standard redox potentials of several redox couples and the energy scales of the normal hydrogen electrode (NHE) and the vacuum level.[11] However, it should be noted that the Fermi level E_F of a semiconductor in thermodynamic equilibrium cannot be used to describe the conditions under illumination. Instead, the electron and hole densities should be described separately by the quasi-Fermi level of electrons and holes $^*E_{Fn}$ and $^*E_{Fp}$, respectively, as shown in Fig. 2.4top. Therefore, more precisely the energy difference $\Delta\mu$ between $^*E_{Fn}$ and $^*E_{Fp}$ has to be larger than the redox potential of e.g. water for overall water splitting.

The efficiency of a photocatalytic process is mainly determined by the recombination rate of photo-generated electrons and holes. Recombination either occurs directly after photo-excitation (5) or the trapped electrons and holes recombine in a secondary process (6) (Fig.
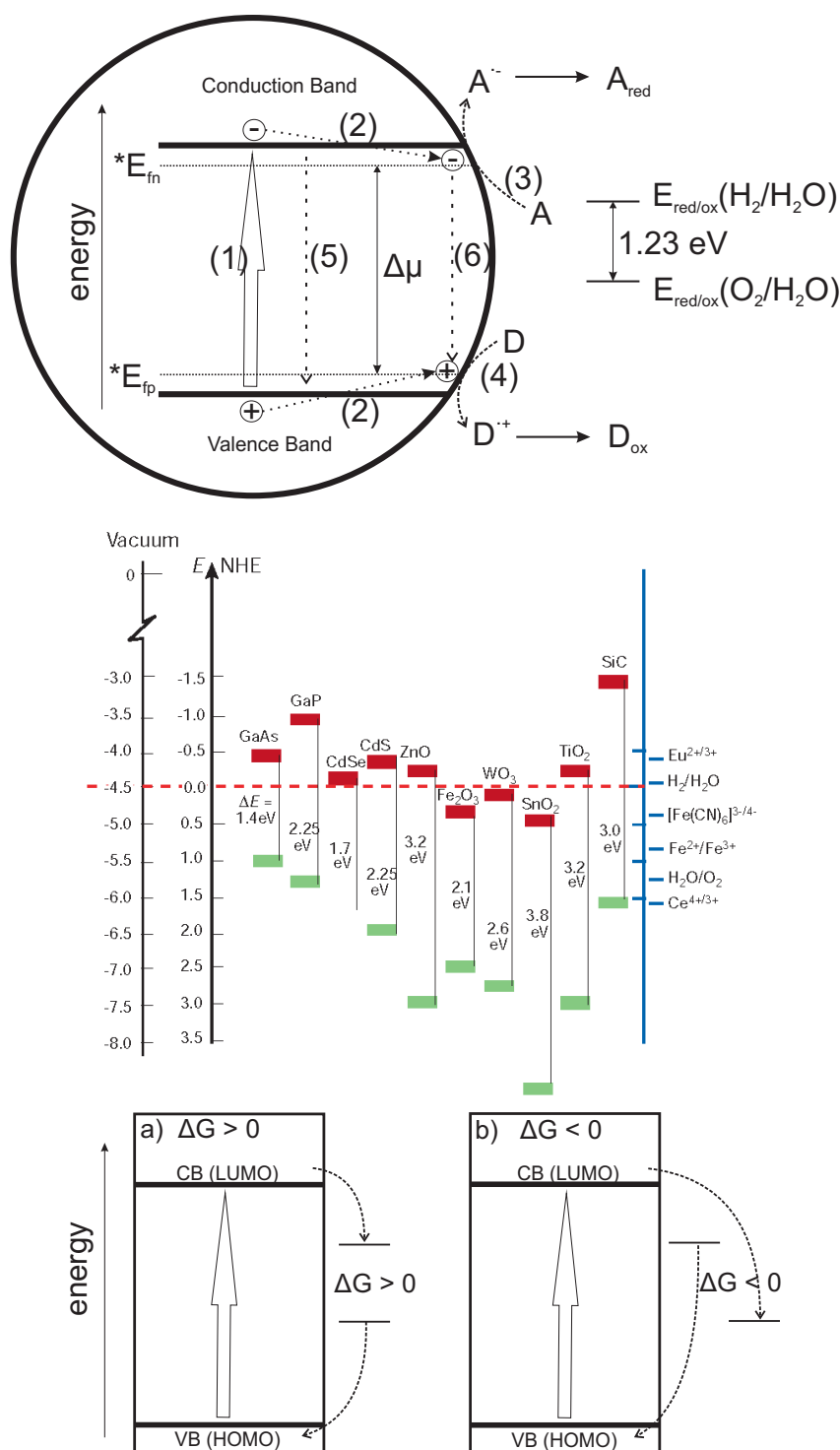
Figure 2.4: top: Schematic representation of the main processes, which take place at a semiconductor particle during photocatalysis. The figure was partially adapted from Kaiser et al. [26] and Park et al. [29] middle: Relationship between band structure of a semiconductor and the redox potentials of water splitting. The figure was adapted from Grätzel et al. [11] bottom: Changes in Gibbs energy in photocatalytic reactions, a) uphill and b) downhill reaction. The figure was adapted from Ohtani et al. [25]

2.4top). Finally, the efficiency of the overall photo-initiated process is also determined by the back-reaction of the primary reaction products $A^{\cdot-}$ and $D^{\cdot+}$.[18,20]

Additionally, an important advantage of light-driven reactions at semiconducting materials is shown in Fig. 2.4bottom, which is the ability to drive reactions even though the change in Gibbs energy is positive ($\Delta G > 0$).[25,30] For most reactions in photocatalysis, like the oxidative decomposition of organic matter, $\Delta G < 0$, whereas some energy-storing reactions with $\Delta G > 0$, like photocatalytic overall water splitting and photocatalytic CO_2 reduction, can be driven by photocatalysis if the two redox reactions are spatially or chemically separated.[25]

2.2.1 Oxide Photocatalysts - Band gap Engineering

It is well known that the conduction bands of stable oxide photocatalysts, like TiO_2, are comprised of empty orbitals of metal cations with d^0 or d^{10} configuration and that the valence band of these oxides are usually consisting of O 2p orbitals.[30] Due to the position of the CB edge with respect to the standard redox potential of desired reactions, like proton reduction, it is mostly desirable to raise the VB in order to decrease the band gap of a specific oxide. Thus, new energy levels above the VB have to be created by the incorporation of elements which either form discrete electron donor levels (DL in Fig. 2.5a) within the band gap or which form a new VB (Fig. 2.5b).[30] For certain oxides the formation of a solid solution is feasible, in which the VB and the CB are shifted (Fig. 2.5c).[30] In any case the obtained states or new bands should offer the thermodynamic potential and the kinetic ability to drive the desired redox reaction.
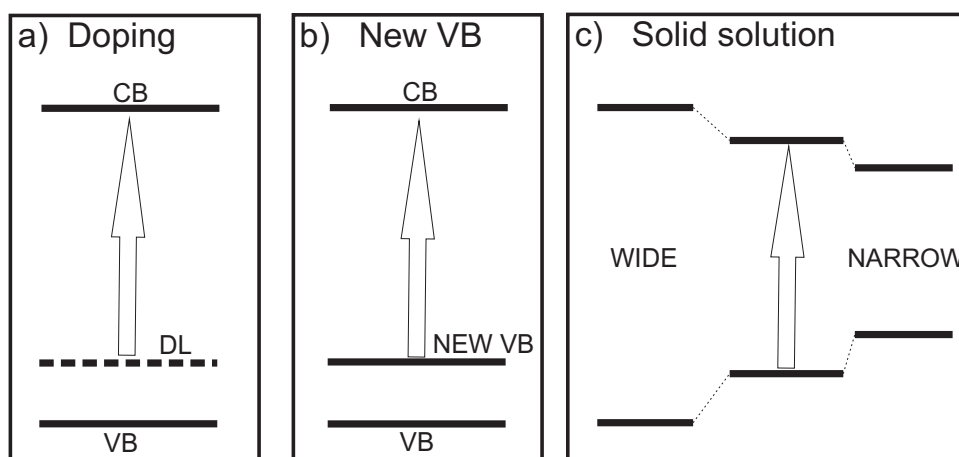
Figure 2.5: a) Donor levels created in the band gap by foreign element doping. b) Creation of a new VB within the band gap. c) Formation of a solid solution. The figure was adapted from Kudo et al.[30]

Typical examples for the formation of new DL within the band gap are metal or non-metal doping of TiO_2 or $SrTiO_3$, like Rh^{3+}, Cr^{3+}, or nitrogen doping. The drawback of this strategy is the discrete character of the DL, which is inconvenient for hole migration and which is

considered to act as a recombination site.[18,25,31,32] New VBs, which ensure the mobility of holes, can be formed by orbitals of Pb 6s in Pb^{2+}, Sn 5s in Sn^{2+}, Ag 4d in Ag^+, and Bi 6s in Bi^{3+}, as in $BiVO_4$.[30] GaN:ZnO is a well-known example of a solid solution containing a metal oxide. Furthermore, this system is one of the rare examples of successful implementation of photocatalytic water splitting on nanoparticular photocatalysts by visible light.[33–36] A different strategy to achieve visible light activity of oxide photocatalysts is by sensitization with organic dyes, metal complexes, and metal nanoparticles.[11,25,37] Sensitization by organic dyes or metal complexes is used in dye-sensitized solar cells, in which electrons are excited from the HOMO to the LUMO of the dye and the electron is subsequently injected into the conduction band of the oxide photocatalyst.[11] Sensitization of a photocatalyst by metal nanoparticles is extensively discussed in literature.[29,37–40] Mainly Au nanoparticles deposited on TiO_2 were shown to act as sensitizer. While the mechanism of visible light sensitization is not fully understand yet, it is believed that excitation of small Au nanoparticles on the Au plasmon can lead to an electron injection into the CB of the semiconductor.[29,37–40] Furthermore, trapping of electrons on metal co-catalysts due to a metal/photocatalyst junction preventing electron-hole recombination is discussed in the following section.

2.2.2 Metal-modified Photocatalysts

In general, the interaction between metal nanoparticles and a semiconducting photocatalyst can be explained by the junctions formed in metal/semiconductors. Two different interactions between metal and semiconductor might be discussed, the Ohmic contact and the Schottky junction.[22] While the formation of an Ohmic contact is discussed[25] it is generally excepted that Schottky junctions are formed on metal-modified photocatalysts, and thus the ohmic contact will be neglected in the following considerations.[18,29,41,42] Considering an n-type semiconductor and a metal, which are electrically neutral and isolated from each other the Fermi level of the semiconductor is situated close to the CB. The semiconductor's work function φ_S is therefore determined by the energy difference between the vacuum level and the Fermi level (Fig. 2.6a). The work function of a metal φ_M is normally larger compared to φ_S of a n-type semiconductor. Hence, the Fermi level of a metal is situated at a more anodic position, and thus it is more difficult to promote an electron from the metal to the vacuum level.

Upon contacting the metal and the semiconductor metal and semiconductor can be regarded as being short-circuited with each other.[25] The junction is formed as electrons are transferred from the semiconductor to the metal and the Fermi level of the metal is shifted upwards (cathodically) until the Fermi levels are aligned (Fig. 2.6b). The flow of electrons from the semiconductor to the metal will cause an accumulation of positive charges at the semiconductor interface and an accumulation of negative charges on the metal. The semiconductor's VB is bent upwards in a Schottky junction.[18]

The effect on the photocatalytic performance of different metal co-catalysts can be thus ex-
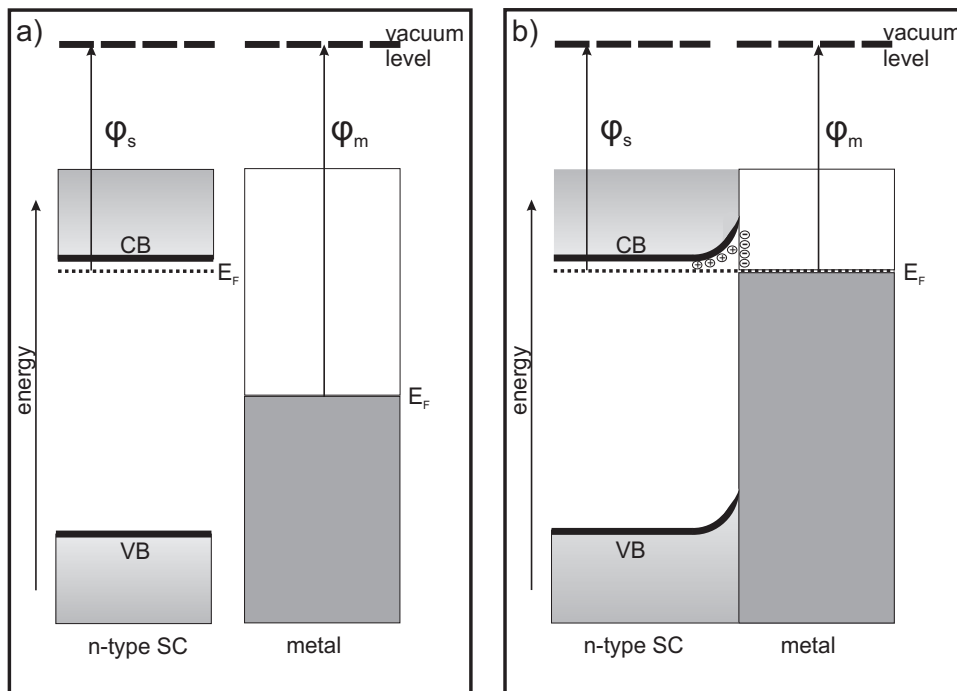
Figure 2.6: a) Position of the work functions φ_M φ_S for separated metals and n-type semiconductors. b) Formation of a Schottky junction (depletion layer) for metal/n-type semiconductor junctions. The figure was adapted from Yates et al. [43]

plained by the differences in the metal/semiconductor work functions. The larger φ_M the higher is the Schottky junction. Photo-generated electrons are expected to be more efficiently trapped on metals with higher work function. Experimental results of Au-, Ag-, and Pt-modified TiO_2 showed that H_2 evolution due to photocatalytic reforming of alcohols increased in the order Ag < Au < Pt in agreement with the increase of the work functions of the metals. [41]

2.3 TiO_2 in Photocatalysis

Titanium dioxide is the most important titanium compound for technical applications. This compound is nontoxic, stable against acids and bases and with a melting point of 1850 °C resistant against severe temperature. Usually TiO_2 is a white powder, which is used as a pigment and in cosmetics. [19,44] Catalysis is another important area of application of TiO_2 where it is used either as promoter, support material, additive, or as the catalytically active compound.

The most stable modification is the tetragonal rutile phase. Other possible modifications are the tetragonal anatase and the orthorhombic brookit structures, which convert into the rutile structure upon heating to temperatures above 580 °C. [46] Of these different modifications the anatase phase is the most widely used TiO_2 polymorph for photo-related processes. All modifications consist of titanium ions coordinated by six oxygen ions arranged in an octahedral structure. Therefore, all oxygen ions are involved in three coordination spheres. The different thermody-

Figure 2.7: Crystal structure of (a) the rutile and (b) the anatase TiO$_2$ polymorph. The figure was adapted from Glassford et al.[45]

namic stabilities, different optical and electronic properties, and differences in density of the modifications can be explained by TiO$_6$-octahedron distortion, e.g. in anatase phase Ti-Ti distances are bigger and Ti-O distances are smaller (Fig. 2.7). Well established characterization methods to differentiate between the phases are XRD, Raman, and UV-Vis spectroscopy.[47–49]
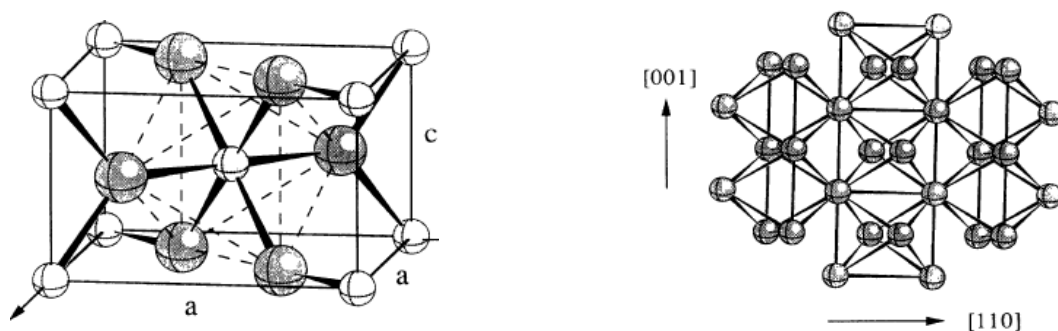
Titanium dioxide is either referred to be an insulator or a wide-band gap semiconductor material with an indirect allowed optical transition of around 3.0 eV in the rutile and around 3.2 eV in the anatase phase.[19] The valence bands of TiO$_2$ are composed of O 2p states hybridized by Ti 3d, resulting in a band width of around 6 eV.[45,50] The conduction bands are dominated by unoccupied Ti 3d, 4s, and 4p states.[18] However, these statements and values are only valid for stoichiometric bulk material. The surface structure mostly differs from the bulk structure. This is due to the formation of defect sites created by different atmospheres and/or oxygen partial pressures during synthesis. Common defects are oxygen vacancies and titanium interstitials. A consequence of oxygen vacancies are electron-donating Ti 3d states (Ti^{3+}) states appearing at 1.18 eV below the conduction band, similar to states introduced by n-type doping. Consequently, the conductivity of TiO$_2$ crystals is mainly determined by defects and increases with increasing defect density.[19] The number of oxygen vacancies can be increased by reversible reduction treatments, however, in ambient atmosphere oxygen vacancies are generally compensated by physisorption or dissociative chemisorption of water.[51] High defect densities, especially at the surface, can also change the optical properties of the TiO$_2$ and depending on the reduction conditions and the resulting electron states within the band gap colored titanium suboxides can be obtained. The color varies from green to black for highly reduced samples.

The photocatalytic properties of TiO$_2$ have been reviewed by several articles.[18–20,37] Usually, the white, defect-free TiO$_2$ is used in photocatalysis and it was shown to be applicable in the photocatalytic oxidation of organic compounds and hydrogen evolution due to photocatalytic reforming of alcohols.[18,37] Furthermore, TiO$_2$ is used as electron collector in dye-sensitized solar cells and inorganic/organic hybrids for photoelectrochemical water splitting.[52–54] The main drawback of TiO$_2$ is the inherent large band gap. Thus, only small fractions of the solar light spectrum can be utilized by TiO$_2$. Therefore, metal and non-metal doping as well as

sensitization by metal nanoparticles are currently discussed to improve the light absorption properties of TiO_2.[18,37] Within these efforts non-metal doping, especially nitrogen doping, was proven to enhance the visible light activity. However, the beneficial activity under visible light operation is mostly associated with a decrease of the overall activity.[55] More recently, blue or black TiO_2 was shown to exhibit significant activity in visible light-driven reactions although defects are generally expected to decrease the catalytic activity.[56,57]

2.4 Single-site Photocatalysts

So far photocatalysis has exclusively been related to semiconductor materials and the redox reactions performed at the surfaces of the semiconductor particles. One of the first examples of the photocatalytic activity of isolated metal oxide species was reported by Anpo et al.[58] They showed that the photoreduction of CO_2 on highly dispersed or even isolated metal oxide species, in this case TiO_4 species, was feasible.[58] Since then isolated metal oxides received some interest in heterogeneous catalysis, as isolated metal oxides offer a generally applicable strategy for the design of new heterogeneous catalysts.[59,60] More recently, the interest in single-site photocatalysts is increasing and successful examples of molybdenum, copper, and chromium single-site photocatalysts were reported.[61,62]
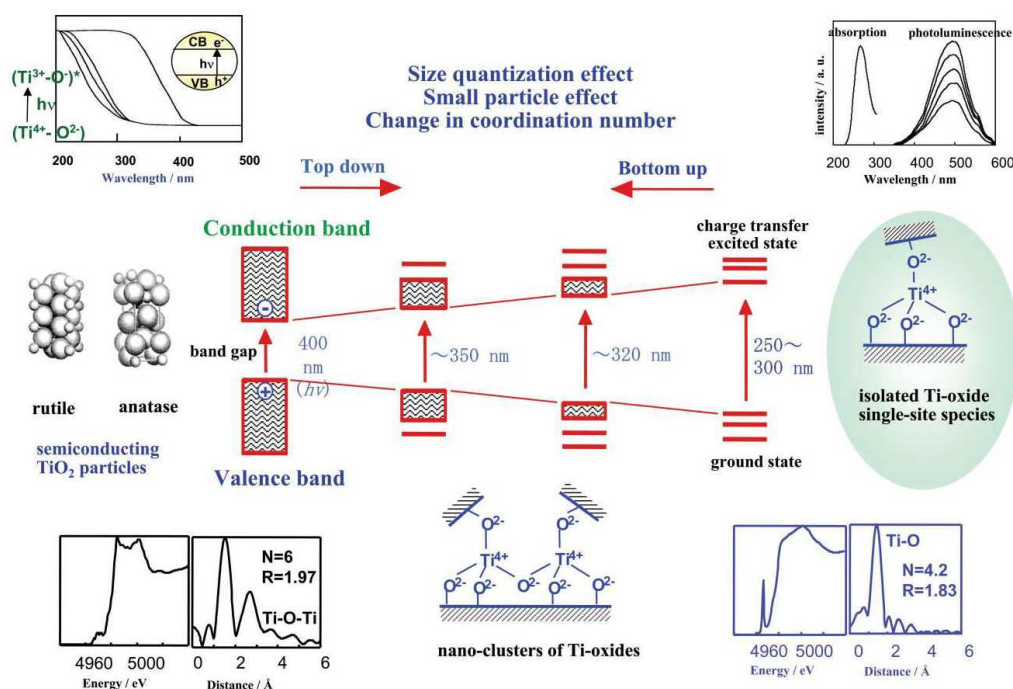

Figure 2.8: From TiO_2 semiconductors to Ti-oxide single-site catalysts. Illustration of: size quantization effect, small particle effect, and change in coordination number. The figure was adapted from Anpo et al.[61]

While for semiconductor particles the excitation of electrons occurs from the VB to the CB the creation of excited electronic states proceeds differently in the case of isolated surface species. As shown in Fig. 2.8 and explained previously for the energy band model electronic states in single atoms are characterized by discrete levels. Therefore, with decreasing TiO_x domain sizes the overlap between bonding, antibonding, and non-bonding states are reduced and they appear to be more discrete.

The excitation process in an isolated metal oxide species is a Ligand to Metal Charge Transfer (LMCT) and corresponds to an electron being excited from the VB to the CB leaving a hole (h^+) and an electron in the conduction band (e^-) in a semiconductor particle (Fig. 2.8). Ultimately, the excitation of an electron, whether through the formation of excitons or an LMCT, is the result of the absorption of radiation. The required energy is in the case of isolated species the distance between Highest Occupied Molecular Orbital (HOMO) and Lowest Unoccupied Molecular Orbital (LUMO). Accompanied with the mentioned changes an increase in the absorption can be observed due to a lowering of the VB edge and the rise of the CB edge, which is also known as the quantum size effect. Therefore, UV-vis spectroscopy is frequently employed to determine if a metal oxide is present as an isolated species. [63]

Table 2.2: Correlation of UV-Vis absorption and degree of isolation of TiO_x species.

	isolated	dimeric/one dimensional	polymeric/two dimensional
Ti [wt%]	1.05	6.6	15
LMCT band wavenumber [cm^{-1}]	47,600	40,600	39,000
LMCT band wavelength [nm]	210	246	256

Different supports can be used to synthesize isolated metal oxides, however, mesoporous silica is commonly used due to the high specific surface area. For isolated, dimeric, and two-dimensional polymerized TiO_x species on SiO_2 the absorption maxima determined by UV-Vis spectroscopy are summarized in Table 2.2. For highly isolated TiO_x species the LMCT enabling photocatalytic reactions is believed to be due to a charge transfer in the tetrahedral $Ti(OH)(OSi)_3$ species as described in eq. 2.5.

$$Ti^{4+} + O^{2-} \xrightarrow{h\nu} Ti^{3+} + O^- \tag{2.5}$$

The TiO_x loadings listed in Table 2.2 are standard values and might change with the support or the preparation technique. [64,65]

3 Literature Review - Photocatalytic CO$_2$ Reduction on TiO$_2$-related Materials
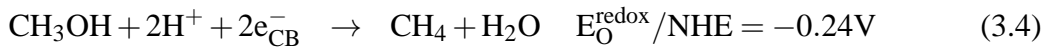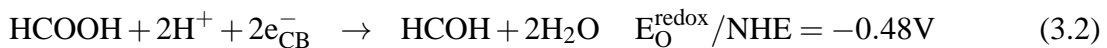
Several molecular approaches to photocatalytic reduction CO$_2$ were recently reviewed by Morris et al.[66] and more specifically the photocatalytic CO$_2$ reduction on TiO$_2$-related materials was reviewed by Dhakshinamoorthy et al.[14] Most of the reviewed work within these two articles performed photocatalytic CO$_2$ reduction in the liquid phase, which cannot easily be linked to gas-phase reactions. Therefore, this chapter will mainly focus on the studies performed with mesoporous silicates containing isolated/polymerized titania sites usually performed in the gas-phase, and the recent results on the mechanistic aspects of photocatalytic CO$_2$ reduction will be discussed, which are normally discussed for bulk TiO$_2$ materials.

Even though photocatalytic CO$_2$ reduction was first published in 1979 by Inoue et al.[5], the first report of a successful reduction of CO$_2$ at isolated or highly dispersed titania under UV irradiation was published by Anpo and coworkers in 1992.[58] In contrast to bulk-like TiO$_2$ where electrons are excited form the valence band to the conduction band of the material, the excitation in isolated titania can be described by a ligand-to-metal charge transfer (LMCT) from the oxygen anion to the titanium cation. In this pioneering work isolated or highly dispersed titania was obtained by the reaction of TiCl$_4$ with the OH-terminated surface of a porous glass yielding an active anchored Ti-photocatalyst for the formation of mainly methane in the presence of gas-phase CO$_2$ and H$_2$O. Furthermore, minor contributions of methanol, ethane, ethylene, carbon monoxide, and dioxygen were detected.[58] The product distribution was confirmed to strongly depend on the H$_2$O/CO$_2$ ratio in the feed gas resulting in the highest product yields for a H$_2$O/CO$_2$ ratio of 5.[58] Continuing their research Anpo et al.[67] were able to confirm the presence of isolated titania in the active anchored Ti-photocatalyst by means of X-ray absorption spectroscopy (XAS). They proposed a mechanism, in which the formation of methane occurred by the photoreduction of CO$_2$ into bare carbon radicals, which subsequently react with hydrogen atoms produced by the reduction of protons supplied from adsorbed water.[58,67] The radical mechanism was mainly based on *in-situ* electron paramagnetic resonance spectroscopy (EPR) studies evidencing the formation of the radicals upon illumination of the photocatalsyt. Thorough investigations of mesoporous materials containing a variety of different titania structures, from isolated tetrahedrally coordinated Ti-sites to octahedral coordinated Ti-sites with

bulk TiO_2 characteristics, revealed that the tetrahedrally coordinated Ti-sites show a higher selectivity to methanol compared with the octahedral Ti-sites. However, methane was always the main product independent of the Ti-coordination.[68] The comparison of the obtained total rates of CH_4 and CH_3OH formation indicated that the formation of methanol depends on the Ti-coordination in the mesoporous photocatalyst and a high selectivity towards methanol formation was obtained for the catalysts containing mostly tetrahedrally coordinated Ti-sites. Based on these results Anpo et al.[68] assumed that the spatial separation of photo-excited electrons and holes is of major importance for the product distribution. In consideration of their proposed radical mechanism the formation of methanol on isolated tetrahedrally coordinated Ti-sites was explained by the following reactions:

- CO_2 photoreduction to carbon radicals occurs at the isolated Ti-site,

- H_2O photoreduction to hydrogen atoms occurs at the isolated Ti-site,

- simultaneously OH anions can react with trapped holes to form OH radicals at the isolated Ti-site.

Thus, they proposed that the OH radicals can easily react with the carbon radicals formed by photoreduction. Additionally, hydrogen atoms and carbon radicals can recombine to form methane. On the other hand, the reaction between OH and carbon radicals can be neglected for samples with bulk TiO_2-like structure as in the samples containing octahedral Ti-sites. The photo-excited electrons and holes are rapidly separated in the bulk-like TiO_2 samples and photooxidation of the OH anion to an OH radicals occurs at a different active site, and therefore according to Anpo et al.[68], the spatial separation of the active sites determines the product distribution. It was also considered beneficial that the lifetime of photo-excited LMCT states, as in isolated titania, is significantly higher and the electron and hole transfer to CO_2 and H_2O is favored.

$$CO_2 + 2H^+ + 2e^-_{CB} \rightarrow HCOOH \quad E^{redox}_O/NHE = -0.61\,V \quad (3.1)$$

$$HCOOH + 2H^+ + 2e^-_{CB} \rightarrow HCOH + 2H_2O \quad E^{redox}_O/NHE = -0.48\,V \quad (3.2)$$

$$HCOH + 2H^+ + 2e^-_{CB} \rightarrow CH_3OH \quad E^{redox}_O/NHE = -0.38\,V \quad (3.3)$$

$$CH_3OH + 2H^+ + 2e^-_{CB} \rightarrow CH_4 + H_2O \quad E^{redox}_O/NHE = -0.24\,V \quad (3.4)$$

$$H_2O + h^+_{CB} \rightarrow OH + H^+ \quad E^{redox}_O/NHE = 2.32\,V \quad (3.5)$$

$$2H_2O + 2h^+_{CB} \rightarrow H_2O_2 + 2H^+ \quad E^{redox}_O/NHE = 1.35\,V \quad (3.6)$$

$$2H_2O + 4h^+_{CB} \rightarrow O_2 + 4H^+ \quad E^{redox}_O/NHE = 0.82\,V \quad (3.7)$$

The potentials of all reactions were obtained at pH 7.

Here, it should be noted that Inoue et al.[5] already proposed a relation between the conduction band edge position of a semiconductor and the methanol yield. The yields of methanol significantly increase as the reduction potential becomes more negative, which is in agreement with the redox potentials shown below in eq. 3.1-3.7.[69] Certainly, the reduction potential of

photo-excited electrons is more negative for isolated titania species, and therefore the increase in methanol yield might also be rationalized with the higher reduction potential of electrons.

More recently, Anpo's group reported that higher methane yields can be obtained with hydrophillic samples and that more open pore structures are beneficial for the photocatalytic CO_2 reduction.[21,70] Additionally, the selectivity towards the formation of methane was reported to be promoted upon incorporation of noble metal co-catalysts, e.g. platinum or palladium.[21,68]

Inspired by the pioneering work of Anpo et al.[58,67] mesoporous materials containing isolated titania sites were also studied by Frei et al.[71,72] and Mul et al.[73] *In-situ* infrared spectroscopy was performed by Frei et al.[71] using either H_2 or methanol as sacrificial electron donor. Only in the presence of sacrificial methanol formic acid formation associated with the formation of CO was observed, whereas the only product for the reduction of CO_2 was CO.[71] In presence of water no hydrogen atom able to reduce activated CO_2 is formed, and instead two OH radicals recombine to hydrogen peroxide and subsequently oxygen is released. Mul et al.[73] followed the mechanism proposed by Frei et al.[71] However, as mainly methane and longer chain hydrocarbons were observed by Mul et al.[73] the reaction mechanism was extended and formaldehyde was identified as a possible reaction intermediate, which can easily be converted to methane. Similar to the studies by Anpo et al.[58,67] and Frei et al.[71,72] all reactions proceed at one Ti-center. Recently, Stair et al.[74] doubted that CO_2 sufficiently interacts with isolated titania. They unambiguously showed that isolated titania is interacting with water by means of UV-Raman spectroscopy, but the interaction with CO_2 was not confirmed. Anpo et el.[21,68] tried to confirm the interaction by photoluminescence spectroscopy. A quenching of the characteristic photoluminescence band was observed, which was attributed to a transfer of the photo-excited electron from the Ti-center to CO_2.[21,68] Theoretical studies by Kanai et al.[75] indicated that there is a significantly reduced energy barrier for the first reduction of CO_2 at isolated titania, which might be attributed to a physical or chemical interaction. However, the the photoluminescence studies performed by Anpo et al.[21,68] are no direct evidence for the interaction of isolated titania and CO_2 as the quenching of a photoluminescence band might be the result of different optical properties of the materials in presence of CO_2. Furthermore, the studies were performed at 77 K and it is reasonable to assume that CO_2 is in the solid state. Thus, until know, the interaction of CO_2 with isolated titania is still not fully understood, and it is reasonable to assume that an improved interaction will lead to strong improvements in the efficiencies.[73]

Even though there is a discrepancy in the observed product distributions, the CO_2 interaction, and the suggested reaction mechanisms, a detailed knowledge of the different steps involved in the overall photocatalytic CO_2 processes is of great interest. Mechanistic studies of TiO_2 surfaces might provide further insights. The interaction of CO_2 and TiO_2 is well known and the photocatalytic properties of TiO_2 are better understood.[18–20,37] It certainly should be determined whether or not the reaction proceeding at isolated titania is different from the reaction mechanism on bulk-like TiO_2 structures[14] as Anpo et al.[21] showed that the reaction on iso-

lated titania is drastically enhanced and lower energy barriers were observed by Kanai et al.[75] facilitating the formation of CO. However, the discussed mechanisms for CO$_2$ reduction on isolated titania should be compared to *in-situ* spectroscopic studies and theoretical calculations on TiO$_2$ surfaces, which may not provide complementary information to the mechanistic studies on isolated titania.[14]

The recent experimental studies and theoretical calculations by Zapol et al.[69,76] and Rajah et al.[77] should be mentioned: The role of water and carbonates in the formation of methane was investigated by Zapol et al.[69] The EPR results showed the formation of hydrogen atoms, hydroxyl radicals, and CO$_3^-$ and it was specified that water is involved in the formation of OH radicals, competes with CO$_2$ as electron acceptor and efficiently stabilizes charges diminishing electron-hole recombination.[69] The influence of possible reaction intermediates like methanol, formaldehyde, and formic acid in the multistep CO$_2$ reduction process to methane (eq. 3.1-3.7) on TiO$_2$ was studied by Rajah et al.[77] also by means of EPR. They concluded that formic acid can be a reaction intermediate, which is subsequently reduced to methane, whereas methanol and formaldehyde are mainly acting as hole scavengers and tend to photooxidize.[77] Within this study the simplest reaction scheme for CO$_2$ reduction to methane was considered consisting of four consecutive two-electron proton-coupled reactions (eq. 3.1-3.4). All reaction intermediates in this sequence are one carbon atom molecules. Recently, Zapol et al.[76] considered a reaction mechanism in which reaction intermediates with two carbon atom molecules are involved. Interestingly, the molecules are formed spontaneously upon photooxidation of methanol and formaldehyde and are therefore complementary to the studies by Rajah et al.[77] It should be emphasized that mainly EPR was used, which is exclusively able to detect radical species. This may not give a complete picture of all the reaction pathways and intermediates involved.[14]

Finally, it should be noted that performing photocatalytic CO$_2$ reduction is rather challenging and thorough blind experiments have to be performed as carbon contaminations on the catalyst surface significantly influence the product yields[73] and photolysis of CO$_2$ to methane can take place at 185 nm irradiation regardless of the presence of any solid.[78]

4 Development of a Gas-phase Photoreactor
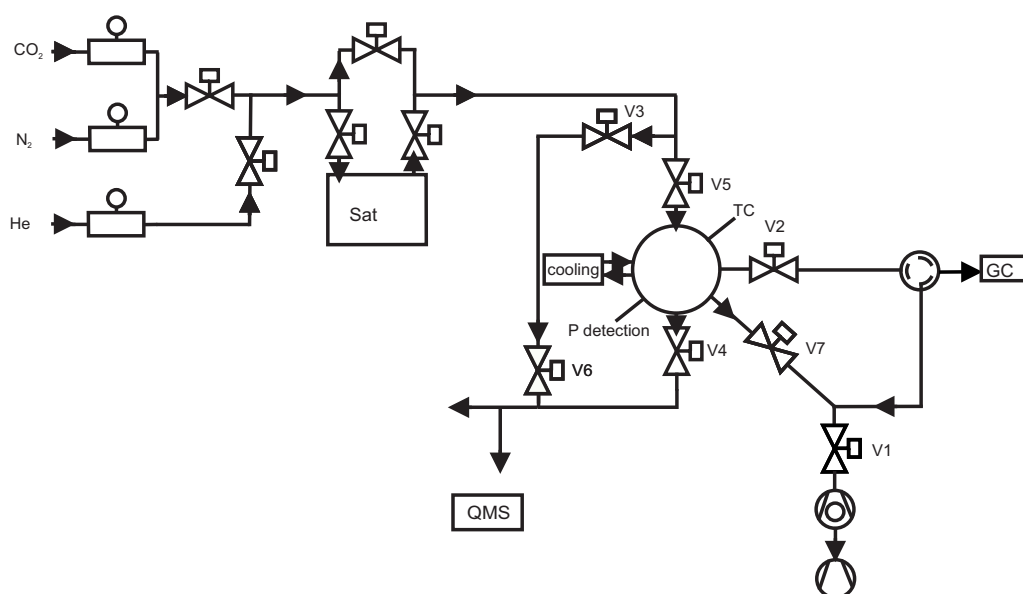
Figure 4.1: Flow scheme of the photoreactor set-up including the gas supply and the analysis devices.

A gas-phase photoreactor on the basis of a set-up design recently presented by Grimes et al.[17,79] was developed. A schematic drawing of the photoreactor is shown in Fig. 4.1. Pictures of the set-up are shown in Fig A1. The set-up mainly consists of a gas supply, a saturator, a reactor, analysis devices (Gas Chromatograph and Quadrupol Mass Spectrometer), and a pump system. Thus, the fully metal sealed home-made set-up has a total volume of 27 ml, which can be pumped down to a pressure of 10^{-8} mbar. While the temperature of the reactor and the saturator are maintained by water cooling, the gas lines can be heated to avoid water condensation. Reactions can be performed either in continuous or in batch mode. For this purpose product gases can be analyzed by a Quadrupol Mass Spectrometer (QMS, Balzer, Omnistar) in continuous mode and a Gas Chromatograph (GC, Shimadzu 14B) in batch mode. Trace gas analysis is performed with the GC, which is equipped with Thermal Conductivity Detector (TCD) and Flame Ionization Detector (FID) detectors. Two Porapak N columns and one molecular sieve column are used for separation. The photocatalyst is spread out on the bottom of the reactor to obtain a homogeneous light illumination. A 200 W Hg/Xe (Newport Oriel) lamp is used to irra-

diate the samples through a quartz window allowing for high transmissions of high energy UV light. The lamp is equipped with a water filter to avoid heating of the system by infrared (IR) irradiation. Thus, the light irradiance at the sample surface was measured to be 200 mW/cm^2 and 110 mW/cm^2 using a 320 nm cut-off filter. The gas supply consists of three different gas lines connected to helium, nitrogen, and carbon dioxide, which can be used as feed gases. Helium is mainly used to vary the carbon dioxide concentration in the feed gas. However, in case of water splitting experiments the helium feed is saturated with water. Nitrogen instead is mainly used as an internal standard during batch mode operation to adjust for the pressure drop during sampling.
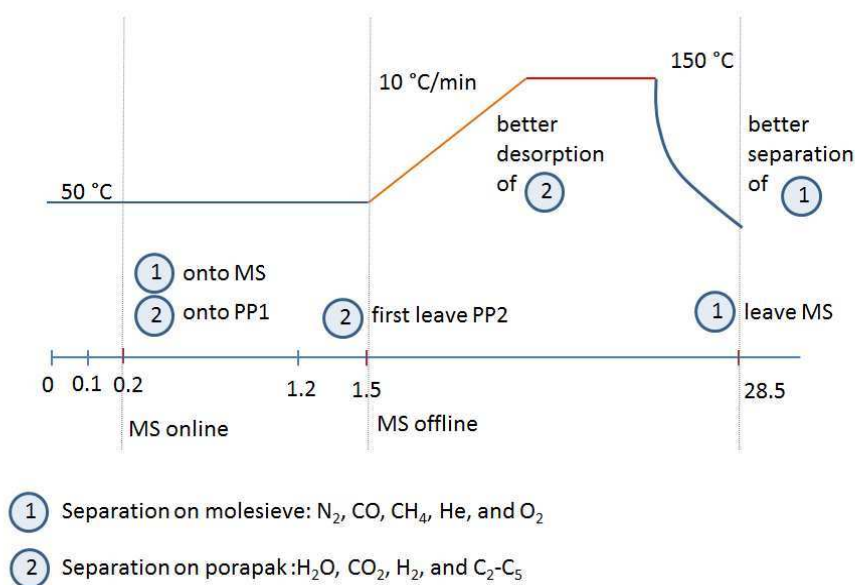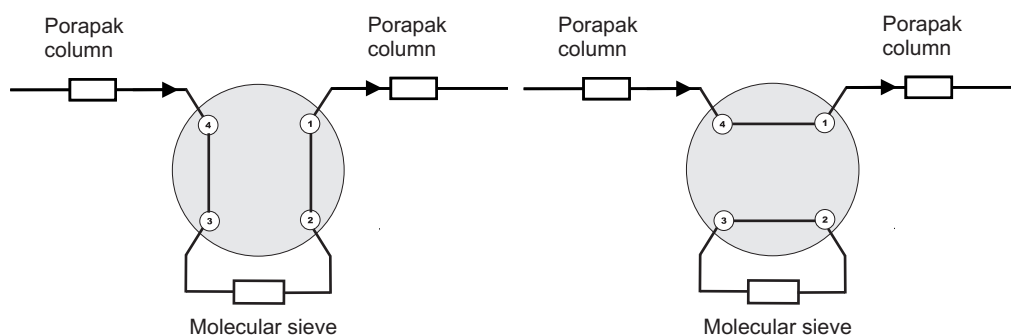
Figure 4.2: a) GC program containing the column- and the temperature program, the separation of gas molecules according to time is indicated. Flow sheet of the column arrangement in their switching events, to either set the molecular sieve column online (b) (event 92) or bypass (c) (event -92).

While the QMS, as mentioned, is mainly used for gas-phase water splitting experiments in a continuous mode, the GC was adjusted allowing for trace gas analysis of short-chain hydrocarbons. Trace gas analysis was achieved by the GC equipped with two Porapak N columns

Table 4.1: Standard GC settings. Temperature and current of the TCD are chosen to avoid water condensation.

detector	temperature	current
FID	200 °C	-
TCD	150 °C	50 mA

carrier gas flow behind the columns	19.2 ml/min	
adjusted carrier gas pressure	500 kPa	
adjusted reference gas pressure	165 kPa	

and a molecular sieve column. Furthermore, a Thermal Conductivity Detector (TCD) and a Flame Ionization Detector (FID) connected in series at the column outlet are used. The standard settings of the GC are summarized in Table 4.1. With this arrangement of columns and detectors the analysis of the different compounds in the reaction product stream is feasible. The product gas stream normally containing nitrogen (N_2), helium (He), carbon dioxide (CO_2), and water (H_2O), as well as the desired products, such as C_1 to C_4 hydrocarbons and alcohols can be separated using a temperature program and column switching procedure as shown in Fig. 4.2. In a first step of the analysis programm the gases, which are not interacting with the Porapak N column, are flushed straight to the molecular sieve column. Afterwards, the molecular sieve column is set bypass and the molecules are stored there, while mainly H_2O, CO_2, H_2, and C_2-C_4 are separated by the Porapak N column. Reasonable retention times of the gases are achieved by heating the Porapak N column. After cooling the system the molecular sieve column is switched online and the retaining molecules are analyzed. While small or incombustible gases like CO_2, N_2, H_2O, H_2, O_2, and CO are detected by the TCD, all gases being easily flammable (C_1-C_5 and small alcohols) are detected by an FID.

Table 4.2: Retention times of different molecules using the specified sampling settings. Assignment of the molecules to the separation column and the appropriate detector.

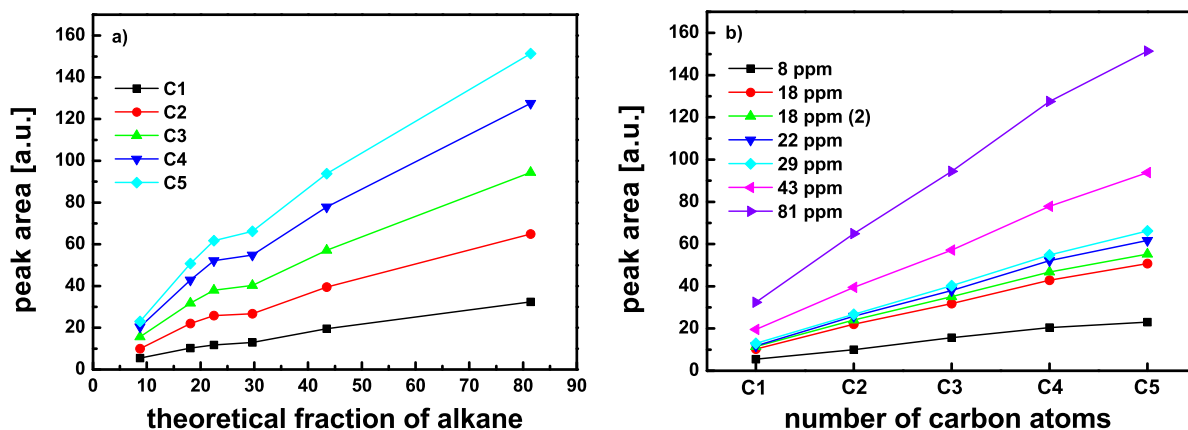| molecule	retention time	column	detector
H_2O	10	PP	TCD
N_2	30.2 min	MS	TCD
CO_2	2.8 min	PP	TCD
CH_4	31.9 min	MS	FID
C_2H_4	3.4 min	PP	FID
C_2H_6	3.7 min	PP	FID
C_3H_8	7.8 min	PP	FID
C_4H_{10}	11.9 min	PP	FID
C_4H_{12}	17.4 min	PP	FID
CH_3OH	11.6 min	PP	FID

Figure 4.3: a) Plot of peak area derived by the integration of the peak area of the respective FID signal vs. the theoretical fraction of the C1-C5 alkanes in the feed gas. b) GC calibration with C1-C5 hydrocarbons, peak area vs. the number of carbon atoms in the respected hydrocarbon.

Calibration of the GC for quantitative product analysis

To study the detection of small substance concentrations with the gas chromatograph, a dilution series was applied. Therefore, a gas mixture containing 1000 ppm of C_1-C_5 hydrocarbons and 10 % N_2 balanced with He was used and mixed with high purity He (6.0). Thus, C_1-C_5 hydrocarbon concentrations of 9 ppm were achieved.

The integrated peak areas plotted against the calculated fraction in ppm of different hydrocarbons are shown in Fig. 4.3a. Additionally, the peak areas plotted against the number of carbon atoms are shown in Fig. 4.3b. It is evident from these plots that the signal area increases for each compound with increasing number of carbon atoms in a linear manner, demonstrating the high quality of the calibration procedure. Furthermore, it can be seen that the peak area also increases linearly with the overall concentration of the detected compound. The deviations from the linear graph shape is caused by an overall increasing gas flow in the dilution series necessary to achieve low C_1-C_5 hydrocarbon concentrations, and thus an increase in the reactor pressure. However, as mainly low C_1-C_5 hydrocarbon concentrations are expected a linear fit was chosen in agreement with the low concentration region (Fig. 4.3a). Besides C_1-C_5 hydrocarbons, methanol was calibrated using a 3000 ppm MeOH/He gas mixture. Concentrations of 25 ppm MeOH were achieved using the dilution procedure with He, which was easily detected by the GC. By repeating the calibration procedure for different hydrocarbon concentrations an uncertainty of the calibration of 5% was estimated. The retention times of the most frequently detected molecules using the explained sampling programm are summarized in Table 4.2.

Photocatalytic CO2 reduction experiments

Even though the reactor was mainly developed for gas-phase photocatalytic CO_2 reduction it is also possible to perform gas-phase photocatalytic water splitting experiments in continuous

mode using the QMS as mentioned above. Photocatalytic CO_2 reduction experiments are normally performed in batch mode due to the low product yields. Due to the low product formation yields a pretreatment of the photocatalyst by irradiating the material in humid He is necessary to confirm that possible carbon contaminations on the catalyst surface are not involved in the product formation.[73] The actual photocatalytic CO_2 reaction is conducted by introducing a water-saturated reactant feed containing x% CO_2/1% N_2 balanced by He into the photoreactor. The water content in the reactant feed is mainly determined by the temperature of the two stainless steel saturators, which can be easily adjusted between 0 °C and 25 °C using a cryostat. Thus, the water content can be varied between 6042 ppm and 3.14 %. Prior to the actual CO_2 reduction experiment the reactor is pumped down to 5 x 10^{-3} mbar by means of a rotary pump or a turbomolecular pump if lower pressures are required. In this way a base pressure of 5 x 10^{-8} mbar can be achieved. Afterwards, the reactant feed is introduced into the reactor until atmospheric pressure is obtained. A fully water-saturated gas-phase can be achieved by flowing the reactant feed through the reactor for a certain period of time or by repeating pumping/dosing cycles. Afterwards, the reactor pressure is adjusted to a desired value and the reactor is closed. Thus, the reaction is performed in batch mode by illumination the sample for 7 h. Sampling can be performed at given time intervals, which is mainly limited by the sampling time of the GC programm. With the described settings sampling takes 50 min in total. Each sampling causes a pressure drop in the reactor of 100 mbar. A quantitative analysis of the products is achieved using 1% N_2 as internal standard.

5 Photocatalytic CO$_2$ Reduction - Single-site TiO$_x$ Materials

In this chapter Ti-single site catalysts for the photocatalytic reduction of CO$_2$ are presented. In the first section synthesis and characterization of the single-site photocatalysts are described and the incorporation of additional CO$_2$ by means of isolated ZnO$_x$ species is introduced. The second section is dealing with the photocatalytic CO$_2$ reduction on isolated TiO$_x$ species and the effect of photo-deposited Au nanoparticles is discussed. Finally, the photocatalytic activity of the as-synthesized and Au-modified materials with respect to TiO$_x$ loading and the state of ZnO$_x$ species is discussed.

5.1 Modification of titanate-loaded mesoporous silica by grafting of zinc oxide

Abstract[1]

Mesoporous silica (SBA-15) loaded with TiO$_x$ species was synthesized by anhydrous grafting of titanium isopropoxide, and a novel procedure for the preparation of ZnO$_x$/SBA-15 materials by grafting of Zn(acac)$_2$ was explored. The TiO$_x$/SBA-15 and ZnO$_x$/SBA-15 materials as well as subsequently prepared bifunctional ZnO$_x$- and TiO$_x$-containing SBA-15 materials were characterized in depth by combining N$_2$ physisorption measurements, UV-Vis, X-ray photoelectron and X-ray absorption spectroscopy, and CO$_2$ and NH$_3$ temperature-programmed desorption experiments. The characterization results confirmed a close proximity of ZnO$_x$ and TiO$_x$ in the subsequently grafted materials. Due to strong interactions between the Zn precursor and the SiO$_2$ surface the order of the ZnO$_x$ and TiO$_x$ grafting steps affected the amount of Ti-O-Zn bonds formed in the materials. When ZnO$_x$ is present in SBA-15, subsequently grafted TiO$_x$ is higher coordinated and more Ti-O-Zn bonds are formed compared to SBA-15 in which TiO$_x$ was introduced first indicating strong interactions between the Ti precursor and ZnO$_x$. While all TiO$_x$ and ZnO$_x$-containing samples exhibit a large amount of acidic sites, ZnO$_x$ present as isolated species or small clusters in SBA-15 significantly improves the CO$_2$ adsorption capacity by introducing basic sites. In the subsequently grafted samples the amount of acidic and basic sites is found to be unaffected by the order in which the two transition metals are introduced.

5.1.1 Short Introduction

In recent years single-site catalysts have been widely studied, and especially TiO_2 dispersed in mesoporous SiO_2 has attracted much attention as catalyst or catalyst support in various fields such as photocatalysis or acid catalysis.[65,80,81] Due to its different coordination, the reactivity and selectivity of TiO_x species in mesoporous materials considerably differs from that of bulk TiO_2. Differences in the activity and selectivity were observed in liquid-phase and vapor-phase epoxidation reactions,[82–84] or in the gas-phase oxidation of methanol.[80,85] In these studies different preparation routes have been developed to achieve a maximum amount of isolated TiO_x sites. While the incorporation of the tetrahedrally coordinated TiO_4 species into the silica walls has the highest probability of yielding exclusively isolated sites, the maximum amount that can be incorporated is very low,[73] and a considerable fraction of the sites may not even be accessible within the wall structure. Impregnation or chemical vapor deposition, on the other hand, make it possible to achieve a much higher loading of the transition metal on the silica surface, but the probability of the Ti species being isolated decreases significantly.[86,87] In this respect, anhydrous grafting is a powerful method: the selective reaction of the precursor with the silanol groups makes it possible to achieve rather high loadings of relatively isolated species on the silica walls.[60,65,88] Furthermore, it was shown that anhydrous grafting is an effective method to control both the amount and the degree of agglomeration of TiO_x species.[65]

Different degrees of agglomeration of the titania component on the silica surface influence their behavior. For example, previous work on TiO_x grafted onto MCM-48 has shown that the reducibility of the titania component is a function of its degree of agglomeration.[89] It is reasonable to assume that the degree of agglomeration, the mobility/delocalization of the electrons or the reactivity of the lattice oxygen may influence the product spectrum in many (photo)catalytic reactions.

In their pioneering work, Anpo et al.[58,67,68,90] demonstrated that isolated tetrahedral TiO_x species on silica are active photocatalysts for the formation of methane and methanol from CO_2. It was suggested that both CO_2 and H_2O adsorb on the tetrahedral TiO_4 species, and the mechanism was postulated to involve hydrogen and methyl radicals, which were both detected by electron paramagnetic resonance (EPR) spectroscopy.[67]

There is currently a dispute about the adsorption of the reactants CO_2 and H_2O at the tetrahedral titania site. Anpo's group observed that the addition of either of the two reactants decreased the photoluminescence emission originating from the electron-hole recombination at the tetrahedral Ti site.[67] It was inferred that the recombination does not take place, because the electron is transferred to the adsorbate. A study by Danon et al.[74] monitored the UV resonance Raman vibrational band of the tetrahedral TiO_4 species upon adsorption of CO_2 or H_2O confirming the adsorption of H_2O at this site, but there was no indication for the adsorption of CO_2. Neither the studies by Anpo et al.[67] nor that by Danon et al.[74] proved the adsorption of CO_2 on isolated TiO_x species by means of a direct or quantitative technique such as temperature-programmed

desorption (TPD), thermogravimetry, or microcalorimetry. The adsorption of CO$_2$ usually requires the presence of basic sites, and CO$_2$ is a frequently used probe molecule for the detection of basic sites.[91] The acidic properties of grafted TiO$_2$/SiO$_2$ materials have been characterized by Iengo et al.[92] by means of TPD of pyridine. In a study of amine-functionalized TiO$_x$/SBA-15 Srivastava et al.[93] detected a small amount of CO$_2$ adsorbed on amine-free TiO$_x$/SBA-15. However, the amount did not differ from the bare SBA-15 and no activated CO$_2$ was found by infrared spectroscopy. Only the amine-functionalized TiO$_x$/SBA-15 materials were shown to effectively activate CO$_2$ in chloropropene and styrene carbonate synthesis.[93]

Magnesium- and alumina-modified SBA-15, as well as amine-functionalized TiO$_x$/SBA-15, have been reported to possess acidic and basic sites, however, no transition metal-modified TiO$_x$/SBA-15 material providing both acidic and basic sites has been reported yet.[93–95] Zinc oxide is known for the amphoteric nature of its surface, adsorbing CO$_2$ on a variety of basic sites.[91,96,97] Apart from the weakly adsorbed linear species, a variety of carbonates and bicarbonates can be observed.[98] ZnO is a photocatalyst with a similar band gap as TiO$_2$. Moreover, it is a common active ingredient of methanol synthesis catalysts such as ZnO/Cr$_2$O$_3$ and Cu/ZnO/Al$_2$O$_3$.[99] With respect to the photocatalytic CO$_2$ reduction it appears to be favorable to combine TiO$_x$ with ZnO or ZnO$_x$ species in a close interfacial contact in order to make use of the water splitting properties of titania and the CO$_2$ sorption properties of ZnO. Similar to the thermal catalytic processes, the adsorption of the reactants can be one of the rate-limiting steps in photocatalytic reactions. It has also been suggested that due to the generally fast electron-hole recombination kinetics, an interfacial electron transfer seems only kinetically competitive, when the reactant is already preadsorbed.[74,100] Therefore, it is desirable not only to characterize, but also to increase the amount of surface-bound CO$_2$ and H$_2$O.[93] While the synthesis of ZnO inside micro- or mesoporous silica has previously been reported, the acid/base properties of the obtained species are barely characterized.[101–104] Furthermore, a reproducible grafting technique for small, well-defined ZnO$_x$ domains in silica using Zn(acac)$_2$ has not been reported yet.

In this contribution, titania and zinc oxide species in SBA-15 are synthesized on the silica surface by means of anhydrous grafting of chloride-free precursors. A thorough characterization with different spectroscopic techniques revealed that high loadings of isolated or slightly agglomerated TiO$_x$ species can be obtained. With respect to ZnO$_x$, it is shown that grafting of Zn acetylacetonate results in the formation of isolated ZnO$_x$ species. When both ZnO$_x$ and TiO$_x$ are present on SBA-15, there is an interaction between these species. The characterization results indicate that the structure of titania depends on the order in which the transition metals are introduced into SBA-15.

Furthermore, it is shown that both TiO$_x$ and ZnO$_x$ in SBA-15 act as acidic sites. In addition, the presence of ZnO$_x$ enhances the sorption capacities of CO$_2$, as it introduces basic sites. In spite of the differences that were observed in the coordination of titania, the order in which

the transition metals are grafted onto SBA-15 does not influence the total amount of acidic and basic sites.

Experimental

Sample synthesis

The SBA-15 support was synthesized according to well-established procedures.[105] 4 g of Pluronic P123 (Sigma Aldrich) were dissolved in 30 ml of deionized water and stirred for 4 h to ensure good mixing. After adding 120 ml of 2 M HCl, stirring was continued for 1 h at room temperature and for 1 h at 313 K. At this temperature, 9 g (8.4 ml) of tetraethylorthosilicate (TEOS) were added dropwise under vigorous stirring. The mixture was kept at 313 K for 24 h and afterwards at 373 K for 48 h. The reaction mixture was cooled to room temperature, filtered, washed with deionized water and dried for 2 h. Calcination was performed in synthetic air ramping the temperature at 1 K min^{-1} from room temperature to 623 K, holding the temperature for 1 h, then ramping to 823 K at 1 K min^{-1} with a holding step of 6 h.

The grafting procedure has been reported previously for the deposition of TiO$_x$ on MCM-48.[89,106] It is completely performed under inert atmosphere to avoid the presence of H$_2$O. 2 g of the support material (here SBA-15) were dried over night at 393 K. The precursor Ti(O^{i}Pr)$_4$ (99.999 %, Sigma Aldrich, stored in a glove box) was dissolved in about 50 ml of dry toluene. The amount was chosen according to the desired surface coverage, but it was never higher than an equivalent of 1.5 Ti nm^{-2}. The precursor solution was brought in contact with the dry support at room temperature and stirred for at least 4 h. The support was separated from the solution either by sedimentation or centrifugation (6000 min^{-1} for 3 to 5 min). The support was washed three times with dry toluene (about 30 ml), separating sample and solution each time as mentioned above. It was then dried under dynamic vacuum.

Calcination was performed by heating the sample with 2 K min^{-1} in a flow of 100 ml min^{-1} N$_2$ to 573 K holding the temperature for 1 h. During the time at 573 K, the gas flow was switched to synthetic air, before the temperature was ramped at 2 K min^{-1} to 773 K and kept for 4 h. The samples were stored in a desiccator prior to use.

The grafting of ZnO$_x$ species was performed using zinc acetylacetonate (Zn(acac)$_2$) as precursor (Alfa Aesar). Due to the undefined purity and high water content of the precursor, it was purified by means of sublimation. All steps of the grafting were similar except for the solvent, which was changed from toluene to dry tetrahydrofurane (THF). The temperature during the final calcination was lowered, so that the sample was heated in N$_2$ to 523 K only, and in synthetic air only up to 673 K.

Characterization

The materials were investigated by means of elemental analysis, nitrogen physisorption, UV-Vis spectroscopy, UHV-Fourier-Transformed Infrared spectroscopy(UHV-FTIR), X-ray photoelectron spectroscopy (XPS), X-ray absorption spectroscopy (XAS), and temperature pro-

grammed desorption (TPD). Elemental analysis was performed by inductively coupled plasma optical emission spectroscopy (ICP-OES) to determine the amount of titanium in the samples, while atomic absorption spectroscopy (AAS) was used to determine the Zn content. ICP-OES measurements were performed with a PU701 instrument supplied by UNICAM. A SpectrAA 220 instrument (Varian) was used for AAS measurements. Static N$_2$ physisorption experiments were performed at the boiling point of liquid N$_2$ subsequent to out-gassing at 200 °C for 2 h in a Bellsorp max instrument from Belcat, Inc. The surface areas of all samples were estimated according to the method by Brunauer, Emmett and Teller (BET), whereas the pore size distribution was obtained applying the method by Barrett, Joyner and Halenda (BJH).[107,108]

Micropore volumina were calculated using the t-method.[109] UV-Vis diffuse reflectance spectra (DRS) were recorded in a Perkin Elmer Lambda 650 UV-Vis spectrometer equipped with a Praying-Mantis mirror construction using MgO as the 100 % reflection reference. The samples were dehydrated in flowing syn. air in an *in-situ* UV-Vis cell (Harrick) at 400 °C for 1 h prior to the measurement. As TiO$_x$/SiO$_2$ is not a semiconductor, nor a structurally homogeneous material, the Tauc-Plot cannot be used to determine the absorption on sets. Instead, absorption onsets were estimated from a linear fit to the incline of the Kubelka-Munk function.

XPS was performed in a UHV set-up equipped with a Gammadata-Scienta SES 2002 analyzer. The base pressure in the measurement chamber was 5 x 10^{-10} mbar. Monochromatic Al Kα (1486.6 eV; 13.5 kV; 37 mA) was used as incident radiation, and a pass energy of 200 eV was chosen resulting in an effective instrument resolution higher than 0.6 eV. Charging effects were compensated using a flood gun, and binding energies were calibrated based on positioning the main C 1s peak at 285 eV, which originates from carbon contaminations. Prior to the measurements the samples were dehydrated at 200 °C under ultra-high vacuum (UHV) conditions. Measured data were fitted using Shirley-type backgrounds and a combination of Gaussian-Lorentzian functions with the CasaXPS software. The Ti/Si atomic concentration ratios were obtained by determining the integral area of the Gaussian-Lorentzian functions and correcting the values by the specific atomic sensitivity factors proposed by Wagner.[110]

UHV-FTIR experiments with the materials were carried out using a UHV apparatus, which combines a state-of-the-art vacuum IR spectrometer (Bruker, VERTEX 80v) with a novel UHV system (Prevac). (For details, please see ref.[111]) The powder samples were first pressed into a gold covered stainless steel grid and then mounted on a sample holder that was particularly designed for the FTIR transmission measurements under UHV conditions. The base pressure in the measurement chamber was 2 x 10^{-10} mbar. The optical path inside the IR spectrometer and the space between the spectrometer and UHV chamber was evacuated to avoid atmospheric moisture adsorption, thus resulting in a high sensitivity and long-term stability.

XAS around the Ti K-edge (4966 eV) and the Zn K-edge (9659 eV) was measured in transmission mode at Hasylab, beamline C (Hamburg, Germany). Both X-ray absorption near edge spectroscopy (XANES) and extended X-ray absorption fine structure (EXAFS) were measured.

The double Si(111) crystal monochromator was detuned to 50 % of its maximum intensity to reduce the higher harmonics. Prior to the measurements, the samples were re-calcined at 773 K for 1 h in synthetic air, purged with nitrogen and sealed in Kapton tape inside a glove box. The spectra were then recorded under vacuum at liquid nitrogen temperature. A foil of Ti or Zn, respectively, inserted between the second and third ionization chamber, was measured simultaneously and used as a reference for energy calibration. Data treatment was carried out with the software package VIPER.[112] In the spectra of the absorption coefficient μ, a Victoreen polynomial was fitted to the pre-edge region for background subtraction. A smooth atomic background μ_0 was evaluated using a smoothing cubic spline. The Fourier analysis of the km^2-weighted experimental function $\mu = (\mu - \mu_0)/\mu_0$ was performed with a Kaiser window.

TPD measurements were performed in a stainless-steel flow set-up equipped with a calibrated on-line mass spectrometer (Balzers GAM400). In a typical experimental sequence 50 mg of catalyst were placed in a quartz-lined stainless-steel U-tube reactor. A thermocouple was placed into the catalyst bed to measure the temperature during the desorption experiments. As a pre-treatment the sample was heated to 400 °C with a heating ramp of 10 K min^{-1} in 50 Nml min^{-1} 1 % O_2/He and then kept for 1 h. After cooling to room temperature the reactor was purged with He and subsequently CO_2 adsorption was performed with a flow rate of 50 Nml min^{-1} 4.1 % CO_2/He for 15 min. After purging with He for 30 min the temperature was increased to 400 °C with a heating ramp of 10 K min^{-1} and held at this temperature for 1 h. During desorption the concentrations of CO_2 and He were measured continuously. Afterwards, NH_3 was adsorbed at 100 °C with a flow rate of 50 Nml min^{-1} 0.8 % NH_3/He for 15 min and subsequently, after cooling to 60 °C in He, the NH_3 TPD was conducted similarly.

5.1.2 Results and Discussion

Structural characterization

The synthesis of the SBA-15 support was repeated several times, and surface areas from 787 m^2 g^{-1} to 830 m^2 g^{-1} were obtained reproducibly, resulting in an average surface area of 800 m^2 g^{-1} and an average pore radius of 3.5 nm.

The transition metal loading of the Ti(x)/SBA-15 materials was obtained by means of ICP-OES, where x is specified in Ti atoms nm^{-2}. The Ti loadings and the corresponding band edges are summarized in Table 5.1. The weight percentages of Ti determined by ICP-OES were converted to Ti nm^{-2} using the BET surface of SBA-15 of 800 m^2 g^{-1}, according to Ti/nm^2 = (m(Ti)/M(Ti) x NA) / (800 m^2/g x (1-m(Ti)-m(Zn)) x 1018 nm^2/m^2) in which m(Ti) denotes the grams of Ti per gram of sample, M(Ti) is the molar mass of titanium, and N_A is the Avogadro number. For Zn/nm^2 calculations were done accordingly. The calculated values show that the desired loading of Ti is obtained for the Ti0.3/SBA sample. A loading of $\sim$ 1 Ti nm^{-2} is obtained reproducibly, when an equivalent amount of 1.5 Ti nm^{-2} as in case of Ti1.0/SBA is

Table 5.1: Ti and Zn contents, edge energies, and BET surface areas of the grafted samples.

Sample[a]	Ti loading (ICP-OES)		Zn loading (AAS)		Edge energy (UV-Vis)	BET surface area
	[wt% Ti]	[Ti/nm^2]	[wt% Zn]	[Zn/nm^2]	[eV]	[m^2/g]
Ti0.3/SBA	2.1	0.3	-	-	4.34	749
Ti1.0/SBA	6.3	1.0	-	-	4.11	653
Ti2.0/SBA	11.3	2.0	-	-	3.87	575
Ti2.7/SBA	14.8	2.7	-	-	3.77	460
Zn1.0/SBA	-	-	7.5	1.0	-	760
Ti0.9/Zn0.9/SBA	4.5	0.9	6.7	0.9	4.21	515
Zn0.7/Ti0.9/SBA	4.9	0.9	4.9	0.7	4.08	508
Zn0.3/SBA	-	-	2.3	0.3	-	760
Zn0.3/Ti1.2/SBA	6.7	1.2	2.6	0.3	4.13	552
Ti1.2/Zn0.3/SBA	6.9	1.2	2.3	0.3	4.15	n. d.

[a] Ti(x)/Zn(y)/SBA: x and y denote atoms nm^{-2}

used in the grafting procedure. Furthermore, subsequent grafting of two or even three times using a solution equivalent to 1.5 Ti nm^{-2} resulted in $\sim$ 2 Ti nm^{-2} and $\sim$ 2.7 Ti nm^{-2} in case of Ti2.0/SBA and Ti2.7/SBA. These results indicate that a maximum of 1 Ti nm^{-2} can be deposited per grafting step. The same observation has been made for the grafting of Ti(OiPr)$_4$ onto MCM-48,[89] and a maximum achievable loading of roughly 12 to 13 wt % TiO$_2$ (not Ti metal) has previously been reported in a study of different grafting procedures on SBA-15.[80,88] The increase in coverage by about 1 Ti nm^{-2} after each grafting step also suggests that the OH groups as anchoring sites for the precursor are recovered after the calcination step.[113]

In order to check for the possible segregation of TiO$_x$ to the external surface of the SBA-15 particles, the surface Ti/Si ratios were determined by XPS measurements. The results of the XPS measurements are shown in Fig. 5.1. Surface segregation of Ti can be excluded as the Ti/Si ratios determined by ICP-OES match those derived from XPS. Obviously, the diffusion of the precursor through the pores of the SBA-15 support material is fast and the TiO$_x$ species are evenly distributed within the pores of the SBA-15.

For the synthesis of Zn-containing samples the as-received Ti1.0/SBA sample was subsequently grafted with the equivalent amount of 1.5 Zn/nm^2 resulting in the sample labeled Zn0.7/Ti0.9/SBA. Furthermore, in sample Ti0.9/Zn0.9/SBA the order of grafting steps was changed, so that Ti was grafted on a sample that already contained Zn. Finally, Zn1.0/SBA was prepared without an additional grafting of Ti to investigate the effect of ZnO$_x$ species incorporated in a SBA-15 matrix. The Zn and the Ti loadings are summarized in Table 5.1. Small differences in the calculated surface loadings (in metal nm^{-2}) might be attributed to a slightly different surface area or the error limit in the results obtained by AAS or ICP-OES. In agree-
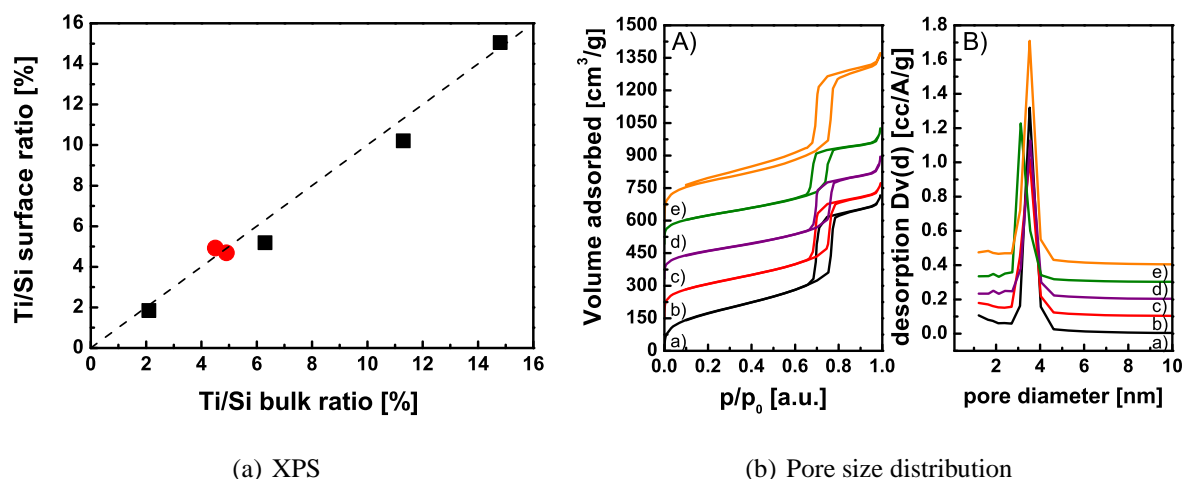
(a) XPS   (b) Pore size distribution

Figure 5.1: (a) Ti/Si surface ratios derived from XPS as a function of the Ti/Si bulk ratios; Ti(x)/SBA (black squares), Zn-containing samples (red circles). (b) A) N_2 isotherms obtained with a) SBA-15, b) Ti1.0/SBA, c) Zn0.7/Ti0.9/SBA, d) Ti0.9/Zn0.9/SBA, and e) Zn1.0/SBA. B) Pore size distribution of these samples derived by applying the BJH equation to the desorption branch of the isotherms.

ment with the results obtained for Ti(x)/SBA-15 materials, the maximum loading of Zn which can be obtained in one grafting step is 1 Zn/nm^2.

The N_2 isotherms and the pore size distribution of the synthesized materials shown in Fig. 5.1 are nearly unchanged for all materials independent of the grafting order or the species deposited onto SBA-15 with a narrow intense signal with a pore size maximum at a radius of 3.5 nm. The overall pore volume decreases after the first grafting step for Ti1.0/SBA accompanied by a decrease in BET surface area of roughly 150 m^2/g. This is not observed when only a small amount of Ti (0.3 Ti/nm^2) is deposited (Table 5.1). The BET surface area and the pore volume of Zn1.0/SBA are almost unchanged compared to the bare SBA-15 support. SBA-15 displays a certain degree of microporosity,[114,115] and the decrease in surface area in Ti(x)/SBA-15 materials is attributed to a clogging of the micropores by TiO_x species, whereas the micropores were unchanged after grafting of Zn.[116] Using the t-method we confirmed this suggestion by calculating the micropore volume of the SBA-15, Ti1.0/SBA, and the Zn1.0/SBA material. A micropore volume of 0.054 cm^3/g was calculated for the SBA-15. The micropore volume was not changed upon grafting of Zn as in Zn1.0/SBA (0.06 cm^3/g), whereas the micropore volume drops to 0.02 cm^3/g in case of Ti1.0/SBA. For higher loaded samples there is no further decrease in the overall pore volume, while the specific BET surface area decreases further in Ti2.0/SBA, Ti2.7/SBA, and in the subsequently grafted samples Zn0.7/Ti0.9/SBA and Ti0.9/Zn0.9/SBA. This can be attributed to a higher content of heavier elements that do not contribute to the surface area. Interestingly, the decrease in surface in the subsequently grafted samples Ti0.9/Zn0.9/SBA and Zn0.7/Ti0.9/SBA is more pronounced than in Ti2.0/SBA.
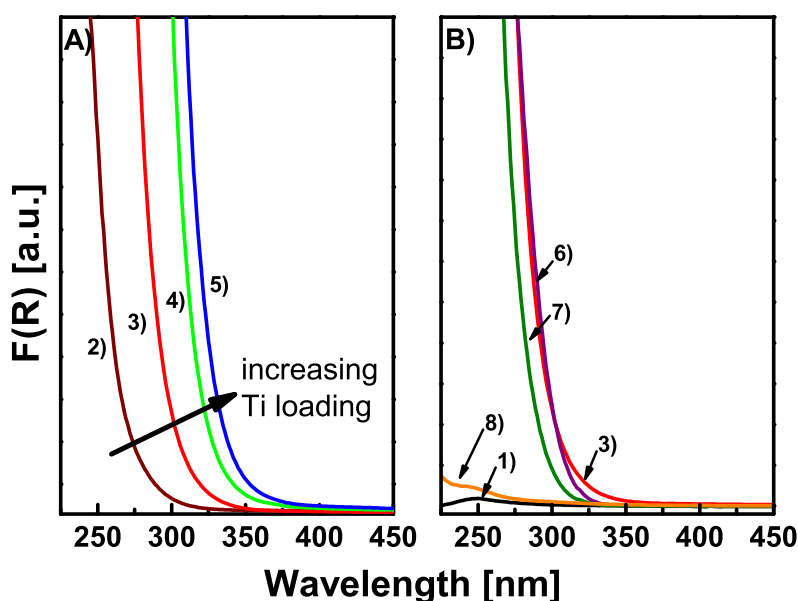
Figure 5.2: A) Diffuse reflectance UV-Vis spectra of dehydrated Ti(x)/SBA-15 materials with vary-
ing Ti loading and B) DR UV-Vis spectra of dehydrated samples containing ZnO$_x$
species. 1) SBA-15, 2) Ti0.3/SBA, 3) Ti1.0/SBA, 4) Ti2.0/SBA, 5) Ti2.7/SBA, 6)
Zn0.7/Ti0.9/SBA, 7) Ti0.9/Zn0.9/SBA, and 8) Zn1.0/SBA materials.

UV-Vis diffuse reflectance spectroscopy, XPS, and XAS were used in order to investigate the
chemical state and the relative dispersion of Ti and Zn within the SBA-15 matrix.

From UV-Vis diffuse reflectance measurements, the light absorption of the Ti(x)/SBA-15 mate-
rials was estimated by using the Kubelka-Munk function. The edge energies for all samples are
summarized in Table 5.1. The absorption onsets of the four different dehydrated Ti(x)/SBA-
15 materials are shown in Fig. 5.2A. All samples exhibit an absorption onset in the range of
270 - 350 nm, which is clearly blueshifted compared to bulk anatase. While SBA-15 shows
no clear absorption feature in the UV-Vis spectrum, Ti0.3/SBA absorbs below 270 nm. Thus,
the absorption feature observed in the UV-Vis measurements is solely influenced by the pres-
ence and the local electronic structure of TiO$_x$. The absorption edge of Ti0.3/SBA was derived
to be 4.34 eV. Compared to Ti0.3/SBA the higher loaded sample Ti1.0/SBA is redshifted by
$\sim$ 0.2 eV. Ti2.0/SBA and Ti2.7/SBA are further redshifted, and the corresponding absorption
edge energies were calculated to be 3.87 and 3.77 eV, respectively. UV-Vis measurements per-
formed by Wachs et al.[65] showed that the absorption edge clearly depends on the degree of
agglomeration of the TiO$_x$ domains. They obtained an absorption edge energy of 4.3 eV for
isolated tetrahedrally coordinated TiO$_x$, which is in good agreement with the absorption edge
energy determined for Ti0.3/SBA. Furthermore, they pointed out that absorption edge energies
close to 3.4 eV can be observed for polymeric TiO$_x$ chains. Similar trends with increasing Ti
content were reported by Brub et al.[84,117] and Yamashita et al.[118]. The assignment of the
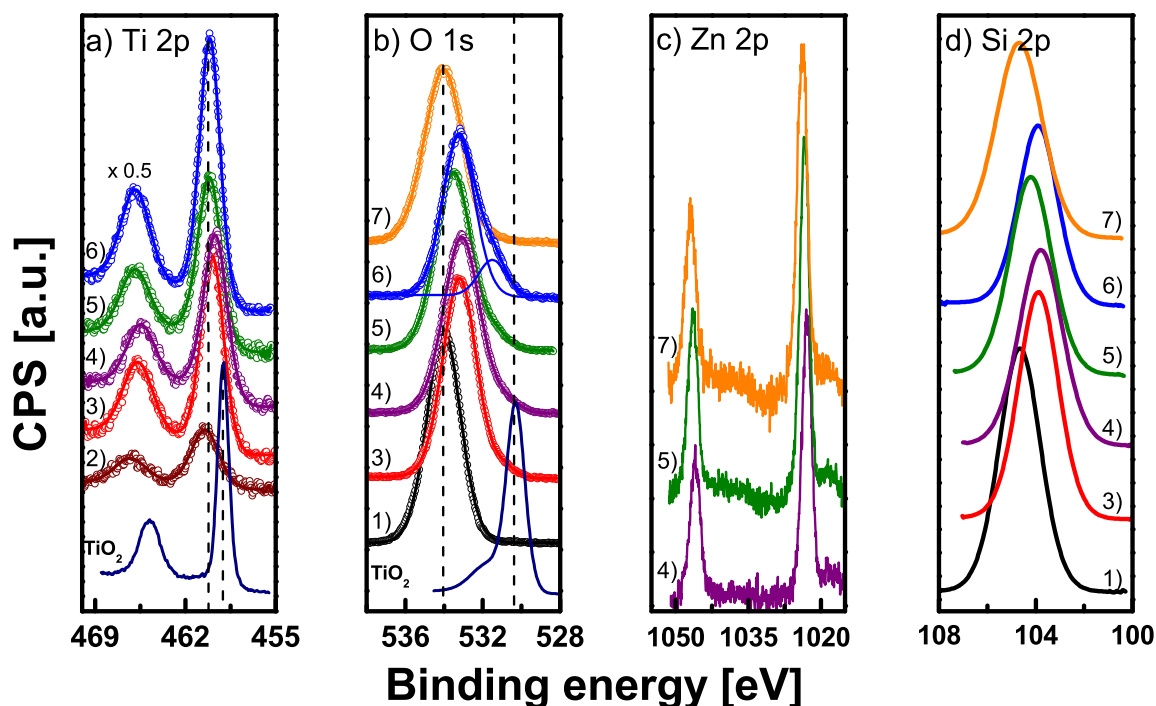
Figure 5.3: XP spectra in the a) Ti 2p region, b) O 1s region, c) Zn 2p region, and d) Si 2p region: 1) SBA-15, 2) Ti0.3/SBA, 3) Ti1.0/SBA, 4) Zn0.7/Ti0.9/SBA, 5) Ti0.9/Zn0.9/SBA, 6) Ti2.7/SBA, and 7) Zn1.0/SBA. Bulk TiO_2 is included as a reference.

intermediate species with absorption edge energies in between those values is still not fully clear.

In Fig. 5.2B the UV-Vis spectra of the different Zn-containing SBA-15 materials and the Ti1.0/SBA sample are shown. Zn1.0/SBA (Fig. 5.2B, trace 8)) absorbs some deep UV light comparable to the bare SBA-15 support (Fig. 5.2B, trace 1)). No indication for the presence of bulk ZnO is observed. Similar UV-Vis spectra were reported by Chen et al.[101,119] for sub-nanometric ZnO_x clusters in zeolites and Mihai et al.[103] for amorphous ZnO_x supported on SBA-15. Subsequently grafted samples containing TiO_x and ZnO_x species show absorption features, which are clearly related to TiO_x grafted onto the SBA-15 supports. While the absorption onsets of Zn0.7/Ti0.9/SBA, Zn0.3/Ti1.2/SBA, and Ti1.2/Zn0.3/SBA match the onset of Ti1.0/SBA, there is a blueshift of the absorption onset in case of Ti0.9/Zn0.9/SBA (Fig. 5.2B, trace 7)). This suggests that the TiO_x species has a lower coordination in this sample probably due to the slightly lower Ti loading (Table 5.1).

Characteristic XP spectra of all samples in the Ti 2p, O 1s and Zn 2p regions of different materials are shown in Fig. 5.3. The Ti $2p_{3/2}$ peak of Ti0.3/SBA is centered at 460.4 eV and shifts to 459.9 eV in Ti1.0/SBA. No further shift to lower binding energies was observed when either the Ti loading was increased or when Zn was added to the SBA-15 materials. These values are significantly higher than those of Ti $2p_{3/2}$ for bulk TiO_2 at a binding energy of 459.0 eV (Fig.

5.3). Xia et al.[87] showed that already small quantities of bulk TiO_2 can be resolved with XPS, and therefore the formation of bulk TiO_2 can be excluded in the Ti(x)/SBA-15 materials. Generally, it has been reported that binding energies of isomorphously substituted Ti in silicates are shifted to higher values as compared to the oxides.[120,121] A binding energy of the Ti $2p_{3/2}$ peak of 460.3 - 460.7 eV for tetrahedrally coordinated Ti was observed by Brube et al.[84] for samples with Ti/Si ratios smaller than 5 %. With increasing Ti/Si ratio they observed a continuous shift to lower binding energies. Stakheev et al.[122] also observed a decrease in binding energy with increasing Ti content. However, they pointed out that the binding energy remains relatively stable up to 10 wt% TiO_2. In these studies XP spectra were measured for TiO_2/SiO_2 materials with no specific pretreatment. Gao et al.[80] performed XPS measurements after dehydration of the TiO_2/SiO_2 powders. They observed a shift of the Ti $2p_{3/2}$ binding energy with increasing TiO_2 content from 1 wt% to 5 wt%, but they did not observe a further shift with increasing TiO_2 content up to 15 wt%. Therefore, titanium species in the Ti0.3/SBA material can be attributed to tetrahedrally coordinated TiO4. Furthermore, we observed a broader Ti 2p signal and a larger Ti 2p splitting in the Ti(x)/SBA-15 materials with a FWHM of 2.5 eV and Ti 2p splitting of 5.8 eV for the Ti0.3/SBA sample compared to a FWHM of 1.0 eV and a Ti 2p splitting value of 5.7 eV for the TiO_2 bulk reference material. With increasing Ti loading a decrease in the Ti 2p peak width and a decrease in the Ti 2p splitting values for the Ti(x)/SBA-15 were observed. The decrease in the Ti 2p signal width might be explained by an increase in the amount of higher coordinated Ti atoms in the Ti(x)/SBA-15 materials at higher Ti loadings as shown by UV-Vis spectroscopy. This trend is in agreement with the observed shifts of the Ti 2p signals to lower binding energies which can also be explained with a higher coordination of the Ti atom.[84] The larger Ti 2p splitting might be rationalized by a relaxation occurring in the Ti atom due to its observed lower coordination.

The addition of Zn did not significantly alter the Ti XP spectra. The peak positions and the line shapes of the Ti $2p_{3/2}$ peaks of the Ti0.9/Zn0.9/SBA and the Zn0.7/Ti0.9/SBA samples are in good agreement with those of Ti1.0/SBA-15. It becomes more evident that Zn did not significantly change the XPS data by analyzing the O 1s XP spectra, which are shown in Fig. 5.3b. The O 1s signal of pure SBA-15 consists of one intense line centered at 534 eV. With increasing Ti content the peak position of the O 1s signal shifts to 533.5 eV for the Ti0.3/SBA sample and is further shifted to 533.2 eV for the Ti1.0/SBA signal (Fig. 5.3). A gradual decrease is also observed for the Si 2p signal. These shifts of the O 1s and the Si 2p signals are well known for silicon oxides containing small amounts of Ti or other transition metals and can be attributed to Si-O-Ti bonds.[84] In addition to the shifts to lower binding energies a new feature at 531.5 eV can be resolved, which increases in intensity with increasing Ti content. The comparison with the O 1s signal observed for bulk TiO_2 indicates that this feature cannot be associated with oxygen species in bulk TiO_2, because their XPS peak is centered at a binding energy of 530.2 eV. Gao et al.[80] observed a similar feature at $\sim$ 531.2 eV for samples containing at least 10 wt% TiO_2. They assigned this peak to Si-O-Ti bonds, which

were not resolved at lower loadings. The shift of the O 1s peak to higher binding energies compared to TiO_2, i.e. oxygen in a Ti-O-Ti bond, was explained with more electronegative and less polarizable Si atoms being bound to oxygen in a Si-O-Ti bond. The energy difference Δ(Ti $2p_{3/2}$-O 1s) was calculated to be 73.1 eV for the Ti0.3/SBA, while 71.3 eV were calculated for the reference sample. However, the energy difference between Δ(Si 2p-O 1s) was comparable for the SBA-15 and the Ti(x)/SBA-15 materials. Considering these energy differences it is evident that the Ti-O bond is more affected than the Si-O bond. Hence, the shift and the low binding energy feature observed in this study are attributed to Si-O-Ti bonds.

In contrast to these observations, Zn1.0/SBA exhibits essentially the same peak position and the same line shape in the O 1s region as the bare SBA-15 support. The lack of a peak shift can be attributed to a smaller difference in electronegativity between Zn and Si compared to Ti and Si. Similarly, the O 1s region of Zn0.7/Ti0.9/SBA is comparable to Ti1.0/SBA indicating that the amount of Ti-O-Si bonds is similar. In contrast, the O 1s peak of Ti0.9/Zn0.9/SBA is shifted to higher binding energy compared to Ti1.0/SBA indicating that less Ti-O-Si bonds are formed. For this sample differences in coordination have also been suggested by UV-Vis spectroscopy. The XP Zn 2p spectra are shown in Fig. 5.3c. Zn $2p_{3/2}$ peaks with binding energies of 1022.9 - 1023.9 eV can be detected, which are about 0.7 - 1.7 eV higher than that of bulk ZnO.[109] Similar shifts of the Zn $2p_{3/2}$ binding energy were reported by Tkachenko et al.[102] This shift is indicative for reasonably well isolated ZnO_x species with Zn in the divalent oxidation state in all samples as explained above for isolated TiO_x. For the Zn1.0/SBA sample the highest binding energy of the Zn $2p_{3/2}$ signal is observed. Depending on the order of the grafting steps, the Zn $2p_{3/2}$ peaks shift to lower binding energy with the lowest binding energy observed for Zn0.7/Ti0.9/SBA. The shift of the peak position in the subsequently grafted samples Zn0.7/Ti0.9/SBA and Ti0.9/Zn0.9/SBA can be attributed to an effective blocking of surface sites by TiO_x species, and therefore ZnO_x species seem to be less isolated compared to Zn1.0/SBA.

The Ti and Zn K-edge XANES spectra were measured in order to gain further information about the coordination of dehydrated Ti(x)/SBA-15 and Ti(x)/Zn(x)/SBA-15 materials. The XANES spectra of bulk TiO_2 in the anatase and rutile phase and Ti0.3/SBA are shown in Fig. 5.4a. XANES measurements revealed that the pre-edge features of Ti(x)/SBA-15, showing one distinct pre-edge peak maximum, clearly differ from the pre-edge feature of octahedrally coordinated bulk TiO_2 exhibiting three weak pre-edge peaks.[67] In agreement with the UV-Vis and XPS results the formation of crystalline bulk-like structures can be excluded from the XANES measurements for each Ti(x)/SBA-15 sample. The intensities of the pre-edge feature determined by the normalized XANES data are plotted against the Ti loading in Ti/nm^2 in Fig. 5.4b. For Ti(x)/SBA-15 materials a linear relationship between the Ti loading and the pre-edge intensity was found, that is, with increasing Ti loading the pre-edge height decreases linearly. Farges et al.[123] found that reliable information about the Ti coordination can be obtained by the pre-edge intensity. They also pointed out that the pre-edge position of the Ti K-edge XANES
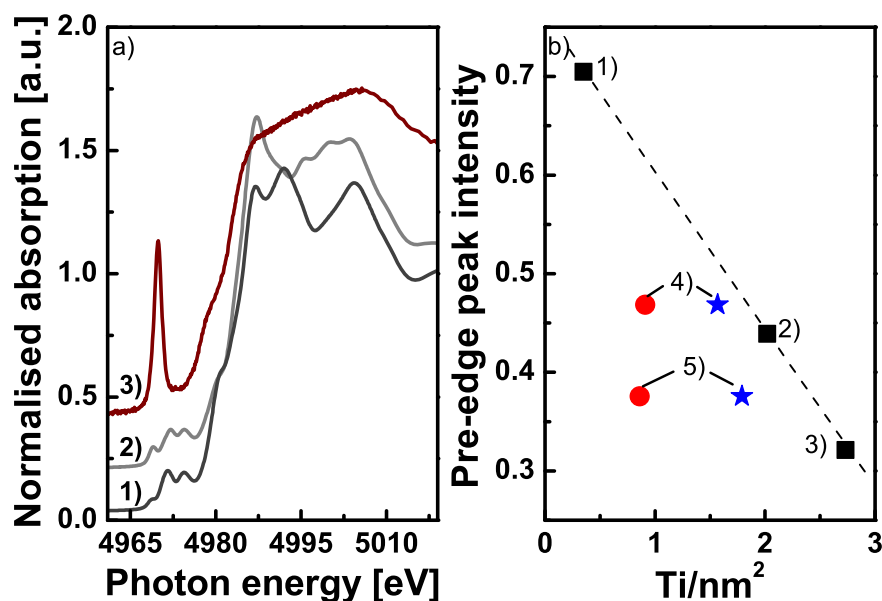
Figure 5.4: a) Comparison of the XANES spectra of 1) TiO$_2$ rutile modification, 2) TiO$_2$ anatase modification, and 3) isolated TiO$_x$ in Ti0.3/SBA. b) Pre-edge intensities obtained from normalized Ti K-edge XANES of Ti(x)/SBA-15 materials plotted against the Ti loading in Ti/nm^2 obtained from ICP-OES. The red circles are obtained by plotting the Ti pre-edge intensity of Zn0.7/Ti0.9/SBA and Ti0.9/Zn0.9/SBA against the Ti loading, whereas blue stars are obtained for Ti pre-edge intensities plotted against the overall transition metal content. 1) Ti0.3/SBA, 2) Ti2.0/SBA, 3) Ti2.7/SBA, 4) Zn0.7/Ti0.9/SBA, 5) Ti0.9/Zn0.9/SBA.

spectra should be taken into account. Based on these variables three different well-defined groups were identified, namely four-, five-, and sixfold coordinated titania. These observations were successfully adopted to determine the coordination of Ti in different TiO$_2$/SiO$_2$ materials by Gao et al.[80] In the present study the pre-edge peak maximum was centered at photon energies ranging from 4669.9 eV for Ti0.3/SBA to 4670.1 eV for Ti2.7/SBA. According to Farges' results these pre-edge energies identify fourfold coordinated Ti species.[123] For Ti0.3/SBA the pre-edge intensity perfectly fits into the predicted range. However, the pre-edge intensity is far too low in case of Ti2.0/SBA and Ti2.7/SBA to be exclusively fourfold coordinated indicating the presence of mixtures of different Ti coordination spheres. As pointed out by Vining et al.[106], a distortion of the tetrahedral geometry of TiO$_x$ causes a less intense pre-edge peak attributed to lower Ti 3d-4p orbital hybridization and less overlap with the O 2p orbitals. Correspondingly, for Ti2.0/SBA it is reasonable to assume a mixture of predominantly four- and fivefold coordinated titania with minor contributions of sixfold coordinated titania and slightly distorted tetrahedral TiO$_x$ structures. In case of Ti2.7/SBA the amount of sixfold coordinated Ti is clearly increased.

The Ti pre-edge peak intensities of the subsequently grafted samples Zn0.7/Ti0.9/SBA and Ti0.9/Zn0.9/SBA plotted against the loading of Ti (Ti/nm^2, red circle) and plotted against the
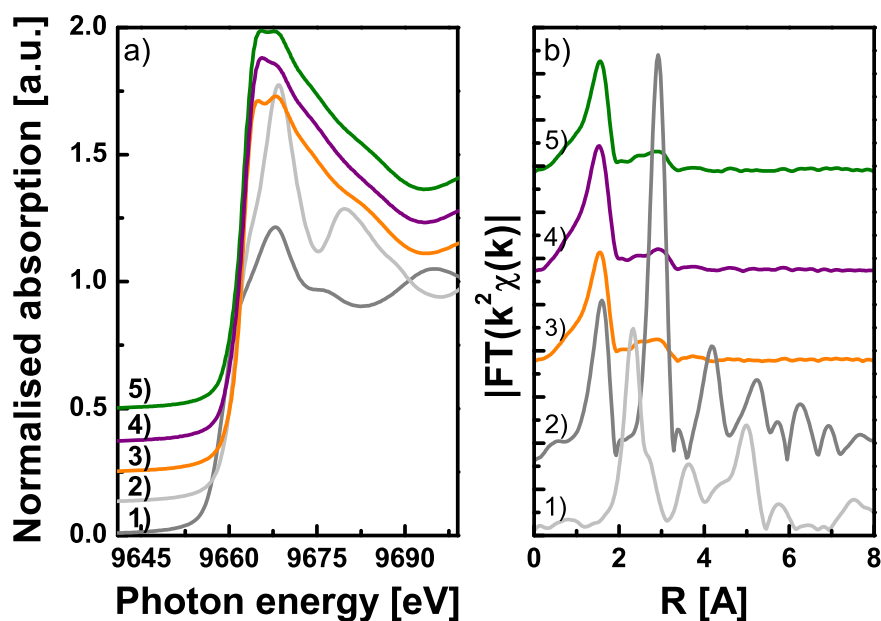
Figure 5.5: a) XANES spectra and b) Fourier-transformed EXAFS spectra (Zn K-edge) of Zn-containing SBA-15 materials. 1) Zn foil, 2) ZnO, 3) Zn1.0/SBA, 4) Zn0.7/Ti0.9/SBA, and 5) Ti0.9/Zn0.9/SBA.

total transition metal loading ($(Zn+Ti)/nm^2$, blue stars) are also shown in Fig. 5.4b. Compared to the pure Ti(x)/SBA-15 materials, titania in Zn0.7/Ti0.9/SBA and Ti0.9/Zn0.9/SBA appears to be higher coordinated, especially in the Ti0.9/Zn0.9/SBA sample. While the Ti coordination in Zn0.7/Ti0.9/SBA is quite similar to the Ti2.0/SBA sample, the Ti coordination in the Ti0.9/Zn0.9/SBA sample resembles that of Ti2.7/SBA. A similar trend in the Ti pre-edge peak intensity was reported by Vining et al.[106] for subsequently prepared $VO_x/TiO_x/SiO_2$ material with different V/Ti ratios, which was attributed to V-Ti-interactions. Therefore, the results of the present study indicate a Zn-O-Ti interaction after subsequent grafting in the Ti(x)/Zn(x)/SBA-15 materials. Less Zn-O-Ti interactions are formed in Zn0.7/Ti0.9/SBA compared to the Ti0.9/Zn0.9/SBA material. On the contrary, more Zn-O-Ti interactions are present in Ti0.9/Zn0.9/SBA. The small differences in total transition metal loading cannot explain the differences in pre-edge intensities. Instead, they may be an indication for a preferred interaction of the Ti precursor with surface ZnO_x species during the sequential grafting. This is in agreement with the presence of less Ti-O-Si bridges as indicated by the XPS results and the blueshift of the absorption edge as observed by UV-Vis spectroscopy. On the other hand, the Zn precursor does not seem to coordinate to TiO_x species preferably, indicating that the order of grafting steps significantly affects the Ti coordination.

Comparing the Zn absorption edge position measured by XANES of the Zn1.0/SBA and the Ti(x)/Zn(x)/SBA materials indicates that Zn in all samples is exclusively present in the 2+ state and not in the metallic state (Fig. 5.5a). The FT-EXAFS spectra of the Zn region of the three

Zn-containing samples Zn1.0/SBA, Zn0.7/Ti0.9/SBA, and Ti0.9/Zn0.9/SBA are shown in Fig. 5.5b. ZnO and Zn foil references are also included.

While the first coordination shell is significantly lower compared to the ZnO reference, the second and further coordination shells can be barely seen in FT-EXAFS plots of the SBA-15 materials. Similar FT-EXAFS results were reported previously.[102,104] Tkachenko et al.[102] pointed out that the best agreement between experimental and model spectra is obtained with Si as second neighbor. Based on the FT-EXAFS data it can be concluded that the ZnO$_x$ species are present as isolated species in all Zn-containing materials, while the presence of very small islands cannot be excluded. It has to be noticed that a thorough inspection of the region between 2 and 4 Å in the Fourier-transformed EXAFS spectra revealed the second coordination shell to be slightly more pronounced in the Zn0.7/Ti0.9/SBA sample. This might be another indication that during subsequent grafting of Zn onto TiO$_x$/SBA-15, the Zn precursor does not coordinate to TiO$_x$, but rather ZnO$_x$ species are formed in closer proximity on the remaining silica surface, which is not blocked by TiO$_x$, due to a strong interaction between Zn and silica as already reported by Tkachenko et al.[102] Combining the results obtained by the UV-Vis, XPS, and XAS studies the structure of TiO$_x$ in dehydrated SBA-15 can be described as isolated, tetrahedrally coordinated TiO$_4$ at low Ti loadings, while with increasing Ti content agglomerates are formed. These findings are in good agreement with the results obtained by Wachs et al.[65,80] ZnO$_x$ in all samples was found to be isolated or agglomerated in very small clusters. The tendency to form higher agglomerated ZnO$_x$ seems to be increased when TiO$_x$ is already present on the surface of the material due to a less favorable interaction between the Zn precursor and TiO$_x$ species and a strong interaction between Zn and the silica support.[102] In contrast, the Ti precursor seems to interact with ZnO$_x$ preferably. Correspondingly, in the two subsequently grafted samples, TiO$_x$ and ZnO$_x$ are in close proximity, but more Ti-O-Si bonds of isolated TiO$_x$ species are present in Zn0.7/Ti0.9/SBA.

CO$_2$/NH$_3$ adsorption capacities determined by TPD

Having established the structures and interactions of surface TiO$_x$ and ZnO$_x$ species, the question needs to be addressed as to whether they are accessible for adsorption and whether they act as acidic or basic sites. The CO$_2$ adsorption capacities of the Ti(x)/SBA and the Ti(x)/Zn(x)/SBA samples were evaluated by TPD experiments. The obtained desorption profiles are shown in Fig. 5.6, and the calculated amounts of desorbed CO$_2$ are summarized in Table 5.2.

ZnO is known to favor the adsorption of CO$_2$,[96,124] and indeed the TPD results indicate that all SBA-15 materials loaded with ZnO$_x$ species adsorb CO$_2$. Zn1.0/SBA shows the most intense CO$_2$ desorption signal in the low-temperature region and a small increase at higher temperatures above 650 K. The high-temperature desorption is related to strongly chemisorbed CO$_2$, most likely in the form of carbonates. The heating ramp was not extended beyond the pre-treatment temperature in order to quantify the amount of the high-temperature carbonate, as it
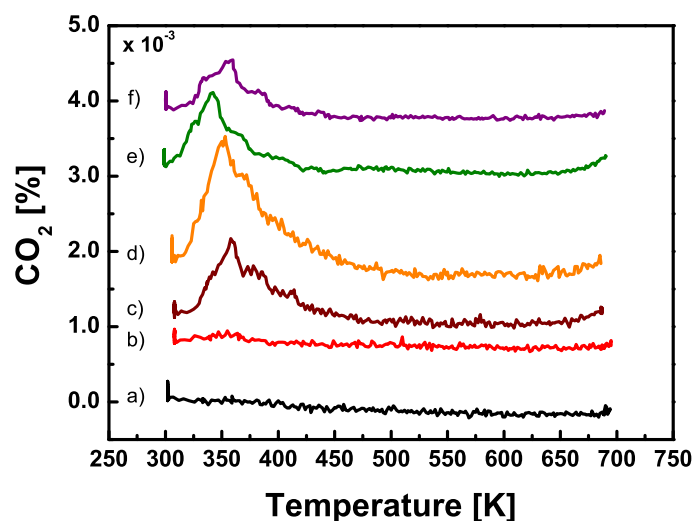
Figure 5.6: CO_2 TPD profiles obtained with a) SBA-15, b) Ti1.0/SBA, c) Zn0.3/SBA, d) Zn1.0/SBA, e) Ti0.9/Zn0.9/SBA, and f) Zn0.7/Ti0.9/SBA.

cannot be excluded that the desorbing species have been present already prior to CO_2 adsorption. Furthermore, species desorbing at such high temperature are likely irrelevant in catalysis or for the use as reversible adsorbent. The high-temperature desorption feature was not included in the integration of the adsorbed amount of CO_2 for all samples. Zn0.7/Ti0.9/SBA and Ti0.9/Zn0.9/SBA also exhibit a CO_2 desorption signal in the low-temperature region.

With decreasing Zn content the signal intensity clearly decreases in the low-temperature region and the high-temperature desorption feature more or less disappears. The total CO_2 adsorption capacity decreases in the order Zn1.0/SBA > Zn0.3/SBA > Ti0.9/Zn0.9/SBA > Zn0.7/Ti0.9/SBA. Calculations of the amount of CO_2 desorbed normalized by the Zn content as determined by AAS, i.e. the number of adsorbed CO_2 molecules per ZnO_x site present in the materials, revealed that only a small fraction of the ZnO_x species adsorb CO_2. It is possible that only those ZnO_x species that have a certain geometric arrangement are suitable for CO_2 adsorption. The amount of CO_2 per ZnO_x site is similar for Ti0.9/Zn0.9/SBA and Zn0.7/Ti0.9/SBA, but lower than for titanium-free samples. This observation implies that the presence of TiO_x lowers the amount of CO_2 adsorbed, but this effect is not influenced by the order of the grafting steps. This indicates that the grafting of TiO_x onto ZnO_x/SBA-15, during which the Ti-precursor seems to coordinate preferably to ZnO_x, does not lead to an additional blocking of adsorption sites for CO_2.

Furthermore, the CO_2 TPD measurements revealed that SBA-15 materials, which do not contain ZnO_x species, do not exhibit any significant CO_2 desorption signals. As the adsorption of CO_2 is a general indicator for basic sites on surfaces, it can be concluded that the samples contain hardly any basic sites in the absence of ZnO_x.[125] Srivastava et al.[93,126] and Srinivas et al.[127] observed a small amount of CO_2 during the TPD experiments. However, a similar amount of CO_2 was adsorbed on the bare SBA-15 support. In the present study bare SBA-15

Table 5.2: Amount of acidic and basic sites determined by NH_3 and CO_2 TPD measurements for the Ti(x)/Zn(y)/SBA samples.

Amount of substance	sample								
	SBA-15	Ti0.3/SBA	Ti1.0/SBA	Ti2.0/SBA	Ti2.7/SBA	Zn0.3/SBA	Zn1.0/SBA	Zn0.7/Ti0.9/SBA	Ti0.9/Zn0.9/SBA
CO_2 [mol/g]	0.0	0.0	0.2	0.4	0.5	2.3	4.4	1.4	2.0
NH_3 [mol/g]	0.0	92.1	204.0	360.0	465.3	151.3	272.8	389.4	422.7
Zn [mol/g]	-	-	-	-	-	520	1147	750	1025
metal[a] [mol/g]	-	438	1315	2359	3090	520	1147	1772	1964
$n(CO_2)/n(Zn)$	-	-	-	-	-	4.4×10^{-3}	3.8×10^{-3}	1.9×10^{-3}	1.9×10^{-3}
$n(NH_3)/n(metal)$	-	0.21	0.16	0.15	0.15	0.30	0.24	0.22	0.22

[a] total transition metal content (Ti+Zn) from elemental analysis

did not adsorb any CO_2. Differences in the observations may be explained by different calcinations and the pretreatment temperatures. Srivastava et al.[126] pointed out that probably surface OH groups are the sites were CO_2 adsorption or activation of the CO_2 molecule takes place. As the pre-treatment temperature in this study was higher, these surface sites may have been removed. In a recent study Danon et al.[74] studied the interaction of TiO_x/SBA-15 with CO_2 and H_2O by means of Raman spectroscopy. In agreement with the results of our study, they observed that there is hardly any interaction between CO_2 and TiO_x/SBA-15.

On the contrary, all TiO_x-grafted and subsequently grafted ZnO_x/TiO_x samples contain acidic sites as shown by adsorption-desorption experiments using NH_3. The amount of acidic sites is about a factor of 102 larger than the amount of basic sites in all materials. The NH_3 adsorption capacity increases linearly with increasing Ti loading except for the Ti0.3/SBA sample. This observation points to an improved interaction between fully isolated TiO_x and NH_3. The presence of acidic sites in similar systems was already reported by Iengo et al.[92] Using pyridine as basic probe molecule for TPD experiments they reported a nearly linear relationship between the TiO_x content and the surface acidic sites.[64] In a more recent study Srivastava et al.[126] pointed out that Ti-SBA-15 possesses only weak Lewis centers, whereas SBA-15 did not contain any acidic sites. These observations are in good agreement with our observations that all Ti atoms in Ti(x)/SBA-15 materials seem to be accessible for NH_3 adsorption. In case of the two subsequently grafted samples Zn0.7/Ti0.9/SBA and Ti0.9/Zn0.9/SBA, NH_3 adsorption is slightly more favorable in the Ti0.9/Zn0.9/SBA material. This is in good agreement with the Zn and Ti loadings determined by ICP-OES measurements revealing that a higher Zn content was achieved in Ti0.9/Zn0.9/SBA. Furthermore, these results illustrate that the overall amount of NH_3 adsorbed on Ti0.9/Zn0.9/SBA is approximately equal to the sum of the amount adsorbed on Ti1.0/SBA and the amount adsorbed on Zn1.0/SBA. Consequently, subsequent grafting of Zn and Ti did not block a significant number of acidic adsorption sites, indicating that the species do not block each other.

In summary, it was shown that the grafting of either TiO_x or ZnO_x introduces acidic sites, and that the amount scales almost linearly with the total amount of transition metals. Basic sites can be generated by the grafting of ZnO_x, but their number is a factor of 102 smaller than that of the acidic sites. Further studies are required concerning the nature of the adsorbed species formed from CO_2 on TiO_x/ZnO_x/SBA-15.

CO_2 adsorption studied by UHV-FTIR

The interaction of CO_2 was studied using Fourier-Transformed Infrared (FTIR) spectroscopy. The FTIR spectrometer is coupled to a UHV system allowing for high sensitivities and low contamination levels during the measurements. Prior to CO_2 adsorption the samples were pretreated at 700 K in vacuum. The adsorption studies were performed at 90 K. The stability of adsorbed species was evaluated by heating the samples up to 300 K after CO_2 adsorption. Additional CO_2 adsorption experiments were carried at 300 K.
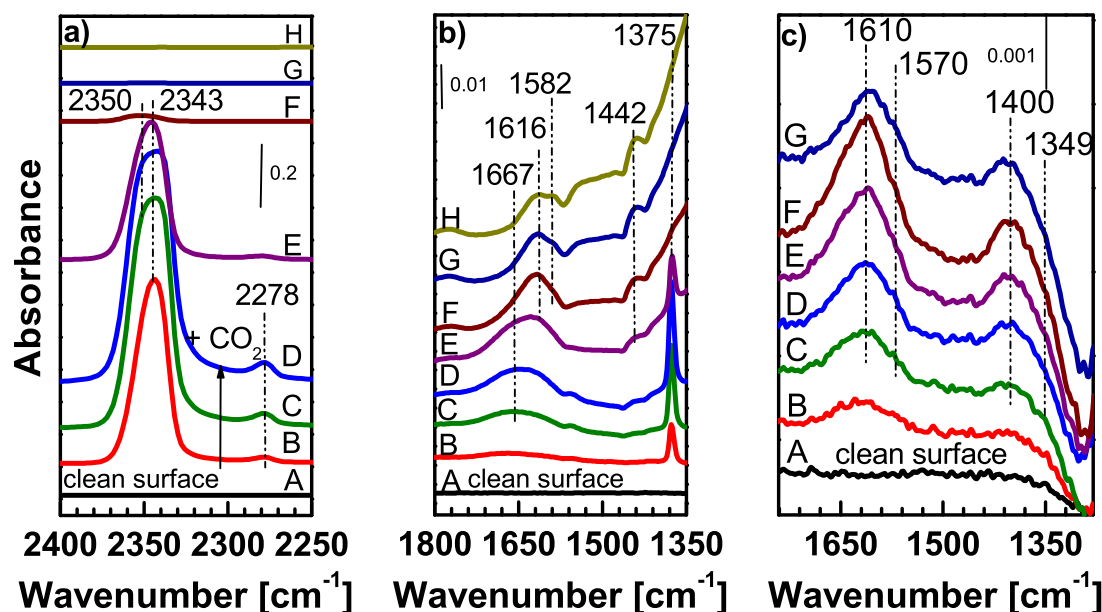
Figure 5.7: UHV-FTIR spectra obtained after exposing the clean Zn1.0/SBA-15 sample to CO_2 at 90 K: (A) clean sample, (B) 1×10^{-5} mbar CO_2, (C) 5×10^{-5} mbar CO_2, (D) 1×10^{-4} mbar CO_2, and heating to: (E) 150 K, (F) 200 K, (G) 250 K, and (H) 300 K. a) CO_2 range, b) carbonate range. c) CO_2 dosing at 300 K: (A) clean surface, (B) 1×10^{-6} mbar CO_2, (C) 5×10^{-6} mbar CO_2, (D) 1×10^{-5} mbar CO_2, (E) 5×10^{-5} mbar CO_2, and (F) 1×10^{-4} mbar CO_2. Afterwards the sample was evacuated for (G) 10 min.

The UHV-FTIR spectra obtained upon CO_2 adsorption at 90 K at different CO_2 pressures on Zn1.0/SBA and upon subsequent heating of the Zn1.0/SBA sample are shown in Fig. 5.7a and Fig. 5.7b. Obviously, three bands appear at relatively low pressures of 1×10^{-6} mbar CO_2. These bands are situated at 2343, 2278, and 1375 cm^{-1}. With increasing CO_2 pressures a broad band at ~ 1660 cm^{-1} appears. Additionally, the band at 2343 cm^{-1} is getting broader. ZnO nanoparticles were recently studied under similar conditions by Noei et al.[98]. Based on their assignments the intense band at 2343 cm^{-1} can be related to linearly physisorbed CO_2. As Noei et al.[98] already pointed out that these values are close to those wavenumber observed for gas-phase CO_2, and interestingly they also observed a broadening or even a splitting of this band upon larger CO_2 doses. Finally, the assignment of this broad band at 2343 cm^{-1} to linearly physisorbed CO_2 was verified by the fact that it disappeared during heating to 200 K.[98] During heating of the sample the weak band at 2278 cm^{-1} and the sharp band at 1375 cm^{-1} decreased, too. During heating a so far unresolved band at 1442 cm^{-1} appeared due to the disappearance of the sharp band at 1375 cm^{-1}. Furthermore, the heating procedure revealed that the band at ~ 1660 cm^{-1} remained unchanged up to 150 K. However, the band maxima was shifted to lower wavenumbers (1616 cm^{-1}) and a shoulder at 1582 cm^{-1} appeared upon further heating to 300 K. A similar shift of certain bands upon heating was also observed by Noei et al.[98] Usually, the bands observed at wavenumbers between 1300 and 1700 cm^{-1} are assigned to carbonate or carboxylate species at different ZnO surfaces.[98,124,128] Especially

bicarbonates that are reversibly adsorbed at room temperature were assigned to bands at 1635 cm^{-1} and 1424 cm^{-1}.[124] However, in the case of Zn1.0/SBA the assignment of the bands in this region to a certain ZnO surface or a certain carbonate/carboxylate species is not feasible. The above presented characterization results (UV-Vis, EXAFS, and XPS) clearly indicate that there is no defined bulk-like ZnO structure in case of the Zn/SBA material. The ZnO$_x$ species are rather isolated, and therefore comparison to ZnO nanoparticles is not possible. Esken et al.[128] studied ZnO nanoparticles with a diameter of $\sim$ 2 nm, which were incorporated into a host system. Given that the CO_2 adsorption features are similar to the results reported by Noei et al.[98] the ZnO$_x$ species in Zn1.0/SBA are much smaller. Nevertheless, the UHV-FTIR data unambiguously provide evidence for the interaction of CO_2 and Zn1.0/SBA and the formation of carbonate-like species at the surface of the Zn1.0/SBA material upon exposure to CO_2 at 90 K might be possible. Furthermore, it was shown that certain species remained on the surface even after heating to 300 K.

The observation of the formation of carbonate-like species was strengthened by the CO_2 adsorption experiments performed at 300 K. The results of these experiments are shown in Fig. 5.7c. During adsorption at different CO_2 pressures two broad bands appear at 1400 cm^{-1} and 1610 cm^{-1}. As mentioned above similar bands at 1635 cm^{-1} and 1424 cm^{-1} were assigned to reversibly adsorbed bicarbonates.[124] These bands remained stable during evacuation of the system, which is a clear evidence of a strong absorption at the surface of the Zn1.0/SBA sample. The bands are less intense demonstrating that the interaction of CO_2 with the surface of Zn/SBA is less likely at elevated temperatures. By combining the UHV-FTIR results and the above presented TPD results it was possible to show that CO_2 adsorption occurs at the surface of Zn1.0/SBA, and that the TPD signal at low temperatures is possibly due to weakly bound carbonate species, thus desorbing at low temperatures.

The adsorption of CO_2 was also studied for Zn0.7/Ti0.9/SBA and Ti1.0/SBA by means of UHV-FTIR measurements. The results obtained for low-temperature CO_2 at different CO_2 pressures as well as representative data recorded during heating of the Zn0.7/Ti0.9/SBA and Ti1.0/SBA samples are shown in Fig. 5.8, Fig. 5.9, and Fig. A2, respectively. Similar to the Zn1.0/SBA a band was observed for the Zn0.7/Ti0.9/SBA sample in the CO_2 region of the FTIR spectra at $\sim$ 2345 cm^{-1}, which can be assigned to linearly physisorbed CO_2. However, the intensity of this band is weaker and the band is significantly broader compared to the Zn1.0/SBA. Thus, an additional species situated at lower wavenumber ($\sim$ 2336 cm^{-1}) is present for the Zn0.7/Ti0.9/SBA sample upon CO_2. Even though the signal gets narrower and the overall intensity of the signal decreases upon heating the linearly physisorbed CO_2 appeared to be more stable at the surface of Zn0.7/Ti0.9/SBA, because at 220 K the band $\sim$ 2345 cm^{-1} can be still observed. Finally, the band at 2278 cm^{-1} was also observed for the Zn0.7/Ti0.9/SBA sample. It is striking that the intensity ratio between the two signals at $\sim$ 2345 cm^{-1} and $\sim$ 2278 cm^{-1} was much smaller for the Zn0.7/Ti0.9/SBA.

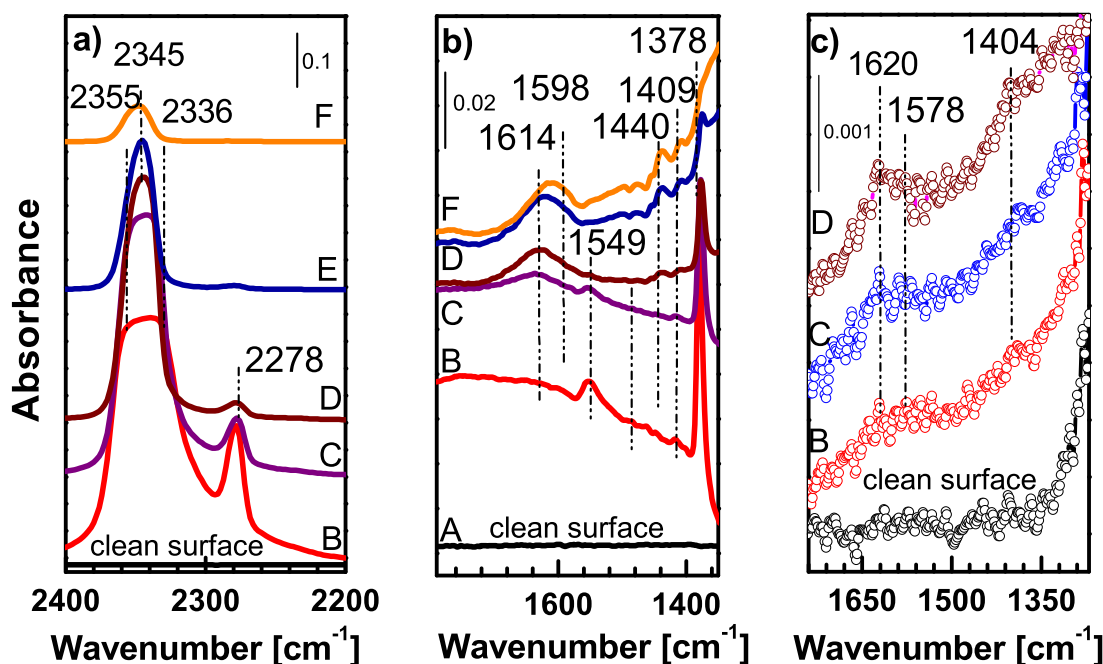In agreement with the UHV-FTIR CO_2 adsorption results obtained for Zn1.0/SBA carbonate-

Figure 5.8: UHV-FTIR spectra obtained after exposing the clean Zn0.7/Ti0.9/SBA sample to CO$_2$ at 90 K: (A) clean surface, (B) 1x10^{-4} mbar CO$_2$, and heating to: (C) 150 K, (D) 175 K, (E) 200 K, and (F) 220 K. a) CO$_2$ range, b) carbonate range. c) CO$_2$ dosing at 300 K: (A) clean surface, (B) 1x10^{-6} mbar CO$_2$, (C) 1x10^{-5} mbar CO$_2$, and (D) 1x10^{-4} mbar CO$_2$.

related bands between 1300 and 1700 cm^{-1} were detected for the Zn0.7/Ti0.9/SBA sample upon adsorption of CO$_2$ at 90 K, but the bands are less intense compared to the Zn1.0/SBA material. While a sharp signal at 1378 cm^{-1} was the most intense feature observed in the carbonate region, which is in good agreement with the results of the Zn/SBA sample, a small signal at 1549 cm^{-1}, which was absent or barely detectable for the Zn1.0/SBA sample, was resolved for the Zn0.7/Ti0.9/SBA sample. Furthermore, the broad signal at $\sim$ 1660 cm^{-1} observed for the Zn1.0/SBA could not be detected for the Zn0.7/Ti0.9/SBA sample upon CO$_2$ adsorption. The results of CO$_2$ adsorption experiments performed with the Zn1.0/SBA and the Zn0.7/Ti0.9/SBA indicate that the broadening of the band detected at $\sim$ 2345 cm^{-1}, the band at $\sim$ 2278 cm^{-1} and the sharp feature observed in the carbonate region at $\sim$ 1378 cm^{-1} are likely to be related with each other. During heating the sharp band at 1378 cm^{-1} and the smaller signal at 1549 cm^{-1} disappeared and new signals at 1409 cm^{-1}, 1440 cm^{-1}, and 1616 cm^{-1} were resolved. The enhanced stability observed for the bands in the CO$_2$ region corresponds to the enhanced stability of the band at 1378 cm^{-1} further indicating the relationship of the two signals. Besides this enhancement in stability the species observed after heating of the Zn/Ti/SBA are similar to the species observed for Zn/SBA sample, and it is resonable to conclude that the influence of TiO$_x$ species on the CO$_2$ adsorption is small when CO$_2$ is adsorbed at 90 K and the sample is heated afterwards. An influence of TiO$_x$ can be only assumed at 90 K because of the absence of the broad band at $\sim$ 1660 cm^{-1} observed for Zn1.0/SBA.
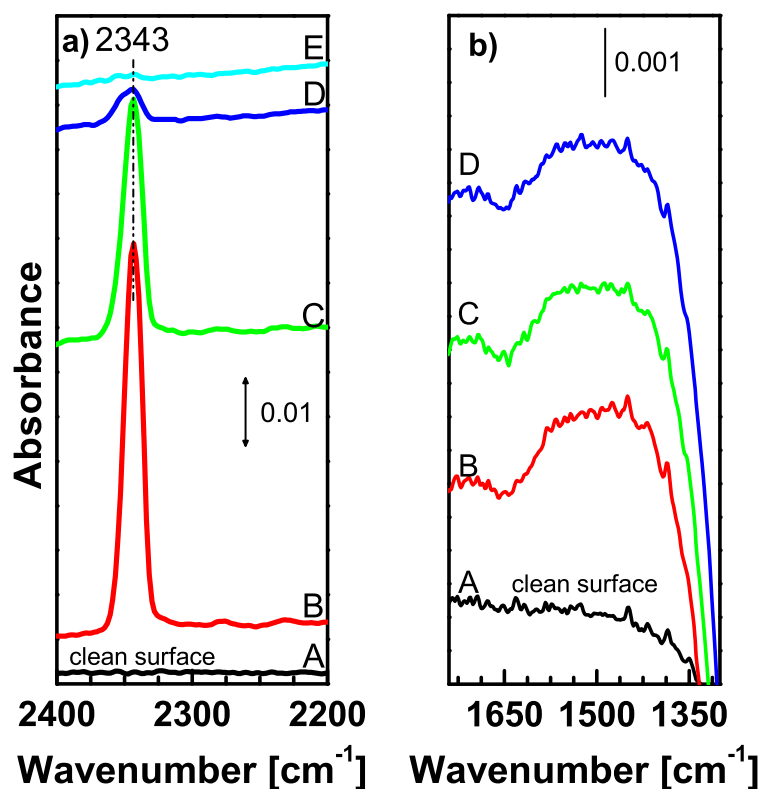
Figure 5.9: a) UHV-FTIR spectra obtained after exposing the clean Ti1.0/SBA sample to CO_2 at 90 K: (A) clean surface, (B) $1x10^{-4}$ mbar CO_2, and annealing to: (C) 120 K, (D) 150 K, and (E) 170 K. b) Spectra obtained (carbonate region) after exposing the clean TiOx/SBA-15 sample to CO_2 at 90 K in the CO_2 range: (A) clean surface, (B) $1x10^{-6}$ mbar CO_2, (C) $1x10^{-5}$ mbar CO_2, and (D) $1x10^{-4}$ mbar CO_2.

For CO_2 adsorption on Zn0.7/Ti0.9/SBA performed at 300 K weak bands at 1620 cm^{-1} and 1404 cm^{-1} at high CO_2 pressures were detected (Fig. 5.8c). Based on the CO_2 adsorption results obtained at 90 K and 300 K it can be concluded that in both cases reversibly adsorbed bicarbonates are present at 300 K.[124] At lower temperatures additional absorption modes were observed, which disappeared or shifted during heating. Additionally, it can be concluded that the structure of the ZnO_x species in Zn1.0/SBA and Zn0.7/Ti0.9/SBA is similar. Given that the intensity of all bands is smaller in case of the Zn0.7/Ti0.9/SBA compared to the Zn1.0/SBA sample less CO_2 can be adsorbed at the Zn0.7/Ti0.9/SBA sample. This observation is in good agreement with the smaller CO_2 adsorption capacity determined by TPD experiments.

In contrast to the results obtained for Zn1.0/SBA and Zn0.7/Ti0.9/SBA a different CO_2 adsorption behavior was observed for the Ti1.0/SBA sample. The CO_2 region upon CO_2 adsorption at 90 K of the Ti1.0/SBA is shown in Fig. 5.9a. The corresponding carbonate region during CO_2 dosing is shown in Fig. 5.9b. Again, linearly physisorbed CO_2 at 2343 cm^{-1} was detected. The additional peak usually observed at 2278 cm^{-1} is absent in case of CO_2 adsorption on Ti1.0/SBA. Furthermore, the peak at 2343 cm^{-1} appeared to be completely symmetric even at high CO_2 pressures and in contrast to Zn1.0/SBA and Zn0.7/Ti0.9/SBA samples a slight broad-

ening of the signal at 2343 cm^{-1} is only observed during heating. In the carbonate region only a broad band appeared during the CO_2 dosing (Fig. 5.9b), which disappeared during heating. Based on these observations it can be concluded that the typical features at 2278 cm^{-1} and 1378 cm^{-1} are due to the presence of ZnO_x species in the Zn1.0/SBA and Zn0.7/Ti0.9/SBA samples. Accordant to the results of low temperature CO_2 adsorption on Ti1.0/SBA, adsorption of CO_2 at 300 K revealed that there is no specific interaction between the Ti1.0/SBA sample and CO_2 at elevated temperatures (Fig. A3). This is in agreement with the presented CO_2 TPD data evidencing that CO_2 adsorption at RT is unlikely at isolated TiO_x species as present in the Ti1.0/SBA sample.

In summary, UHV-FTIR measurements of CO_2 adsorption at Ti1.0/SBA, Zn1.0/SBA, and Zn0.7/Ti0.9/SBA performed at 90 K and at 300 K provide insight into the interaction of the different materials with CO_2. It was shown that during adsorption at 300 K carbonates are formed on Zn1.0/SBA and Zn0.7/Ti0.9/SBA. On Ti1.0/SBA CO_2 was mainly adsorbed linearly at 90 K, and the formation of carbonates upon CO_2 dosing at 90 K and 300 K can be excluded. Therefore, the CO_2 adsorption capacities as determined by TPD measurements of Zn0.7/Ti0.9/SBA can be clearly attributed to the presence of ZnO_x species rather than the presence of TiO_x. However, the UHV-FTIR measurements show that TiO_x species influence the modes of CO_2 adsorption in the Zn0.7/Ti0.9/SBA sample during CO_2 dosing at 90 K. In general, the obtained results are in good agreement with the structural characterization of the Zn0.7/Ti0.9/SBA sample indicating that the structure of ZnO_x species is similar to the structure of ZnO_x species in Zn1.0/SBA.

5.1.3 Conclusions

Using an efficient grafting procedure, TiO_x- and ZnO_x-containing SBA-15 materials with different transition metal loadings were synthesized. The extensive characterization of the prepared materials showed that depending on the Ti loading isolated and polymerized TiO_x species were obtained. ZnO_x species were found to be present as isolated species or very small islands. XPS and X-ray absorption spectroscopy measurements indicated strong interactions between ZnO_x and TiO_x species. When titania is grafted first, the sample contains considerable amounts of isolated titania species. In the subsequent grafting of ZnO_x onto TiO_x/SBA-15 Zn(acac)$_2$ interacts preferably with the free silica surface. Therefore, there is a tendency to form higher agglomerated ZnO_x species, while the decrease in the total number of isolated titania species is less pronounced. In contrast, when TiO_x is grafted on ZnO_x/SBA-15 a preferred interaction between the Ti precursor and surface ZnO_x species was observed. Due to this interaction more Ti-O-Zn and less Ti-O-Si bonds are formed in the material, and titania appears to be higher coordinated. Using NH$_3$ TPD a large amount of acidic sites was found in all materials. A significant CO_2 adsorption capacity was observed only for the Zn-containing materials. The total amount of acidic and basic sites was not influenced by the order of the grafting steps, indicating

that the transition metal oxide species do not block each other. UHV-FTIR studies confirm that CO_2 is interacting with ZnO_x species incorporated into SBA-15. No specific interaction at 300 K was observed for TiO_x species.

5.2 Photocatalytic CO$_2$ reduction using Au-modified TiO$_x$/SBA-15 materials

Abstract[2]

Photo-deposition of Au nanoparticles enhances the hydrogenation rate in photocatalytic CO_2 reduction to methane on titanate in SBA-15. Product formation from contaminants is ruled out experimentally by a thorough pre-cleaning of the samples and the design of the vacuum-tight gas-phase photoreactor. Without Au, an active carbon pool accumulates on the catalyst and higher hydrocarbons are formed. By infrared spectroscopy it was found that the carbon pool consists of formaldehyde/paraformaldehyde. Furthermore, the obtained results indicate that adsorbed water in the mesopores of the catalyst is sufficient to achieve CO_2 reduction and convert CO_2 mainly to methane. The results contribute to the understanding and systematic improvement of photocatalysts.

5.2.1 Short Introduction

Chemical fixation of CO$_2$ into value-added materials or fuels by photocatalytic reduction at semiconductor surfaces is currently attracting much attention as this kind of artificial photo-synthesis is a promising technology for the future energy supply.[129] TiO$_2$-related materials in various shapes and with different kinds of metal or non-metal doping are the most frequently studied materials for this application.[14] It was already shown by Anpo et al.[58,67] in their pioneering work that isolated TiO$_x$-species incorporated into different matrices are active materials for the photocatalytic reduction of CO$_2$. More recently, it was shown by Anpo et al.[58,67] that these materials exhibit better performance than bulk TiO$_2$ when compared on a per gram Ti basis.[130] However, there is still the need to further understand the processes involved in photocatalytic reduction. It was suggested that CO is a likely intermediate by Frei et al.[71] This was further supported by Mul et al.[73], who proposed that formaldehyde is another likely intermediate generated by CO and water. Furthermore, there is currently a dispute about CO$_2$ adsorption on isolated Ti-species. While Anpo et al.[67] used the quenching of the characteristic TiO$_x$ photoluminescence feature in presence of CO$_2$ as an indication for the interaction between CO$_2$ and the titania site, no specific interaction was observed by Stair et al.[74] by means of UV Raman spectroscopy.

It was already shown by Mori et al.[131,132] that the deposition of noble metals like Au, Ni, or Pd by a photo-assisted procedure is feasible for Ti single-site catalysts. Even though noble metals are widely accepted to enhance photocatalytic activities due to an enhanced charge separation, there is, to the best of our knowledge, no report about the effect of noble metals or a comparative study between noble metal-modified and unmodified Ti single-site catalysts. Therefore, we report for the first time on the effect of photo-deposited Au on the photocatalytic CO$_2$ reduction activities of Ti/SBA-15 materials.

Experimental

Sample synthesis

Photo-deposition of Au nanoparticles was performed in a continuous flow stirred-tank reactor equipped with a 700 W Hg immersion lamp cooled by water circulating in a double wall jacket.[133] During photo-deposition the concentration of CO$_2$, O$_2$, and H$_2$ were analyzed with a non-dispersive IR photometer, a paramagnetic and a thermal conductivity detector (XStream, Emerson Process Management), respectively. 350 mg of catalyst were dispersed in a solution of 550 ml dest. H$_2$O and 50 ml MeOH. The reactor was deaerated for 60 min using pure N$_2$ prior to irradiation. The activity for photocatalytic methanol reforming of the Ti/SBA was evaluated by irradiation for 60 min (in the absence of the Au precursor). 3.5 ml of a 1.5 x 10^{-3} molar auric acid solution (HAuCl$_4$ 99.9 %, Sigma Aldrich) were added to the suspension and the reactor was again deaerated for 60 min using pure N$_2$. Photo-deposition was performed at

30 °C with 50 % irradiation power (350 W) for 2.5 h. After successful photo-deposition the materials were filtered and freeze-dried over night.

Characterization

DRIFT spectra of the samples diluted with diamond powder in a 1:1 ratio (by weight) were recorded at different temperatures between RT and 400 °C to remove surface-adsorbed water. At 120 °C the temperature was kept constant while the spectra were measured. The obtained spectra were first converted to log(1/R) and then normalized to the absorption of the harmonic vibration of SiO$_2$ ($\sim$2088 cm-1 - $\sim$1718 cm-1). Difference spectra were obtained as follows: For spectrum a) the spectrum of Ti/SBA-15 (as-prepared) was subtracted from Ti/SBA-15 after photocatalytic CO$_2$ reduction. Both spectra were measured after drying at 120 °C. Spectrum b) was obtained by subtracting the spectrum of Ti/SBA-15 after photocatalytic CO$_2$ reduction from the spectrum of Au/Ti/SBA-15 after photocatalytic CO$_2$ reduction. Both spectra were measured after drying at 120 °C. Spectrum c) was obtained by subtracting the spectra of Ti/SBA-15 after photocatalytic CO$_2$ reduction and the spectra Au/Ti/SBA-15 after photocatalytic CO$_2$ measured after drying at 400 °C. XPS and UV-Vis spectra were obtained as described previously.

5.2.2 Results and Discussion

The preparation and in-depth characterization of the Ti/SBA-15 material was described in detail in the previous section.[134] In short, it was proven by UV-Vis, X-ray photoelectron and X-ray absorption spectroscopy that tetrahedrally coordinated TiO$_4$-species were obtained within the mesoporous SBA-15 matrix. The Ti content was confirmed to be 2 wt% resulting in 0.3 Ti/nm^2.

Deposition of Au nanoparticles onto the Ti/SBA-15 support was achieved by a photo-assisted deposition procedure,[133] in which Au is deposited from auric acid in an aqueous methanol solution. The evolution of H$_2$ was constantly measured during the photo-deposition procedure revealing that hydrogen evolution took place in the presence of auric acid (Fig. A4). This observation is a first indication of the successful deposition of Au nanoparticles onto Ti/SBA-15. However, to further proof the existence of Au nanoparticles diffuse reflectance UV-Vis spectroscopy was employed showing a characteristic plasmon absorption peak of metallic Au at $\sim$ 550 nm.[135,136] Elemental analysis revealed that the obtained Au/Ti/SBA-15 sample contains 0.25 wt% of Au corresponding to the amount supplied during photo-assisted deposition. Therefore, all the supplied Au ions were successfully deposited onto the support material.

The two different materials Ti/SBA-15 and Au/Ti/SBA-15 were thoroughly cleaned by illumination in humid He under static conditions in a fully metal-sealed gas-phase photoreactor (Chapter 4). Recently, Mul et al.[73,137] showed that this pre-illumination procedure in the presence of water vapor is mandatory to achieve reliable results in the photocatalytic activity in gas-phase CO$_2$ reduction. During the cleaning procedure in humid He mainly CH$_4$, C$_2$H$_4$,
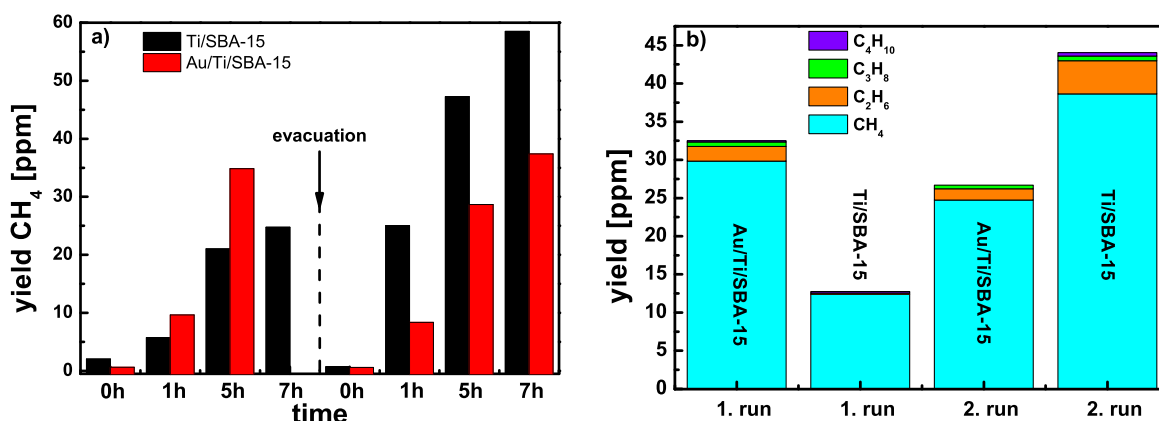
Figure 5.10: a) Time course of the methane evolution observed for Ti/SBA-15 and Au/Ti/SBA-15 during two subsequent CO_2 reduction experiments with 7h of irradiation, uncorrected values. For Au/Ti/SBA-15, no GC sampling of products was performed after 7 h in the first run. b) Evolution of different hydrocarbon species after 5 h of irradiation in two subsequent CO_2 reduction experiments. The yield of the four different hydrocarbon species is corrected for possible carbon contaminations left on the catalyst.

C_2H_6, and C_3H_8 were detected (Fig. A5), which is in good agreement with the carbon contaminations observed by Mul et al.[73] In addition to these hydrocarbons the evolution of MeOH was observed for Au/Ti/SBA-15, which is most likely a result of the photo-deposition procedure, in which methanol was used as sacrificial electron donor. MeOH was presumably converted to CO_2, which was detected throughout prolonged irradiation in the Au photo-deposition procedure. It is remarkable that the overall amount of carbon contaminations was higher than the contamination previously observed by Mul et al.[73] Therefore, subsequent cleaning steps were necessary to obtain a clean catalyst surface. In case of Ti/SBA-15 four subsequent cleaning steps were conducted, whereas Au/Ti/SBA-15 was cleaned seven times for 7 h each. Additionally, Au/Ti/SBA-15-C was prepared by calcination at 250 °C in synthetic air with the aim to reduce the number of necessary cleaning steps. This calcination temperature has previously been chosen for the calcination of PVA-protected gold colloids on metal oxides.[138] However, four additional cleaning steps in humid He were still necessary to sufficiently remove the carbon contaminations. The decrease of the concentration of the three main contaminants CH_4, C_2H_4, and C_3H_8 of each cleaning step can be represented with high accuracy as an exponential decay curve in case of the Au/Ti/SBA-15. For Ti/SBA-15 and calcined Au/Ti/SBA-15-C, on the other hand, the decrease of the contamination concentration was linear.

The actual CO_2 reduction experiments were performed under static conditions in an atmosphere of 5 % CO_2 and 6000 ppm water, which was balanced by He. These conditions were achieved by saturating a CO_2/He stream with water at 273 K. A CO_2 excess was chosen because of the unfavorable interaction of CO_2 with the isolated titanate species. The initial pressure was adjusted to 1500 mbar. The hydrocarbon formation under illumination with a 200 W Hg/Xe

lamp was monitored during a period of 7 h. For this purpose samples were taken for GC analysis after 1, 5, and 7 h. The decrease in pressure during sampling was taken into account by normalization of the obtained signals to N$_2$ used as an internal standard. After reaction the reactor was pumped down to 5 x 10^{-2} mbar and flushed with high purity He. Blank experiments revealed that no hydrocarbons are formed in the absence of a photocatalyst or in absence of high-energy UV light, which was excluded using a 435 nm cut-off filter. The hydrocarbon formation within 7 h of illumination for Ti/SBA-15 and Au/Ti/SBA-15 is shown in Fig. 5.10. Obviously, in the first reaction run the yield of CH$_4$ is significantly higher for the Au/Ti/SBA-15 sample. However, a subsequent reaction period without further pretreatment revealed that a threefold increase in the CH$_4$ yield is observed for the Ti/SBA-15 sample, whereas the overall yield for the Au/Ti/SBA-15 material is comparable to the first reaction run. Furthermore, it is evident that the yield of CH$_4$ after 1 h of irradiation for Ti/SBA-15 resembles the value obtained after 7 h of irradiation in the first reaction run.

The comparison between the Au/Ti/SBA-15 and the calcined Au/Ti/SBA-15-C sample shows that the CH$_4$ yield is significantly lower for the calcined Au/Ti/SBA-15-C sample (Fig. A6). After an additional surface cleaning in humid He, the performances of the different materials were reproduced. The CH$_4$ yields were similar for two subsequently performed reactions on Au/Ti/SBA-15 and Au/Ti/SBA-15-C. An increase in the CH$_4$ yield was again observed in the 2nd reaction run for Ti/SBA-15. However, it has to be noted that the overall yield was lower indicating that both catalysts deactivated during prolonged irradiation (Fig. A6).

In addition to CH$_4$ longer-chain hydrocarbons were produced in different quantities with both materials. While C$_2$H$_6$, C$_3$H$_8$, and C$_4$H$_{10}$ were produced in the two subsequent reactions using the Au/Ti/SBA-15 catalyst, negligible amounts of longer chain hydrocarbons were detected with Ti/SBA-15 in the first run (Fig. 5.10b). However, after deactivation of the Ti/SBA-15 material longer chain hydrocarbon formation was also observed during the first reaction run (Fig. A6). In addition to the threefold increase in the yield of CH$_4$, a threefold increase in ethane formation was observed in the subsequent reaction on Ti/SBA-15 (Fig. 5.10b). Again, these observations were reproducible after additional surface cleaning in humid He. We therefore suppose that under the present reaction conditions a carbon pool is reproducibly built up during the first reaction run on the Ti/SBA-15 material, which cannot be removed by evacuation. This carbon pool can then participate in the product formation at the beginning of the second run. As a consequence, no time for the accumulation of intermediates is required in the second run, product formation starts earlier and the total yield is higher. It is assumed that saturation of the catalyst surface with these less reactive carbon species is required to achieve high hydrocarbon yields. On the other hand, in the presence of Au, this carbon accumulation does not seem to occur and is either removed by evacuation or these carbon species are not reactive in subsequent reaction runs. Consequently, the yields observed in the second run are similar to the first ones. It is reasonable to assume that a higher hydrogenation rate in the presence of Au leads to a carbon-free surface after the first reaction run. In general, noble metals usually

show high activity in hydrogenation reactions.[139,140] In photocatalytic reactions it is accepted that H_2 formation occurs at these electron trapping sites, and more hydrogen is available in close proximity to gold facilitating hydrogenation.[37,38] It should be noted that this is in agreement with the higher yield of H_2 that has been observed during photo-deposition experiments. Visible light-assisted photoreactions in the presence of Au can be excluded as no product formation was observed when the samples were irradiated with Vis light. The 30 ppm of CH_4 produced within 5 h of irradiation in the presence of Au/Ti/SBA-15 is equivalent to 0.047 mol resulting in 0.188 mol/gcat/h or 9.4 mol/gTi/h. For Ti/SBA-15 the yield in the second run can be calculated to amount to 12.1 mol/gTi/h. The comparison illustrates that on the basis of one gram of catalyst the Au/Ti/SBA-15 is roughly 7 times more active than the catalysts studied by Mul et al.[73] However, comparing the yields on a basis of g^{-1} Ti Mul et al.[73] observed five times higher methane yields as only 0.05 wt% Ti were incorporated into the SBA-15. The applied reaction conditions differ considerably rendering the comparison difficult. Reactions with stoichiometric CO_2/H_2O mixtures are in progress.

To get further insight in the carbon pool formation, two consecutive reaction cycles were performed followed by irradiation of the photocatalysts in humid He. Surprisingly, on both catalysts evolution of hydrocarbons was observed under irradiation in humid He (Fig. 5.11a). A steep increase in methane and longer-chain hydrocarbon formation was observed after 1 h of irradiation for Ti/SBA-15. This is in line with the proposed formation of a carbon pool. For the Au/Ti/SBA-15 sample a slower formation of C_xH_y is characteristic. The formation of hydrocarbons during irradiation in humid He, however, is a clear indication that a carbon pool is also created on Au/Ti/SBA-15, but its effects on hydrocarbon formation are less pronounced. Possibly, the nature or location of these carbon species is different.

Finally, the influence of the water content on the photocatalytic CO_2 reduction reaction was investigated using a reaction gas mixture containing 5 % CO_2/He. Consequently, only preadsorbed water in the pores of the catalysts was available as reducing agent. The results of these reaction conditions with only surface-bound H_2O are shown in Fig. 5.11b. Prior and subsequent to these experiments CO_2 reduction was performed using the reaction gas mixture containing gas-phase water. These results are also included in Fig. 5.11b. Unexpectedly, less longer-chain hydrocarbons are formed in the absence of gas-phase water on both catalysts systems. The CH_4 yield is significantly higher for both catalysts. It should be noted that the carbon pool was already formed on the Ti/SBA-15 surface during a previously performed experiment with gas-phase water. Considering the overall produced carbon content (CH_4, C_2H_6, C_3H_8, C_4H_{10}) the carbon yield (C*) increased by about 20 % in the absence of water, which was mainly due to the higher CH_4 yields compensating the decrease in longer-chain hydrocarbon yields. The overall hydrocarbon yield was even increased in the consecutive experiment performed with the CO_2/H_2O mixture. For Ti/SBA-15 the CH_4 yield decreased, but the C_2H_6 yield was drastically higher (Fig. 5.11b). A higher ethane yield and a higher methane yield were observed for the Au/Ti/SBA-15 sample, which might indicate that a carbon pool was formed on the surface of
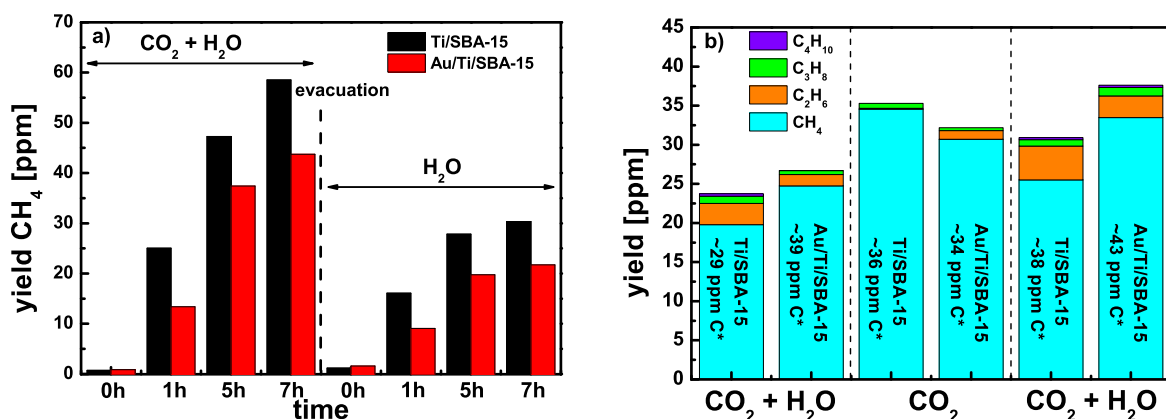
Figure 5.11: a) CH₄ yield during irradiation of the photocatalysts in the reaction gas mixture and CH₄ yield during irradiation in humid He subsequently performed. Evolution of CH₄ during irradiation in humid He is due to remaining carbon species on the surface. b) Hydrocarbon yields in photocatalytic CO_2 reduction experiments obtained with varying gas-phase water contents in the reactant feed after 5 h for the Ti/SBA-15 and Au/Ti/SBA-15 samples. The yield of the four different hydrocarbon species is corrected for possible carbon contaminations left on the catalyst.

the Au/Ti/SBA-15 sample. Furthermore, these experiments show that the water content on the sample surface is sufficient to perform photocatalytic CO_2 reduction for at least five hours of irradiation with both photocatalysts. In contrast to these observations Anpo et al.[58] observed the formation of larger quantities of CH₄ for high H_2O/CO_2 ratios, and only small quantities of CH₄ were produced in the absence of gas-phase water. However, it is well known that water strongly binds to isolated Ti-species and high temperatures are required to remove water effectively.[80] Therefore, the surface of the photocatalysts should be saturated with H_2O and, as a result, CO_2 reduction is feasible. In addition, high methane yields in water-poor conditions are in agreement with a C_2H_6/CH₄ ratio exceeding 1 for stoichiometric CO_2/H_2O mixtures observed by Mul et al.[73], and increasing ethane yield for higher water content reaction gas-mixtures as observed by Anpo et al.[58] Further studies are clearly required to fully explain these observations. However, a hypothesis which should be considered is the inhibition of a subsequent photo-reforming reaction of the produced CH₄ occurring in the presence of gas-phase H_2O. CO and H_2 may be produced due to this process, which then may be involved in the formation of higher hydrocarbons. In terms of irradiation in CO_2, this will diminish the formation of higher hydrocarbons. Furthermore, an influence of the carbon pool in higher hydrocarbon production was observed. Thus, it should be considered that high water contents are required to hydrogenate these species. Furthermore, the water content may influence the mobility of intermediates on the catalyst surface.

After reaction all samples were characterized by DRIFTS, UV-Vis, and XPS and compared to the unreacted materials to get further insight in possible intermediates, the deactivation of the

catalysts, and the carbon pool, which was built up during CO$_2$ reduction. The carbon content as determined by XPS analysis was similar for all the samples. Structural changes of the Ti-species within the course of gas-phase photocatalytic CO$_2$ reduction causing deactivation of the materials can be excluded comparing Ti/SBA-15 before and after reaction or Au/Ti/SBA-15 before and after reaction (XPS results, Fig. A7). UV-Vis indicates a narrowing of the Au plasmon for Au/Ti/SBA-15 after reaction, which may be caused by different Ti-Au interactions (Fig. A8). One has to keep in mind that TiO$_x$-species have the potential to alter the local environment of the Au particles.[135,136] However, there is no clear evidence for a loss of TiO$_x$ or the polymerization of the TiO$_x$ species, which could explain the deactivation of the Ti/SBA-15 and the Au/Ti/SBA-15 during prolonged irradiation.

On the other hand, structural changes of the Ti-species caused by the photo-deposition of Au were detected by UV-Vis and XPS (Fig. A8 and Fig. A9). The Ti 2p signal of the Au/Ti/SBA-15 is shifted to lower binding energies compared to the Ti/SBA-15 sample, and two different Ti-species were needed to obtain a reasonable fit (Fig. A9). This additional signal was in good agreement with an additional shoulder observed in the O 1s region of the Au/Ti/SBA-15. From UV-Vis spectroscopy the absorption onsets of Ti/SBA-15 and Au/Ti/SBA-15 were similar (Fig. A8). However, heating of the sample revealed that there is no increase of the absorption edge energy for Au/Ti/SBA-15 due to the loss of water molecules bound to the Ti-species, which is usually observed after a drying of the samples.[134] These observations clearly point to a change in the coordination of the Ti-species. Most likely the changes of the Ti-species occur in close proximity to the Au nanoparticles. It can be assumed that the combination of Ti and Au in close proximity, rather than the presence of Au alone, might be necessary to obtain the higher hydrogenation activities observed during CO$_2$ reduction. However, based on the presented results a distinction of the different species is not feasible and further studies are required to fully describe the changes of the Ti-species upon Au photo-deposition. A HRTEM study combined with photocatalytic test reactions was performed, which is presented in the next section. Ti/SBA-15 materials containing different TiO$_x$ loadings are used to investigate structural changes and to relate them with the activities.

Difference IR spectra of the reacted and the fresh Ti/SBA-15 revealed that formaldehyde and paraformaldehyde were accumulated at the surface of the Ti/SBA-15 sample after CO$_2$ reduction reaction (Fig. 5.12). The bands observed at 1685 and 2853 cm^{-1} are in good agreement with values of the ν(C=O) and ν(CH$_2$) stretching modes of formaldehyde adsorbed at different surfaces.[141–144] The intense band at 2972 cm^{-1} is representative for the asymmetric stretching (ν_a(CH$_2$)) of paraformaldehyde, which is known to be obtained by the polymerization of formaldehyde at low temperatures (Table 5.3).[141,143,144] The assignment of the bands is clearly verified by the thermal stability of paraformaldehyde. Interestingly, less formaldehyde was detected for the Au/Ti/SBA-15 sample and the signals assigned to paraformaldehyde are shifted to higher wavenumbers (Fig. A10). Assuming that paraformaldehyde is the intermediate of higher hydrocarbons it is likely that it is immediately available at the surface of
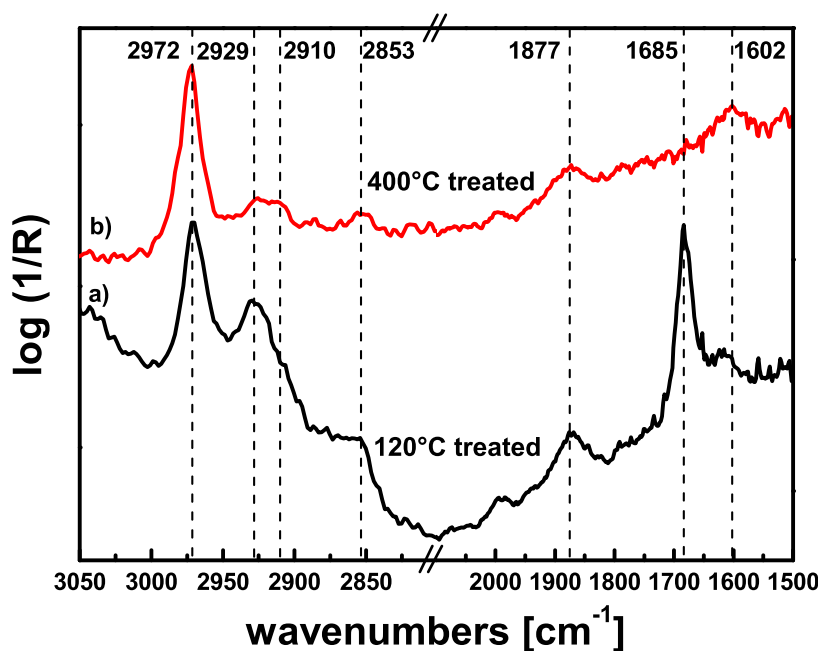
Figure 5.12: Difference DRIFT spectra of the Ti/SBA-15 before and after photocatalytic CO$_2$ re-
duction obtained after heating to 120 °C and 400 °C. Difference spectra were obtained
as follows: For spectrum a) the spectrum of Ti/SBA-15 (as-prepared) was subtracted
from Ti/SBA-15 after photocatalytic CO$_2$ reduction. Both spectra were measured af-
ter drying at 120 °C. Spectrum b) was derived by subtracting the spectra obtained after
drying at 400 °C.

the Au/Ti/SBA-15 sample and higher hydrocarbon formation can be produced, whereas at the
Ti/SBA-15 sample paraformaldehyde is formed upon accumulation of formaldehyde at the sur-
face. This might explain the inhibition of ethane production on Ti/SBA-15, as observed during
the 1st reaction run.

In the literature different reaction mechanisms are proposed for photocatalytic CO$_2$ reduction.
Anpo et al.[67] propose a mechanism in which CO$_2$ and H$_2$O decompose competitively into C
and OH radicals at the excited Ti-O centers, presumably with CO as an intermediate species.
Similar observations were recently reported for crystalline TiO$_2$ by Zapol et al.[69] Mul et al.[73]
followed the proposed route by Frei et al.[71] who suggested a mechanism involving CO in the
initial state and formaldehyde, which is converted to CH$_4$ and longer-chain hydrocarbons in
the presence of water. A Ti-hydroperoxid species is assumed to be essential in this process.
Due to the results obtained within this study the mechanism proposed by Mul et al.[73] and Frei
et al.[71] appears to be more likely as 1) formaldehyde and paraformaldehyde were observed
by diffuse reflectance IR measurements, 2) higher CH$_4$ yields are observed for water-poor
reaction conditions, and 3) CO$_2$ is weakly interacting with isolated Ti-species,[134] whereas
water is strongly bound to the surface.

Table 5.3: Wavenumbers (cm^{-1}) and mode assignments of formaldehyde and paraformaldehyde on different substrates reported in literature.

Mode Assignment	H$_2$CO[144]	(H$_2$CO)$_n$[144]	H$_2$CO[141]	(H$_2$CO)$_n$[141]	H$_2$CO[143]	(H$_2$CO)$_n$[143]
ν_a(CH$_2$)	2884	2982	2928	2928	2894	2980
ν_s(CH$_2$)	2820	2917	2928	2928	2830	
ν(C=O)	1727	-	1694	-	1717	-

5.2.3 Conclusions

In summary, Ti/SBA-15 and Au nanoparticles embedded into Ti/SBA-15 were studied in photocatalytic CO$_2$ reduction. Both materials were active in photocatalytic CO$_2$ reduction forming CH$_4$. However, an increase in the hydrogenation ability of the Au-containing catalyst was found, whereas an active carbon pool formation was observed on Ti/SBA-15. Unlike the less reactive carbon pool formed on Au/Ti/SBA-15 the carbon pool on Ti/SBA-15 can participate in subsequent reactions. Experiments with varying water content indicate that the carbon chain growth is significantly affected by the gas-phase water content, and formaldehyde/paraformaldehyde were identified as reaction intermediates.

5.3 Effects of Au and ZnO on the structure and photocatalytic activity of TiO$_x$/SBA-15 materials

Abstract[3]

Gold nanoparticles can be efficiently photo-deposited on titanate-loaded SBA-15, and the formation of hydrogen is observed during the photo-deposition process. Additionally, the presence of the gold nanoparticles greatly enhances the performance of Ti(x)/SBA-15 in the photocatalytic hydroxylation of terephthalic acid. HRTEM studies show that larger Au nanoparticles are photo-deposited at the outer surface of Ti(x)/SBA-15 materials and that TiO$_x$ tends to form agglomerates in close proximity to the Au nanoparticles. The activity of Au/Ti(x)/SBA-15 materials was found to be dependent on the TiO$_x$ loading. Photocatalytic tests indicated that the amount of initially isolated TiO$_4$ tetrahedra determines the activity of the Au/Ti(x)/SBA-15, and Au/Ti(x)/SBA-15 catalysts in which the TiO$_x$ species are already clustered showed lower photocatalytic activities. When isolated zinc oxide (ZnO$_x$) species are present on TiO$_x$/SBA-15, the photo-deposited gold nanoparticles are smaller, well dispersed within the pore structure of SBA-15, and agglomeration of TiO$_x$-species can be neglected. The dispersion of Au in the SBA-15 matrix obtained due to the photo-deposition procedure seems to depend on the mobility of the TiO$_x$-species, which is mainly determined by the agglomeration of TiO$_x$. Effective hydrogen evolution requires Au/TiO$_x$ assemblies as in Au/Ti(x)/SBA-15, whereas hydroxylation of terephthalic acid can also be performed with Au/ZnO$_x$/TiO$_x$/SBA-15 materials. However, isolated TiO$_x$ species have to be grafted onto the support prior to the zinc oxide species. In conclusion, the results are strong evidence for the necessary presence Ti-O-Si bridges for high photocatalytic activity in terephthalic acid hydroxylation.

5.3.1 Short Introduction

In the last decades highly dispersed Au nanoparticles on metal oxides have become of major interest for several reactions such as CO oxidation, selective oxidation of alcohols or methanol synthesis.[139,145–147] Recently, the potential of Au nanoparticles in photocatalysis has received considerable attention.[37,38] Within several studies improved photocatalytic performance due to visible light absorption of the Au plasmon and due to good electron storage capacities are reported.[148,149] One of the most studied composites in this regard are Au/TiO$_2$ materials, which exhibit catalytic activity in organic pollutant degradation and hydrogen evolution due to photocatalytic reforming of alcohols. Usually the utilized composites are obtained by deposition-precipitation, colloidal synthesis, or by photo-deposition of Au nanoparticles.[37,138] Even though bulk TiO$_2$ and Au/TiO$_2$ are versatile materials, single-site titania catalysts are widely studied particularly in photocatalytic CO$_2$ reduction, which was already shown by Anpo et al.[58] Mori et al.[131,132] showed that the deposition of Au nanoparticles using photo-excited Ti-containing zeolites is feasible. We demonstrated that Au/Ti/SBA composite materials prepared by a photo-deposition procedure of Au were highly active in photocatalytic CO$_2$ reduction, presumably due to a higher hydrogenation activity of the composite material in presence of Au nanoparticles. However, the UV-Vis spectroscopic results and the XPS characterization showed that the Ti coordination of the isolated TiO$_4$ tetrahedra changed upon Au photo-deposition. Two different TiO$_x$ species were observed by XPS and UV-Vis spectroscopy results inidcated that less water interacts with the Au/Ti/SBA material. However, the interaction between the TiO$_x$ species and photo-deposited Au is still unclear and the origin of the effect of Au on the photocatalytic activity of the Ti/SBA material is not yet solved.

Recently, we have shown that using a reproducible grafting method of Ti(O^{i}Pr)$_4$ high loadings of isolated or slightly agglomerated TiO$_x$ species can be obtained.[134] Furthermore, we were able to introduce ZnO$_x$ species into the materials by grafting of Zn(acac)$_2$.[134] Crucial properties of the photocatalysts, such as light absorption, CO$_2$ adsorption, basic and acidic sites on the surface of the different materials were studied.[134] It was shown that ZnO$_x$ species significantly enhance the CO$_2$ adsorption properties, whereas the light absorption is mainly depending on the HOMO-LUMO excitation of the TiO$_x$ species. XPS and EXAFS showed that preferably Ti-O-Zn bonds are formed when ZnO$_x$ is grafted first.[134] In this contribution in-depth characterization of photo-deposited Au nanoparticles was performed depending on the TiO$_x$ loading in Ti(x)/SBA samples. The activity of the as-received and Au-modified materials was determined by hydrogen evolution reaction due to photo-reforming of methanol and the hydroxylation of terephthalic acid. Thus, the electron and the hole availability upon photo-excitation were assessed. Furthermore, the effect of ZnO$_x$ species was determined.

It is shown that the photo-deposition of Au nanoparticles enhances the photocatalytic properties of the materials regarding photocatalytic hydrogen production and hydroxylation of organic compounds. Agglomeration of TiO$_x$ species occurring during the diffusion-controlled photo-

deposition of Au is independent of the initial TiO$_x$ loading, but the agglomeration of TiO$_x$ in the presence of ZnO$_x$ is clearly inhibited and Au is photo-deposited homogeneously throughout the whole material. Furthermore, our results provide evidence that Ti-O-Si bonds are essential for photocatalytic activities in the terephthalic acid hydroxylation reaction.

Experimental

Sample synthesis

The synthesis of SBA-15 and the grafting procedure for obtaining isolated and slightly agglomerated TiO$_x$ and ZnO$_x$ species on the SBA-15 surface have been described in detail in the previous section.[134] In brief, Ti(O^{i}Pr)$_4$ (99.999 %, Sigma-Aldrich) or Zn(acac)$_2$ (98 %, Alfa Aesar, purified by means of sublimation) were dissolved in dry toluene and contacted with the dried SBA-15 support at room temperature. After 4 h of stirring, the solution was removed by sedimentation or centrifugation. Samples were washed three times with dry toluene, dried in vacuum and calcined. Coverages up to 1 Ti nm^{-2} or 1 Zn nm^{-2} can be obtained in one grafting step, while for higher coverages the grafting procedure had to be repeated.

Characterization

Characterization of the Au-modified materials was performed by elemental analysis, UV-Vis spectroscopy, and Transmission Electron Microscopy (TEM). In-depth characterization of the different as-received TiO$_x$- and ZnO$_x$-grafted SBA-15 supports by means of elemental analysis, nitrogen physisorption, UV-Vis spectroscopy, X-ray photoelectron spectroscopy (XPS), and X-ray absorption spectroscopy (XAS) is described in the previous section.[134]

UV-Vis diffuse reflectance spectra (DRS) were recorded in a Perkin Elmer Lambda 650 UV-Vis spectrometer equipped with a Praying-Mantis mirror construction using MgO as the 100 % reflection reference.

XPS was performed in a UHV set-up equipped with a Gammadata-Scienta SES 2002 analyzer. The base pressure in the measurement chamber was 5 x 10^{-10} mbar. Monochromatic Al Kα (1486.6 eV; 14.5 kV; 30 mA) was used as incident radiation, and a pass energy of 200 eV was chosen resulting in an effective instrument resolution higher than 0.6 eV. Charging effects were compensated using a flood gun, and binding energies were calibrated based on positioning the main C 1s peak at 285 eV, which originates from carbon contaminations. Prior to the measurements the samples were dehydrated at 200 °C under ultra-high vacuum (UHV) conditions. Measured data were fitted using Shirley-type backgrounds and a combination of Gaussian-Lorentzian functions with the CasaXPS software. The Ti/Si atomic concentration ratios were obtained by determining the integral area of the Gaussian-Lorentzian functions and correcting the values by the specific atomic sensitivity factors proposed by Wagner.[110]

Bright field TEM, high resolution TEM (HRTEM), electron energy-loss spectroscopy (EELS), and energy-filtered TEM (EFTEM) were conducted on a Philips CM30 equipped with a Schottky field emission gun and a post-column GIF 200 energy filter, operated at 300 kV. High-angle

annular dark-field scanning transmission electron microscopy (HAADF-STEM), spatially resolved energy-dispersive X-ray spectroscopy (STEM-EDX), and the electron tomography series were acquired on a FEI Tecnai G2 equipped with a Schottky field emission gun operated at 200 kV and FEI Titan "cubed" microscope equipped with a probe corrector, operated at 300 kV. EDX spectra were recorded on Philips CM20 microscope equipped with a LaB6 filament operated at 200 kV.

Photocatalytic measurements

Photo-deposition of Au was performed in a continuous flow stirred-tank reactor equipped with a 700 W Hg immersion lamp cooled by water circulating in a double wall jacket.[133] During photo-deposition the concentration of CO_2, O_2, and H_2 were analyzed with a non-dispersive IR photometer, a paramagnetic and a thermal conductivity detector (XStream, Emerson Process Management), respectively. 350 mg of catalyst were dispersed in a solution of 550 ml dest. H_2O, 50 ml MeOH, and 3.5 ml of a 1.5 x 10^{-3} molar auric acid solution (HAuCl$_4$ 99.9 %, Sigma Aldrich). The reactor was deaerated for 60 min using pure N_2 prior to irradiation. Photo-deposition was performed at 30 °C with 50 % irradiation power (350 W) for 2.5 h. After successful photo-deposition the materials were filtered and freeze-dried over night. Terephthalic acid (TA) hydroxylation was performed to determine the amount of OH radicals generated during irradiation. 150 mg of catalyst was ultra-sonicated for 5 min in 500 ml of a 0.01 M NaOH solution containing 3 mM TA.[150] The suspension was stirred for additional 30 min in the dark before illumination was started by means of a 150 W Xe immersion lamp cooled by water circulating in a double wall jacket. Samples were taken every 15 min, filtered with a Filtropur S and the fluorescence spectra were measured with a double monochromatic fluorescence spectrometer (Fluorolog FL3-22, HORIBAJobin Scientific). The emission wavelength was set to 320 nm and the characteristic fluorescence at 426 nm which is directly correlated with the OH radicals generated was measured.

5.3.2 Results and Discussion

Sample structure of the as-received materials

Characterization of the Ti(x)/SBA and TiO$_x$- and ZnO$_x$-grafted SBA-15 support materials is described in the previous section.[134] In short, UV-Vis, X-ray photoelectron (XPS), and X-ray absorption spectroscopy (XAS) proved that in dry samples TiO$_4$ species in a tetrahedral coordination sphere were obtained within the SBA-15 material at low Ti loadings of 2.1 wt%. With increasing titania loading the species start to polymerize, however, for Ti loadings up to 7 wt%, corresponding to about 1 Ti nm^{-2}, most of the TiO$_x$ species are still isolated. For all materials a homogeneous titania distribution was obtained as evidenced by XPS and EFTEM. A wavelength of less than 300 nm is required to excite electrons across the HOMO-LUMO gap in case of fully isolated TiO$_x$ species. For agglomerated TiO$_x$ at a loading of 2.7 Ti nm^{-2}, the re-
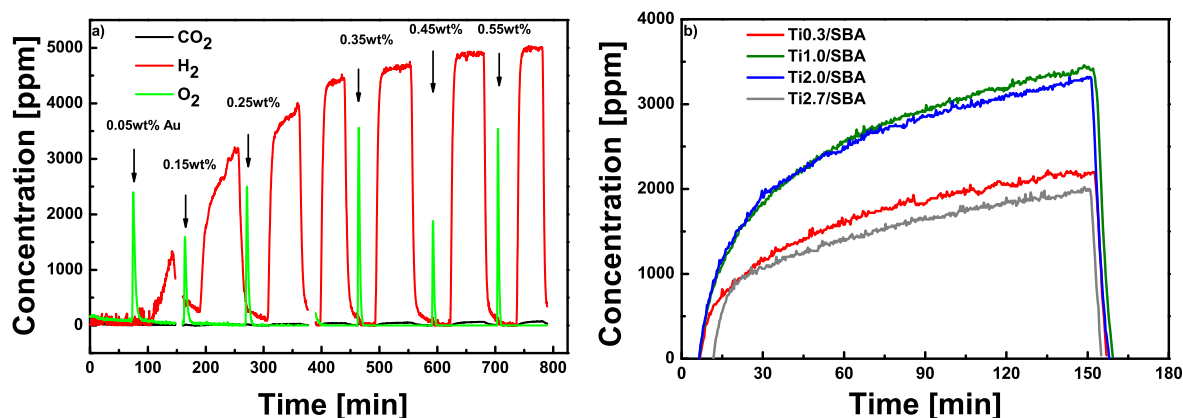
Figure 5.13: a) The H_2 evolution during the stepwise photo-deposition of Au nanoparticles on Ti2.0/SBA is shown and the overall amount of deposited Au is indicated. b) H_2 evolution measured during the photo-deposition process of Au (0.25 wt%) on Ti(x)/SBA materials with increasing Ti loading.

quired wavelength shifts to 320 nm. For the TiO_x- and ZnO_x-grafted SBA-15 samples, namely Ti1.2/Zn0.3/SBA and Zn0.3/Ti1.2/SBA, strong interactions between TiO_x- and ZnO_x were detected. The TiO_x species were shown to be modified by the order of the grafting steps, and more isolated TiO_x was obtained when ZnO_x was grafted subsequent to TiO_x as in Zn0.3/Ti1.2/SBA.

Photocatalytic hydrogen evolution in presence of Au

It is well known that Au can act as a co-catalyst in photocatalysis.[37,38] In general metal co-catalysts are assumed to act as an electron or hole sink enhancing the electron-hole lifetime in photocatalysis.[37,38] Furthermore, the photo-deposition procedure is reported to be a suitable technique to deposit Au or other metal co-catalysts on the surface of a photoactive material.[131,132] Thus, Au was photo-deposited using methanol as sacrificial agent.[148] During photo-deposition, the hydrogen evolved due to sacrificial water splitting was measured online.[133] For all measurements it was confirmed that H_2 evolution occurs only in a dispersion of Ti(x)/SBA-15 samples in auric acid solution under irradiation, whereas no H_2 was detected in absence of any of the components. Bowker et al.[148] as well as other groups reported that there is a maximum amount of co-catalyst which is beneficial for photocatalytic reactions. In these studies they pointed out that too high loadings might block active sites which would, at a certain loading, overwhelm the otherwise positive effect of the co-catalyst. Therefore, the maximum amount of deposited gold was evaluated using a stepwise photo-deposition procedure, following the amount of H_2 evolved during photo-deposition as previously reported by Busser et al.[133]

For low gold loadings of 0.05 wt% deposited on Ti2.0/SBA the evolution of hydrogen slowly increases within 60 min of irradiation time (Fig. 5.13a). Afterwards, the Au concentration was increased stepwise and during each deposition interval irradiation was performed for ~ 60 min. The slow increase in hydrogen evolution was observed for Au loadings of up to 0.35 wt%, at

which the hydrogen evolution stabilizes, and the maximum hydrogen evolution was observed for a gold content between 0.45 and 0.55 wt% Au for the Ti2.0/SBA material (Fig. 5.13a). The same trend in hydrogen evolution with increasing Au loading was observed for Ti1.0/SBA. Therefore, the maximum Au loading for the Ti(x)/SBA materials was estimated to be 0.45 wt% for the two materials.

In a second set of experiments the amount of Au in the solution was fixed to 0.25 wt% of Au with respect to the amount of sample dispersed in the solution. These experiments were performed in order to study the effect of the different Ti loadings as well as the effect of Zn. The amount of Au was chosen to be lower than the maximum beneficial Au loading obtained during the stepwise deposition procedure to avoid blocking of active sites for samples grafted with lower TiO$_x$ loadings. The evolution of hydrogen as a function of irradiation time during the in-situ photo-deposition experiments is shown in Fig. 5.13b for different Ti(x)/SBA materials. From these results it can be clearly seen that the measurable amount of H$_2$ in the gas-phase significantly increases with the Ti loading up to 7 wt% as in Ti1.0/SBA, while it decreases afterwards with higher Ti loadings as in case of Ti2.0/SBA and Ti2.7/SBA. This trend is a first indication for different activities of the isolated and polymerized TiO$_x$ species. The higher loaded Ti1.0/SBA is more active compared to the Ti0.3/SBA, however, in both cases Ti is mostly present as isolated sites that have a tetrahedral coordination sphere in the dry state. Those species should be entirely surrounded by Ti-O-Si bonds and are able to coordinate two water molecules, upon which they change into an octahedral configuration.[80] For the higher loaded Ti1.0/SBA more of these isolated species can contribute to the hydrogen generation. Increasing the TiO$_x$ loadings the evolved hydrogen drops off due to polymerization of the TiO$_x$ species. Therefore, less isolated TiO$_4$ is present on the SBA-15 support that can contribute to the hydrogen generation. The beneficial effect of Au supported on different semiconductors in photocatalytic H$_2$ production or photocatalytic dye degradation has already been demonstrated by several research groups.[37,38,149] It is supposed that Au-containing materials show enhanced dye degradation rates and a significant increase in H$_2$ productivity due to efficient electron storage on the Au nanoparticles resulting in a decrease in recombination rates and due to the ability of the Au nanoparticles to act as an electron transfer site.[38,149] An influence of the Au loading on the H$_2$ production rate has been reported recently.[38,148] In the present study the influence of Au loading on the hydrogen evolution rate was confirmed for the Ti(x)/SBA-15 materials, and it is reasonable to assume that H$_2$ evolution measured during photo-deposition of gold onto Ti(x)/SBA materials was due to water splitting in presence of methanol as sacrificial agent. Furthermore, at a fixed Au loading the obtained results indicate an effect of the TiO$_x$ coordination and agglomeration on the hydrogen evolution ability.

For the Zn0.3/Ti1.2/SBA and Ti1.2/Zn0.3/SBA catalysts no hydrogen evolution was observed during deposition of 0.25 wt% Au. However, the Zn0.3/Ti1.2/SBA and the Ti1.2/Zn0.3/SBA material became bluish after the experiments, which was also observed for the Ti(x)/SBA samples. Furthermore, it should be mentioned that within the detection limit also no hydrogen
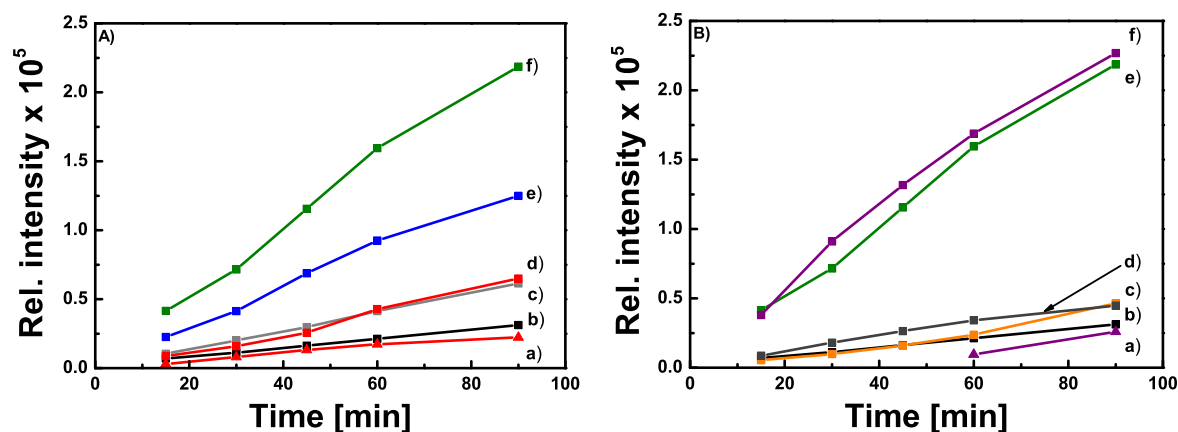
Figure 5.14: A) Time-dependent terephthalic acid hydroxylation reaction for a) Ti0.3SBA, b) Au/SBA-15, c) Au/Ti2.7/SBA, d) Au/Ti0.3/SBA, e) Au/Ti2.0/SBA, and f) Au/Ti1.0/SBA. B) Time-dependent terephthalic acid hydroxylation reaction for a) Zn0.3/Ti1.2/SBA, b) Au/SBA-15, c) Au/Zn0.3/SBA, d) Au/Ti1.2/Zn0.3/SBA, e) Au/Ti1.0/SBA, and f) Au/Zn0.3/Ti1.2/SBA.

evolution was observed for the Zn0.3/SBA sample or the bare SBA-15 support and the samples remain white after the photo-deposition experiments.

Measurements of the photocatalytic H$_2$ evolution mainly probed the availability of photo-generated electrons upon light irradiation. To probe the availability of photo-generated holes for photocatalytic reactions the terephthalic acid (TA) hydroxylation was used as a simple test reaction. It is known that the OH radical, which is formed upon reaction of surface adsorbed water or hydroxyl groups, can react with terephthalic acid (TA) to generate 2-hydroxy tereph-thalic acid (TAOH), which, in its terephthalate form, emits unique fluorescence at around 425 nm.[151,152] Firstly, the as-prepared Ti(x)/SBA and TiO$_x$- and ZnO$_x$-grafted SBA-15 materials were tested. The TA test revealed that the as-made materials, regardless of the coverage of titanate species or the presence of ZnO$_x$, do not show significant photocatalytic activity under the experimental conditions for the hydroxylation of TA, which result in a strong increase in the characteristic TAOH fluorescence band. This was expected as a Xe lamp was used, which does not emit intense UV radiation to excite the isolated or polymerized TiO$_x$ species in the Ti(x)/SBA and TiO$_x$- and ZnO$_x$-grafted SBA-15 materials. The two possible reasons for the low activity may be the low intensity of deep UV light and a fast electron-hole recombination. The influence of the latter should be diminished using the Au-modified Ti(x)/SBA and TiO$_x$- and ZnO$_x$-grafted SBA-15 samples obtained after photo-deposition experiments.

The TA hydroxylation test reaction was repeated with the Au/Ti(x)/SBA, Au/Zn0.3/Ti1.2/SBA, and Au/Ti1.2/Zn0.3/SBA samples. The obtained results are shown in Fig. 5.14a and Fig. 5.14b, respectively. The TA test results indicate that the Au/Ti(x)/SBA-15 materials are able to gener-ate OH radicals, which can easily react with terephthalic acid to form TAOH, whereas Au/SBA-15 is nearly inactive. Furthermore, the almost linear relationship between irradiation time and

fluorescence signal intensity indicates that Au/Ti(x)/SBA-15 materials are stable under these reaction conditions. A small formation of TAOH in the case of Au/SBA-15 may be related to surface hydroxyl groups of the SBA-15 support participating in the reaction. It has to be noted that in a blank experiment without the addition of a catalyst or SBA-15 substrate material no reaction was observed. However, all Au/Ti(x)/SBA catalysts exhibit higher fluorescence signals of TAOH compared to Au/SBA-15. Within the Au/Ti(x)/SBA materials, Au/Ti1.0/SBA shows the highest production rate of TAOH. The higher loaded samples Au/Ti2.0/SBA and Au/Ti2.7/SBA and the Au/Ti0.3/SBA sample with the low Ti loading are clearly less active. These samples contain many isolated TiO$_4$ species as shown by XAS and XPS.[134] Higher loaded samples contain mainly polymerized TiO$_x$ chains, which appear to be less active. It is striking that the activity of Au/Ti0.3/SBA is as low as the activity of Au/Ti2.7/SBA, even though it was shown that only isolated TiO$_x$ species are present. This observation may be attributed to the larger absorption edge energy in case of Ti0.3/SBA or the lower amount of active TiO$_x$ centers. However, the observed trend in the TA test reaction is in good agreement with the hydrogen evolution rates obtained during Au photo-deposition. Thus, the results strongly suggest that isolated TiO$_x$ species are required to achieve high activities in the TA hydroxylation reaction and the photocatalytic reforming of methanol.

The time-dependent evolution of hydroxylated TA for all Zn-containing SBA-15 samples is shown in Fig. 5.14b. Au/Ti1.0/SBA is shown for comparison. While Au/Zn0.3/Ti1.2/SBA is at least as active as Au/Ti1.0/SBA, the other two Zn-containing samples, especially Au/Zn0.3/SBA, are significantly less active in the TA hydroxylation test reaction. These results indicate that TiO$_x$ species rather than ZnO$_x$ species bound to the silica surface are the photocatalytically active species. Furthermore, these results demonstrate that the order of the grafting steps clearly influences the photocatalytic activity: Au/Ti1.2/Zn0.3/SBA is clearly less active than Au/Zn0.3/Ti1.2/SBA. In the case of Au/Ti1.2/Zn0.3/SBA TiO$_x$ is grafted onto a Zn0.3/SBA, thus it is likely that Ti-O-Zn bonds are formed rather than Ti-O-Si bonds. Indeed, the characterization results based on X-ray photoelectron spectroscopy and X-ray absorption spectroscopy indicate an intense interaction between Zn and Ti in samples prepared with a similar composition as the Au/Ti1.2/Zn0.3/SBA material.[134] In the opposite case as in Au/Zn0.3/Ti1.2/SBA, where ZnO$_x$ is grafted after TiO$_x$ grafting is completed, the photocatalytic activity in TA hydroxylation is still high. For this material it can be assumed that Ti-O-Si bonds are formed during the first grafting step and that the formation of Zn-O-Ti bonds due to the post grafting of ZnO$_x$ is negligible. In summary, a structure-activity correlation was observed for the ZnO$_x$-containing materials, as the order of the grafting steps significantly influences the photocatalytic activity especially in the TA hydroxylation test reaction. Ti-O-Si bonds rather than Ti-O-Zn bonds are required to run the catalytic reaction. Additionally, it was shown that ZnO$_x$ species are not able to perform the photocatalytic TA hydroxylation reaction, which is in agreement with the poor absorption properties.[134]

By comparing the photocatalytic activity towards hydroxylation of TA of all the as-prepared

materials and all the Au-modified samples it can be clearly seen that Au is able to enhance the photocatalytic activity of the Ti(x)/SBA materials and the ZnO$_x$/TiO$_x$/SBA samples. Presumably, Au is acting as a co-catalyst in these cases. Based on these results it is not clear whether Au is acting as an electron sink or additionally enables the materials to be activated by visible light due to the Au plasmon absorption. Recent results for photocatalytic CO$_2$ reduction indicate that visible light-driven CO$_2$ reduction by excitation of the Au plasmon was not feasible for the Au/Ti03/SBA catalyst, and thus Au is mainly acting as an electron sink in these samples (Chapter 5.2). However, it is striking that even in the presence of Au photocatalytic reforming of methanol was obviously not possible for Au/Zn0.3/Ti1.2/SBA as no hydrogen was evolved. On the other hand, Au/Zn0.3/Ti1.2/SBA exhibited similar photocatalytic activity towards TA hydroxylation as the most active Au/Ti1.0/SBA sample. In order to elucidate this phenomena on the different materials were characterized regarding the nature of the Au particles. Characterization was performed by means of ICP-OES, UV-Vis spectroscopy, XPS, and TEM analysis.

Characterization of Au particles

Table 5.4: Au content after stepwise and photo-deposition as determined by ICP-OES measurements for Au/Ti(x)/SBA-15, Au/Zn0.3/Ti1.2/SBA, and Au/Ti1.2/Zn0.3/SBA materials.

Sample	Au/Ti0.3/SBA	Au/Ti1.0/SBA	Au/Ti2.0/SBA	Au/Ti2.7/SBA
Au [wt%]	0.25	0.29/0.54	0.27/0.55	0.28
Sample	Au/SBA-15	Au/Zn0.3/SBA	Au/Ti1.2/Zn0.3/SBA	Au/Zn0.3/Ti1.2/SBA
Au [wt%]	0.02	0.05	0.1	0.14

ICP-OES results indicate that the amount of deposited Au is in good agreement with the loading of 0.25 wt% and the 0.55 wt% supplied during the different photo-deposition procedures on the Au/Ti(x)/SBA materials (Table 5.4). As expected, Au can hardly be deposited on Au/SBA-15, most likely due to a lack of photoactive sites. The residual Au found on Au/SBA-15 was probably due to a simple decomposition or photobleaching process of auric acid on the support, which is not necessarily photo-induced. For the Zn-containing materials Au/Zn0.3/Ti1.2/SBA and Au/Ti1.2/Zn0.3/SBA it can be clearly seen that less Au was deposited, however, the results show that the presence of TiO$_x$ species is required for the photo-deposition of Au driven by a photocatalytic reduction of auric acid. In case of Au/Zn0.3/SBA, where no TiO$_x$ species are present in the material, clearly less Au can be detected by ICP-OES. The deposition of Au in this case may be related to a photo-bleaching process of auric acid solution as observed for the bare SBA-15 material rather than to the photocatalytic reduction, and indeed the measured values of Au are quite similar for Au/SBA-15 and Au/Zn0.3/SBA materials. Additionally, ICP-OES results confirmed that leaching of Ti or Zn species during the photo-deposition process can be neglected (results not shown).
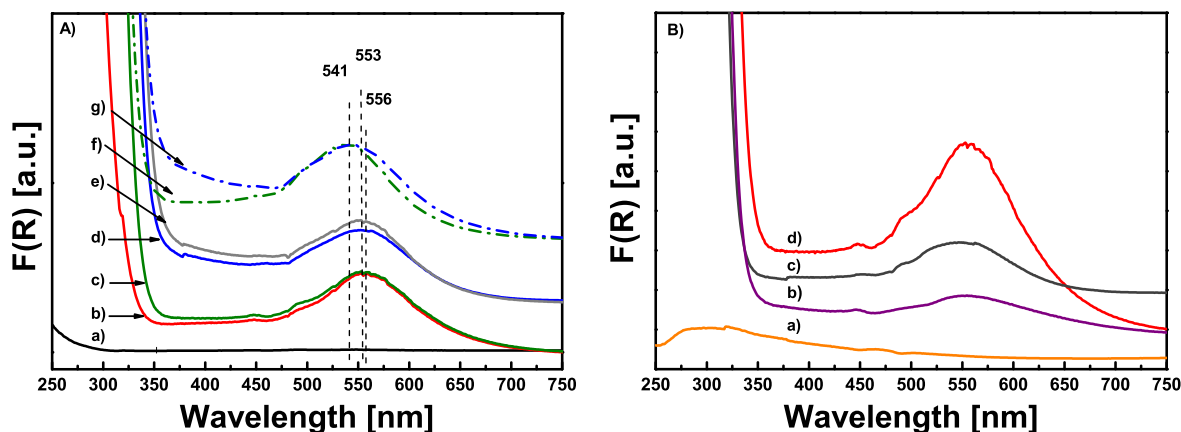
Figure 5.15: A) Diffuse reflectance UV-Vis spectra of Au-modified materials with varying Ti loading a) Au/SBA-15, b) Au/Ti0.3/SBA, c) Au/Ti1.0/SBA, d) Au/Ti2.0/SBA, e) Au/Ti2.7/SBA, f) Au/Ti1.0/SBA (0.55 wt% Au), g) Au/Ti2.0/SBA (0.55 wt% Au). B) Diffuse reflectance UV-Vis spectra of the Au-modified materials containing ZnO$_x$ in the SBA-15 matrix a) Au/Zn0.3/SBA, b) Au/Zn0.3/Ti1.2/SBA, c) Au/Ti1.2/Zn0.3/SBA, and d) Au/Ti1.0/SBA.

The structure and position of the Au plasmon peaks were analyzed by UV-Vis spectroscopy. The results obtained for the Au/Ti(x)/SBA samples are shown in Fig. 5.15a. Except for Au/SBA-15, all materials showed a characteristic Au plasmon absorption at ~ 550 nm. There are obvious differences in the position of the plasmon absorption depending on the Au and the Ti loading. A plasmon centered at a wavelength higher than 550 nm is observed after photo-deposition of 0.25 wt% Au. The plasmon bands of the stepwise prepared 0.55 wt% Au samples are clearly shifted to shorter wavelength. Additionally, the Au plasmon is shifted to slightly lower wavelength with higher Ti loading. This phenomenon can be related to the Au particle size, the reflective index of the supporting materials, or to different TiO$_x$ structures. [135,136] For the subsequently grafted samples Au/Zn0.3/Ti1.2/SBA and Au/Ti1.2/Zn0.3/SBA the plasmon peak is also centered at ~ 550 nm (Fig. 5.15b). However, there are certain differences in the nature of photo-deposited Au nanoparticles of the Zn-containing samples compared with the Au/Ti(x)/SBA materials. Thus, it can be assumed that the differences clearly depend on the presence of ZnO$_x$-species incorporated in the SBA-15 matrix. A more intense Au plasmon was observed in case of Au/Ti1.2/Zn0.3/SBA compared to the Au plasmon of Au/Zn0.3/Ti1.2/SBA. The overall intensities of these plasmon peaks are lower for the Au/Zn0.3/Ti1.2/SBA and Au/Ti1.2/Zn0.3/SBA materials compared to the Au/Ti(x)/SBA samples, which is in good agreement with the ICP-OES results indicating that less Au was photo-deposited on the Zn-containing samples. However, the Au/Ti1.2/Zn0.3/SBA sample with a lower loading of Au as measured by ICP-OES exhibits the higher plasmon peak, possibly due to different scattering properties of the sample. For the Au/Zn0.3/Ti1.2/SBA and the Au/Ti1.2/Zn0.3/SBA samples it can be assumed that metallic Au is present, as the plasmon of Au in the metallic state is
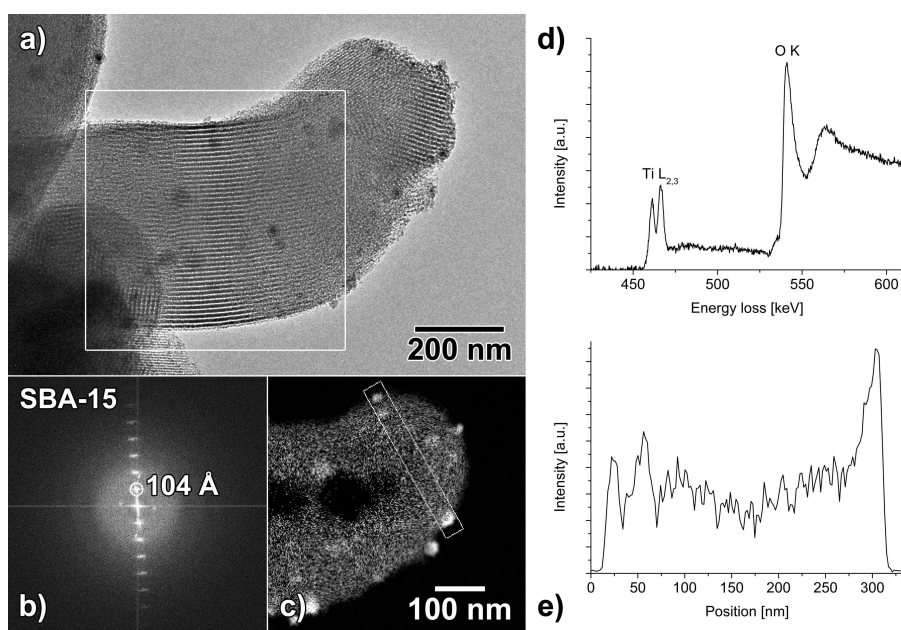
Figure 5.16: a) Typical BF-TEM of Au/Ti1.0/SBA. NPs are imaged as dark contrast, and are poly-disperse. The SBA-15 channels are visibly intact. b) A FFT analysis of the white frame in a) shows the pore spacing to be 104 Å. c) EFTEM Ti map of the tip of the crystal visible in a). Some of the particles visible in a) give rise to strong Ti signals. The dark area in the middle of the crystal is due to thickness effects. d) EELS spectrum of Au/Ti1.0/SBA showing the Ti-L$_{2,3}$ and the O-K edge. e) Intensity profile following the stripe in c) from top left to down right. Besides the particle, a clear Ti background is present throughout the material.

accepted to be in the range of 500 - 600 nm.[135,136] No Au plasmon peak was observed for the Au/Zn0.3/SBA sample most likely due to the low Au loading.

In-depth high-resolution TEM analysis was performed for the three samples with similar TiO$_x$ loading, namely Au/Ti1.0/SBA, Au/Zn0.3/Ti1.2/SBA, and Au/Ti1.2/Zn0.3/SBA samples. BF-TEM images of Au/Ti1.0/SBA showed the presence of intact channels as sxpected for SBA-15 mesoporous materials (Fig. 5.16a). The channels are highly ordered and exhibit a channel spacing of 104 Å, determined by FFT analysis (Fig. 5.16b) of the area in the white frame in Fig. 5.16a. The channel spacing does, however, slightly change from crystal to crystal. The average distance found in both characterized samples is approximately 100 Å. The nanoparticles that are visible in the material shown in Fig. 5.16a are quite polydisperse with diameters ranging from 10 to 90 nm.

The presence of Ti and O in the Au/Ti1.0/SBA material were proven by EELS. The EELS spectrum acquired from the material (Fig. 5.16d) shows the presence of both the Ti-L$_{2,3}$ and the O-K edges. The Ti-L$_{2,3}$ signal was used to acquire an Ti elemental map using EFTEM (Fig. 5.16c). This elemental map shows a homogeneous Ti distribution in the tip of the SBA-15 crystal as shown in Fig. 5.16c. The dark contrast at the center of the Au/Ti1.0/SBA crystal
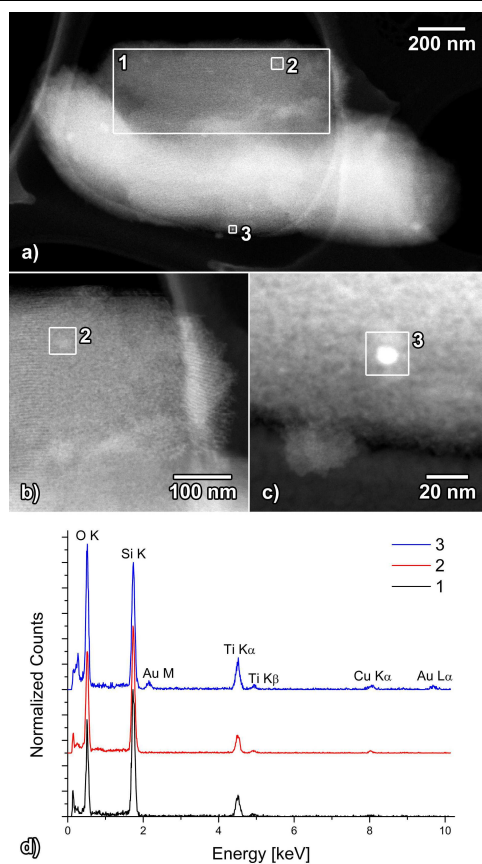
Figure 5.17: a) HAADF-STEM images of Au/Ti1.0/SBA. Numbered white frames label the areas where STEM-EDX spectra were recorded. b) and c) show magnified HAADF-STEM images of the areas where spectrum 2 and 3 were recorded. d) EDX spectra of the material in the areas 1 (black), 2 (red) and 3 (blue), only 3 shows an Au signal.

is an imaging artifact (thickness effect). Fig. 5.16e shows the intensity profile over the line indicated in the Ti map in Fig. 5.16c, from top left to bottom right. Some of the particles visible in BF-TEM in Fig. 5.16a give rise to strong signals in the Ti map (Fig. 5.16c) and resulted in peaks in the Ti intensity profile (Fig. 5.16e). Thus, these particles are then clearly enriched in Ti. STEM-EDX (Fig. 5.17) and HR HAADF-STEM (Fig. 5.18) was used to further explore the nature of these particles.

Most of the particles of Au/Ti1.0/SBA, which are visible in BF-TEM (Fig. 5.16c) and HAADF-STEM proved to be Ti-rich. STEM-EDX spectra, however, reveal that there are two types of nanoparticles in this material; most particles exhibit only a small contrast difference with respect to the framework material in the mass-thickness sensitive HAADF-STEM images (Fig. 5.17a and 5.17b area 2) are Ti-rich nanoparticles as proven by STEM-EDX spectra (Fig. 5.17d spectra 1 and 2). Au nanoparticles detected based on the stronger image contrast with respect to the framework material and the according STEM-EDX spectrum (Fig. 5.17d spectrum 3) are also present. Often these Au nanoparticles are embedded in shells that exhibit a very similar composition as the framework material.
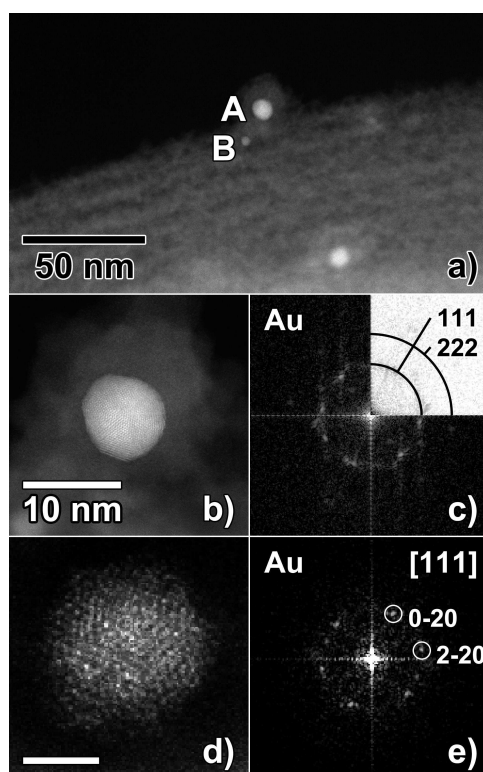
Figure 5.18: a) HAADF-STEM image of Au/Ti1.0/SBA showing the presence of several Au nanoparticles (bright white contrast). b) High-resolution HAADF-STEM image of a single Au nanoparticle A, covered by a low-contrast, amorphous shell. c) The FFT analysis of (b) confirms the particle is crystalline Au. d) Au nanoparticle B imaged along the [111] zone axis orientation, as evidenced by FFT analysis shown in e) (scale bar 2 nm).

The Au particles of Au/Ti1.0/SBA were further investigated by a FFT analysis of HAADF-STEM images in atomic resolution. Particle A in Fig. 5.18a exhibits the presence of multiple twinning defects, typical for small Au nanoparticles. The FFT (Fig. 5.18c) of the HAADF-STEM image depicting it in atomic resolution shows only reflections fitting to the FCC Au crystal structure. Fig. 5.18b shows a typical low-contrast amorphous shell surrounding the gold nanoparticle. Particle B (Fig. 5.18d) is smaller than A and is a non-defected Au particle imaged along its [111] zone axis as proven by the FFT analysis (Fig. 5.18e). Even though analysis was not performed in similar detail, HRTEM images of the Au/Ti0.3/SBA and Au/Ti2.0/SBA revealed that polydisperse nanoparticles are formed, as was observed for Au/Ti1.0/SBA and have been proven to be Ti-rich in nature. Furthermore, it can be assumed that the Au particles detected for the Au/Ti0.3/SBA and Au/Ti2.0/SBA are embedded in similar shells (Fig. 5.18b). It is likely that the formation of these core-shell structures and the Ti-enrichment in the Au/Ti1.0/SBA sample observed at several positions occurs during photo-deposition of Au, because the presence of Ti-rich areas was excluded by HRTEM measurements for a Ti1.0/SBA support sample.

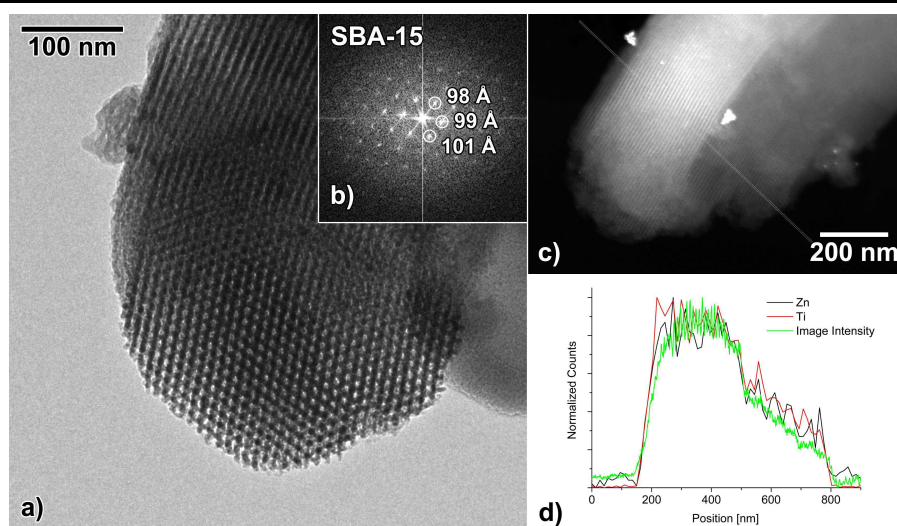Similarly to the intact channel structure of the Au/Ti1.0/SBA sample the HRTEM image

Figure 5.19: a) HRTEM image of a typical Au/Zn0.3/Ti1.2/SBA crystal. The channels are visibly intact. The FFT of a) (displayed in b)) reveals an average distance of approximately 100 Å. c) HAADF-STEM image of a typical Au/Zn0.3/Ti1.2/SBA crystal. d) HAADF-STEM image signal intensity and Ti-K/Zn-L EDX intensity profiles over the grey line in a) from the top left to the bottom right (Zn-L, black; Ti-K, red; image intensity, green).

(Fig. 5.19a) of the Au/Zn0.3/Ti1.2/SBA material shows intact channels with an average distance of $\sim$ 100 Å (Fig. 5.19b). From BF imaging the presence of nanoparticles as observed for Au/Ti1.0/SBA was excluded and Au particles incorporated by photo-deposition into the Au/Zn0.3/Ti1.2/SBA sample were hardly visible. Only vague shadows were imaged (Fig. 5.19a). Again, the HAADF-STEM mode was used to further characterize the Au/Zn0.3/Ti1.2/SBA material. Using HAADF-STEM it was again verified that the channel structure of SBA-15 support material is intact and the Au particles incorporated in the material due to the photo-deposition procedure became visible (Fig. 5.19c). Most likely the large particles that can be seen at the outer surface are agglomerates of Au particles. These are found very rarely and most of the Au particles within these agglomerates as well as in the channels of the Au/Zn0.3/Ti1.2/SBA sample are monodisperse, with an average size of 8 ± 2 nm (see size distribution in Fig. A11). A 2D line scan was performed in STEM-EDX to measure the Ti and Zn distribution. Both elements are evenly distributed as it can be seen in the according element profiles in Fig. 5.19d. The presence of Ti, Zn, and Au in Au/Zn0.3/Ti1.2/SBA was proven by EDX (Fig. A12) and the Ti distribution was shown to be homogeneous without Ti-rich areas (Fig. A13).

The position of the Au nanoparticles within the Au/Zn0.3/Ti1.2/SBA material was investigated by electron tomography. Using the electron tomography technique, a three-dimensional reconstruction of the investigated material was retrieved. Fig. 5.20 shows a slice through the three-dimensionally reconstructed volume of the investigated Au/Zn0.3/Ti1.2/SBA material. The intact SBA-15 channels are resolved in the reconstruction, and the Au particles are visibly

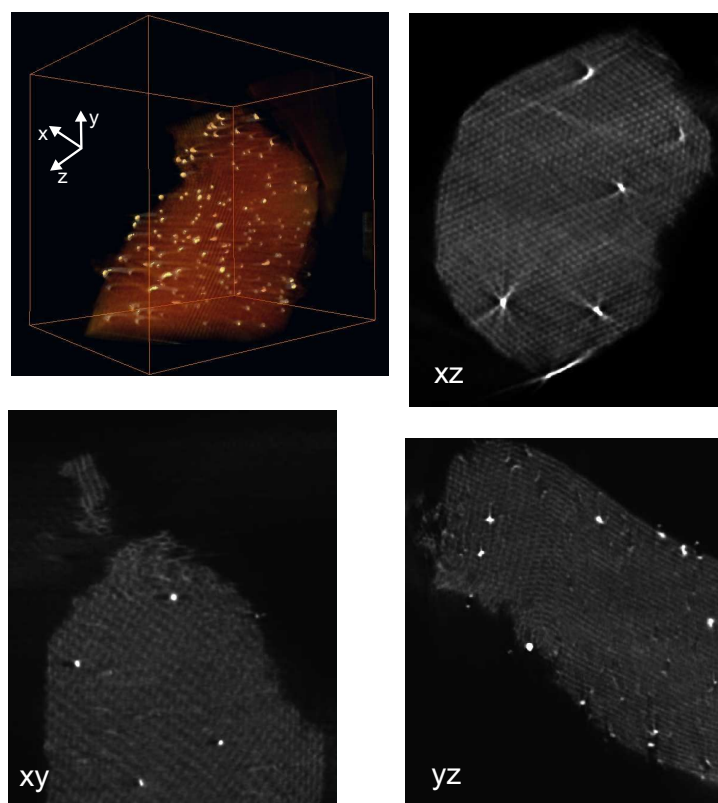**Figure 5.20:** Tomographic reconstruction of a typical Au/Zn0.3/Ti1.2/SBA crystal, reconstruction
size = 622x738x817 nm (boundaries indicated by the orange box). In the 3D repre-
sentation (left top) the Au nanoparticles are displayed in yellow, the SBA framework
in soft-red. The arrangement of the channels is clearly visible as well as the Au parti-
cles. The orthoslices through the reconstruction show that the SBA framework pores
are resolved. The Au nanoparticles are found within the SBA-15 crystal as well as at
the surface.

distributed throughout the whole SBA-15 crystal, and at the surface of the Au/Zn0.3/Ti1.2/SBA
material. The artifacts in the reconstruction are a result of the missing wedge and the tendency
of the material to charge under the beam which can result in movement of the SBA-15 crys-
tal. Using HRTEM measurements it was unambiguously shown that larger Au particles and
Ti-rich areas, observed for the Au/Ti1.0/SBA, were not existing in the Au/Zn0.3/Ti1.2/SBA
sample. The HRTEM measurements are supported by UV-Vis measurements, which reveal
that the intensity of the characteristic Au plasmon of the Au/Zn0.3/Ti1.2/SBA sample is less
intense. It can be assumed that monodisperse homogeneously distributed Au particles within
a mesoporous matrix certainly will possess a less intense Au plasmon compared with larger
particles mainly situated at the outer surface of a material. Taking this into account small Au
particles mainly in the pores of the material are expected for the Au/Ti1.2/Zn0.3/SBA sample
and indeed HRTEM images confirmed the presence of small Au particles (Fig. A14). However,
a slight enrichment of Ti in certain areas, possibly associated with larger Au particles was ob-
served in the Ti EFTEM images for the Au/Ti1.2/Zn0.3/SBA. The photocatalytic activity of the

three different materials clearly decreases in the order Au/Ti1.0/SBA > Au/Zn0.3/Ti1.2/SBA > Au/Ti1.2/Zn0.3/SBA as Au/Ti1.0/SBA was active for the evolution of H$_2$ and the hydroxylation of TA. Regarding the presented HRTEM characterization results these differences in photocatalytic activity can be explained by the enrichment in TiO$_x$ and the differences in the particle sizes of the incorporated Au nanoparticles.

The above presented results provide evidence that highly active isolated or slightly polymerized TiO$_x$ were obtained by the anhydrous grafting of Ti(O^{i}Pr)$_4$ on SBA-15 support. The isolated species appear to be mobile, at least during photo-deposition of nanoparticular Au, and tend to agglomerate during the irradiation process. Due to the high photocatalytic activity of the initially isolated and presumably then agglomerated TiO$_x$ species photo-deposition of Au nanoparticles is mainly taking place at the outer surface: larger Au particles are photo-deposited and the probability of Au precursor diffusion into the channels of the Au/Ti(x)/SBA samples is low. The agglomeration and photo-deposition of larger Au particles was observed for all Au/Ti(x)/SBA samples and a relation between the hydrogen evolution activity and these in-situ generated Au/TiO$_x$ assemblies is likely. Even though it was not possible to be definitively confirmed by means of HRTEM, the observed trends of photocatalytic hydrogen evolution due to methanol steam reforming for the Au/Ti(x)/SBA samples might be explained as follows: Less hydrogen was evolved during Au photo-deposition in presence of Ti0.3/SBA compared to Ti1.0/SBA due to the lower TiO$_x$ loading. With increasing TiO$_x$ loading as in Ti2.0/SBA or in Ti2.7/SBA again less hydrogen was evolved during photo-deposition. These samples exhibited less isolated TiO$_x$ species. Instead, TiO$_x$ species are present as oligomers and even polymerized TiO$_x$ at the surface of the SBA-15 was confirmed.[134] Presumably, these interconnected TiO$_x$ species are less mobile at the surface and only remaining isolated TiO$_x$ sites are able to move. Thus, less Au/TiO$_x$ assemblies can be formed in the photo-deposition resulting in less active sites and lower hydrogen evolution. It is also possible to assume that Ti-O-Si bonds still need to be present in the agglomerates formed around the gold nanoparticles as the composition of the shell was confirmed to be similar to the framework of the material.

In case of the Au/Zn0.3/Ti1.2/SBA and the Au/Ti1.2/Zn0.3/SBA samples monodisperse, evenly distributed particles are photo-deposited in the channels and at the outer surface of the material. Furthermore, less Au is deposited on both samples compared to Au/Ti(x)/SBA materials as evidenced by ICP-OES measurements. The mobility of the TiO$_x$ species after subsequent deposition of ZnO$_x$ appears to be lower or is even inhibited in analogy to the higher loaded Ti2.0/SBA and Ti2.7/SBA samples, and thus the agglomeration of TiO$_x$ is avoided. The TiO$_x$ species remain mainly isolated and the photo-deposition of Au is slow for the Zn0.3/Ti1.2/SBA sample resulting in a lower Au loading after 90 min of irradiation and the hydrogen evolution due to photoreforming of methanol, if occurring at all, is below the detection limit.

The Au/Zn0.3/Ti1.2/SBA and the Au/Ti1.0/SAB samples exhibit similar photocatalytic activities towards TA hydroxylation. Two different sites seem to be responsible for the hydrogen evolution reaction and the TA hydroxylation, e.g. Au/TiO$_x$ assemblies arranged in a core-shell like

structure as observed for Au/Ti(x)/SBA samples may be responsible for the hydrogen evolution and Au in close contact to isolated TiO$_x$ species facilitates the hydroxylation of TA. Although the Au distribution of the Au/Ti1.2/Zn0.3/SBA sample is similar to the Au/Zn0.3/Ti1.2/SBA sample it is less active in the TA test reaction, and therefore the lower activity is exclusively assigned to the formation of Ti-O-Zn bonds instead of Ti-O-Si bonds as already explained.

Finally, it should be mentioned that the observed behavior of Ti(x)/SBA-15 materials during Au photo-deposition resembles the SMSI effect observed for metal/TiO$_2$ materials. It is believed that reduction of TiO$_2$ gives rise to TiO$_x$ suboxide species (x < 2), which is believed to migrate onto metal particles. The state of titania present in the Ti(x)/SBA-15 materials can be considered as a TiO$_x$ species, which can migrate onto the metal particles. Furthermore, the desired reduction of titania can be achieved by the UV-light excitation of the isolated Ti-sites. The SMSI effect is in good agreement with the considerations of an enhanced mobility of the titania in species Ti(x)/SBA-15.

5.3.3 Conclusions and Outlook

The presented results show that Au/Ti(x)/SBA-15 samples are photocatalytically active in the hydrogen production by the photoreforming reaction of methanol and in the hydroxylation of terephthalic acid. Therefore, the availability of electrons and holes upon photo-excitation was proven. Furthermore, a correlation of titania loading and photocatalytic activity was observed: the highest activity was observed for materials with the majority of isolated titania sites. In contrast to the behavior observed for Au/Ti(x)/SBA-15, the photocatalytic activity is drastically changed upon incorporation of zinc oxide species as in Au/Zn0.3/Ti1.2/SBA and Au/Ti1.2/Zn0.3/SBA. A photocatalytic activity resembling the activity of the most active Au/Ti(x)/SBA-15 was only observed for the Au/Zn0.3/Ti1.2/SBA sample. The differences in activity were attributed to titania species in a Zn-O-Ti environment, which appeared to be unfavorable for the photocatalytic activity. Moreover, HRTEM studies indicated a diffusion-controlled photo-deposition of Au for Ti(x)/SBA-15, and larger Au particles at the outer surface of the Au/Ti(x)/SBA-15 were detected. These particles were mostly associated with a shell of similar composition as the framework material, and it seems that Au-Ti agglomerates are formed. These agglomerates were completely absent in Au/Zn0.3/Ti1.2/SBA and Au/Ti1.2/Zn0.3/SBA, and only small Au particles in the pores of the SBA-15 were observed. The presence of ZnO$_x$ seems to decrease the mobility of titania species required to form the Au-Ti agglomerates.

6 Heterogeneous Photoelectrochemistry and Photocatalysis of TiO$_2$ Nanomaterials

In this chapter Nb-doped TiO$_2$ bulk materials are discussed. In the first section a novel synthesis procedure is described. In-depth characterization of the synthesized materials is used to proof the suitability of the procedure. The improvement in photo-to-current in hybrid photoelectrodes prepared with the Nb-doped TiO$_2$ samples as electron collector material are reported in the second chapter and a strategy to improve non-metal doping is discussed in the third section of this chapter.

6.1 The synthesis of Nb-doped TiO$_2$ nanoparticles by spray drying

Abstract[1]

Nb-doped TiO$_2$ nanoparticles were prepared by a continuous spray drying process using ammonium niobate (V) oxalate and titaniumoxysulfate as water-soluble precursors. The structural and electronic properties were investigated using thermogravimetric analysis, X-ray diffraction, X-ray photoelectron spectroscopy, and Raman spectroscopy. Nb was found to be mainly incorporated as Nb^{5+} into the TiO$_2$ lattice resulting in a charge compensation by Ti vacancies. The characterization results indicate that Nb was homogeneously distributed within the titania lattice, and that the surface segregation of Nb, which is commonly observed for Nb-doped TiO$_2$, was significantly less pronounced. The high homogeneity and the lower extent of surface segregation originate from the efficient atomization of homogeneous precursor solutions and the fast evaporation of the solvent in the spray drying process. As a result, the ion mobility is diminished and spheres of well-mixed precursor materials are formed. Using the continuous spray drying process followed by a controlled heat treatment, the phase composition, the crystal size, and the surface area of the Nb-doped TiO$_2$ nanoparticles are easily adjustable.
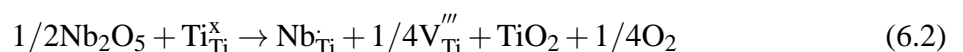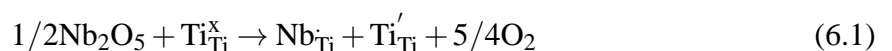

6.1.1 Short Introduction

Transition metal oxides such as titanium dioxide (TiO$_2$) have been extensively studied in the last decades for various applications. TiO$_2$-based materials of different particle size and morphology are used in scientifically and technologically interesting areas such as the photocatalytic splitting of water,[153] environmental cleanup,[154] gas sensing,[155,156] and in fuel cells.[157] Furthermore, TiO$_2$ is applied as support material in heterogeneous catalysis due to strong metal-support interactions, high stability in oxidizing environments, low cost, and commercial availability.[18] Due to the wide band gaps of the commonly used TiO$_2$ modifications anatase (3.2 eV) and rutile (3.0 eV), it is often necessary to modify their band structure.[18,158,159] For photocatalytic applications the modification of the band structure is intended to lead to visible light absorption, whereas in electrochemical applications the conductivity of TiO$_2$ needs to be enhanced by tuning its band gap.

The applicability of wide band gap oxides can be improved by different methods including doping with anions or cations.[160,161] Typically, anions such as N, C, F, or S can be used to substitute lattice oxygen anions, whereas transition metal cations substitute Ti cations.[19,162–164] Depending on the application it is crucial to consider the splitting of the d orbitals of transition metals and the effect of their different electron configurations. In addition, the formation of solid solutions of two or more oxides is commonly used to change the band structures of wide band gap oxides.

In recent years Nb was employed to dope TiO$_2$ particles or films for different applications.[156,157,165,166] These investigations showed that the doped materials can be applied as conductive support for cathode catalysts in polymer electrolyte membrane fuel cells (PEM-FCs),[157,167] as counter electrode in dye-sensitized solar cells (DSSCs),[168–170] and as transparent conductive oxides (TCOs).[171]

The incorporation of Nb into the titania lattice leads to changes in the electronic structure, which are extensively discussed in literature. The charge compensation of Nb^{5+} substituting Ti^{4+} depends on the oxygen partial pressure, the temperature applied during the synthesis, and the Nb concentration. It can be achieved by two mechanisms: one possibility is the reduction of one Ti^{4+} to Ti^{3+} for every Nb^{5+} incorporated (eq. 6.1), the other possibility is the formation of one Ti vacancy per four Nb^{5+} introduced (eq. 6.2).

$$1/2Nb_2O_5 + Ti^x_{Ti} \rightarrow Nb^{\cdot}_{Ti} + Ti^{'}_{Ti} + 5/4O_2 \tag{6.1}$$

$$1/2Nb_2O_5 + Ti^x_{Ti} \rightarrow Nb^{\cdot}_{Ti} + 1/4V^{'''}_{Ti} + TiO_2 + 1/4O_2 \tag{6.2}$$

Reaction (6.1) mainly occurs at low oxygen partial pressures and in the synthesis of samples with high Nb content. In this case one excess electron occupies the Ti 3d orbital leading to an increase of the electron density. Using high oxygen partial pressures favors the formation of titanium vacancies (eq. 6.2). In addition, the substitution of Ti^{4+} by Nb^{4+} can be obtained

by a high temperature treatment in reducing atmosphere. The preparation of doped powder materials can be achieved by different methods, such as hydrothermal synthesis,[157,169] pyrolysis,[172][173] high temperature ceramic routes,[174–176] and sol-gel methods.[162,177–179] These methods usually involve complicated processes, and the resulting properties of the product strongly depend on the various process parameters. Furthermore, the scale-up of these methods is rather difficult. For instance, Kubacka et al.[162,163] prepared doped TiO$_2$ materials by a microemulsion method. This sophisticated preparation comprises stirring for 24 h followed by several additional steps, such as centrifugation, drying, and washing, which is rather time-consuming. The synthesis of Nb-doped TiO$_2$ by a hydrothermal method described by Park and Seol[157] is another example for a rather time-consuming process. Furthermore, both preparation techniques require very hydrophilic materials, which have to be handled skillfully. The high-temperature ceramic route used for the synthesis of doped TiO$_2$ is an energy-intensive process. For example, Morris et al.[174] used ceramics for valence band studies, where the starting materials were treated at temperatures as high as 1000 °C for several days.

Recently, spray drying has been successfully employed as a fast and scalable method for the preparation of oxide materials. Kaluza et al.[180–182] used a coupled precipitation-spray drying approach to prepare high surface area ZnO nanoparticles and ZnO-Al$_2$O$_3$ nanocomposites as supports for copper catalysts applied in methanol synthesis. By using this spray drying technique, it was possible to investigate the aging process of the polycrystalline precipitates as well as the role of the post-treatment during the catalyst preparation. Hence, important preparation parameters can be easily controlled using this approach, whereas in conventional batch processes the investigation of the aging of the precipitate appeared to be rather difficult. Spray drying has also been used for the synthesis of TiO$_2$ materials. Sizgek et al.[183] prepared titanates by a coupled sol-gel and spray drying approach resulting in well-defined microspheres. This method revealed that the particle porosity and morphology strongly depend on the dispersion of the used sol. Porous TiO$_2$ nanowires and macroporous particles for photocatalytic applications were prepared by Zhang et al.[184] and Iskandar et al.[185] Zhang et al.[184] used suspensions of powdered nanowires and a surfactant to synthesize hierarchically porous TiO$_2$ microspheres consisting of nanowires, whereas Iskandar et al.[185] focused on the preparation of macroporous brookite nanoparticles using suspensions of brookite nanoparticles together with a template for spray drying. The obtained macroporous particles showed higher photocatalytic activity in waste water treatment compared to dense particles due to higher surface area.[185] Thus, applying the spray drying approach combines several major advantages, such as homogeneous particle size distribution, fast drying under mild conditions, and good parameter control. However, finding a soluble TiO$_2$ precursor suitable for spray drying is challenging, and, to the best of our knowledge, the synthesis of cation-doped TiO$_2$ by spray drying has not yet been reported.

In this contribution, we present a continuous method for the synthesis of Nb-doped TiO$_2$ nanoparticles by spray drying. A peristaltic pump transports an acidic solution containing Nb

and Ti ions into the two-fluid nozzle of the spray dryer. After rapid evaporation of the liquid and separation of the gas, the solid can be collected as colorless powder. The segregation of the ions and particle aggregation are avoided due to the rapid drying process. Thus, the Nb and Ti cations are well mixed within the powder. The spray drying process leads to a narrow particle size distribution, because the ion content of the feed solution is homogeneously dispersed and the atomization by the nozzle is well defined. Furthermore, the scale-up of this synthesis route to an industrial level is easily feasible.

Experimental

Sample Preparation

Titaniumoxysulfate sulfuric acid hydrate (TiOSO$_4$ x H$_2$SO$_4$ x H$_2$O, synthesis grade) and ammonium niobate (V) oxalate hydrate ((NH$_4$)NbO(C$_2$O$_4$)$_2$ x H$_2$O, 99.9 %, denoted as ANO) were supplied by Aldrich and used as received. The Ti complex was dissolved in nitric acid solution (c = 1 mol L^{-1}) by stirring for at least 4 h. Subsequently, a predetermined amount of the ANO complex was added to the colorless solution to achieve Nb concentrations between 0.2 - 50 at % relative to Ti. The obtained solution was stirred for 1 h and used for the synthesis of Nb-doped TiO$_2$ precursor materials through a continuous spray drying method. A bench-top spray dryer (B-290, Büchi) with a two-fluid nozzle was used for fast evaporation of the fluid.[180–182] The colorless powder samples were collected from the dryer and calcined under flowing synthetic air (20.5 % O$_2$ in He, 100 sccm) at 600 °C, 700 °C or 800 °C for 1 h. A heating rate of 1 K min^{-1} was applied leaving sufficient time for flushing out volatile species evolving during the decomposition of the precursors. After calcination the samples were thoroughly washed with distilled water and dried in static air for 24 h at 110 °C. The prepared samples are labeled based on the composition and the calcination temperature. For instance, Ti$_{0.998}$Nb$_{0.002}$-700 indicates a theoretical composition of 99.8 at% Ti ions and 0.2 at% Nb ions and a calcination temperature of 700 °C. For comparison, monometallic Ti or Nb oxides were prepared using single Ti or Nb sources, where ANO was also dissolved in acidic solution.

Characterization Methods

The materials were investigated by means of thermogravimetry coupled with mass spectrometry (TG-MS), X-ray diffraction (XRD), Raman spectroscopy, UV-Vis spectroscopy, nitrogen physisorption, and X-ray photoelectron spectroscopy (XPS). TG-MS analysis was carried out in a Cahn TG2131 thermobalance coupled with a quadrupole mass spectrometer (Balzer, Omnistar). Samples were heated to 800 °C with a heating rate of 2 K min^{-1} in synthetic air with at total flow rate of 30 sccm. XRD studies were performed with a PANalytical MPD diffractometer with Cu Kα radiation in a 2θ range from 10 to 70°. Powder Diffraction Files (PDF2) from the International Centre of Diffraction Data (ICDD) combined with the XPert Line software (Panalytical, Almelo) were used for qualitative phase analysis. Raman measurements were performed with a Nexus FT-NIR spectrometer equipped with a nitrogen-cooled germanium detector and a 1064 nm laser (Nd:YAG) provided by Thermo Fisher Scientific. UV-Vis

spectra were recorded in the diffuse reflectance mode in a Perkin Elmer Lambda 650 UV-Vis spectrometer equipped with a Praying-Mantis mirror construction. The obtained spectra were converted by the Kubelka-Munk function F(R) into absorption spectra using $BaSO_4$ as white standard. Static nitrogen physisorption experiments were performed at the boiling point of liquid N_2 subsequent to out-gassing at 150 °C in a Quantachrome Autosorb-1-MP setup. Data were analyzed according to the BET equation assuming that the area covered by one nitrogen molecule is 0.162 nm^2. The mean diameter d(BET) was calculated based on the assumption of non-porous spherical particles. The density of anatase ($\rho_{anatase}$ = 3.85 x 10^3 kg m^{-3})[186] was used in all cases. It has to be noted that this is only a rough approximation for materials with imperfect structures. The pore size distribution was obtained applying the BJH equation. XPS measurements were carried out in an UHV set-up equipped with a Gammadata-Scienta SES 2002 analyzer. The base pressure in the measurement chamber was 5 x 10^{-10} mbar. Monochromatic Al Kα (1486.6 eV; 13.5 kV; 37 mA) was used as incident radiation and a pass energy of 200 eV was chosen resulting in an energy resolution better than 0.6 eV. Charging effects were compensated using a flood gun, and binding energies were calibrated based on positioning the main C 1s peak at 284.5 eV, which originates from carbon contaminations.

6.1.2 Results and Discussion

Common Ti compounds such as $TiCl_4$ are typically air- and water-sensitive rendering them unsuitable as Ti source for spray drying. Titaniumoxysulfate dissolves slowly in HNO_3 under stirring and is stable in acidic solutions. As the spray dryer was equipped with glass reactors and Teflon tubing, it was possible to use the Ti- and Nb- containing acidic solution directly for the spray drying synthesis resulting in colorless powders collected in the product vessel.

TG-MS applied to the precursor materials

The decomposition of the powders obtained from spray drying, i.e. the precursor for mixed TiNb oxides, was first studied by TG-MS in flowing air. The TG-MS results of pure Ti$_1$, pure Nb$_1$, and Ti$_{0.5}$Nb$_{0.5}$ mixed precursors are shown in Fig. 6.1 It can be seen that the weight loss of the pure Ti precursor occurred in two steps: at around 78 °C accompanied by the release of H_2O (m/e = 18), and at about 580 °C accompanied by the release of a small amount of CO_2 (m/e = 44) (Fig. 6.1a). Surprisingly, SO_2 (m/e = 64) and SO_3 (m/e = 80) were not detected by MS in the whole temperature range. Obviously, the Ti precursor decomposed completely to TiO_2 at about 600 °C. Further heating to 800 °C caused a negligible weight loss. The transformation temperature to TiO_2 of 540 - 580 °C is in good agreement with the results reported by Johnson et al.[187] They observed that the weight loss in the temperature region below 540 °C is only related to the release of water. According to the obtained TG data of the spray-dried $TiOSO_4$ sample, water mainly desorbs below 200 °C, and no further weight loss is detected up to 540 °C. Hence, water is bound less strongly to the spray-dried sample. The major weight loss above 540 °C can be assigned to the decomposition of the precursor and the
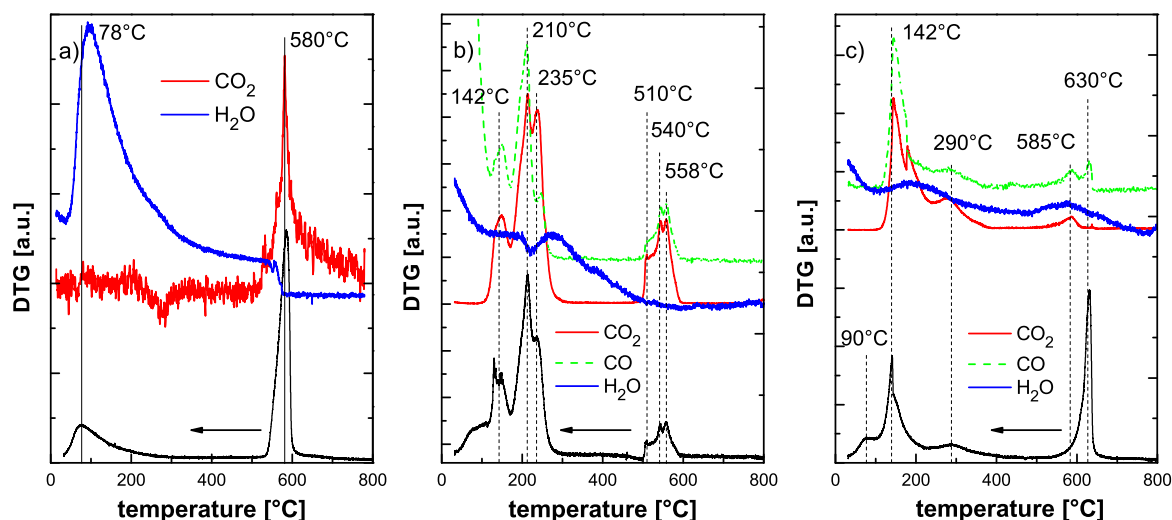
Figure 6.1: DTG curves and MS profiles of the spray-dried materials Ti_1, Nb_1, and $Nb_{0.5}Ti_{0.5}$ using a heating rate of 2 K min^{-1} a) DTG curve of the spray-dried Ti_1 precursor and the MS profile of H_2O and CO_2 during decomposition, b) DTG curve of Nb1 precursor (ANO) and the MS profiles of H_2O, CO, and CO_2, and c) DTG curve of spray-dried $Nb_{0.5}Ti_{0.5}$ precursor and the MS profile of H_2O, CO, and CO_2.

release of different sulfur species as suggested by Johnson et al.[187] Due to the lack of strong contributions from SO_2 and SO_3, the sulfur content in the precursor is presumably released as H_2SO_4 in the applied temperature region. Thus, the decomposition process can be described by the following equation:

$$TiOSO_4 \cdot H_2SO_4 \cdot xH_2O(s) \rightarrow TiO_2(s) + 2H_2SO_4(g) + (x-1)H_2O(g) \qquad (6.3)$$
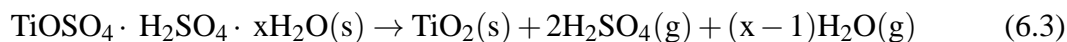
The decomposition profile of the spray-dried ANO precursor shown in Fig. 6.1b can also be divided into two main regions. The first weight loss region from 50 °C to 250 °C is associated with the release of CO (m/e = 28), CO_2 (m/e = 44), and water (m/e = 18). The second decomposition region is indicated by a sharp increase of the CO_2 signal at 510 °C. Furthermore, sharp CO and CO_2 decomposition peaks are detected at 540 and 560 °C, and no further weight loss is observed above 600 °C. The second decomposition can be assigned to the decomposition of strongly bound oxalate or, more likely, to oxalate encapsulated in Nb_2O_5, whereas a weight loss below 200 °C is mainly due to the loss of water and ammonia.[188] The loosely bound oxalate is decomposed between 250 and 350 °C.[188] In case of the spray-dried ANO sample the decomposition of the oxalate already starts at 140 °C and is terminated at 250 °C. Thus, for the spray-dried ANO precursor the conversion into Nb_2O_5 is favored. It is interesting to note that both the low and high temperature regions consist of three different CO and CO_2 peaks. Therefore, the carbon species in the spray-dried ANO powder could exist in three different environments. Hence, the overall equation of the decomposition of the spray-dried ANO
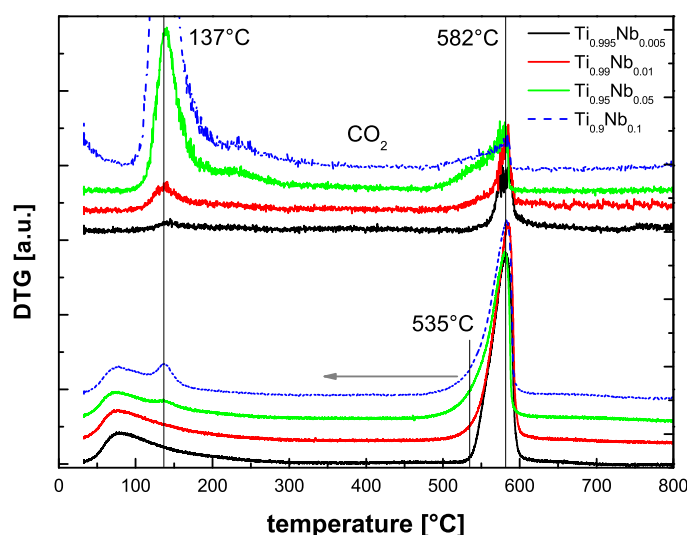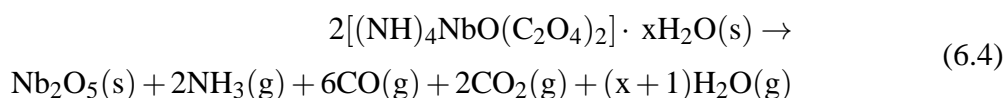
Figure 6.2: DTG curves of the spray-dried precursor powders (bottom) containing 0.5, 1, 5, and 10 at% Nb, and the corresponding CO$_2$ MS profiles (top).

precursor can be described as:

$$2[(NH)_4NbO(C_2O_4)_2] \cdot xH_2O(s) \rightarrow$$
$$Nb_2O_5(s) + 2NH_3(g) + 6CO(g) + 2CO_2(g) + (x+1)H_2O(g) \qquad (6.4)$$

In Fig. 6.1c the decomposition profile of the spray-dried Ti$_{0.5}$Nb$_{0.5}$ precursor is shown. The profile obtained with this sample is more related to the decomposition of a mixed phase rather than the decomposition of pure TiOSO$_4$ (Ti$_1$) or the pure ANO (Nb$_1$) precursor. The first strong weight loss signal is located at 140 °C. This weight loss is clearly related to the evolution of CO and CO$_2$ and can be assigned to the decomposition of the oxalate species from the ANO precursor. A second major weight loss is detected at 290 °C, which is also related to the evolution of CO and CO$_2$ and is not observed in any of the reference samples. Compared to the ANO (Nb$_1$) sample the decomposition accompanied by the release of CO$_2$ is shifted towards higher temperatures. Therefore, this weight loss can be assigned to the decomposition of a mixed phase containing Nb and Ti. The third strong weight loss occurs in the region of 540 to 640 °C with a maximum located at 630 °C. The peak obtained by DTG analysis is rather broad and the MS signals show two decomposition steps. The first step centered at 585 °C may be related to the decomposition of a pure Ti phase, whereas at higher temperatures mixed Ti-Nb phases may be fully converted into oxides. Additionally, it can be seen from Fig. 6.1 that the water signals vary for different precursors. The Ti$_1$ precursor shows mainly one peak with a maximum at around 80 °C and a change in the background of the m/e = 18 signal at 580 °C, which may be related with the release of another species. The ANO precursor exhibits two steps mainly below 500 °C and in case of 1:1 mixtures of Nb and Ti (Ti$_{0.5}$Nb$_{0.5}$) two broad water peaks of low intensity are detected at 150 and 585 °C.

The TG-MS profiles of the precursors containing a small amount of Nb ions between 0.05 -

10 at% are presented in Fig. 6.2. The profiles obtained are quite similar to the decomposition profile of the spray-dried TiOSO$_4$ precursor. With increasing Nb content two new features appear: first, a decomposition peak at low temperatures is observed, which is associated with the evolution of CO$_2$ at 137 °C. In addition, a second weight loss signal in the high temperature region at 582 °C appears, which becomes broader with increasing Nb amount. Thus, the second decomposition process already starts at lower temperature. Due to the low amount of Nb ions the conversion into TiO$_2$ is not significantly affected as indicated by the DTG curve. Even with higher Nb doping the measured TG-MS profiles are similar suggesting that even with a loading of 10 at% the Nb ions are well dispersed within the TiO$_2$ particles without the formation of NbO$_x$ islands. The formation of Nb$_2$O$_5$ or the formation of solid solutions of a NbTi$_x$O$_y$ type should result in TG profiles similar to those presented in Figs. 6.1b and 6.1c, respectively. None of the characteristic peaks in the DTG curves is observed in case of the samples with low Nb content. In comparison with the TG-MS data presented in Figs. 6.1b and 6.1c the decomposition of the loosely bound oxalate occurs at lower temperature, and the release of strongly bound carbon and sulfur species is also shifted to lower temperatures. These shifts can be rationalized by assuming that small amounts of Nb ions have a positive influence on the decomposition of sulfate, and Ti ions are positively influencing the oxidation of carbon species. It is worth mentioning that the oxidation of CO to CO$_2$ is no longer favored for the Ti$_{0.9}$Nb$_{0.1}$ sample and that the MS signal detected at mass 18 becomes broader in this case. Both observations indicate that the local environment of the Nb ions corresponds more and more to the environment of Nb ions in the Ti$_{0.5}$Nb$_{0.5}$ sample forming a solid NbTi$_x$O$_y$ solution.

Structural characterization by XRD and Raman spectroscopy

Based on the TG-MS results the precursors with different Ti to Nb ratios were calcined at 600, 700, or 800 °C. The structures of the calcined samples were characterized by XRD and Raman spectroscopy. The obtained diffraction patterns are shown in Fig. 6.3. The calcination of Ti$_1$ and Ti$_{0.95}$Nb$_{0.05}$ at 600 °C leads to the full decomposition of the precursor as shown by the TG analysis. However, conversion into the tetragonal anatase phase is not fully completed, as minor diffraction lines of the monoclinic β-TiO$_2$ phase are additionally detected (Fig. 6.3a). The β-phase is structurally related to anatase, with which it may be semicoherently intergrown,[189] and to which it irreversibly reacts upon heating.[190] In case of the Ti$_{0.95}$Nb$_{0.05}$-600 sample the diffraction peaks are broader and less intense than those of Ti$_1$-600. Thus, the incorporation of Nb is accompanied by the formation of smaller crystallites (see below). In the 700 °C calcination series, the decomposition of the precursor and the transformation to the anatase structure is complete for samples with low Nb-loading up to 1 at% (Fig. 6.3b). For Ti$_{0.95}$Nb$_{0.05}$-700 and Ti$_{0.9}$Nb$_{0.1}$-700 small diffraction peaks of β-TiO$_2$ are detected in addition to anatase, but no characteristic peaks of the rutile phase are observed in the diffraction patterns. Furthermore, the diffraction maxima of the Nb-doped anatase specimens (corrected with the NIST SRM 660a LaB$_6$ standard for instrumental aberrations in 2θ) slightly shifts to lower diffraction angles indicating the incorporation of Nb ions into Ti lattice sites.[191] The lattice expansion of
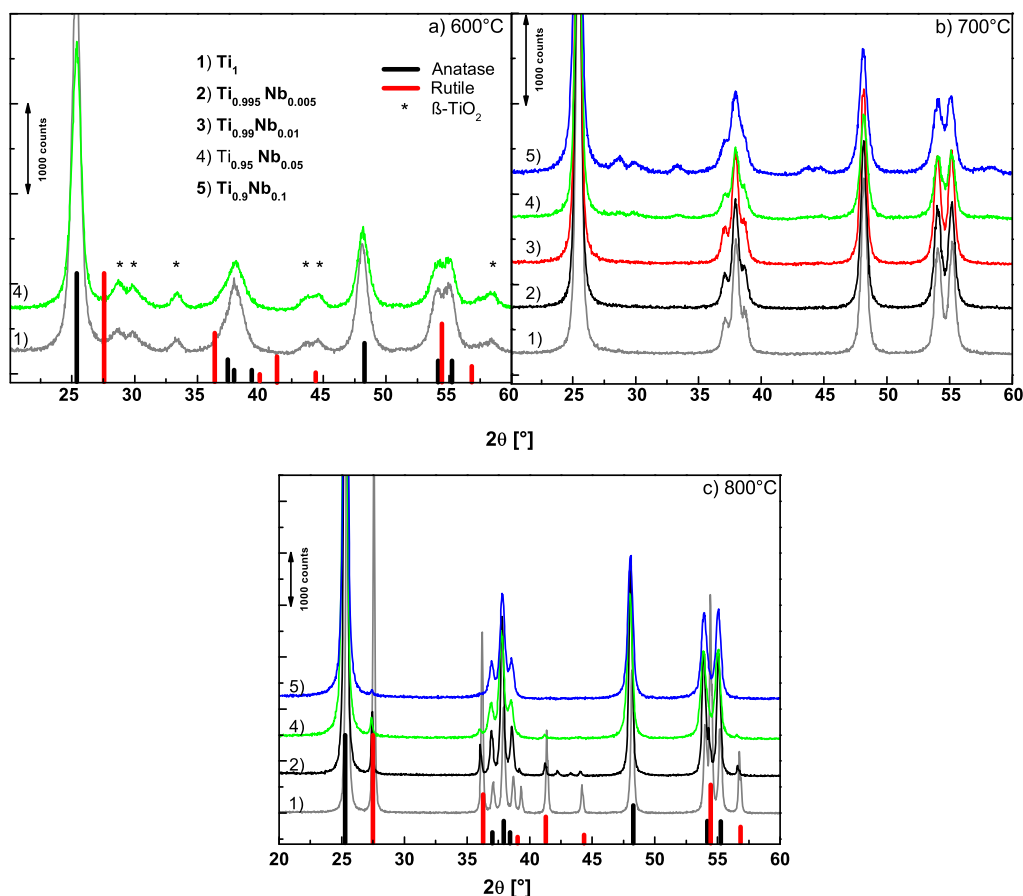
Figure 6.3: X-ray diffraction patterns of the spray-dried precursors calcined at different temperatures. Spray-dried powder without Nb and low Nb doping levels calcined at a) 600 °C, b) 700 °C, and c) 800 °C. The diffraction pattern of anatase TiO$_2$ (21-1272) and rutile TiO$_2$ (88-1175) are included for comparison.

anatase due to the incorporation of Nb is quantified with the refined lattice parameters (Table 6.1). While the lattice parameters of the Ti$_1$-700 anatase are a = 3.784(1) Å and c = 9.505(5) Å, which is in good agreement with values reported in the literature,[192] the cell parameters increase up to a = 3.791(3) Å and c = 9.510(12) Å in the Ti$_{0.9}$Nb$_{0.1}$-700 sample. This increase of the cell parameters with increasing Nb content confirms that Nb is incorporated in the anatase lattice, because the ionic radius of the Nb^{5+} ions into octahedral coordination is larger than that of Ti^{4+}.[193] In addition, the effect of Nb on the size and morphology of anatase crystallites was investigated by means of the integral breadth method.[194] The apparent size of all anatase lattice planes (hkl) (measured by pattern decomposition and corrected for instrumental line broadening) is concordant indicating the absence of crystallite shape anisotropy in all samples. Ignoring the potential minor effects of lattice imperfections (e.g. intercalation of β-TiO$_2$ lamellae with anatase) and strain on line broadening, a volume-weighted mean d(XRD) is calculated from the arithmetic mean of the apparent size values in each sample (Table 6.1). These data clearly suggest a decrease in crystallite size with increasing Nb content.
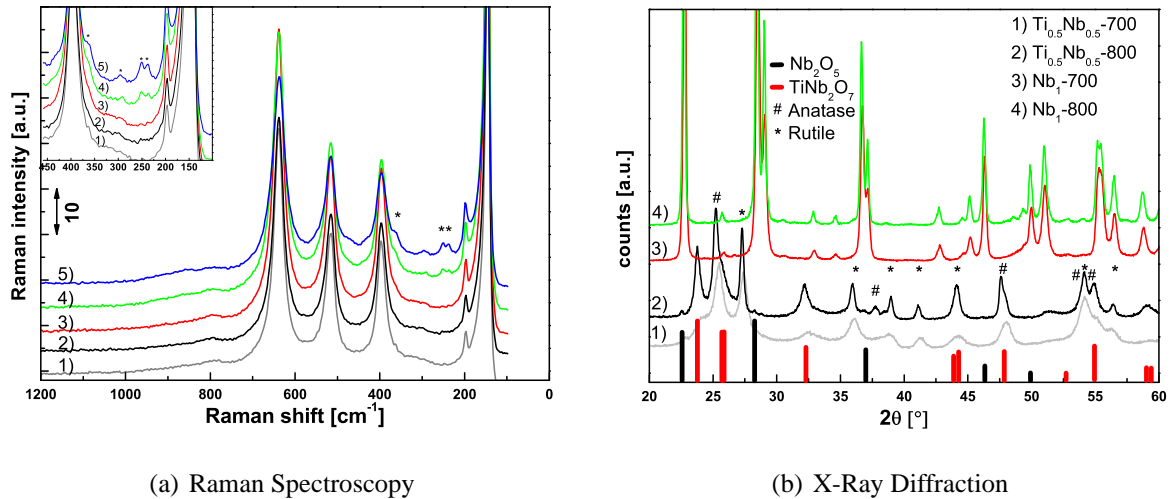
(a) Raman Spectroscopy

(b) X-Ray Diffraction

Figure 6.4: a) Raman spectra of spray-dried Nb-doped TiO$_2$ precursor powders calcined at 700 °C. 1) Ti$_1$, 2) Ti$_{0.995}$Nb$_{0.005}$, 3) Ti$_{0.99}$Nb$_{0.01}$, 4) Ti$_{0.95}$Nb$_{0.05}$, 5) Ti$_{0.9}$Nb$_{0.1}$. Bands assigned to β-phase TiO$_2$ are labeled with an asterisk. b) Spray-dried ANO precursor (Nb$_1$) and spray-dried Ti$_{0.5}$Nb$_{0.5}$ precursor calcined at 700 and 800 °C. The diffraction pattern of anatase TiO$_2$ (21-1272), rutile TiO$_2$ (88-1175), Nb$_2$O$_5$ (30-0873), and TiNb$_2$O$_7$ (72-0116) are included for comparison.

Table 6.1: Refined lattice parameters and volume-averaged crystallite sizes of anatase derived from XRD measurements.

pretreatment sample	700 °C, 1 h		800 °C, 1 h	
	lattice parameter a/c [Å]	d(XRD) [nm]	lattice parameter a/c [Å]	d(XRD) [nm]
Ti$_1$	3.784(1)/9.505(5)	20	3.7828(8)/9.511(3)	41
Ti$_{0.995}$Nb$_{0.005}$	3.784(1)/9.505(6)	18	3.7839(9)/9.516(4)	35
Ti$_{0.99}$Nb$_{0.01}$	3.788(6)/9.510(5)	19	/	/
Ti$_{0.95}$Nb$_{0.05}$	3.791(2)/9.512(8)	14	3.791(1)/9.515(5)	22
Ti$_{0.9}$Nb$_{0.1}$	3.791(3)/9.510(12)	13	3.785(1)/9.513(6)	22

The qualitative phase composition of the 700 °C calcination series obtained from the XRD studies is clearly confirmed by Raman spectroscopy (Fig. 6.4a). It is known that the most characteristic and strongest band of anatase appears at 151 cm^{-1}, and that weaker bands can be detected at 639, 515, 400, and 204 cm^{-1}, whereas the Raman bands of rutile phase can be observed at 612, 448, 240, and 147 cm^{-1}.[46] In all spectra the detected bands can be clearly assigned to the anatase phase. Three weak bands in the 200 - 400 cm^{-1} region of the Ti$_{0.95}$Nb$_{0.05}$ and Ti$_{0.9}$Nb$_{0.1}$ samples are likely due to the presence of β-TiO$_2$. Bands of niobia phases are not observed indicating that there is no phase separation or formation of NbO$_x$ islands on the surface of TiO$_2$ particles. Similar changes in crystallite size and cell parameters with bulk composition are observed for the spray-dried precursors calcined at 800 °C. While a large
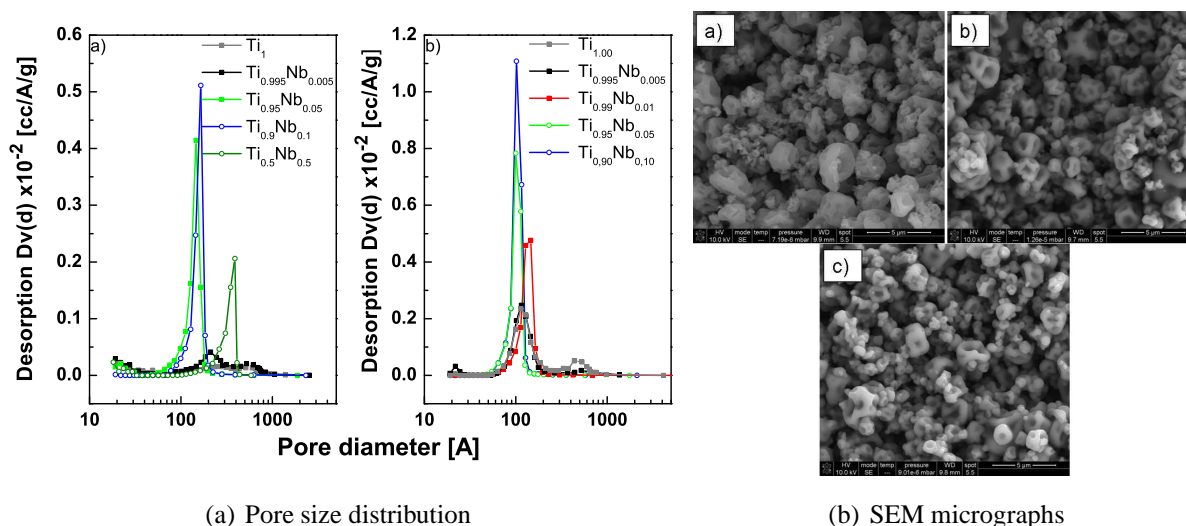
(a) Pore size distribution

(b) SEM micrographs

Figure 6.5: (a) Pore size distribution of Nb-doped TiO$_2$ samples with different Nb content. All samples were treated at a) 800 °C and b) 700 °C. Pore size distribution derived from the N$_2$ physisorption measurements applying the BJH method. (b) SEM micrograph of a) Ti$_1$-700, b) Ti$_{0.95}$Nb$_{0.05}$-700, and Ti$_{0.9}$Nb$_{0.1}$-700.

quantity of Ti$_1$-800 is converted into the rutile phase, the degree of conversion decreases with increasing Nb content.

Figure 6.4b shows the XRD results of the Ti$_{0.5}$Nb$_{0.5}$ and Nb$_1$ reference samples. The Nb1 sample is fully converted into Nb$_2$O$_5$ at both calcination temperatures. The diffraction patterns show sharp diffraction peaks suggesting that these are highly crystalline samples. Detailed analysis of the XRD pattern of the Ti$_{0.5}$Nb$_{0.5}$ sample reveals the presence of anatase and rutile, of TiNb$_2$O$_7$ oxide, and of a minor amount of Nb$_2$O$_5$. At lower calcination temperature the diffraction peaks of the mixed oxide TiNb$_2$O$_7$ are rather weak, and sharp well-defined peaks of the anatase and rutile phases can be detected. When increasing the calcination temperature to 800 °C, a highly crystalline TiNb$_2$O$_7$ oxide phase is observed. The poor crystallinity of the TiNb$_2$O$_7$ oxide in the Ti$_{0.5}$Nb$_{0.5}$-700 sample is in good agreement with the results and the interpretation of the TG-MS data demonstrating the decomposition of the pure Ti-precursor at lower temperatures and the decomposition of a mixed precursor at elevated temperatures. Arbiol et al.[172] explained the phase separation at higher contents of Nb ions by the reduction of stress by removing Nb^{5+} ions from the lattice. However, the high rutile-to-anatase ratio cannot be explained only by removing Nb^{5+} ions from the lattice, as based on the data obtained with Ti$_1$-700 sample, the anatase phase was expected to form exclusively. Possibly, the number of oxygen vacancies, which act as transformation centers is strongly increased compared to Ti$_1$-700 after removing the Nb from the lattice, and therefore, the anatase-to-rutile transformation is favored.[172]

Characterization of the texture and the morphology

The obtained BET surface areas are summarized in Table 6.2. The surface area of the parti-

Table 6.2: Specific BET surfaces areas (BET SA) and particle diameters derived from the N$_2$ physisorption measurements for the differently treated samples with varying Nb content and the respective treatment of the sample.

| pretreatment | 600 °C, 1h | 700 °C, 1h | | 800 °C, 1h | |
sample	BET SA [m^2/g]	BET SA [m^2/g]	d(BET) [nm]	BET SA [m^2/g]	d(BET) [nm]
Ti$_1$	105	56	28	17	91
Ti$_{0.995}$Nb$_{0.005}$	115	51	30	26	59
Ti$_{0.99}$Nb$_{0.01}$	129	60	26	/	/
Ti$_{0.95}$Nb$_{0.05}$	135	69	22	46	33
Ti$_{0.9}$Nb$_{0.1}$	/	90	17	48	32

cles clearly increases with increasing Nb content, while it decreases with increasing calcination temperature. Thus, by varying the calcination temperature or the Nb content the surface area of the particles can be tuned from 40 to 140 m^2/g. A mean particle diameter of the different powders can be calculated from the measured surface area values by assuming spherical particles (Tab. 6.2). Based on this simple calculation, mean particle diameters of 15 - 60 nm were derived, which are in rather good agreement with the crystallite diameters obtained by XRD. It should be mentioned that the density of the anatase particles was used to calculate the mean particle size of the powders. The evolution of the pore size distribution of the samples calcined at 700 and 800 °C is presented in Fig. 6.5 The data are derived from the N$_2$ physisorption experiments applying the BJH equation. The sample Ti$_1$-700 shows two broad signals: smaller pores with a pore size maximum at 100 Å and a less intense signal in the range of 400 - 1000 Å can be observed. After treatment at 800 °C the peak detected at 100 Å disappears and the intensity of the other peak is significantly decreased. Obviously, even a small amount of Nb changes the pore size distribution and increases the number of smaller pores with a diameter of smaller than 200 Å. Further incorporation of Nb up to 10 at % led to even smaller pores. As shown in Fig. 6.5 the intensity of the maxima is changed by changing the calcination temperature. The presence of these small pores can be correlated with the formation of smaller particles. A change in the evolution of the pore size can be seen for the Nb$_{0.5}$Ti$_{0.5}$-800 sample, for which the pore diameter increases, while the overall number of pores decreases reflecting the trend of the N$_2$ physisorption measurements. Characterization of the materials by means of SEM (Fig. 6.5) revealed that the calcined materials consist of collapsed spherical particles. It is known that spray drying led to spherical particles due to fast evaporation of solvent, which collapsed during calcination due to volume contraction resulting from decomposition of the precursors.[180] Furthermore, Nb concentration does not show significant influence on the morphology of the obtained composites, and all the samples show similar morphologies as indicated by SEM studies.

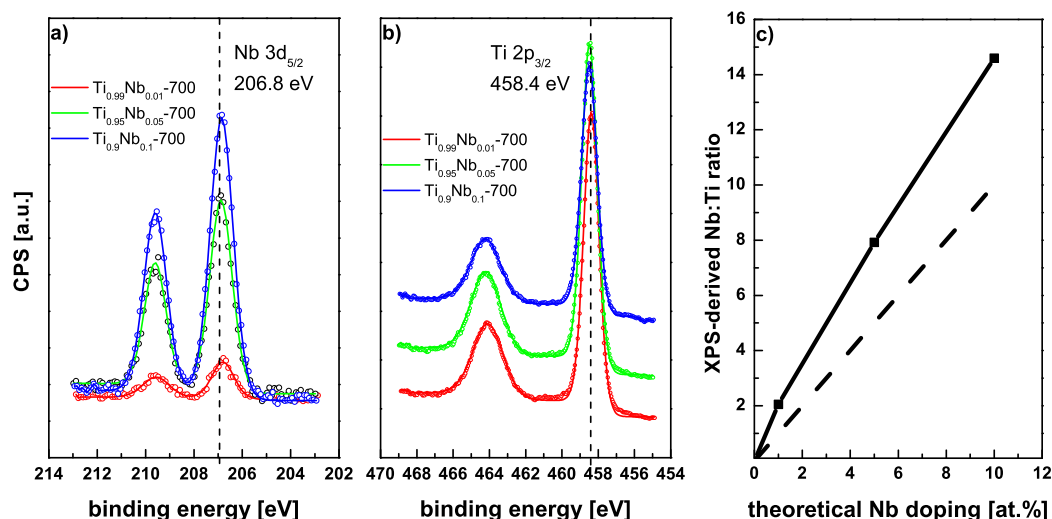*Probing the electronic structure by XPS and UV-Vis*

Figure 6.6: Results of the XPS analysis of samples with Nb content from 1 to 10 at% calcined at
700°C. a) Nb 3d XP spectra, b) Ti 2p XP spectra, and c) the measured (solid line) and
the ideal Nb/Ti ratio (dashed line) based on the XPS analysis vs. the theoretical Nb
doping.

The analysis of the XPS survey spectra (not shown) demonstrated that the sulfate ions had been
removed completely from the sample surface by calcination at 700 °C, as no S 2p signal was
detected. The XP spectra of the undoped and Nb-doped TiO$_2$ powder samples prepared with
different Nb contents (0, 0.01, 0.05, and 0.1), which were annealed at 700 °C, are shown in
Fig. 6.6. Based on the peak positions, the differences of the Ti 2p$_{3/2}$ and the Nb 3d$_{5/2}$ binding
energies and the line shapes, the presence of Ti^{4+} species with a Ti 2p$_{3/2}$ binding energy of
458.3 - 458.5 eV and the presence of Nb^{5+} ions with a Nb 3d$_{5/2}$ binding energy of 206.8 eV is
clearly detected.[174] Within the XPS information depth there is no evidence for Ti^{3+} species,
which are usually observed at 1.8 eV lower binding energy than that of Ti^{4+}.[195] Furthermore,
there is no evidence for the presence of Nb^{4+} species, which are normally observed at binding
energies below 206.5 eV.[165,196] By deriving the Nb:Ti atomic ratio from the Ti 2p$_{3/2}$ and the
Nb 3d$_{5/2}$ peaks a slight enrichment of the Nb ions at the sample surface can be detected as
shown in Fig. 6.6c.

It is well known that the doping of heteroatoms can change the band gap of TiO$_2$. In Fig. 6.7
the results of the UV-Vis measurements of the undoped, the Ti$_{0.995}$Nb$_{0.005}$, and the Ti$_{0.95}$Nb$_{0.05}$
samples calcined at 600, 700, and 800 °C are shown. From these spectra the band gap values
can be derived, and unoccupied electronic states can be detected. The measured band gap of the
Ti$_1$ samples amounts to 3.2 eV, which is in good agreement with reported values of the anatase
modification. It shifts to 3.0 eV corresponding to the rutile modification when calcining at 800
°C. The band gap of the doped TiO$_2$ sample is slightly shifted to lower values with increasing
calcination temperature. The changes in the magnitude of the band gap can be explained by
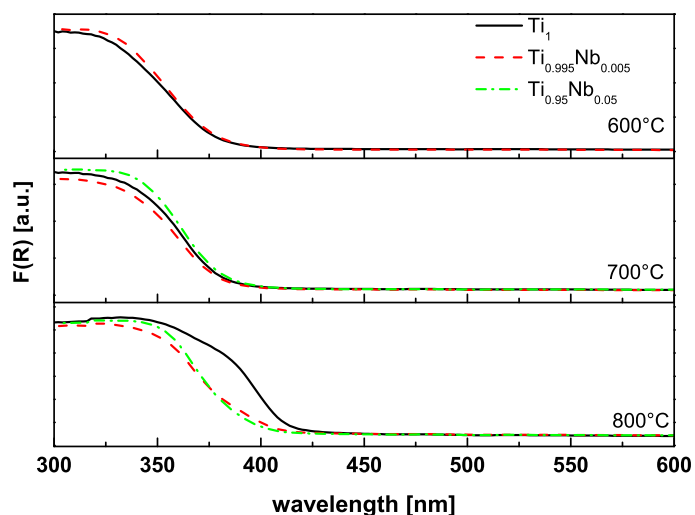the different anatase-to-rutile ratios of the samples: the undoped sample was converted into

Figure 6.7: UV-Vis results of the Ti$_1$, the Ti$_{0.995}$Nb$_{0.005}$, and the Ti$_{0.95}$Nb$_{0.05}$ precursor powders calcined at 600, 700, and 800 °C.

the more stable rutile modification, whereas the degree of phase transformation of the doped sample is low due to the hindered phase transition. Therefore, the shift in the band gap is less pronounced. In case of the samples calcined at 700 °C a slight blueshift of the adsorption edge of the low doped Ti$_{0.995}$Nb$_{0.005}$-700 sample and a slight redshift of the Ti$_{0.95}$Nb$_{0.05}$-700 sample compared with the adsorption edge of the undoped titania Ti$_1$-700 is observed. It is important to mention that no additional electronic states giving rise to electronic transitions were found at higher wavelength for all samples.

Discussion

The characterization of the structural properties and the texture analysis of the synthesized powder materials are in good agreement. The XRD results show that the crystallite size of the materials as well as the particle size derived from BET measurements decrease with increasing Nb content. The differences in the XRD- and BET-derived crystallite sizes can be explained by agglomeration effects influencing the physisorption results. However, the trend in both cases is clearly maintained. The inhibition of grain growth and the hindered anatase to rutile phase transformation are in good agreement with other studies using sol-gel methods[167,173] or laser-induced pyrolysis[172] for the preparation of Nb-doped TiO$_2$. The inhibition of grain growth is mostly explained by stress introduced into the lattice by the slightly larger Nb^{5+} ions,[172,178] and the different phase transformation behavior is explained by the lower oxygen vacancy concentration acting as transformation centers.[19,178] On the other hand, Pittmann and Bell,[197] who studied titania-supported niobia using Raman spectroscopy, pointed out that the formation of strong Nb-O-Ti bonds at the surface inhibits the Ti movement and hinders the phase transformation from anatase to rutile, because the Ti mobility is required to initiate the phase transformation.[198] These Nb-O-Ti bonds are formed, when the surface of titania is covered by NbO$_x$ islands.[197] However, in the present study it is not likely that amorphous NbO$_x$ is-

lands are present on the surface of samples with low Nb content. This is clearly supported by the increase of the refined cell parameter with increasing Nb content and the absence of any feature in the XRD and Raman spectra, which can be found in case of high Nb content. The increase of the cell parameters verifying Vegard's law is a strong hint for the effectiveness of doping as pointed out by Hirano et al.[191] Combining the results of the XRD, Raman, and BET analysis, it is highly likely that Nb is incorporated in the lattice of TiO$_2$. Thus, using the simple spray drying approach, Ti ions are substituted by Nb ions at low doping levels, and solid solutions are formed. The chemical oxidation state of Nb derived by the XPS measurements is 5+. This is in good agreement with other studies using sol-gel methods[178,198] or other preparation procedures.[162,172] Furthermore, the XPS analysis did not reveal any evidence of Ti^{3+}, and the UV-Vis measurements did not show any additional absorption. It is therefore reasonable to assume that charge compensation is achieved by the formation of Ti vacancies according to equation 6.2.

The blueshift of the absorption edge of the Ti$_{0.995}$Nb$_{0.005}$-700 is in good agreement with previous studies on Nb-doped TiO$_2$. Density functional theory calculations of the electronic structure of the pure and the Nb-doped anatase by Liu et al.[199] showed that the difference between the top of the valence band and the Fermi level is larger in doped samples. As a result, the electron transition from the valence band to the conduction band requires more energy, which is clearly consistent with the observed blueshift in the UV-Vis spectra. Furthermore, Chandiran et al.[192] recently observed a similar blueshift of the absorption edge in low content Nb-doped TiO$_2$. They ascribed this blueshift to the Burstein-Moss effect, and the higher visible light transparency and enhanced charge collection efficiency resulted in an increase in power conversion in dye-sensitized solar cells.[192] A redshift in higher doped samples was measured by Lü et al.[169] They used Nb-doped TiO$_2$ with loadings above 2.5 mol% Nb to enhance the performance of the photoanode in a dye-sensitized solar cell and observed a small redshift of the adsorption edge upon Nb doping, which is in agreement with our measurements. However, the redshift in the higher doped Ti$_{0.95}$Nb$_{0.05}$-700 may also be ascribed to the presence of the beta-TiO$_2$ phase, which was detected by XRD and Raman measurements.

Finally, the advantages of the spray drying process compared to the conventional methods have to be addressed. Ruiz et al.[198] studied solid solutions of Nb$_x$Ti$_{1-x}$O$_2$ prepared by a sol-gel method with a Nb content of $0 < x < 0.1$ and found that the solubility limit of Nb in the anatase phase is higher than 0.1. However, the XPS analysis revealed that there is a large discrepancy between the concentration of Nb at the surface and the theoretical loading. Even at low calcination temperature the measured surface concentration was two times higher than the theoretical loading. Similar discrepancies between theoretical loading and surface concentration were found by Chandiran et al.[192], who used a rather complicated hydrothermal process and subsequent annealing treatment to synthesize Nb-doped TiO$_2$ materials. Even though there is also a minor discrepancy between the theoretical Nb content and the actual amount of Nb in the near-surface region detected by XPS, it should be pointed out that the surface segregation is

much less pronounced, and at calcination temperatures of 700 °C and a theoretical Nb content of 10 at% the detectable amount of Nb at the surface is less than 15 %. Thus, more Nb should remain in the bulk of the material effectively doping the titania particles. The differences in segregation behavior are assumed to be due to the rapid evaporation in the spray drying process compared to the slow gelation process in the sol-gel approach. Furthermore, XRD and Raman results provide evidence that there is no additional phase, and it is not likely that NbO$_x$ islands are present on the surface of the material. Hence, Nb is well distributed in the bulk of the spray-dried materials. In summary, spray drying is considered an efficient and advantageous synthetic method leading to high levels of Nb doping in TiO$_2$.

6.1.3 Conclusions

Spray drying was applied as efficient, scalable, and reliable method for the synthesis of doped metal oxides using Nb-doped TiO$_2$ as a test system. The suppression of the ion mobility by the fast evaporation of water during the spray drying process is assumed to favor the homogeneous distribution of the Nb ions. The subsequent calcination in the temperature range from at 600 to 800 °C results in crystalline materials with narrow pore size distributions. Subsequent to calcination, the fully oxidized Nb ions were found to be homogenously distributed in the crystalline TiO$_2$ powder materials, and Nb surface segregation had occurred only to a minor extent in spite of the high-temperature treatment. By using different levels of Nb doping, the particle size and the anatase-to-rutile ratio can be easily adjusted: with increasing Nb content up to Ti$_{0.9}$Nb$_{0.11}$ the particle size decreases continuously, and the transformation of anatase into rutile at high temperatures is more kinetically hindered. The spray drying approach combined with a controlled high-temperature calcination is considered a promising technique for the homogeneous doping of TiO$_2$ and other oxides with various metal ions. Future work should focus on the development of more suitable precursor molecules.

6.2 TiO$_2$-polyheptazine hybrid materials

Abstract[2]

Nb-doped TiO$_2$ prepared by spray drying exhibits enhanced photoelectrochemical performance both in its bare form (under UV irradiation) and when used as an electron collector in hybrid TiO$_2$-polyheptazine photoanodes for water photooxidation under visible ($\lambda > 420$ nm) light.

6.2.1 Short Introduction

Direct conversion of solar energy into chemical energy by sunlight-driven water splitting into hydrogen and oxygen in a photoelectrochemical cell is one of promising strategies to secure the future supply of clean and sustainable energy.[200] Although very high solar-to-hydrogen efficiency of up to 18 % have been already achieved, such cells were typically based on multijunction photoelectrodes using expensive materials.[201,202] An economically viable solution, therefore, requires the development of new, low-cost materials. Notably, due to the complex chemistry involved in four-electron oxidation of water to dioxygen,[203] the major challenge in photoelectrochemical water splitting is the development of cheap, efficient, and stable photoanodes. The research efforts have mostly focused on low-band gap transition metal oxides, like WO$_3$ (2.6 eV, $\sim$ 480 nm)[204,205] or α-Fe$_2$O$_3$ (2.1 eV, $\sim$ 590 nm),[206–208] which combine light absorption in the visible with high stability. However, their rather positive conduction band edge normally translates into the need to apply significant external electric bias or use tandem cell configurations in order to achieve proton reduction at the counter electrode.

An attractive alternative is to use a nanocrystalline layer of a stable wide-band gap oxide (e.g. TiO$_2$) sensitized by a visible light absorbing dye coupled to a co-catalyst for water oxidation.[209–211] In this approach the oxide is used essentially as a collector for electrons injected from the dye, whereby the positive charges (holes) are channeled to a colloidal co-catalyst for water oxidation (IrO$_2$ nanocrystals). Interestingly, such hybrid photochemical assemblies not only resemble the Photosystem II of green plants by exhibiting kinetic charge separation,[212] but they also take advantage of the relatively negative potential of the conduction band edge of the wide-band gap metal oxide (e.g. -0.15 V vs. RHE for TiO$_2$) which promises significantly reduced need for external bias to drive complete water splitting. Obviously, the stability issue plays a crucial role in this type of devices since many dyes are not stable enough to survive the harsh conditions during water oxidation.[209,211,213]

Recently, we have been developing photoanodes (Figure 6.8) based on a novel class of visible light photoactive inorganic/organic hybrid materials - TiO$_2$ modified at the surface with polyheptazine (also known as "graphitic carbon nitride").[53,54,214,215] The most attractive feature of these inorganic/organic hybrids is the high thermal (up to 550 °C in air) and chemical stability of polyheptazine-type compounds as compared to conventional organic dyes. Notably, we have shown that the optical absorption edge of the TiO$_2$-polyheptazine hybrids is red-shifted into the visible (2.3 eV; $\sim$540 nm) as compared to the band gap of both of the single components - TiO$_2$ (3.2 eV; $\sim$390 nm) and polyheptazine (band gap of 2.9 eV; $\sim$428 nm), which is due to the formation of an interfacial charge-transfer complex between polyheptazine (donor) and TiO$_2$ (acceptor). In other words, the direct optical charge transfer leads to generation of electrons with a relatively negative potential in the conduction band of TiO$_2$, while the holes photogenerated in the surface polyheptazine layer can drive water photooxidation, as evidenced
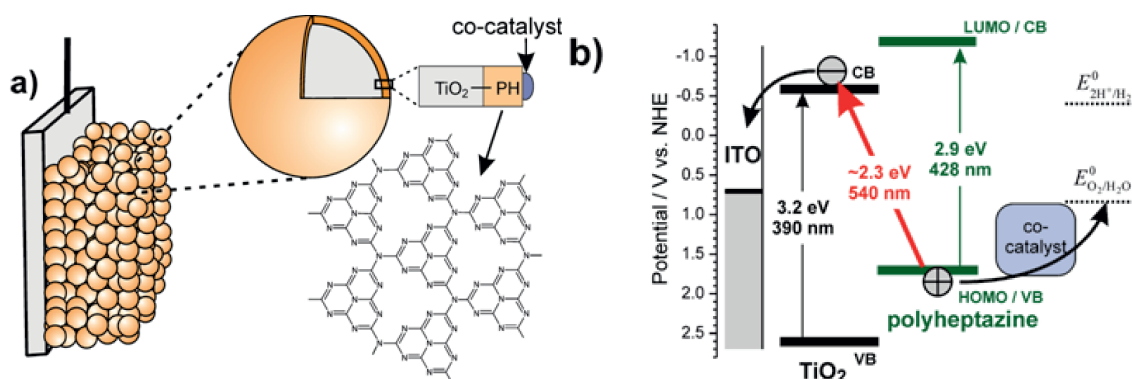
Figure 6.8: a) Hybrid photoelectrode consists of a layer of nanocrystalline TiO₂ powder pressed onto an ITO-glass, sintered, and subsequently modified at the surface with polyheptazine; b) Potential scheme (at pH 7) illustrating the visible light photoactivity of TiO₂-polyheptazine hybrids based on direct optical charge-transfer excitation of an electron from the polyheptazine HOMO (valence band) into the conduction band of TiO₂.

by visible light-driven evolution of dioxygen on hybrid electrodes modified with IrO_x or CoO_x nanoparticles acting as oxygen evolution co-catalysts.[53,54,214,215]

An attractive strategy, so far untried, for improving such hybrid photoelectrodes consists in tuning the electronic properties of the electron-collecting component, i.e. of TiO₂ in our case. In this context, particularly doping of TiO₂ with niobium represents an interesting option since it is known that the replacement of tetravalent Ti with pentavalent Nb can shift the Fermi level closer to the conduction band edge of titania and thus increase significantly its conductivity.[166,198,216,217] The enhanced mobility of photogenerated electrons would then lead to improved charge collection and diminished recombination. Indeed, some promising results along these lines have been recently reported for Nb-doped TiO₂ electrodes used either for water photooxidation[218,219] or as photoanodes in dye-sensitized solar cells.[169,192,192] However, the beneficial effect of Nb doping has not been observed always,[166] and it seems clear that the performance of Nb-doped TiO₂ is highly dependent on Nb content and its preparation conditions.[169,192,192,218,219]

We have recently developed a continuous spray drying approach to synthesize of Nb-doped TiO₂ materials from aqueous solution (Chapter 6.1).[220] This method is not only efficient and scalable but allows also for highly homogeneous distribution of Nb in crystalline TiO₂,[220] which is important in order to avoid formation of undesired defects.[217] Herein, we show that Nb-doped TiO₂ prepared by spray drying exhibits enhanced photoelectrochemical performance both in its UV-only-active bare form and also when used as an electron collector in hybrid photoanodes for water photooxidation under visible light.

Experimental

Nb-doped TiO₂ powders (0-10 at%) were prepared by spray drying followed by calcination at

700 °C.[220] Working electrodes of catalyst materials were prepared on cleaned ITO glass substrates by doctor blading of powder pastes as described previously.[53] The powder pastes were prepared by ultrasonication of a mixture of 0.37 ml ethanol, 0.13 ml titaniumtetraisopropoxid and 100 mg of sample. Modification of the working electrodes with polyheptazine was performed by a procedure described in detail elsewhere.[53] In short, the electrode was statically heated to 450 °C in a two compartment glass flask containing the electrode and 1 g of urea. The electrode was further modified with IrO$_2$ by hydrolysis of Na$_2$IrCl$_6$. Characterization of the as-received materials was performed using Raman spectroscopy using a Nexus FT-NIR spectrometer equipped with a nitrogen-cooled germanium detector and a 1064 nm laser (Nd:YAG) provided by Thermo Fisher Scientific. UV-vis diffuse reflectance spectra (DRS) were recorded in a Perkin-Elmer Lambda 650 UV-vis spectrometer equipped with a Praying-Mantis mirror construction using MgO as the 100 % reflection reference. Photocurrent measurements were performed with a SP-300 BioLogic potentiostat and a three-electrode cell using a Pt counter and a Ag/AgCl (3M KCl) reference electrode in a phosphate buffer solution (pH 7). A tuneable monochromatic light source with a 150 W Xenon lamp was used for sample irradiation. IPCE data for each wavelength were obtained according to the equation IPCE (%)=(i$_{ph}$hc)/(λPq)100, where i$_{ph}$ is the photocurrent density, h is Planck's constant, c the velocity of light, P the light power density, λ the irradiation wavelength, and q the elementary charge. The measurement of quasi-Fermi level of electrons by the suspension method of Roy was carried out in a two electrode setup with a 150 W Xenon lamp equipped with heat absorbing IR filter. The pH dependence of the potential was recorded in the presence of the pH independent electron acceptor methyl viologen as previously reported.[221] Oxygen evolution was measured in a phosphate buffer (pH 7) by an OxySense 325i oxygen analyzer in a two-compartment cell.[53]

6.2.2 Results and Discussion

All investigated photoelectrodes consisted of $\sim$ 6 μm thick porous crystalline powder layers pressed onto an ITO-glass substrate (Fig. A15). A Raman spectroscopy analysis of Nb-doped samples prepared by spray drying and calcined at 700 °C confirmed that as expected exclusively the anatase structure was obtained for a large concentration range of Nb (0.1-10 at% Nb with respect to Ti).[220] The optical absorption properties of undoped and Nb-doped materials were nearly the same, exhibiting a band gap of 3.2 eV (Fig. A16). The photocurrent response of Nb-doped TiO$_2$ electrodes was strongly dependent on the doping concentration as shown by the wavelength-dependent photocurrent measurements (Figure 6.9a; raw data in Fig. A17). The Nb-doped TiO$_2$ with 0.1 at% Nb content ("Nb01") has shown the best UV-light photoresponse exhibiting the monochromatic incident photon-to-current efficiency (IPCE) values higher by ca. 25 % as compared to a pristine TiO$_2$ reference, whereby a maximum is observed at 350 nm. The drop of the photocurrent at low wavelengths is due to enhanced recombination which is a typical consequence of photogeneration of charges in a thin surface layer upon irradiation
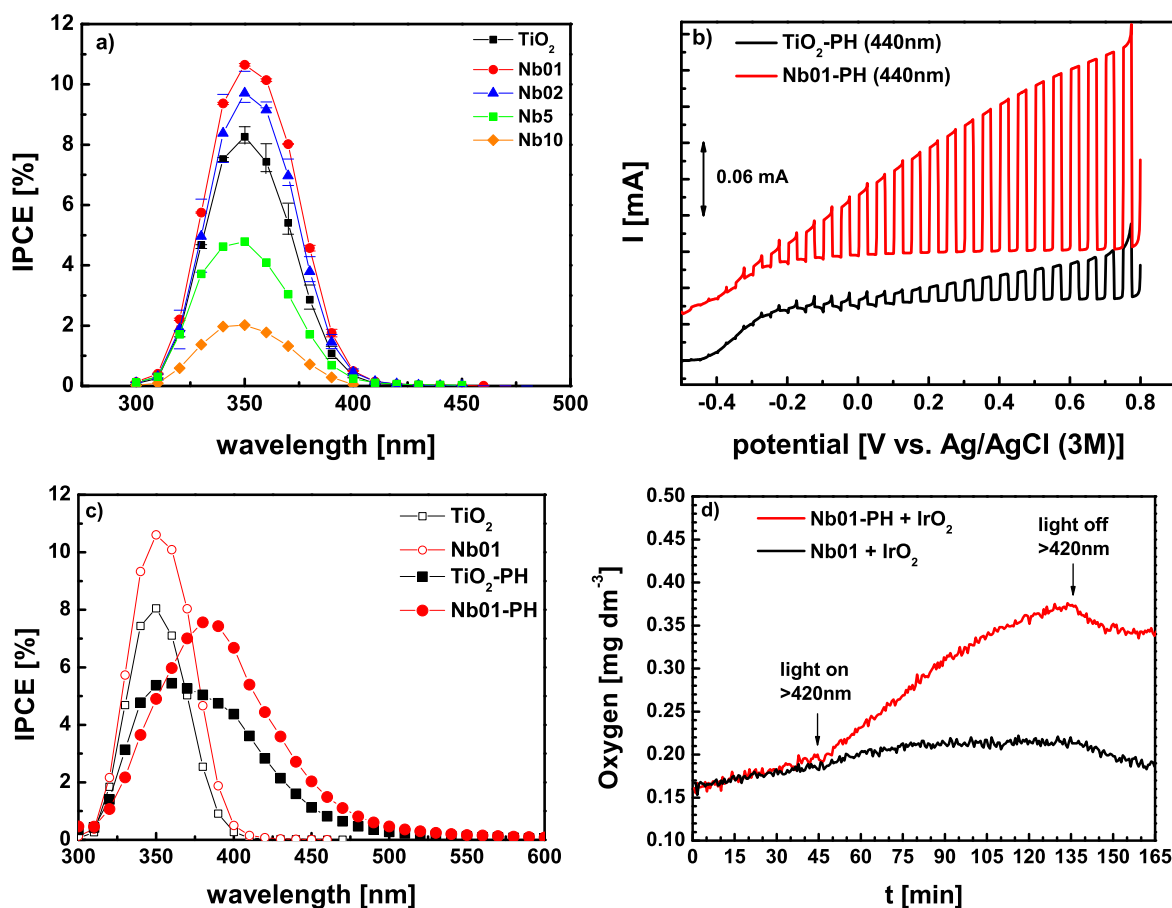
Figure 6.9: a) Photoaction spectra measured in a phosphate buffer solution (pH 7) at 0.5 V vs. Ag/AgCl for a TiO₂ reference and Nb-doped TiO₂ materials with different Nb concentrations (0.1-10 at%). b) Potential-dependent and c) wavelength-dependent photocurrents measured at different excitation wavelength for the polyheptazine-modified TiO₂ reference and Nb-doped TiO₂ materials. d) Oxygen evolution measured at 0.5 V vs. Ag/AgCl in the liquid phase upon visible light irradiation for the two materials. IrO₂ was used as an oxygen evolution co-catalyst.

with short wavelength light. When increasing the Nb concentration to 0.2 at% Nb a decrease in photocurrent was observed, which is further pronounced with increasing Nb concentration. This can be explained by an increase in the number of defects within the TiO₂ lattice which will increase the recombination rate.

A similar trend has been recently observed by Schmuki et al.[218,219] However, it should be noted that Nb-doped TiO₂ nanotubes investigated by Schmuki et al.[218,219] contained significant portion of rutile, whereas our samples contain only the anatase phase and the effect of Nb incorporation into the TiO₂ lattice can be evaluated without any interference of structural changes. We can therefore conclude that in our case the observed photocurrent enhancement is chiefly due to Nb incorporation into the TiO₂ lattice, which increases the mobility of photogenerated electrons and diminishes the recombination. Interestingly, under potentiodynamic

conditions only a small improvement of the photocurrents can be observed at high bias potentials, and first at more negative potentials the improvement becomes obvious at the 0.1 at% Nb electrode (Fig. A18a). This is in line with our assumption that the enhancement is due to improved electron transport properties, which can be expected to make itself apparent particularly at low bias potentials. Furthermore, we exclude the possibility that the enhancement is simply due to the shift of the band edges in the Nb-doped TiO_2. The photocurrent onset potential was determined to be $\sim$ -0.5 V vs. Ag/AgCl (at pH 7) for both the pristine TiO_2 and Nb-doped TiO_2 (Fig. A18b). Similarly, the quasi-Fermi level of electrons (i.e. the electrochemical potential of photogenerated electrons), as determined by the suspension method of Roy,[221] shows only a very small difference (-0.56 V vs. NHE for pristine TiO_2 and -0.59 V vs. NHE for Nb-doped TiO_2 at pH 7; Fig. A19). Though this difference is well within the experimental error of this measurement, it cannot be completely excluded that the difference is precisely due to the presence of new donor levels in Nb-doped samples which leads to an increase of conductivity and shifts thereby also the quasi-Fermi level closer to the conduction band edge.[198,216,217]

Modification with a thin (1-3 nm) layer of polyheptazine using a chemical vapor deposition method[53,54,214,215] did not significantly change the morphology of the electrodes as evidenced by SEM analysis (not shown). The optical absorption edge has been shifted to 2.3 eV upon modification (Fig. A20). As compared to polyheptazine-free photoanodes, the photocurrent onset, measured under monochromatic visible (λ = 440 nm) light irradiation, has been shifted anodically by 0.2 V to -0.3 V vs. Ag/AgCl for hybrid photoelectrodes based on both pristine and Nb-doped TiO_2 (Figure 6.9b). This shift is in agreement with our previous observations and can be ascribed to enhanced recombination rate due to slower kinetics of holes and their accumulation in the polyheptazine layer.[214] However, more importantly, the Nb-doped samples show much better performance, particularly at low-bias potentials. This can clearly be attributed to the enhanced mobility of electrons in the Nb-doped TiO_2 which renders the electron transport into the ITO substrate more efficient and the charge recombination less likely. In accord with the behavior of polyheptazine-free electrodes, also in case of hybrids the best performing photoanodes were those with 0.1 at% Nb. The enhanced performance of Nb-doped samples is also clearly apparent from the IPCE photoaction spectra (Fig. 6.9c). The beneficial effect of Nb doping is more pronounced at lower-energy light (longer wavelengths) where the influence of electron mobility in Nb-doped TiO_2 can be expected to exert major influence on recombination processes. As compared to irradiation by short wavelength light where nearly all charges are photogenerated in a small volume near the ITO glass (electrodes are irradiated from the backside - through the ITO glass), the longer-wavelength light penetrates deeper into the porous electrode and renders the transport of electrons more important. Accordingly, at wavelengths longer than 450 nm the IPCE values are practically doubled as compared to hybrid photoanodes based on pristine TiO_2.[3] After depositing IrO_2 nanoparticles as a water

---

[3]It has to be noted that the relatively smaller enhancement of IPCE values as compared to photocurrents measured under potentiodynamic conditions (Fig. 6.9a) is due to the fact that the IPCE values were measured under potentiostatic conditions where the photocurrent transients show a strong spike-like behavior.[214]

oxidation co-catalyst, polychromatic visible light ($\lambda > 420$ nm) induced dioxygen evolution on Nb-doped TiO$_2$-polyheptazine hybrids (Fig. 6.9c), while the unmodified 0.1 wt% Nb-doped TiO$_2$ did not show any oxygen evolution. The corresponding photocurrent transient (Fig. A21) reveals insufficient stability, which is mainly related to poor coupling to the IrO$_2$ co-catalyst that is far from optimum in this case. Our current work is mainly focused on solving this issue.

6.2.3 Conclusions

In summary, Nb-doped TiO$_2$ prepared by spray drying exhibits enhanced photoelectrochemical performance both in its bare form and when used as an electron collector in visible light-active TiO$_2$-polyheptazine hybrid photoanodes for water photooxidation. The optimum Nb content was 0.1 at%, and the photoelectrochemical analysis indicates that the enhancement is chiefly due to enhanced mobility of electrons in the Nb-doped samples. Finally, our findings highlight the importance of modulation of electronic properties of electron-collecting substrates in hybrid photoelectrochemical devices.

6.3 Nitrogen-modified Nb-doped TiO$_2$: Towards red TiO$_2$

Abstract[4]

Nb-doped TiO$_2$ prepared by spray drying were subsequently treated by ammonia to obtain Nb/N co-doped TiO$_2$. The as-received Nb-doped TiO$_2$ and ammonia-modified Nb/N co-doped TiO$_2$ were tested for the photocatalytic activity for the degradation of organic dyes. Surface adsorption of the dye was found to significantly affect the photocatalytic activity of the photocatalysts and incorporation of up to 5 at% of Nb into TiO$_2$ exhibit beneficial degradation properties for the degradation of methylene blue (MB). The photocatalytic activities of the Nb/N co-doped TiO$_2$ catalysts were small. However, an optimum in the photocatalytic activity of the Nb/N co-doped TiO$_2$ materials was determined for the ammonia-modified Nb-doped TiO$_2$ with 10 at% of Nb. By means of elemental analysis and X-ray photoelectron spectroscopy a correlation between the Nb and nitrogen content incorporated into the TiO$_2$ materials was observed indicating that nitrogen incorporation is improved in the Nb-doped TiO$_2$ materials. Based on this preliminary results possible strategies are discussed to further improve the nitrogen incorporation into TiO$_2$-based materials and enhance the photocatalytic activity under visible light irradiation.

---

[4]To be published as "Nb/N co-doped TiO$_2$: Improvement of the visible light activity by effective charge compensation".

6.3.1 Short Introduction

Recently, co-doping of TiO$_2$ by non-metal/non-metal or metal/non-metal co-incorporation into the anatase TiO$_2$ structure attracted some interest.[32,36,222–227] Several examples discussed in literature demonstrate that the visible light photocatalytic activity is mainly found to be lower than that of pure TiO$_2$ under UV irradiation, although visible light absorption can be achieved by doping. This can be ascribed to different problems occurring for doped TiO$_2$:[32,55]

- High formation energies and differences in ionic radius prevent high doping levels.[32]

- The recombination of charge carriers is increased due to localized states in the band gap acting as recombination centers.[228]

- The migration of charge carriers is limited and the oxidation power of the localized states is lower.[32]

Synergetic effects between two complementary doping species are believed to reduce the defects introduced during doping by charge compensation, and thus partially overcome the problems of single-doped TiO$_2$.[226] An interesting example of successful co-doping of TiO$_2$ was recently presented by Liu et al.[224] They synthesized a TiO$_2$ material with boron-enriched surface, which was subsequently treated in ammonia atmosphere yielding a red anatase. Characterization of the red anatase revealed that no Ti^{3+}-related defects were created at the surface of the sample during the synthesis, and boron was shown to be present in BN-like environment. Finally, the B/N co-doped TiO$_2$ was shown to exhibit enhanced visible light performances in a photoelectrochemical cell.[224] Another study by Ikeda et al.[36] with Cr/Sb co-doped TiO$_2$ showed that the ratio of Cr and Sb is of a high relevance to obtain a visible light active material. While the material was black in color and photocatalytically inactive for high Cr to Sb-ratios, the color changed to orange and visible light activity in the oxygen evolution reaction in presence of a sacrificial agent was observed.[36]

A more recent theoretical study based on density functional theory suggest that certain combinations of metal/non-metal co-incorporation into anatase TiO$_2$, or more generally spoken alloying donor-acceptor combinations with anatase TiO$_2$, are promising materials for photoanodes in a photoelectrochemical cell.[229] According to the calculations they should fulfil the main requirements of a photoanode such as an appropriate optical band gap and suitable valence and conduction band-edge positions with respect to the redox potential for hydrogen and oxygen evolution.[229] Within this study two different concentration regimes and several donor-acceptor combinations were calculated. Finally, four different combinations were suggested. For the low concentration alloys, where 3.1 or 6.2 % of oxygen were replaced by electron acceptors depending on the donor atom, a combination of Mo and N or W and N appeared to be good choices. In the high alloy concentration regime Nb/N and Ta/N combinations passed the selection criteria.

So far, only one experimental study was performed aiming at an improvement of the visible light absorption by co-alloying TiO_2 with Nb and N or Ta and N.[222,230] Indeed, it was shown that Nb/N co-alloying enhanced the photocatalytic activity towards methylene blue decolorization.[222] A reddish Nb/N co-alloyed TiO_2 sample was obtained after ammonia treatment of a material with a molar Nb/Ti ratio of 1:3. Within this study the Nb/Ti ratio was fixed, and only the effect of slight variations in the sample pretreatment were presented.[222] Obviously, the B/N and the Nb/N co-doped TiO_2 materials synthesized by Liu et al.[224] and Breault et al.[222] exhibit similar absorption properties. Niobium is well known to segregate to the surface. Therefore, a Nb gradient within the anatase particle is feasible, which will result in a similar structure than the B/N co-doped TiO_2.[172,198] Ta/N co-doped TiO_2 materials with undefined Ta and N concentrations were used for photoelectrochemical water oxidation.[230] By means of TEM investigations Hoang et al.[230] observed a suppression of the formation of an amorphous layer during the nitridation process and noted that the enhanced photoelectrochemical performance of the Ta/N co-doped TiO_2 is due to less recombination centers. Therefore, it is reasonable to assume that co-doping is a suitable strategy to enhance the photocatalytic activity compared to single-doped materials. Due to the above mentioned reasons further investigations with Nb/N co-doped TiO_2 are necessary to understand the effect of co-doping and to evaluate the photocatalytic performance of co-doped materials. Here, a larger Nb concentration range is explored in order to obtain a better match of Nb and N. Again spray drying was used to synthesize Nb-doped TiO_2. Based on the experimental results and theoretical calculations samples with Nb/Ti ratios of up to 1:3 were prepared.[222,229]. For a comparison with the experimental results presented by Breault et al.[222] the photocatalytic activity with respect to decolorization of organic dyes was used as a test reaction to evaluate the photocatalytic properties of the as-received Nb-doped TiO_2 and the subsequently NH_3-modified Nb-doped TiO_2 samples.

Experimental

Nb-doped TiO_2 was prepared by spray drying as explained in this chapter. All samples were calcined at 700 °C to obtain the anatase structure exclusively using the described heating procedure.[220] The ammonia treatment was performed at different temperatures in a vertical furnace using pure ammonia with a flow rate of 150 ml/min. The design of the furnace allows for a homogeneous distribution of the NH_3, and thus a homogeneous nitrogen doping can be achieved. Photocatalytic degradation of organic dyes was performed by suspending 50 mg of catalyst in 85 ml of a 10 ppm methylene blue (MB) (20 ppm methyl orange (MO)) solution. The absorption-desorption equilibrium was obtained by stirring for 60 min in the dark. Irradiation of the suspension was performed with a 150 W Xe lamp equipped with an IR filter and a 320 nm cutoff filter. The solution was permanently saturated by bubbling synthetic air through the suspension. The degradation of the dyes was monitored by taking 2 ml of the solution at constant time intervals. The catalyst was removed by filtering, and the characteristic absorbance of the dye was recorded by means of UV-Vis spectroscopy.
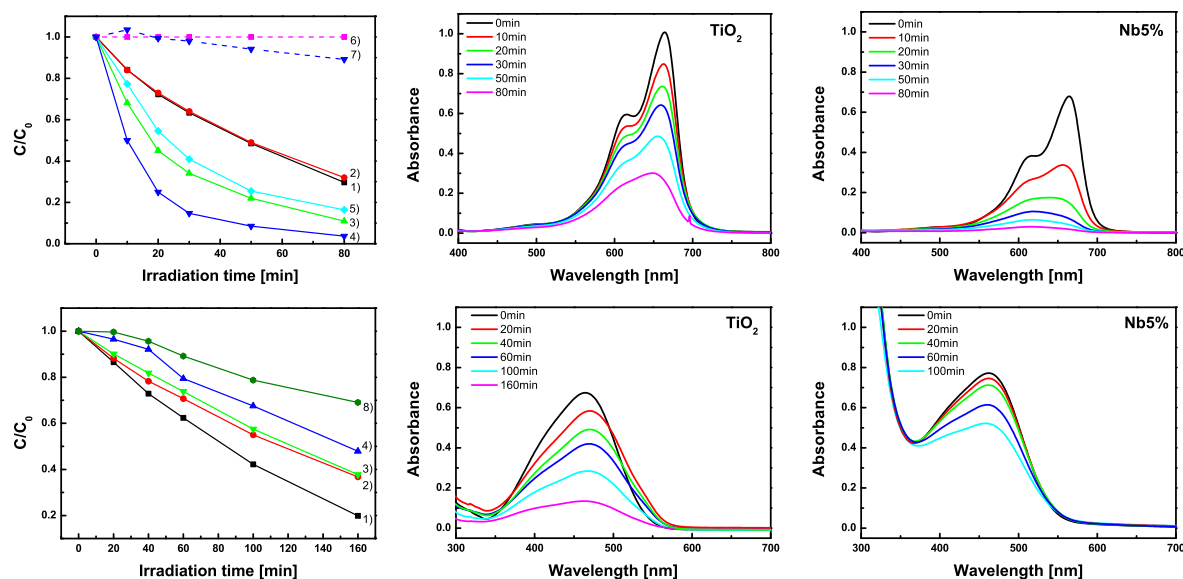
6.3.2 Results and Discussion

Figure 6.10: First row: Results obtained for the MB degradation experiments (10 ppm MB). Second row: Degradation of MO (20 ppm solution) with different Nb-doped TiO$_2$ samples. 1) TiO$_2$, 2) Nb 1 at%, 3) Nb 2 at%, 4) Nb 5 at%, 5) Nb 10 at%, 6) TiO$_2$, 400 nm filter, 7) Nb 5 at%, 400 nm filter , 8) Nb 15 at%.

Initially the as-received Nb-doped TiO$_2$ materials with different Nb concentrations were characterized regarding their structure and absorption characteristics and afterwards tested as photocatalysts. In short, characterization by means of Raman and UV-Vis spectroscopy revealed that the desired anatase structure was obtained exclusively and that all samples posses an band edge of 3.2 eV, which is usually observed for the anatase structure.[220] The activities towards methylene blue (MB) degradation are shown in Fig. 6.10. Obviously, there is an increase in the activity towards MB decolorization upon Nb doping of up to 5 at%. For the Nb-doped TiO$_2$ with 10 at% the activity is still higher than the pristine TiO$_2$ material. However, it is necessary to take the MB adsorption at the materials surface into account. Nearly no adsorption was observed at the pristine TiO$_2$, but with increasing Nb doping concentration the surface absorption of MB is getting more pronounced. This is evident by comparing the UV-Vis absorption spectra measured during the degradation reactions of pristine TiO$_2$ and Nb 5 at%. It is obvious that $\sim$ 40 % of MB is pre-adsorbed at the Nb 5 at%, as in Ti$_{0.95}$Nb$_{0.05}$, surface at the beginning of the reaction (Fig. 6.10). Pre-adsorbed MB might change the decolorization mechanism. An indication of changes upon adsorption was obtained by studying MB decolorization under visible light irradiation using a 400 nm cutoff filter. While no decrease in the characteristic MB absorption spectra was observed for pristine TiO$_2$, the intensity of the MB peak maximum at 664 nm is slightly decreasing upon irradiation (Fig. 6.10). The UV-Vis absorption spectra show that the band gap of TiO$_2$ samples is unchanged upon Nb doping (Fig. 6.7). Only UV light can be absorbed, and electron excitation from the valence band to the conduction band to

Table 6.3: Chemical composition of the spray-dried samples with different Nb content after NH$_3$ treatment at 500 °C in 150 ml/min for 4 h.

sample	Ti content [wt%]	Nb content [wt%]	N content [wt%]	XPS(N/Ti)-ratio)
TiO$_2$	57.52	-	0.1	0.05
Ti$_{0.99}$Nb$_{0.01}$	56.63	0.81	0.2	-
Ti$_{0.98}$Nb$_{0.02}$	55.82	1.42	0.37	-
Ti$_{0.95}$Nb$_{0.05}$	55.11	3.07	0.45	0.11
Ti$_{0.9}$Nb$_{0.1}$	51.05	6.06	0.7	0.13
Ti$_{0.85}$Nb$_{0.15}$	47.36	8.85	1.02	-
Ti$_{0.8}$Nb$_{0.2}$	47.20	12.16	1.32	0.27
Ti$_{0.75}$Nb$_{0.25}$	44.77	15.38	1.83	-

create electron-hole pairs is not feasible. Therefore, the decolorization of MB may be due to visible light absorption of MB and charge injection into the conduction band of the material. This sensitization seems to be favored upon MB adsorption.

To further study the influence of surface adsorption of the dye onto the photocatalytic activity of the samples the degradation experiments were performed with a different dye. Methyl orange (MO) was chosen instead of MB (cationic dye) due to the anionic nature of MO. The results of the degradation experiments are also included in Fig. 6.10. Upon Nb doping of TiO$_2$ the activity towards the decolorization of MO is steadily decreasing with increasing Nb concentration. Additionally, a different trend in MO adsorption was observed. As shown by the UV-Vis absorption spectra obtained at different reaction times for pristine TiO$_2$ and Nb 5 at% (Ti$_{0.95}$Nb$_{0.05}$) (Fig. 6.10) MO is preferably adsorbed at the pristine TiO$_2$. The two presented sets of photocatalytic dye degradation demonstrate that dye adsorption is indeed an important factor considerably changing the activities of a material. The importance of adsorption can be rationalized by the different types of degradation mechanisms.[231,232] While it is widely believed that dye degradation is occurring by the attack of generated OH radicals, the direct degradation by holes has to be taken into account.[232] OH radicals are mainly produced by the reaction of surface adsorbed water with holes. The presented results show that direct degradation by holes is responsible for the degradation of MB at TiO$_2$-like samples. However, it is evident that surface adsorption of dyes has to be considered when organic dye decolarization/degradation is used as a test reaction to measure photocatalytic activities. The indirect oxidation of the dye by activated oxygen is neglected in this considerations due to the lower oxidation potential.[232] To obtain further insight into the photocatalytic activities of the different Nb-doped TiO$_2$ samples the determination of the total organic carbon content (TOC) during photocatalytic degradation of the different dyes would be necessary.

Subsequently to calcination in synthetic air at 700 °C the Nb-doped TiO$_2$ materials with different Nb contents were treated in pure NH$_3$ at different temperatures to obtain co-doped Nb/N-

TiO$_2$. The materials described in the following section were obtained after ammonia treatment at 500 °C for 4 h. Elemental analysis of the samples revealed that with increasing Nb concentration the amount of nitrogen incorporated into the materials is increasing from 0.1 wt% for the pristine TiO$_2$ to $\sim$ 1.8 wt% for the Ti$_{0.75}$Nb$_{0.25}$ (Table 6.3). According to the overall increase in nitrogen content the XPS analysis showed that the N/Ti-ratio at the surface of the materials steadily increased (Table 6.3). Furthermore, the XPS analysis indicates that two different species can be detected at binding energies of $\sim$ 396 eV and $\sim$ 400 eV (Fig. 6.11). The latter signal is usually assigned to interstitial nitrogen (N$_i$) and the low binding energy signal is assigned to substitutional nitrogen (N$_s$).[233] The intensity of both signals increases and the ratio of N$_s$/N$_i$ changes with increasing Nb content in the Nb/N co-doped TiO$_2$ samples. While N$_s$ could be almost neglected for N-doped TiO$_2$ the ratio of N$_s$/N$_i$ is already almost 1 for the Nb/N co-doped Ti$_{0.9}$Nb$_{0.1}$ sample. The substitutional N$_s$ compound was determined to be the main nitrogen compound in the Nb/N co-doped Ti$_{0.8}$Nb$_{0.2}$ sample. Elemental analysis additionally confirmed that the Nb content in the different materials is still in good agreement with the theoretical Nb concentrations (Table 6.3). After ammonia treatment with increasing Nb content the color of the Nb/N co-doped samples is gradually changing from yellowish for the ammonia-treated pristine TiO$_2$ to dark green for the ammonia-treated Ti$_{0.75}$Nb$_{0.25}$. The visually observed change in color is supported by an increase in the visible light absorption at higher wavelength (600 - 800 nm) with increasing Nb content in the Nb/N co-doped TiO$_2$ materials as determined by UV-Vis spectroscopy. Additionally, from the XRD measurements it is evident that structural changes due to the ammonia treatment at 500 °C can be neglected as shown in Fig. A22. For all samples, regardless of the Nb- or N-content incorporated into the TiO$_2$ lattice, the anatase structure was obtained exclusively.
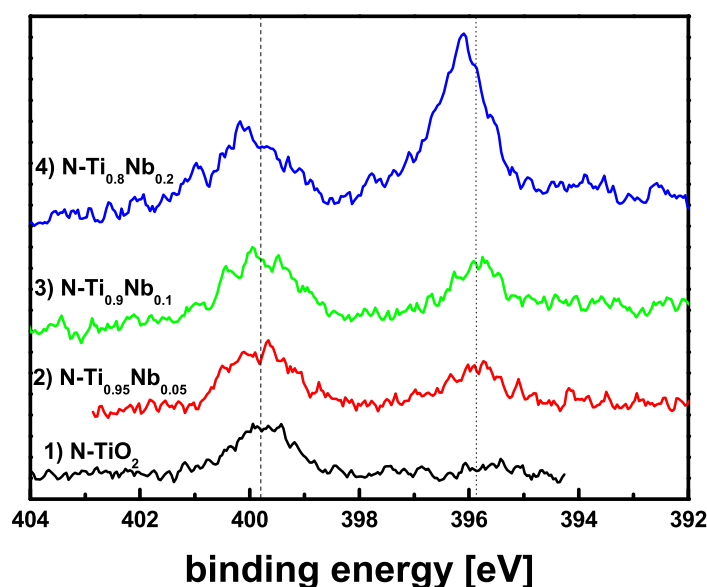

Figure 6.11: XPS N 1s region scans of Nb-doped TiO$_2$ materials with different Nb concentrations treated at 500 °C in 150 ml/min NH$_3$ for 4 h. The theoretical Nb content in the different materials was 1) 0 at%, 2) 5 at%, 3) 10 at%, and 4) 20 at%.

The photocatalytic activity of the materials was tested by the degradation of MB and MO. Surprisingly, none of the ammonia-modified materials exhibit any activity for the degradation of MO and only a slight degradation of MB was detected. In the MB degradation tests the Nb/N co-doped TiO$_2$ sample theoretically containing 10 at% Nb (Ti$_{0.9}$Nb$_{0.1}$) showed the highest degradation rates (in this comparison differences in MB adsorption on the Nb/N co-doped TiO$_2$ samples were neglected). However, the photocatalytic activity towards degradation of MB was still significantly lower for the ammonia-treated Ti$_{0.9}$Nb$_{0.1}$ sample compared with photocatalytic activities of the pristine TiO$_2$ and the Ti$_{0.95}$Nb$_{0.05}$ samples.

For the Ti$_{0.9}$Nb$_{0.1}$ sample showing the best photocatalytic activities in the applied test reactions different ammonia treatment temperatures up to 700 °C were tested. The photocatalytic activity towards degradation of MB decreased with increasing temperature. X-ray diffraction (Fig. A22) and XPS (Fig. 6.11) measurements revealed that the Ti$_{0.9}$Nb$_{0.1}$ sample treated at 700 °C was mainly converted into a the corresponding nitride, which certainly explains the loss in activity. While the XRD results point to the complete transformation of the anatase phase into the nitride (Fig. A22), the XPS results reveal that Ti in a TiO$_2$-like and Nb in a Nb$_2$O$_5$-like state are also present in the near surface region of the material. Interestingly, the Nb content as determined by XPS was lower for the ammonia-modified Ti$_{0.9}$Nb$_{0.1}$ sample. The interdiffusion of Ti in TiN/NbN single crystals is well-known, and it can be assumed that the decrease in the surface concentration of Nb is due to the diffusion of Ti to the surface or Nb into the bulk of the material.[234] For the B/N co-doped TiO$_2$ samples prepared by Liu et al.[224] diffusion of B to the surface of TiO$_2$ was observed, thus reducing the defect formation during nitridation. The opposite trend as observed for the Nb/N co-doped TiO$_2$ might facilitate homogeneous doping of the materials increasing the visible light absorption.

Strategies for improved nitrogen incorporation

The above presented results clearly show that there is a preferential incorporation of nitrogen into the TiO$_2$ lattice depending on the concentration of Nb in the Nb-doped TiO$_2$ materials. The improved nitrogen incorporation is considered to be necessary reduce the defect formation in TiO$_2$ during ammonia treatment by charge compensation, to increase the nitrogen content, and to enhance the visible light response of N-doped TiO$_2$.[226] Thus, the results are in agreement with the theoretical calculations by Yin et al.[229] and the experimental results by Breault et al.[222]. Even though there is no clear indication of charge compensation by Nb in the Nb/N co-doping TiO$_2$ samples resulting in superior photocatalytic properties of the materials with respect to visible light-driven photocatalytic reactions the performance of the Nb/N co-doped Ti$_{0.9}$Nb$_{0.1}$ sample exceeded the performance of N-doped TiO$_2$ sample in the MB degradation test reaction. In the experimental work by Breault et al.[222] the obtained material with high photocatalytic activity was red. A similar color was obtained for the B/N co-doped TiO$_2$ prepared by Liu et al.[224] The materials prepared here are yellowish and tend to get black with increasing Nb content. This is a clear indication for defects at the surface of the material, which are usually considered to act as recombination sites. Therefore, a preparation resulting in a less

defective surface is needed, which can be obtained by ammonia treatments at lower temperatures with lower ammonia concentrations for nitrogen incorporation or post-calcination of the ammonia-treated samples. Preliminary results show that defects can be significantly reduced by post-annealing. Post-treatment at 400 °C for 30 min in static air of the 500 °C ammonia-modified Ti$_{0.9}$Nb$_{0.1}$ and the Ti$_{0.8}$Nb$_{0.2}$ samples showed that the color changes to a bright yellow, which is indicative for a less defective surface. First XPS results indicate that mainly the surface concentration of the substitutional N$_s$ species decreased, whereas the interstitial N$_i$ was nearly unchanged after post-treatment (Fig. A23). Similarly, the color of the 700 °C ammonia-modified Ti$_{0.9}$Nb$_{0.1}$ sample changed to brown/red upon post-treatment. The nitrogen content determined by XPS decreased significantly. The substitutional nitrogen N$_s$ was still the main nitrogen species and a new nitrogen species at $\sim$ 402 eV was detected, which is usually attributed to nitrogen adsorbed on surface oxygen sites, instead of interstitial N$_i$ with a binding energy of $\sim$ 400 eV .[235,236] Furthermore, region scans of the Ti 2p and the Nb 3d region showed that only Ti^{4+} as in TiO$_2$ and Nb^{5+} as in Nb$_2$O$_5$ was detected indicating a lower surface defect concentration. XRD measurements showed that a composite of the nitride and the oxide was obtained after calcination, and it is reasonable to assume that the surface mainly consists of the oxide and nitride is still present in the bulk of the material. Thus, post-treatment appears to be a suitable method to enhance the photocatalytic activity of Nb/N co-doped TiO$_2$. Again, it should be emphasized that the Nb to N-ratio is of major importance.

6.3.3 Conclusions and Outlook

First studies of the photocatalytic properties of Nb-doped and Nb/N co-doped TiO$_2$ were performed. While the optimum Nb concentration for effective MB degradation was determined to be 5 at%, it was shown using the anionic MO dye that adsorption of the cationic MB on the surface is crucial for the beneficial degradation rates. Therefore, it is emphasized that the total organic carbon content (TOC) should always be determined to verify the activity data obtained by simple dye degradation test reactions. Although the photocatalytic activities determined for the Nb/N co-doped TiO$_2$ materials were small compared to the untreated Nb-doped TiO$_2$ samples a correlation between the Nb and the N content incorporated into TiO$_2$ was observed. The results show that there is a certain potential of metal/anion co-doping of TiO$_2$, and particularly for Nb/N co-doping, to increase the visible light activity of TiO$_2$-based materials.

7 Summary and Prospects

It is well known that the activity of a photocatalyst is determined by a variety of properties, and it is assumed that a photocatalyst has to be designed for each specific reaction. TiO_2 was shown to be one of the most versatile photocatalysts suffering mainly from its large band gap. A variety of TiO_2 materials with different structures and numerous modifications were already tested, but till now the processes involved in photocatalytic reactions are not fully understood and a knowledge-based approach to design a photocatalytically active material is still missing. This is particularly true for rather challenging photocatalytic reactions such as the overall water splitting or the photocatalytic CO_2 reduction with water as reducing agent involving the thermodynamic stable molecules CO_2 and H_2O. In both reactions energy is absorbed by the reactants and energy-rich molecules, like hydrogen and methane, are obtained. A successful implementation of this technology is of major importance for the future energy supply. However, a photocatalyst has to be developed working on an industrial scale. So far the number of active photocatalysts, especially for photocatalytic CO_2 reduction, is rather limited. However, titania-based materials were proven to exhibit a reasonable activity for the photocatalytic reduction of CO_2. Among the different titania materials tested isolated tetrahedrally coordinated Ti-sites were reported to offer high activities and significant selectivity towards methanol, whereas methane production is favored at the octahedral coordinated Ti-sites mainly present in bulk TiO_2 materials. The specific interaction of the reactants with the photocatalyst, particularly the interaction of CO_2 with isolated titania, is not fully understood and the intermediates involved in the photocatalytic CO_2 reduction mechanism, either on tetrahedral or on octahedral Ti-sites, are still not known. Therefore, several species are discussed to be possible intermediates in CO_2 reduction and responsible for the product distributions. Regardless of the coordination of the Ti-site, all materials have in common that their photocatalytic activities are still not sufficient. Among others this is normally attributed to the inherent poor light absorption properties of titania. In case of photocatalysts with isolated titania the low achievable loadings of isolated titania are discussed to be responsible for the low activities and additionally it is speculated that the adsorption of CO_2 in close proximity to the active titania site will enhance the activity of the photocatalyst.

Several questions are raised by the results presented in literature, namely:

1. What is the active site in titania-based photocatalysts in the photocatalytic reduction of CO_2?

2. How to correlate titania coordination and activity?

3. Are the reactants interacting with the photocatalyst, e.g. is there any specific interaction between isolated Ti-sites and CO_2?

4. How to increase the photocatalytic activity for CO_2 reduction of titania-based photocatalysts?

Addressing these questions was the main scope of this work. In chapter 5 the received results are presented, which can be summarized as follows: In the first part of chapter 5 the photocatalyst was synthesized. A synthesis procedure was chosen facilitating the selective synthesis of differently coordinated titania in a host material. SBA-15, a mesoporous silica, was used as support material, since SBA-15 can be easily synthesized and high surfaces areas can be obtained reproducibly. The incorporation of titania was achieved by the anhydrous grafting of $Ti(O^iPr)_4$. The suitability of the applied synthesis procedure with respect to the titania loading and the titania coordination was verified by in-depth characterization of the materials by UV-Vis spectroscopy and X-ray spectroscopic methods (XAS, XPS). It was unambiguously confirmed that isolated titania can be obtained with reasonably high titania loadings and that the titania coordination can be easily controlled by the applied synthesis procedure. With increasing titania loading the coordination gradually changed from isolated tetrahedrally to octahedrally coordinated titania species. Therefore, titania incorporated in a mesoporous matrix (Ti/SBA-15) is a suitable model catalyst to study the photocatalytic CO_2 reduction, and a valuable pool of catalysts with varying titania coordination was readily available. Simultaneously, the interaction of the materials with CO_2 was studied by means of temperature-programmed desorption experiments and infrared spectroscopy. It was proven by means of the direct, quantitative temperature-programmed desorption technique that isolated titania is not able to adsorb CO_2 at standard conditions usually applied in CO_2 reduction. These results were clearly confirmed by IR spectroscopy. Even though the adsorption of CO_2 was found to be negligible, the Ti/SBA-15 materials were shown to exhibit reasonable photocatalytic activities in different test reactions, and in case of solely isolated titania species the activity for the photocatalytic CO_2 reduction was demonstrated (Chapter 5.2). Within the photocatalytic CO_2 reduction tests formaldehyde/paraformaldehyde were found to be potential reaction intermediates of the CO_2 reduction. Furthermore, structure-activity relationships were confirmed for the Ti/SBA-15 materials with varying titania coordination (Chapter 5.3). The photocatalytic activity data presented in Chapter 5.3 obtained for the photoreforming of methanol and the photocatalytic hydroxylation of terephthalic acid confirmed that there is a correlation of the titania coordination and the activity of the photocatalyst (at least in presence of Au co-catalysts).

Two strategies were subsequently developed to increase the activity of Ti/SBA-15: the modification of Ti/SBA-15 with a material known to exhibit an amphoteric nature of the surface to increase the CO_2 adsorption properties, and the incorporation of a noble metal co-catalyst. Zinc oxide was chosen, which is known to facilitate the adsorption of different carbonates and

bicarbonates. Moreover, ZnO was chosen as it is a common active ingredient of the methanol synthesis catalyst and it is a photocatalyst by itself. Similarly, to the synthesis of titania species the incorporation of ZnO was also achieved by anhydrous grafting. The characterization routine developed to study the titania coordination was also employed to study the zinc oxide species incorporated into the mesoporous support. Zinc oxide was concluded to be present as an isolated species or as small clusters in SBA-15. The beneficial CO_2 adsorption properties of the prepared Zn/SBA-15 materials were demonstrated by TPD and IR spectroscopy. The CO_2 adsorption capacity can be easily correlated to the ZnO loading (Chapter 5.1). Combinations of zinc oxide and titania-modified SBA-15 were synthesized by subsequent anhydrous grafting of the two compounds. While the CO_2 adsorption properties of the obtained materials were shown to be nearly unchanged by the order of the grafting steps it was found that the titania precursor preferably interacts with zinc oxide species, whereas the zinc precursor favors the interaction with the SBA-15 support (Chapter 5.1). As a result of the preferential interactions of the two precursors it can be concluded that the titania environment is different for the subsequently grafted samples resulting in different photocatalytic activities of the materials especially for the photocatalytic hydroxylation of terephthalic acid, which is discussed in detail in Chapter 5.3. Activities similar to Ti/SAB-15 were observed when titania was grafted first, whereas the interaction of the titania precursor with the zinc oxide species was found to be unfavorable.

Another attempt to increase the photocatalytic activity was based on the incorporation of gold nanoparticles. Gold nanoparticles were incorporated by photo-deposition. It was confirmed that the photocatalytic activity of solely isolated titania species towards the reduction of CO_2 is enhanced in presence of Au nanoparticles. The higher activity is mainly attributed to an increase in the hydrogenation rate of a CO_2 reduction intermediate. It was shown that less formaldehyde/paraformaldehyde species are present on the Au-modified material, and therefore it is reasonable to assume that the hydrogenation of formaldehyde/paraformaldehyde is favored. Additionally, it was confirmed that Au nanoparticles indeed enhance the photocatalytic activity, e.g. for the hydrogen production due to photoreforming of methanol or the hydroxylation of terephthalic acid of the Ti/SBA-15 samples independent of the titania coordination. However, the photocatalysis data obtained for these test reactions showed that upon zinc oxide modification of the materials the photocatalytic activity towards the photoreforming of methanol was negligible, even though the activity towards terephthalic acid hydroxylation resembles the activity of the unmodified titania samples. Yet, this phenomena is not fully understood. Transmission electron microscopy showed that larger Au particles are deposited on the outer surface of the Ti/SBA-15 materials, whereas small particles are deposited in the pores of the materials containing zinc oxide. Furthermore, titania species in close proximity to the Au particles appear to be agglomerated pointing to a high mobility of titania species in Ti/SBA-15. In contrast to these results the distribution of titania is homogeneously and the mobility of the titania species in presence of zinc oxide appears to be lower. So far it can only be speculated that larger agglomerates of titania and Au are required to produce hydrogen due to the pho-

toreforming of methanol. Small Au particles close to titania sites are sufficient to drive the hydroxylation reaction.

In summary, the results presented in Chapter 5 provide clear evidence that the employed strategy, e.g. using Ti/SBA-15 materials obtained by anhydrous grafting as model catalyst, is suitable to study the photocatalytic activity of titania-based materials for the reduction of CO_2. Furthermore, it was shown that the titania coordination can be selectively modified, and thus the Ti/SBA-15 materials are also suitable to study the effect of the titania coordination in great detail. Reasonable attempts were already made to increase the inherent low photocatalytic activities of titania-based photocatalysts, e.g. by the incorporation of gold nanoparticles as cocatalyst and zinc oxide species. Latter act as a CO_2 adsorption site, which might be beneficial for the activity in the photocatalytic CO_2 reduction. While several key questions were answered within the framework of this dissertation further studies are needed to unambiguously confirm the structure-activity relationships observed for the Ti/SBA-15 materials in the photoreforming of methanol and the hydroxylation of terephthalic acid as well as for the CO_2 reduction. Additionally, the presence of CO_2 adsorption sites, e.g. zinc oxide, was not yet proven to be beneficial for the CO_2 reduction.

In addition to these two complementary studies there are interesting approaches to increase the activities of titania-related photocatalysts for CO_2 reduction, which should be considered in further research. First, it should be mentioned that in further studies other transition metals can be used to modify the Ti/SBA-15 materials. It was already shown that isolated vanadate, copper, molybdate, and chromate species can be obtained by anhydrous grafting. Most of them exhibit beneficial light absorption properties compared with the titania and zinc oxide species used in this study. Zinc oxide was mainly used due to the amphoteric character of zinc oxide surfaces. Copper surfaces are also known to adsorb CO_2 and additionally it is known to be active in the electrochemical conversion of CO_2. Furthermore, isolated copper and molybdate species were already shown to possess photocatalytic activities in test reactions like CO oxidation or decomposition of NO.[61] Second, the support for isolated titania sites can be modified. The support used within this study to synthesize isolated titania species is known to be inert in photocatalysis. Therefore, photo-excitation of an electron can only be achieved in the titania species. For isolated titania the number of photo-excited electrons is additionally limited by the number of isolated Ti-sites as only one electron can be excited for each isolated titania site. The combination of a photocatalytically active support, e.g. ZnO or TiO_2, modified with isolated titania sites may be beneficial for the photocatalytic CO_2 reduction properties. For ZnO and TiO_2 it is reported that oxygen evolution from water splitting is feasible increasing the number of protons available for the CO_2 reduction proceeding at the isolated titania site. In this sense the material might work as a bifunctional catalyst. Even though it was already shown that tetrahedrally coordinated titania can be obtained at the surface of TiO_2 by iron doping,[237] it is reasonable to assume that the modification of TiO_2 with isolated Ti-sites by post-treatment will be difficult as an octahedral titania coordination should be favored. A possible disadvantage

of ZnO as support material was already demonstrated by the results obtained within this study. It was shown that isolated Ti-sites in a Zn-O-Ti environment exhibit only negligible photocatalytic activities compared to Ti-sites in Ti-O-Si environments. These problems of ZnO or TiO_2 supports might be addressed by passivation of the surfaces by a thin silica coating, which will favor the formation of isolated Ti-sites as observed for the Ti/SBA-15 materials. Moreover, it was recently calculated that SiO_2 passivation may be beneficial for the photocatalytic properties of TiO_2 materials. [238]

In addition to the studies directly related to the photocatalytic CO_2 reduction a novel synthesis method for the preparation of pristine and doped TiO_2 was developed. A homogeneous distribution of a substitutional atom within the lattice structure of a host is of high relevance and a successful doping can only be achieved when partial enrichment can be avoided. The spray-drying technique used to dope TiO_2 with Nb was shown to be a suitable technique to achieve a homogeneous doping of the TiO_2 lattice. This was confirmed by different characterization techniques in Chapter 6.1. Later on it was additionally shown that Nb-doped TiO_2 can be effectively used in a photoelectrochemical cell (Chapter 6.2). It was concluded that an enhanced mobility of electrons in the Nb-doped samples allows for higher efficiencies in the devices. The properties of the Nb-doped TiO_2 were maintained even upon post-treatment with urea and higher efficiencies compared to the pristine urea-modified TiO_2 were achieved. Finally, first attempts have been made to co-dope the Nb-doped TiO_2 materials by ammonia, and interestingly a preferential incorporation of nitrogen in the TiO_2 lattice with increasing Nb content was confirmed. However, the photocatalytic activity of these materials was negligible compared with the pristine and the Nb-doped TiO_2. Therefore, the obtained results prove that the nitrogen incorporation into the Nb-doped TiO_2 has to be optimized. Most likely, the ammonia treatment temperature, the ammonia treatment time, or the pretreatment have to be modified to achieve photocatalytically active Nb/N co-doped TiO_2 materials. Additionally, calcination of the spray dried precursor powders in pure nitrogen might be useful to obtain photocatalytically active Nb/N co-doped TiO_2 materials, which then may also be suitable substrates for the modification with isolated titania sites as discussed above.

Bibliography

[1] Fujishima, A.; Honda, K. *Nature* **1972**, *238*, 37–38.

[2] Frank, S. N.; Bard, A. J. *J. Phys. Chem.* **1977**, *81*, 1484–1488.

[3] Fujihira, M.; Satoh, Y.; Osa, T. *Nature* **1981**, *293*, 206–208.

[4] Balzani, V. *Electron Transfer in Chemistry*; Wiley-VCH Verlag GmbH: Weinheim, Germany, 2001.

[5] Inoue, T.; Fujishima, A.; Konishi, S.; Honda, K. *Nature* **1979**, *277*, 637–638.

[6] Braslavsky, S. E. *Pure Appl. Chem.* **2007**, *79*, 293–465.

[7] Gray, H. B. *Nature Chemistry* **2009**, *1*, 7.

[8] Dahl, S.; Chorkendorff, I. *Nature Materials* **2012**, *11*, 100–101.

[9] Kruger, P. *Int. J. Hydrogen Energy* **2001**, *26*, 1137–1147.

[10] Kočí, K.; Obalová, L.; Lacný, Z. *Chemical Papers* **2008**, *62*, 1–9.

[11] Grätzel, M. *Nature* **2001**, *414*, 338–344.

[12] Xu, X.; Moulijn, J. A. *Energy & Fuels* **1996**, *10*, 305–325.

[13] Lewis, N. S.; Nocera, D. G. *Proc. Natl. Acad. Sci.* **2006**, *103*, 15729–15735.

[14] Dhakshinamoorthy, A.; Navalon, S.; Corma, A.; Garcia, H. *Energy Environ. Sci.* **2012**, *5*, 9217–9233.

[15] Freund, H.-J.; Roberts, M. *Surf. Sci. Rep.* **1996**, *25*, 225–273.

[16] Choi, S.; Drese, J. H.; Jones, C. W. *ChemSusChem* **2009**, *2*, 796–854.

[17] Roy, S. C.; Varghese, O. K.; Paulose, M.; Grimes, C. A. *ACS Nano* **2010**, *4*, 1259–1278.

[18] Linsebigler, A. L.; Lu, G.; Yates, J. T. *Chem. Rev.* **1995**, *95*, 735–758.

[19] Nowotny, M. K.; Sheppard, L. R.; Bak, T.; Nowotny, J. *J. Phys. Chem. C* **2008**, *112*, 5275–5300.

[20] Hoffmann, M. R.; Martin, S. T.; Choi, W.; Bahnemann, D. W. *Chem. Rev.* **1995**, *95*, 69–96.

[21] Mori, K.; Yamashita, H.; Anpo, M. *RSC Adv.* **2012**, *2*, 3165.

[22] Sze, S. M. *Physics of semiconductor devices*, 2nd ed.; Wiley: New York, 1981.

[23] Kasap, S. O. *Principles of electronic materials and devices*, 3rd ed.; McGraw-Hill: Boston, 2006.

[24] Thomas, J. M.; Thomas, W. J. *Principles and practice of heterogeneous catalysis*; VCH: Weinheim and , New York, 1997.

[25] Ohtani, B. *J. Photochem. Photobiol., C* **2010**, *11*, 157–178.

[26] B. Kaiser, W. J. S. F.; Lewerenz, H.-J. *Bunsen-Magazin* **2011**, *13*, 104–111.

[27] Gates, B. C.; Knözinger, H.; Jentoft, F. *Advances in catalysis*; Academic: London, 2009.

[28] Delannay, F. *Characterization of heterogeneous catalysts*; M. Dekker: New York, 1984.

[29] Park, H.; Park, Y.; Kim, W.; Choi, W. *J. Photochem. Photobiol., C* **2012**.

[30] Kudo, A.; Miseki, Y. *Chem. Soc. Rev.* **2009**, *38*, 253–278.

[31] Osterloh, F. E. *Chem. Mater.* **2008**, *20*, 35–54.

[32] Dozzi, M. V.; Selli, E. *J. Photochem. Photobiol., C* **2012**.

[33] Maeda, K.; Domen, K. *Chem. Mater.* **2010**, *22*, 612–623.

[34] Maeda, K.; Higashi, M.; Lu, D.; Abe, R.; Domen, K. *J. Am. Chem. Soc.* **2010**, *132*, 5858–5868.

[35] Maeda, K.; Takata, T.; Hara, M.; Saito, N.; Inoue, Y.; Kobayashi, H.; Domen, K. *J. Am. Chem. Soc.* **2005**, *127*, 8286–8287.

[36] Maeda, K. *J. Photochem. Photobiol., C* **2011**, *12*, 237–268.

[37] Primo, A.; Corma, A.; García, H. *Phys. Chem. Chem. Phys.* **2010**, *13*, 886.

[38] Murdoch, M.; Waterhouse, G. I. N.; Nadeem, M. A.; Metson, J. B.; Keane, M. A.; Howe, R. F.; Llorca, J.; Idriss, H. *Nature Chemistry* **2011**, 489–492.

[39] Du, L.; Furube, A.; Hara, K.; Katoh, R.; Tachiya, M. *J. Photochem. Photobiol., C* **2012**.

[40] Wang, P.; Huang, B.; Dai, Y.; Whangbo, M.-H. *Phys. Chem. Chem. Phys.* **2012**, *14*, 9813.

[41] Chiarello, G. L.; Aguirre, M. H.; Selli, E. *J. Catal.* **2010**, *273*, 182–190.

[42] Kamat, P. V. *J. Phys. Chem. B* **2002**, *106*, 7729–7744.

[43] Zhang, Z.; Yates, J. T. *Chem. Rev.* **2012**, *112*, 5520–5551.

[44] Wiberg, E.; Wiberg, N. *Lehrbuch der anorganischen Chemie*, 101st ed.; Walter de Gruyter: Berlin, 1995.

[45] Glassford, K.; Chelikowsky, J. *Phys. Rev. B* **1992**, *46*, 1284–1298.

[46] Chang, H.; Huang, P. J. *J. Raman Spectrosc.* **1998**, *29*, 97–102.

[47] Ohsaka, T.; Izumi, F.; Fujiki, Y. *J. Raman Spectrosc.* **1978**, *7*, 321–324.

[48] Kelly, S.; Pollak, F. H.; Tomkiewicz, M. *J. Phys. Chem. B* **1997**, *101*, 2730–2734.

[49] Zhang, J.; Li, M.; Feng, Z.; Chen, J.; Li, C. *J. Phys. Chem. B* **2006**, *110*, 927–935.

[50] Zhang, Z.; Jeng, S.-P.; Henrich, V. *Phys. Rev. B* **1991**, *43*, 12004–12011.

[51] Müller, U. *Anorganische Strukturchemie*, 5th ed.; Teubner: Wiesbaden, 2006.

[52] Grätzel, M. *J. Photochem. Photobiol., C* **2003**, *4*, 145–153.

[53] Bledowski, M.; Wang, L.; Ramakrishnan, A.; Khavryuchenko, O. V.; Khavryuchenko, V. D.; Ricci, P. C.; Strunk, J.; Cremer, T.; Kolbeck, C.; Beranek, R. *Phys. Chem. Chem. Phys.* **2011**, *13*, 21511.

[54] Bledowski, M.; Wang, L.; Ramakrishnan, A.; Bétard, A.; Khavryuchenko, O. V.; Beranek, R. *ChemPhysChem* **2012**, *13*, 3018.

[55] D'Arienzo, M.; Siedl, N.; Sternig, A.; Scotti, R.; Morazzoni, F.; Bernardi, J.; Diwald, O. *J. Phys. Chem. C* **2010**, *114*, 18067–18072.

[56] Chen, X.; Liu, L.; Yu, P. Y.; Mao, S. S. *Science* **2011**, *331*, 746–750.

[57] Hamdy, M. S.; Amrollahi, R.; Mul, G. *ACS Catal.* **2012**, 2641–2647.

[58] Anpo, M.; Chiba, K. *J. Mol. Catal.* **1992**, *74*, 207–212.

[59] Thomas, J. M.; Raja, R.; Lewis, D. W. *Angew. Chem. Int. Ed.* **2005**, *44*, 6456–6482.

[60] Maschmeyer, T.; Rey, F.; Sankar, G.; Thomas, J. M. *Nature* **1995**, *378*, 159–162.

[61] Anpo, M.; Thomas, J. M. *Chem. Comm.* **2006**, 3273.

[62] Amano, F.; Yamaguchi, T.; Tanaka, T. *J. Phys. Chem. B* **2006**, *110*, 281–288.

[63] Lee, E.; Wachs, I. *J. Phys. Chem. C* **2007**, *111*, 14410–14425.

[64] Gao, X.; Wachs, I. E. *Catal. Today* **1999**, *51*, 233–254.

[65] Ross-Medgaarden, E. I.; Wachs, I. E.; Knowles, W. V.; Burrows, A.; Kiely, C. J.; Wong, M. S. *J. Am. Chem. Soc.* **2009**, *131*, 680–687.

[66] Morris, A. J.; Meyer, G. J.; Fujita, E. *Acc. Chem. Res.* **2009**, *42*, 1983–1994.

[67] Anpo, M.; Yamashita, H.; Ichihashi, Y.; Ehara, S. *J. Electroanal. Chem.* **1995**, *396*, 21–26.

[68] Anpo, M.; Yamashita, H.; Ichihashi, Y.; Fujii, Y.; Honda, M. *J. Phys. Chem. B* **1997**, *101*, 2632–2636.

[69] Dimitrijevic, N. M.; Vijayan, B. K.; Poluektov, O. G.; Rajh, T.; Gray, K. A.; He, H.; Zapol, P. *J. Am. Chem. Soc.* **2011**, *133*, 3964–3971.

[70] Ikeue, K.; Yamashita, H.; Anpo, M.; Takewaki, T. *J. Phys. Chem. B* **2001**, *105*, 8350–8355.

[71] Lin, W.; Han, H.; Frei, H. *J. Phys. Chem. B* **2004**, *108*, 18269–18273.

[72] Ulagappan, N.; Frei, H. *J. Phys. Chem. A* **2000**, *104*, 7834–7839.

[73] Yang, C.-C.; Vernimmen, J.; Meynen, V.; Cool, P.; Mul, G. *J. Catal.* **2011**, *284*, 1–8.

[74] Danon, A.; Stair, P. C.; Weitz, E. *Catal. Lett.* **2011**, *141*, 1057–1066.

[75] Lee, D.; Kanai, Y. *J. Am. Chem. Soc.* **2012**, *134*, 20266–20269.

[76] Shkrob, I. A.; Marin, T. W.; He, H.; Zapol, P. *J. Phys. Chem. C* **2012**, *116*, 9450–9460.

[77] Dimitrijevic, N. M.; Shkrob, I. A.; Gosztola, D. J.; Rajh, T. *J. Phys. Chem. C* **2012**, *116*, 878–885.

[78] Sastre, F.; Corma, A.; García, H. *J. Am. Chem. Soc.* **2012**, *134*, 14137–14141.

[79] Varghese, O. K.; Paulose, M.; LaTempa, T. J.; Grimes, C. A. *Nano Lett.* **2009**, *9*, 731–737.

[80] Gao, X.; Bare, S. R.; Fierro, J. L. G.; Banares, M. A.; Wachs, I. E. *J. Phys. Chem. B* **1998**, *102*, 5653–5666.

[81] Ricchiardi, G.; Damin, A.; Bordiga, S.; Lamberti, C.; Spanò, G.; Rivetti, F.; Zecchina, A. *J. Am. Chem. Soc.* **2001**, *123*, 11409–11419.

[82] Sheldon, R. *J. Mol. Catal.* **1980**, *7*, 107–126.

[83] Sinha, A. K.; Seelan, S.; Tsubota, S.; Haruta, M. *Angew. Chem. Int. Ed.* **2004**, *43*, 1546–1548.

[84] Brub, F.; Nohair, B.; Kleitz, F.; Kaliaguine, S. *Chem. Mater.* **2010**, *22*, 1988–2000.

[85] Bronkema, J.; Leo, D.; Bell, A. *J. Phys. Chem. C* **2007**, *111*, 14530–14540.

[86] Yang, H.-C.; Lin, H.-Y.; Chien, Y.-S.; Wu, J. C.-S.; Wu, H.-H. *Catal. Lett.* **2009**, *131*, 381–387.

[87] Xia, W.; Mei, B.; Sánchez, M. D.; Strunk, J.; Muhler, M. *J. Nanosci. Nanotechnol.* **2011**, *11*, 8152–8157.

[88] Perathoner, S.; Lanzafame, P.; Passalacqua, R.; Centi, G.; Schlögl, R.; Su, D. *Micropor. Mesopor. Mater.* **2006**, *90*, 347–361.

[89] Strunk, J.; Vining, W. C.; Bell, A. T. *J. Phys. Chem. C* **2010**, *114*, 16937–16945.

[90] Yamashita, H.; Honda, M.; Harada, M.; Ichihashi, Y.; Anpo, M.; Hirao, T.; Itoh, N.; Iwamoto, N. *J. Phys. Chem. B* **1998**, *102*, 10707–10711.

[91] Auroux, A.; Gervasini, A. *J. Phys. Chem.* **1990**, *94*, 6371–6379.

[92] Iengo, P.; Aprile, G.; Di Serio, M.; Gazzoli, D.; Santacesaria, E. *Appl. Catal. A: General* **1999**, *178*, 97–109.

[93] Srivastava, R.; Srinivas, D.; Ratnasamy, P. *Micropor. Mesopor. Mater.* **2006**, *90*, 314–326.

[94] Shi, L. Y.; Wang, Y. M.; Ji, A.; Gao, L.; Wang, Y. *J. Mater. Chem.* **2005**, *15*, 1392.

[95] Young, P. D.; Notestein, J. M. *ChemSusChem* **2011**, *4*, 1671–1678.

[96] Lavalley, J.; Saussey, J.; Raïs, T. *J. Mol. Catal.* **1982**, *17*, 289–298.

[97] Xia, X.; Strunk, J.; Busser, W.; Naumann d'Alnoncourt, R.; Muhler, M. *J. Phys. Chem. C* **2008**, *112*, 10938–10942.

[98] Noei, H.; Wöll, C.; Muhler, M.; Wang, Y. *J. Phys. Chem. C* **2011**, *115*, 908–914.

[99] Kurtz, M.; Strunk, J.; Hinrichsen, O.; Muhler, M.; Fink, K.; Meyer, B.; Wöll, C. *Angew. Chem. Int. Ed.* **2005**, *44*, 2790–2794.

[100] Fox, M. A.; Dulay, M. T. *Chem. Rev.* **1993**, *93*, 341–357.

[101] Chen, J.; Feng, Z.; Ying, P.; Li, C. *J. Phys. Chem. B* **2004**, *108*, 12669–12676.

[102] Tkachenko, O. P.; Klementiev, K. V.; Löffler, E.; Ritzkopf, I.; Schüth, F.; Bandyopadhyay, M.; Grabowski, S.; Gies, H.; Hagen, V.; Muhler, M.; Lu, L.; Fischer, R. A.; Grünert, W. *Phys. Chem. Chem. Phy.* **2003**, *5*, 4325.

[103] Mihai, G. D.; Meynen, V.; Mertens, M.; Bilba, N.; Cool, P.; Vansant, E. F. *J. Mater. Sci.* **2010**, *45*, 5786–5794.

[104] Almutairi, S. M. T.; Mezari, B.; Magusin, P. C. M. M.; Pidko, E. A.; Hensen, E. J. M. *ACS Catal.* **2011**, 71–83.

[105] Zhao, D.; Huo, Q.; Feng, J.; Chmelka, B. F.; Stucky, G. D. *J. Amer. Chem. Soc.* **1998**, *120*, 6024–6036.

[106] Vining, W. C.; Goodrow, A.; Strunk, J.; Bell, A. T. *J. Catal.* **2010**, *270*, 163–171.

[107] Brunauer, S.; Emmett, P. H.; Teller, E. *J. Am. Chem. Soc.* **1938**, *60*, 309–319.

[108] Barrett, E. P.; Joyner, L. G.; Halenda, P. P. *J. Am. Chem. Soc.* **1951**, *73*, 373–380.

[109] Lippens, B. C.; Boer, J. H. d. *J. Catal.* **1965**, *4*, 319–323.

[110] Moulder, J. F.; Chastain, J. *Handbook of X-ray photoelectron spectroscopy: A reference book of standard spectra for identification and interpretation of XPS data*, update. ed.; Perkin-Elmer Corporation: Eden Prairie, Minn, 1992.

[111] Wang, Y.; Glenz, A.; Muhler, M.; Wöll, C. *Rev. Sci. Instrum.* **2009**, *80*, 113108.

[112] Klementev, K. V. *J. Phys. D: Appl. Phys.* **2001**, *34*, 209–217.

[113] Bouh, A. O.; Rice, G. L.; Scott, S. L. *J. Am. Chem. Soc.* **1999**, *121*, 7201–7210.

[114] Joo, S. H.; Ryoo, R.; Kruk, M.; Jaroniec, M. *J. Phys. Chem. B* **2002**, *106*, 4640–4646.

[115] Ryoo, R.; Ko, C. H.; Kruk, M.; Antochshuk, V.; Jaroniec, M. *J. Phys. Chem. B* **2000**, *104*, 11465–11471.

[116] Strunk, J.; Vining, W. C.; Bell, A. T. *J. Phys. Chem. C* **2011**, *115*, 4114–4126.

[117] Bérubé, F.; Kleitz, F.; Kaliaguine, S. *J. Mater. Sci.* **2009**, *44*, 6727–6735.

[118] Yamashita, H.; Kawasaki, S.; Ichihashi, Y.; Harada, M.; Takeuchi, M.; Anpo, M.; Stewart, G.; Fox, M. A.; Louis, C.; Che, M. *J. Phys. Chem. B* **1998**, *102*, 5870–5875.

[119] Chen, J.; Feng, Z.; Ying, P.; Li, M.; Han, B.; Li, C. *Phys. Chem. Chem. Phys.* **2004**, *6*, 4473.

[120] Grünert, W.; Schlögel, R. *Mol. Sieves*, *2004*, 467.

[121] Vayssilov, G. N. *Catal. Rev.* **1997**, *39*, 209–251.

[122] Stakheev, A. Y.; Shpiro, E. S.; Apijok, J. *J. Phys. Chem.* **1993**, *97*, 5668–5672.

[123] Farges, F.; Brown, G.; Rehr, J. *Phys. Rev. B* **1997**, *56*, 1809–1819.

[124] Saussey, J.; Lavalley, J.-C.; Bovet, C. *J. Chem. Soc., Faraday Trans.* **1982**, *78*, 1457.

[125] Danon, A.; Stair, P. C.; Weitz, E. *J. Phys. Chem. C* **2011**, *115*, 11540–11549.

[126] Srivastava, R.; Srinivas, D.; Ratnasamy, P. *J. Catal.* **2005**, *233*, 1–15.

[127] Srinivas, D.; Ratnasamy, P. *Micropor. Mesopor. Mater.* **2007**, *105*, 170–180.

[128] Esken, D.; Noei, H.; Wang, Y.; Wiktor, C.; Turner, S.; van Tendeloo, G.; Fischer, R. A. *J. Mater. Chem.* **2011**, *21*, 5907.

[129] Hoffmann, M. R.; Moss, J. A.; Baum, M. M. *Dalton Trans.* **2011**, *40*, 5151.

[130] Hwang, J.-S.; Chang, J.-S.; Park, S.-E.; Ikeue, K.; Anpo, M. *Top. Catal.* **2005**, *35*, 311–319.

[131] Fuku, K.; Sakano, T.; Kamegawa, T.; Mori, K.; Yamashita, H. *J. Mater. Chem.* **2012**.

[132] Mori, K.; Miura, Y.; Shironita, S.; Yamashita, H. *Langmuir* **2009**, *25*, 11180–11187.

[133] Busser, G. W.; Mei, B.; Muhler, M. *ChemSusChem* **2012**, *5*, 2200–2206.

[134] Mei, B.; Becerikli, A.; Pougin, A.; Heeskens, D.; Sinev, I.; Grünert, W.; Muhler, M.; Strunk, J. *J. Phys. Chem. C* **2012**, *116*, 14318–14327.

[135] Buso, D.; Pacifico, J.; Martucci, A.; Mulvaney, P. *Adv. Funct. Mater.* **2007**, *17*, 347–354.

[136] Escamilla-Perea, L.; Nava, R.; Pawelec, B.; Rosmaninho, M.; Peza-Ledesma, C.; Fierro, J. *Appl. Catal. A: General* **2010**, *381*, 42–53.

[137] Yang, C.-C.; Yu, Y.-H.; van der Linden, B.; Wu, J. C. S.; Mul, G. *J. Amer. Chem. Soc.* **2010**, *132*, 8398–8406.

[138] Comotti, M.; Li, W.-C.; Spliethoff, B.; Schüth, F. *J. Am. Chem. Soc.* **2006**, *128*, 917–924.

[139] Strunk, J.; Kähler, K.; Xia, X.; Comotti, M.; Schüth, F.; Reinecke, T.; Muhler, M. *Appl. Catal. A: General* **2009**, *359*, 121–128.

[140] Ryndin, Y.; Hicks, R.; Bell, A.; Yermakov, Y. *J. Catal.* **1981**, *70*, 287–297.

[141] Busca, G.; Lamotte, J.; Lavalley, J. C.; Lorenzelli, V. *J. Am. Chem. Soc.* **1987**, *109*, 5197–5202.

[142] McGill, P. R.; Söhnel, T. *Phys. Chem. Chem. Phys.* **2011**, *14*, 858.

[143] Qiu, H.; Idriss, H.; Wang, Y.; Wöll, C. *J. Phys. Chem. C* **2008**, *112*, 9828–9834.

[144] Li, Z.; Zhang, Z.; Kay, B. D.; Dohnlek, Z. *J. Phys. Chem. C* **2011**, *115*, 9692–9700.

[145] Kähler, K.; Holz, M. C.; Rohe, M.; Strunk, J.; Muhler, M. *ChemPhysChem* **2010**, *11*, 2521–2529.

[146] Bond, G. C.; Louis, C.; Thompson, D. T. *Catalysis by gold*; Imperial College Press: London, 2006.

[147] Widmann, D.; Behm, R. J. *Angew. Chem. Int. Ed.* **2011**, *50*, 10241–10245.

[148] Bowker, M.; Millard, L.; Greaves, J.; James, D.; Soares, J. *Gold Bulletin* **2004**, *37*, 170–173.

[149] Du, L.; Furube, A.; Yamamoto, K.; Hara, K.; Katoh, R.; Tachiya, M. *J. Phys. Chem. C* **2009**, *113*, 6454–6462.

[150] Hirakawa, T.; Nosaka, Y. *Langmuir* **2002**, *18*, 3247–3254.

[151] Fang, X.; Mark, G.; Sonntag, C. *Ultrason. Sonochem.* **1996**, *3*, 57–63.

[152] Liu, G.; Wang, L.; Sun, C.; Yan, X.; Wang, X.; Chen, Z.; Smith, S. C.; Cheng, H.-M.; Lu, G. Q. *Chem. Mater.* **2009**, *21*, 1266–1274.

[153] Matsuoka, M.; Kitano, M.; Takeuchi, M.; Tsujimaru, K.; Anpo, M.; Thomas, J. M. *Catal. Today* **2007**, *122*, 51–61.

[154] Ang, T. P.; Toh, C. S.; Han, Y.-F. *J. Phys. Chem. C* **2009**, *113*, 10560–10567.

[155] Atashbar, M. Z.; Sun, H. T.; Gong, B.; Wlodarski, W.; Lamb, R. *Thin Solid Films* **1998**, *326*, 238–244.

[156] Yamada, N.; Hitosugi, T.; Hoang, N. L. H.; Furubayashi, Y.; Hirose, Y.; Konuma, S.; Shimada, T.; Hasegawa, T. *Thin Solid Films* **2008**, *516*, 5754–5757.

[157] Park, K.-W.; Seol, K.-S. *Electrochem. Commun.* **2007**, *9*, 2256–2260.

[158] Liu, G.; Wang, L.; Yang, H. G.; Cheng, H. M.; Lu, G. Q. *J. Mater. Chem.* **2010**, *20*, 831–843.

[159] Choi, W.; Termin, A.; Hoffmann, M. R. *J. Phys. Chem.* **1994**, *98*, 13669–13679.

[160] Kazumoto, N.; Takaaki, K.; Naoya, M.; Toshiki, T.; Teruhisa, O. *Int. J. Photoenergy* **2007**, *2008*.

[161] Anpo, M.; Takeuchi, M. *J. Catal.* **2003**, *216*, 505–516.

[162] Kubacka, A.; Fernández-García, M.; Colón, G. *J. Catal.* **2008**, *254*, 272–284.

[163] Kubacka, A.; Colón, G.; Fernandez-García, M. *Catal. Today* **2009**, *143*, 286–292.

[164] Castro, A. L.; Nunes, M. R.; Carvalho, M. D.; Ferreira, L. P.; Jumas, J. C.; Costa, F. M.; Florêncio, M. H. *J. Solid State Chem.* **2009**, *182*, 1838–1845.

[165] Mattsson, A.; Leideborg, M.; Larsson, K.; Westin, G.; Asterlund, L. *J. Phys. Chem. B* **2006**, *110*, 1210–1220.

[166] Emeline, A. V.; Furubayashi, Y.; Zhang, X.; Jin, M.; Murakami, T.; Fujishima, A. *J. Phys. Chem. B* **2005**, *109*, 24441–24444.

[167] Koninck, M.; Manseau, P.; Marsan, B. *J. Electroanal. Chem.* **2007**, *611*, 67–79.

[168] Hasin, P.; Alpuche-Aviles, M. A.; Li, Y.; Wu, Y. *J. Phys. Chem. C* **2009**, *113*, 7456–7460.

[169] Lü, X.; Mou, X.; Wu, J.; Zhang, D.; Zhang, L.; Huang, F.; Xu, F.; Huang, S. *Adv. Funct. Mater.* **2010**, *20*, 509–515.

[170] Yum, J.-H.; Chen, P.; Grätzel, M.; Nazeeruddin, M. K. *ChemSusChem* **2008**, *1*, 699–707.

[171] Pore, V.; Ritala, M.; Leskela, M.; Saukkonen, T.; Jarn, M. *Cryst. Growth Des.* **2009**, *9*, 2974–2978.

[172] Arbiol, J.; Cerda, J.; Dezanneau, G.; Cirera, A.; Peiro, F.; Cornet, A.; Morante *J. Appl. Phys.* **2002**, *92*, 853.

[173] Almquist, C. B.; Biswas, P. *J. Catal.* **2002**, *212*, 145–156.

[174] Morris, D.; Dou, Y.; Rebane, J.; Mitchell, C. E. J.; Egdell, R. G.; Law, D. S. L.; Vittadini, A.; Casarin, M. *Phys. Rev. B* **2000**, *61*, 13445.

[175] Valigi, M.; Cordischi, D.; Minelli, G.; Natale, P.; Porta, P.; Keijzers, C. P. *J. Solid State Chem.* **1988**, *77*, 255–263.

[176] Guoying, C.; Bare, S. R.; Mallouk, T. E. *J. Electrochem. Soc.* **2002**, *149*, A1092–A1099.

[177] Hidalgo, M. C.; Bahnemann, D. *Appl. Catal. B: Environ.* **2005**, *61*, 259–266.

[178] Pan, H.; Chen, N.; Shen, S.; Huang, J. *J. Sol-Gel Sci. Technol.* **2005**, *34*, 63–69.

[179] Tasbihi, M.; Štangar, U. L.; Černigoj, U.; Kogej, K. *Photochem. Photobiol. Sci.* **2009**, *8*, 719–725.

[180] Kaluza, S.; Schröter, M. K.; Naumann d'Alnoncourt, R.; Reinecke, T.; Muhler, M. *Adv. Funct. Mater.* **2008**, *18*, 3670–3677.

[181] Kaluza, S.; Muhler, M. *J. Mater. Chem.* **2009**, *19*, 3914–3922.

[182] Kaluza, S.; Muhler, M. *Catal. Lett.* **2009**, *129*, 287–292.

[183] Sizgek, E.; Bartlett, J. R.; Brungs, M. P. *J. Sol-Gel Sci. Technol.* **1998**, *13*, 1011–1016.

[184] Zhang, X.; Pan, J. H.; Du, A. J.; Ng, J.; Sun, D. D.; Leckie, J. O. *Mater. Res. Bull.* **2009**, *44*, 1070–1076.

[185] F. Iskandar; A. B. D. Nandiyanto; K. M. Yun; C. J. Hogan Jr.; K. Okuyama; P. Biswas *Adv. Mater.* **2007**, *19*, 1408–1412.

[186] Lide, D. R. *CRC handbook of chemistry and physics*, internet version 2005. ed.; CRC Press: Boca Raton, Fla, 2004.

[187] Johnsson, M.; Pettersson, P.; Nygren, M. *Thermochim. Acta* **1997**, *298*, 47–54.

[188] Brnicevic, N.; Despotovic, Z. *Proceedings Third ICTA Davos, HR Oswald, E. Dubler (Hrsg.)* **1971**, *705*.

[189] J. F. Banfield, D. R. V.; Smith, D. J. *Am. Mineral.*, *1991*, 343–353.

[190] Brohan, L.; Verbaere, A.; Tournoux, M.; Demazeau, G. *Mater. Res. Bull.* **1982**, *17*, 355–361.

[191] Hirano, M.; Matsushima, K. *J. Am. Ceram. Soc.* **2006**, *89*, 110–117.

[192] Chandiran, A. K.; Sauvage, F.; Casas-Cabanas, M.; Comte, P.; Zakeeruddin, S. M.; Grätzel, M. *J. Phys. Chem. C* **2010**, *114*, 15849–15856.

[193] Shannon, R. D.; Prewitt, C. T. *Acta Crystall. B: Stru.* **1970**, *26*, 1046–1048.

[194] J. I. Langford *NIST Spec. Publ.*, *1992*, 110–126.

[195] Gao, Y.; Liang, Y.; Chambers, S. A. *Surf. Sci.* **1996**, *348*, 17–27.

[196] Bahl, M. *J. Phys. Chem. Solids* **1975**, *36*, 485–491.

[197] Pittman, R. M.; Bell, A. T. *J. Phys. Chem. C* **1993**, *97*, 12178–12185.

[198] Ruiz, A. M.; Dezanneau, G.; Arbiol, J.; Cornet, A.; Morante, J. R. *Chem. Mater.* **2004**, *16*, 862–871.

[199] Liu, X. D.; Jiang, E. Y.; Li, Z. Q.; Song, Q. G. *Appl. Phys. Lett.* **2008**, *92*, 252104.

[200] Bard, A. J. *Science* **1980**, *207*, 139–144.

[201] Khaselev, O. *Science* **1998**, *280*, 425–427.

[202] Licht, S. *Int. J. Hydrogen Energy* **2001**, *26*, 653–659.

[203] Dau, H.; Limberg, C.; Reier, T.; Risch, M.; Roggan, S.; Strasser, P. *ChemCatChem* **2010**, *2*, 724–761.

[204] Solarska, R.; Królikowska, A.; Augustyński, J. *Angew. Chem. Int. Ed.* **2010**, *49*, 7980–7983.

[205] Vidyarthi, V. S.; Hofmann, M.; Savan, A.; Sliozberg, K.; König, D.; Beranek, R.; Schuhmann, W.; Ludwig, A. *Int. J. Hydrogen Energy* **2011**, *36*, 4724–4731.

[206] Jorand Sartoretti, C.; Alexander, B. D.; Solarska, R.; Rutkowska, I. A.; Augustynski, J.; Cerny, R. *J. Phys. Chem. B* **2005**, *109*, 13685–13692.

[207] Kay, A.; Cesar, I.; Grätzel, M. *J. Am. Chem. Soc.* **2006**, *128*, 15714–15721.

[208] Upul Wijayantha, K.; Saremi-Yarahmadi, S.; Peter, L. M. *Phys. Chem. Chem. Phy.* **2011**, *13*, 5264.

[209] Youngblood, W. J.; Lee, S. H. A.; Maeda, K.; Mallouk, T. E. *Acc. Chem. Res.* **2009**, *42*, 1966–1973.

[210] Moore, G. F.; Blakemore, J. D.; Milot, R. L.; Hull, J. F.; Song, H.; Cai, L.; Schmuttenmaer, C. A.; Crabtree, R. H.; Brudvig, G. W. *Energy Environ. Sci.* **2011**, *4*, 2389.

[211] Swierk, J. R.; Mallouk, T. E. *Chem. Soc. Rev.* **2013**.

[212] Tributsch, H. *J. Solid State Electrochem.* **2009**, *13*, 1127–1140.

[213] Youngblood, W. J.; Lee, S.-H. A.; Kobayashi, Y.; Hernandez-Pagan, E. A.; Hoertz, P. G.; Moore, T. A.; Moore, A. L.; Gust, D.; Mallouk, T. E. *J. Amer. Chem. Soc.* **2009**, *131*, 926–927.

[214] Wang, L.; Bledowski, M.; Ramakrishnan, A.; Konig, D.; Ludwig, A.; Beranek, R. *J. Electrochem. Soc.* **2012**, *159*, H616–H622.

[215] Bledowski, M.; Wang, L.; Ramakrishnan, A.; Beranek, R. *J. Mater. Res.* **2012**, 1–7.

[216] Furubayashi, Y.; Hitosugi, T.; Yamamoto, Y.; Inaba, K.; Kinoda, G.; Hirose, Y.; Shimada, T.; Hasegawa, T. *Appl. Phys. Lett.* **2005**, *86*, 252101.

[217] Liu, Y.; Szeifert, J. M.; Feckl, J. M.; Mandlmeier, B.; Rathousky, J.; Hayden, O.; Fattakhova-Rohlfing, D.; Bein, T. *ACS Nano* **2010**, *4*, 5373–5381.

[218] Yang, M.; Jha, H.; Liu, N.; Schmuki, P. *J. Mater. Chem.* **2011**, *21*, 15205.

[219] Das, C.; Roy, P.; Yang, M.; Jha, H.; Schmuki, P. *Nanoscale* **2011**, *3*, 3094.

[220] Mei, B.; Sánchez, M. D.; Reinecke, T.; Kaluza, S.; Xia, W.; Muhler, M. *J. Mater. Chem.* **2011**, *21*, 11781.

[221] Beranek, R. *Adv. Chem. Phys.* **2011**, *2011*, 1–20.

[222] Breault, T. M.; Bartlett, B. M. *J. Phys. Chem. C* **2012**, *116*, 5986–5994.

[223] Kubacka, A.; Bachiller-Baeza, B.; Colon, G.; FernaÌndez-Garcia, M. *J. Phys. Chem. C* **2009**, *113*, 8553–8555.

[224] Liu, G.; Yin, L.-C.; Wang, J.; Niu, P.; Zhen, C.; Xie, Y.; Cheng, H.-M. *Energy Environ. Sci.* **2012**, *5*, 9603.

[225] Márquez, A. M.; Plata, J. J.; Ortega, Y.; Sanz, J. F.; Colón, G.; Kubacka, A.; Fernández-García, M. *J. Phys. Chem. C* **2012**, *116*, 18759–18767.

[226] Di Valentin, C.; Finazzi, E.; Pacchioni, G.; Selloni, A.; Livraghi, S.; Czoska, A. M.; Paganini, M. C.; Giamello, E. *Chem. Mater.* **2008**, *20*, 3706–3714.

[227] Neville, E. M.; Mattle, M. J.; Loughrey, D.; Rajesh, B.; Rahman, M.; MacElroy, J. D.; Sullivan, J. A.; Thampi, K. R. *J. Phys. Chem. C* **2012**, *116*, 16511–16521.

[228] Katoh, R.; Furube, A.; Yamanaka, K.; Morikawa, T. *J. Phys. Chem. Lett.* **2010**, *1*, 3261–3265.

[229] Yin, W.-J.; Tang, H.; Wei, S.-H.; Al-Jassim, M.; Turner, J.; Yan, Y. *Phys. Rev. B* **2010**, *82*.

[230] Hoang, S.; Guo, S.; Mullins, C. B. *J. Phys. Chem. C* **2012**, *116*, 23283–23290.

[231] Kohtani, S.; Yoshioka, E.; Saito, K.; Kudo, A.; Miyabe, H. *J. Phys. Chem. C* **2012**, *116*, 17705–17713.

[232] Tada, H.; Jin, Q.; Kobayashi, H. *ChemPhysChem* **2012**, *13*, 3457–3461.

[233] Oropeza, F. E.; Harmer, J.; Egdell, R. G.; Palgrave, R. G. *Phys. Chem. Chem. Phys.* **2010**, *12*, 960–969.

[234] Engström, C.; Birch, J.; Hultman, L.; Lavoie, C.; Cabral, C.; Jordan-Sweet, J. L.; Carlsson, J. R. A. *J. Vac. Sci. Technol., A* **1999**, *17*, 2920.

[235] Chen, X.; Wang, X.; Hou, Y.; Huang, J.; Wu, L.; Fu, X. *J. Catal.* **2008**, *255*, 59–67.

[236] Asahi, R. *Science* **2001**, *293*, 269–271.

[237] Wu, Q.; Zheng, Q.; van de Krol, R. *J. Phys. Chem. C* **2012**, *116*, 7219–7226.

[238] Seriani, N.; Pinilla, C.; Cereda, S.; Vita, A. d.; Scandolo, S. *J. Phys. Chem. C* **2012**, *116*, 11062–11067.

8 Appendix

Figures

8.1 Supporting Figures Chapter 4
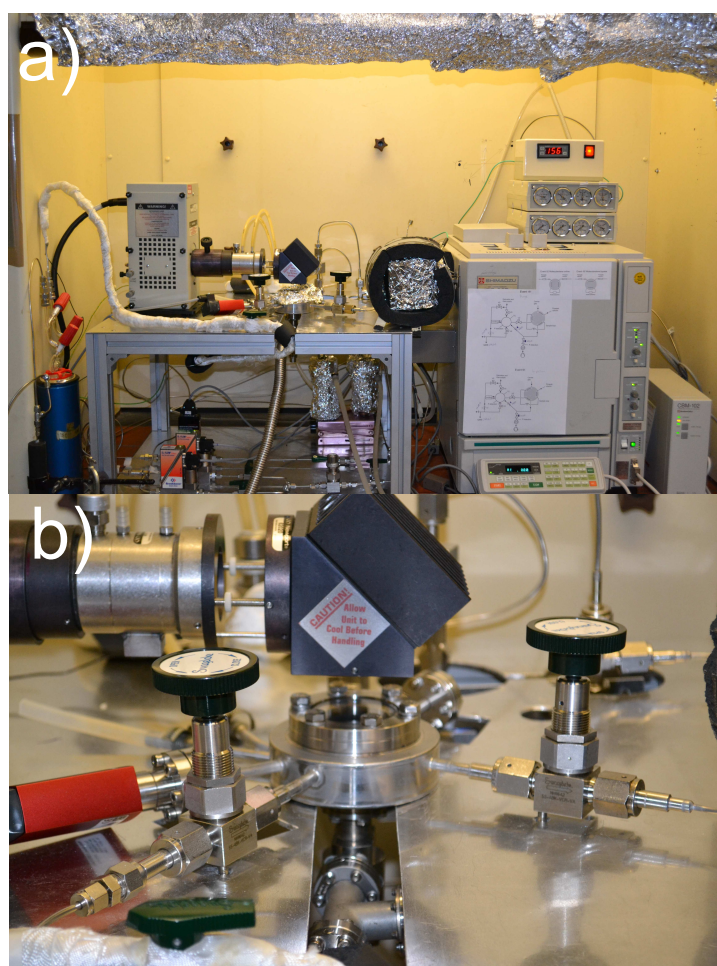
Figure A1: a) Picture of complete photoreactor set-up and b) closeup view of the fully metal sealed home-made photoreactor.

8.2 Supporting Figures Chapter 5
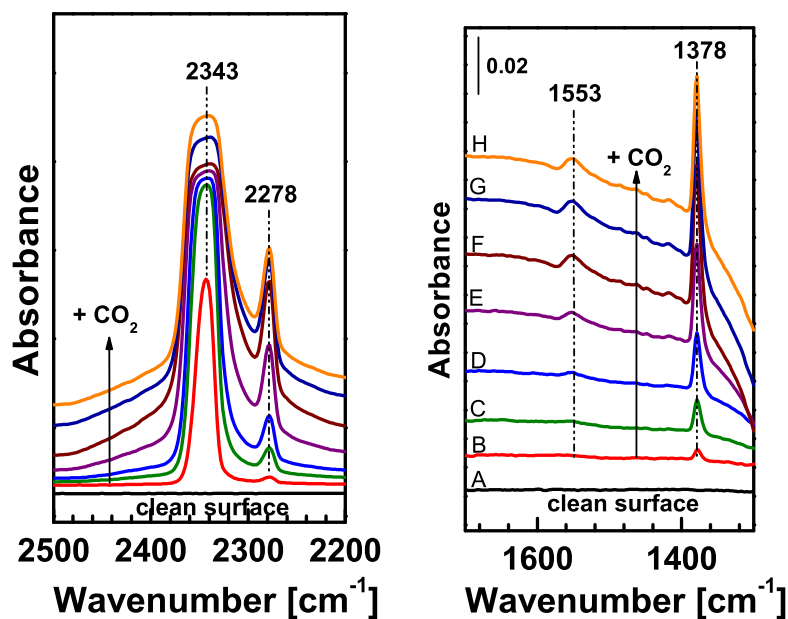
Figure A2: UHV-FTIR spectra obtained after exposing the clean Zn0.7/Ti0.9/SBA-15 sample to CO_2 at 90 K in an UHV chamber. (A) clean surface, (B) $1x10^{-6}$ mbar CO_2, (C) $5x10^{-6}$ mbar CO_2, (D) $1x10^{-5}$ mbar CO_2, (E) $5x10^{-5}$ mbar CO_2, (F) $1x10^{-4}$ mbar CO_2, (G) $1x10^{-4}$ mbar CO_2, and (H) $1x10^{-4}$ mbar CO_2. left) CO_2 range, right) carbonate range.
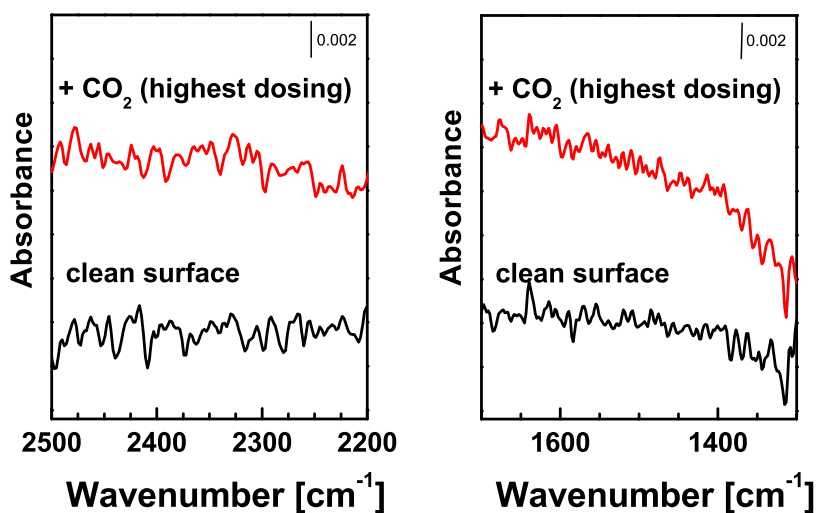
Figure A3: UHV-FTIR spectra obtained after exposing the clean Ti1.0/SBA-15 sample to $1x10^{-4}$ mbar CO_2 at 300 K in an UHV chamber. left: CO_2 range, right: carbonate range.
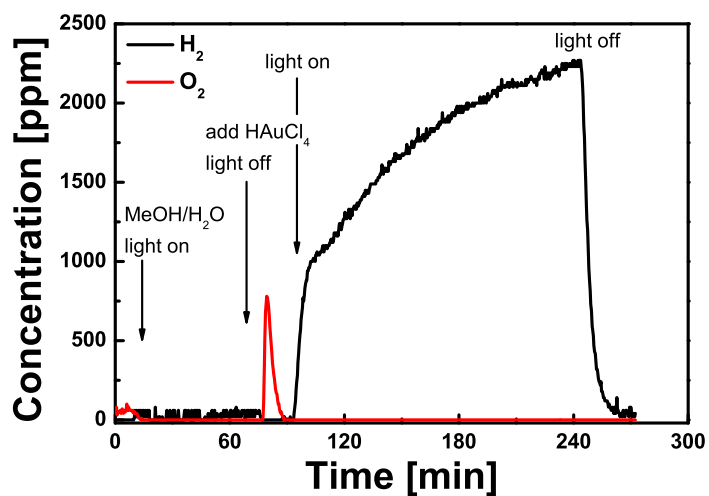
Figure A4: Hydrogen evolution observed during Au photo-deposition onto Ti/SBA-15.
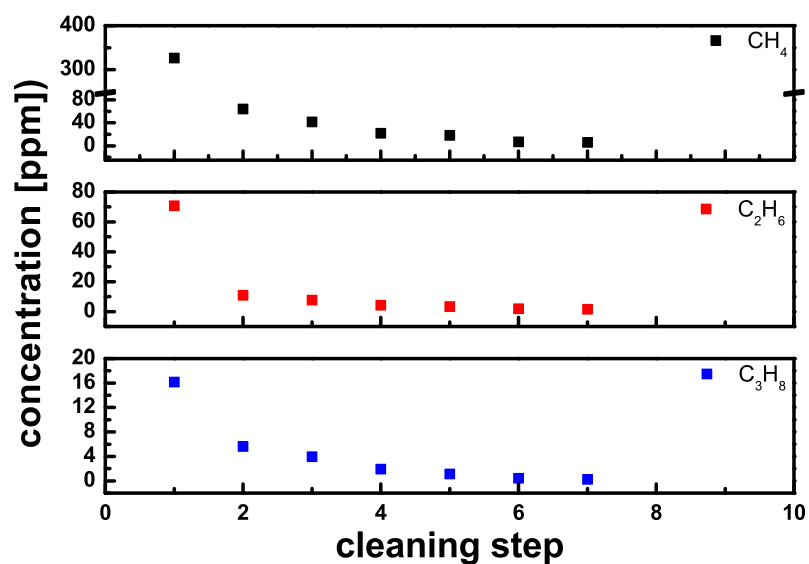
Figure A5: Evolution of different C_xH_y species observed after 5 h of irradiation for the subsequent pretreatment steps in humid He in presence of Au/Ti/SBA-15. The decay of the different compounds was fitted using exponential curves.
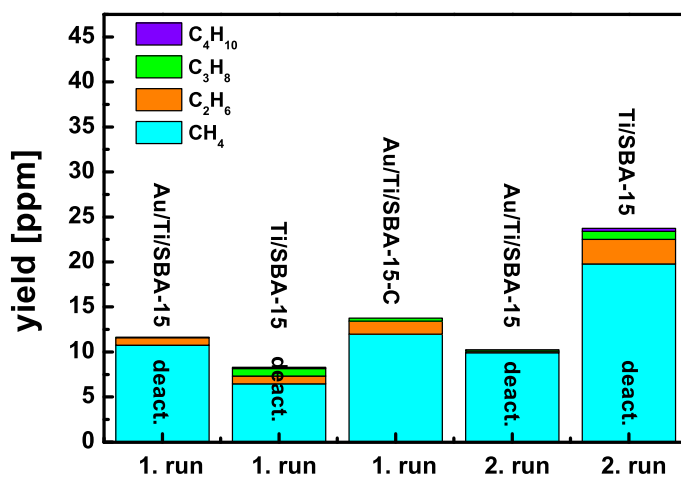
Figure A6: Methane yield after 5 h of irradiation obtained for the deactivated Ti/SBA-15, the deactivated Au/Ti/SBA-15, and the calcined Au/Ti/SBA-15-C samples.
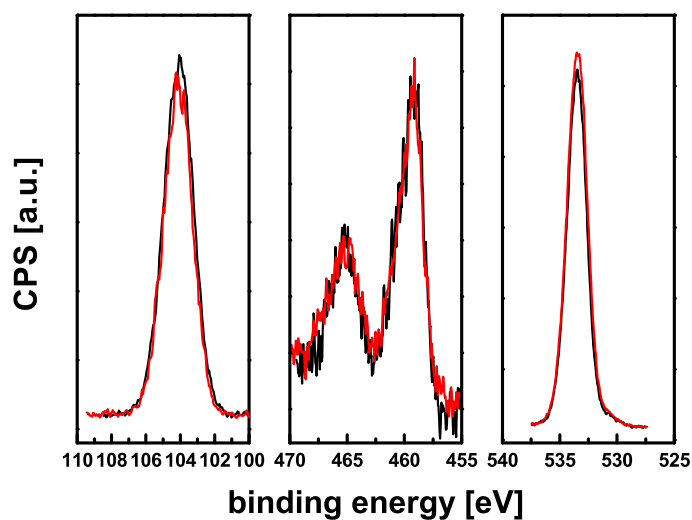
Figure A7: Si 2p, Ti 2p, and O 1s XPS region scans of the fresh (black line) and reacted (red line) Au/Ti/SBA-15 samples.
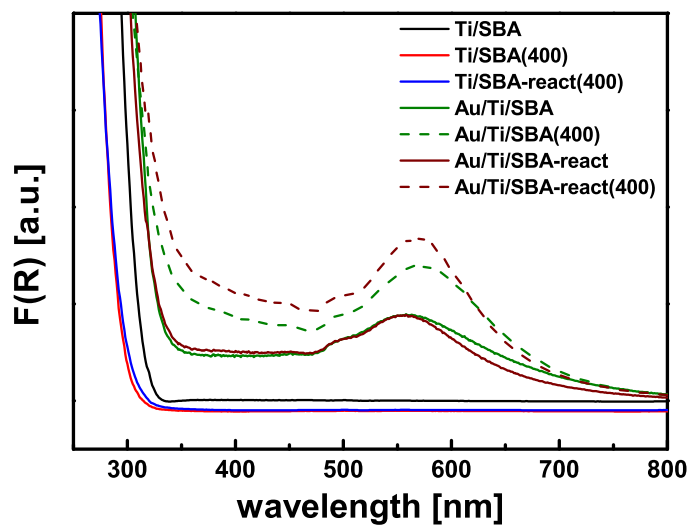
Figure A8: UV-Vis spectra obtained with the reacted and fresh Ti/SBA-15 and Au/Ti/SBA-15 samples. UV-Vis spectra of each sample were recorded before and after heating the sample to 400 °C. Furthermore, a red shift of the characteristic Au plasmon of the Au/Ti/SBA-15-C sample was observed by UV-Vis spectroscopy possibly causing the decrease in activity (not shown).
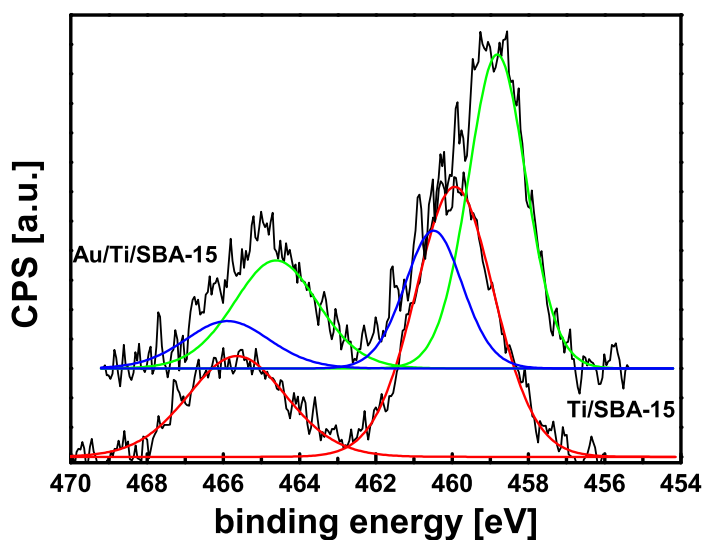
Figure A9: Ti 2p signals of the Ti/SBA-15 and Au/Ti/SBA-15 obtained by XPS
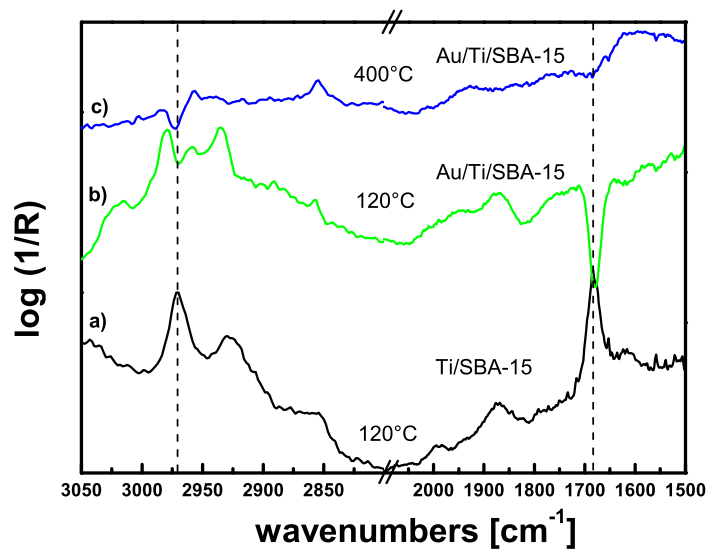
Figure A10: Difference DRIFT spectra obtained for the Ti/SBA-15 sample at 120 °C and for the Au/Ti/SBA-15 at 120 °C and 400 °C, respectively.
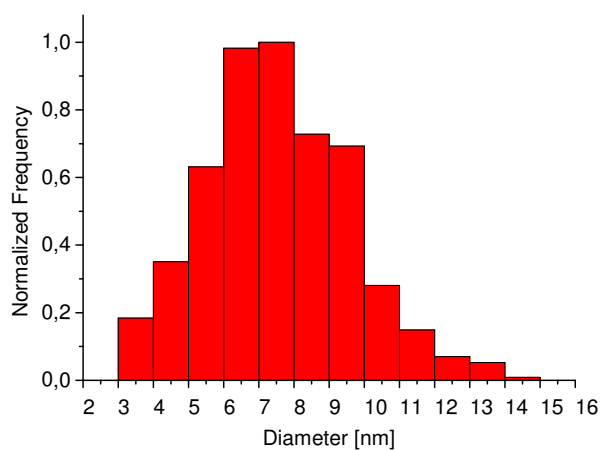
Figure A11: Size distribution of Au particles in the Au/Zn0.3/Ti1.2/SBA material. The size of the particles was determined from HAADF-STEM images. The diameter was calculated by assuming a spherical shape for the particles.

Element	wt%	Δwt%	at%
Si	25,96	0,19	22,56
Ti	6,39	0,10	3,26
Zn	3,71	0,15	1,38
Au	0,56	0,10	0,07
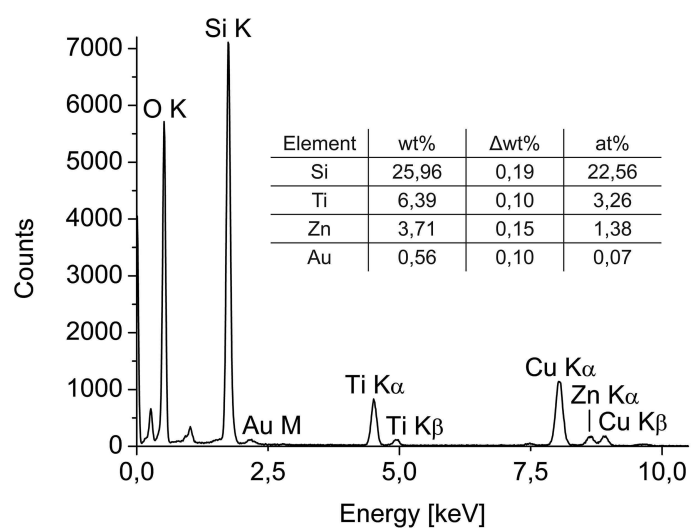
Figure A12: EDX spectrum of a typical Au/Zn0.3/Ti1.2/SBA crystal. The inset table shows the composition of the crystal in wt%, its error, and the composition in at%.
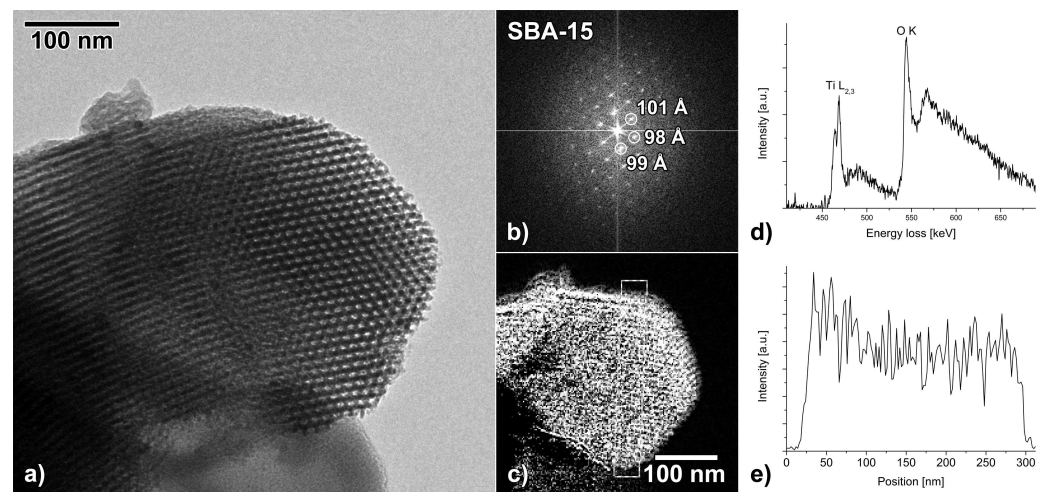
Figure A13: a) HRTEM image of a typical Au/Zn0.3/Ti1.2/SBA crystal. The channels are visibly intact. The FFT of a) (displayed in b)) reveals an average distance of approximately 100 Å. c) EFTEM Ti map of the crystal visible in a). The Ti distribution is homogeneous. There are no visible Ti enrichments. The dark area on the left side is a thickness effect, and is not due to the absence of Ti. d) EELS spectrum of Au/Zn0.3/Ti1.2/SBA showing the Ti-$L_{2,3}$ and the O-K edge. e) Ti-K EDX line profile over c) (from top to bottom).
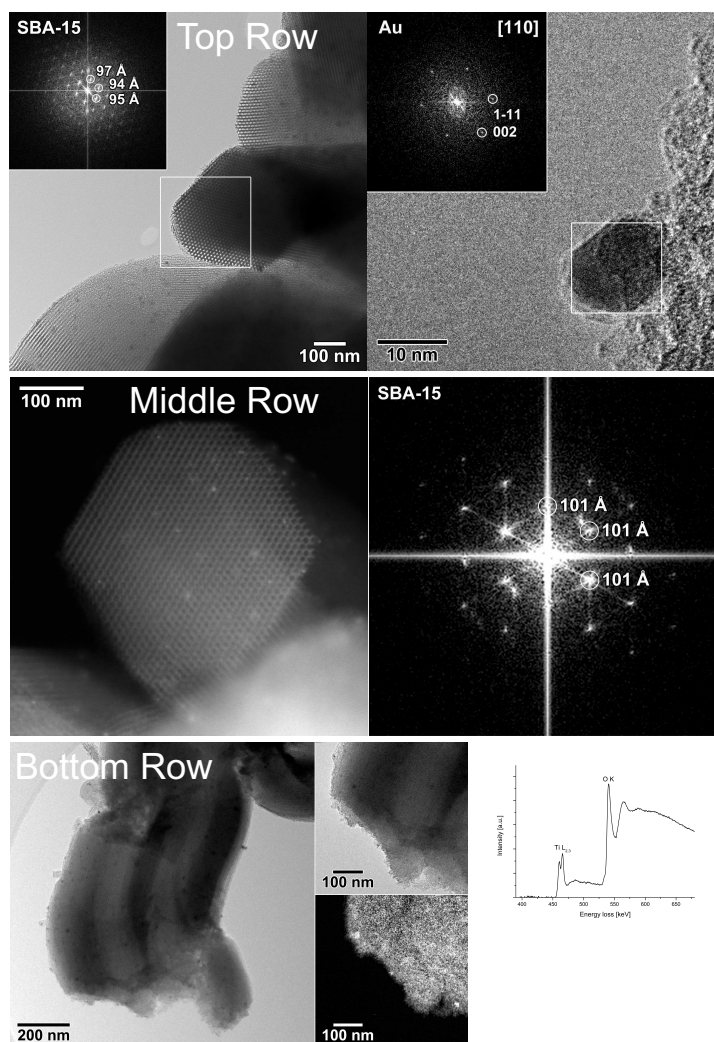
Figure A14: Top row, left: BF-TEM image of Au/Ti1.2/Zn0.3/SBA. The crystal in the center of the image has been imaged along its channel direction. FFT analysis of the area highlighted by the white frame (inset) shows a spacing of approximately 95 Å of the hexagonally packed pores for the imaged crystal. Right: HR-TEM of a gold particle in Au/Ti1.2/Zn0.3/SBA. The particle is imaged along its [110] zone axis orientation as it can be seen in the FFT analysis (inset). Middle row, left: HAADF-STEM image of a Au/Ti1.2/Zn0.3/SBA crystal along its pore direction. Right: FFT analysis of the area highlighted by the white frame (inset) shows a spacing of 101 Å for the imaged crystal. The imaged gold particles are quite monodisperse. Bottom row, left: BF-TEM, magnification the Au/Ti1.2/Zn0.3/SBA material and Ti EFTEM map of the Au/Ti1.2/Zn0.3/SBA crystal shown in the top right. The titanium distribution is homogeneous except for small enrichments (intensity is proportional to the Ti concentration). Right: EELS spectrum of Au/Ti1.2/Zn0.3/SBA showing the Ti-$L_{2,3}$ and the O-K edge.

8.3 Supporting Figures Chapter 6
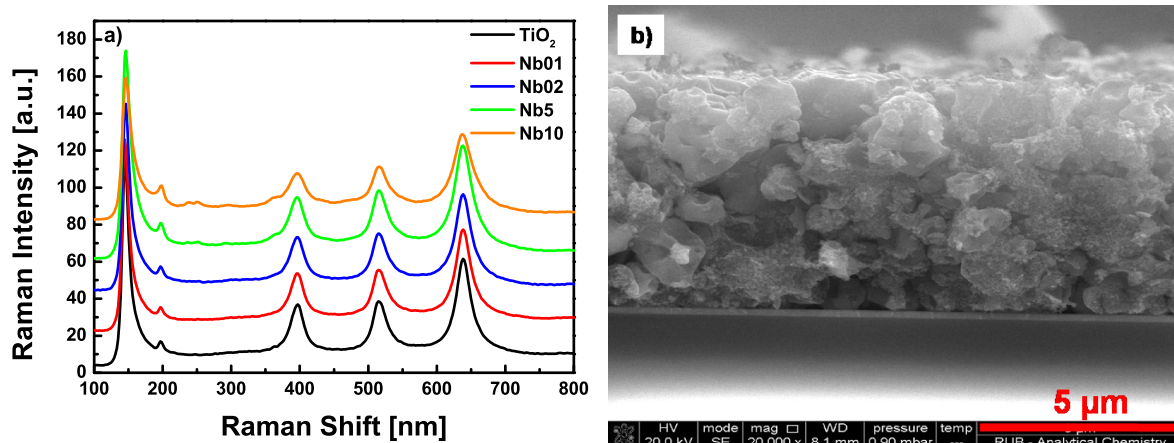
Figure A15: a) Structural characterization of Nb-doped TiO_2 samples with different Nb concentrations, b) SEM picture of the cross-section of a typical anode.
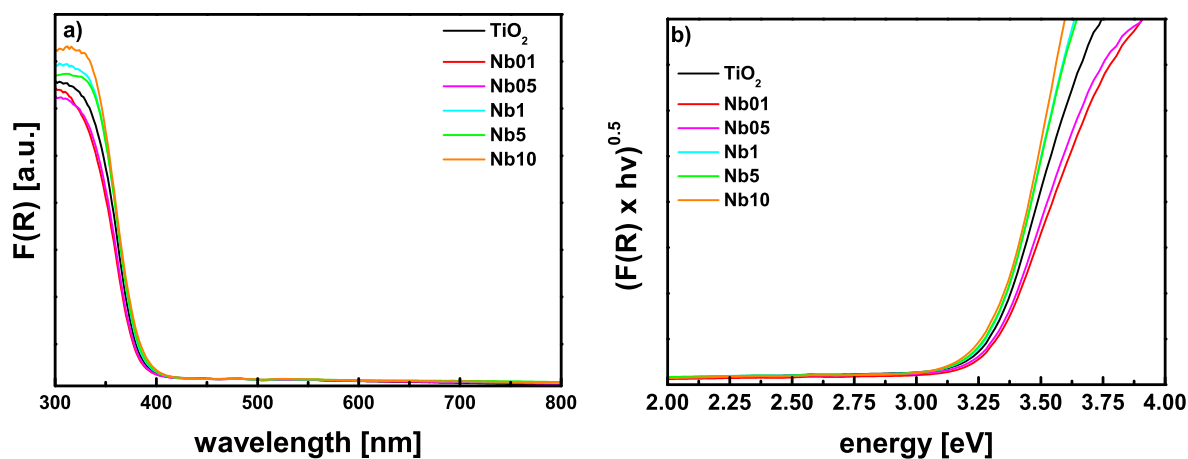

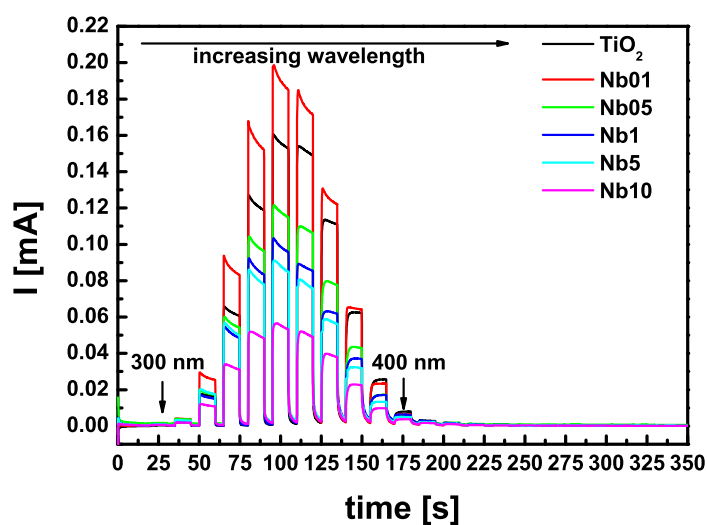**Figure A16:** a) UV-Vis absorption measurements and b) Tauc plots of Nb-doped TiO_2 samples.

Figure A17: Wavelength-dependent photocurrent measurements of different Nb-doped TiO$_2$ samples.
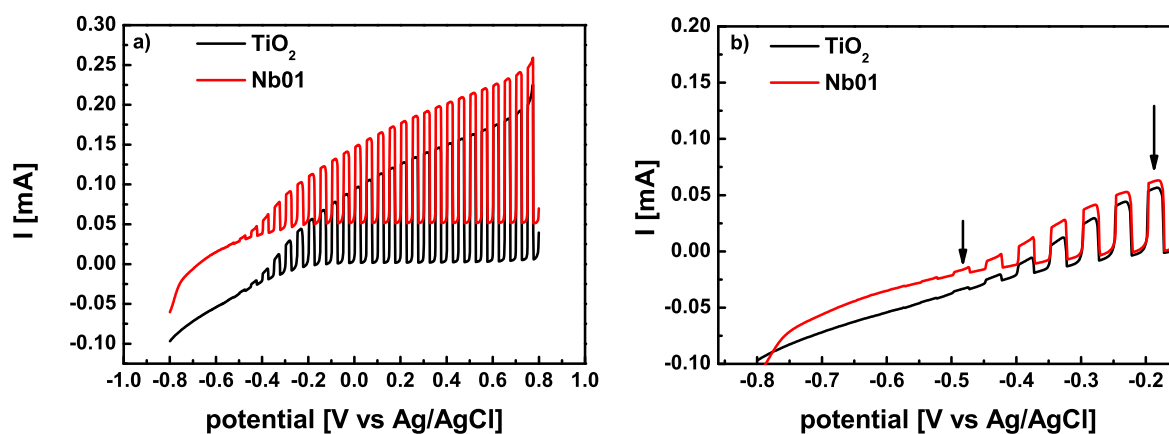

Figure A18: a) Potential-dependent photocurrent response for the TiO$_2$-reference and Nb (0.1 at%) materials irradiated at 350 nm in phosphate buffer (pH 7). b) Magnification of the low potential range of the potential-dependent photocurrent measurements.
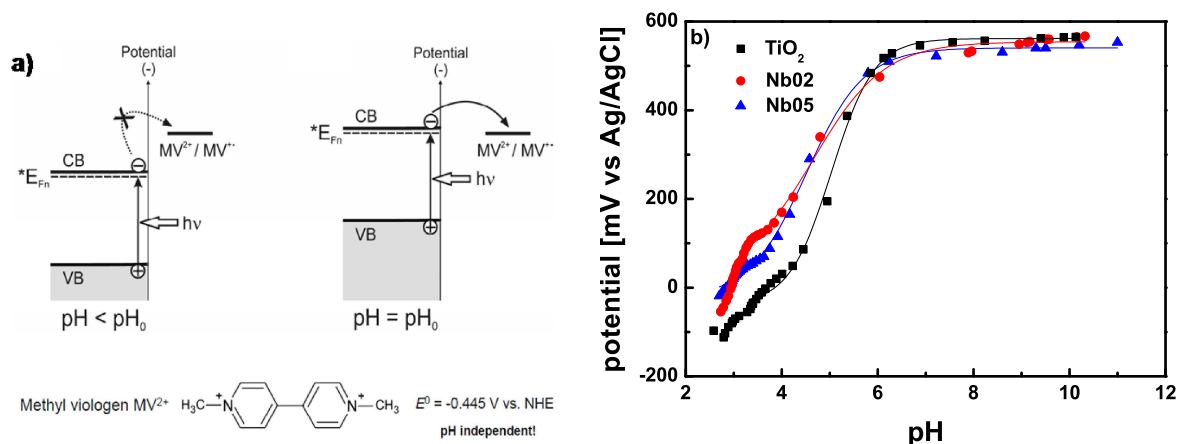
Figure A19: a) Quasi-Fermi level of electrons ($*E_{Fn}$) estimation by the Method of Roy using pH
independent methyl viologen as indicator. This figure was adapted from Ref.[221].
b) Change of the potential of a Pt electrode immersed in an irradiated suspension of
TiO_2 reference sample and different Nb-doped TiO_2 materials with increasing pH.
Assuming Nernstian shift of band edges (0.059 V/pH unit) the values of $* E_{Fn}$ at pH =
7 can be then obtained from equation: $* E_{Fn} = E_{MV^{2+/+\bullet}} + 0.059$ (pH$_0$ - 7), where pH$_0$
is the inflection point on the titration curve. This procedure gives $* E_{Fn}$ = -0.56 V vs.
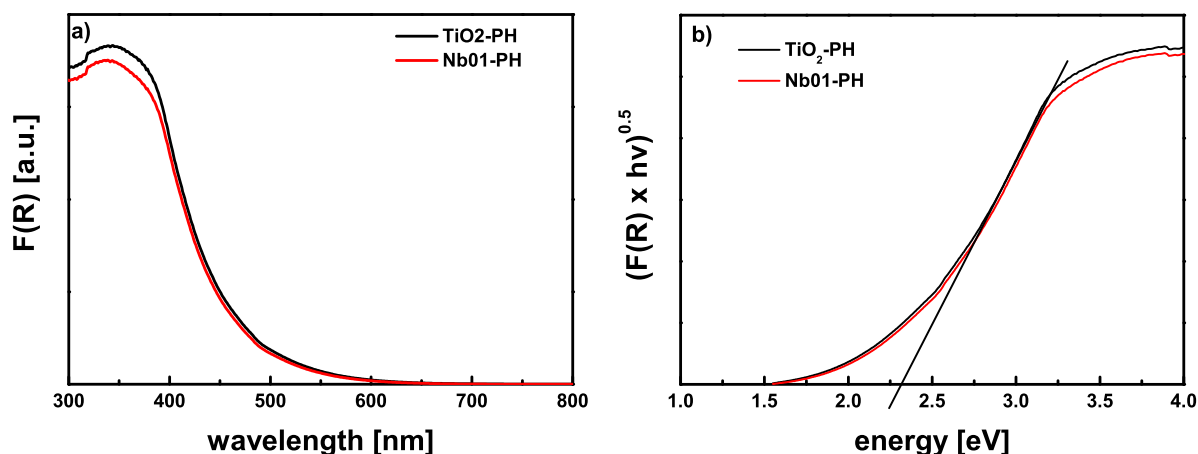NHE for pristine TiO_2 and $* E_{Fn}$ = -0.59 V vs. NHE for Nb-doped TiO_2.

Figure A20: a) UV-Vis absorption measurements and b) Tauc plots of polyheptazine-modified Nb-
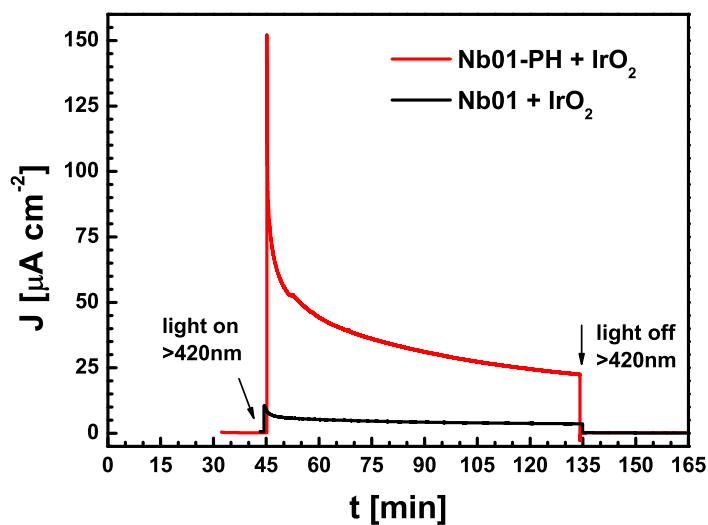doped TiO_2 samples.

Figure A21: Photocurrent response during irradiation with visible light ($\lambda > 420$ nm).
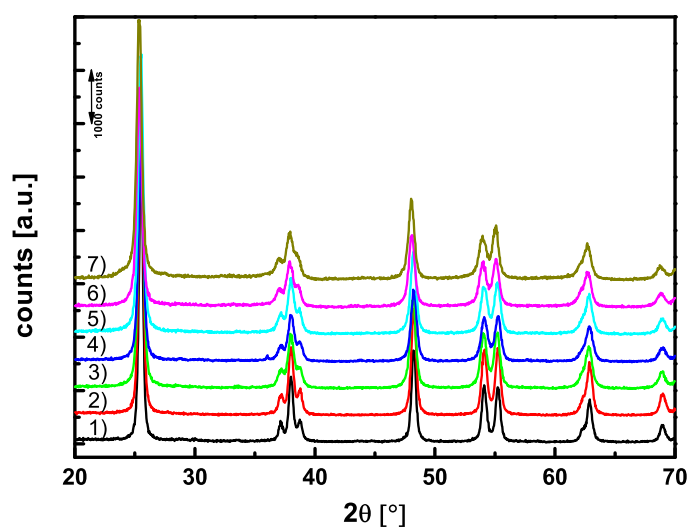

Figure A22: X-ray diffraction pattern of Nb-doped TiO_2 materials with different Nb concentrations treated at 500 °C in 150 ml/min NH_3 for 4 h. The theoretical Nb content in the different materials was 1) 1 at%, 2) 2 at%, 3) 5 at%, 4) 10 at%, 5) 15 at%, 6) 20 at%, and 7) 25 at%.
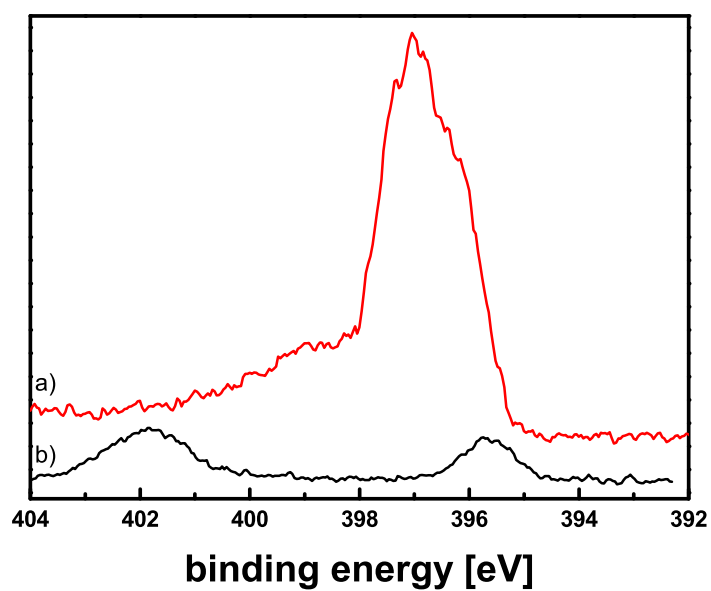
Figure A23: XPS N 1s region scans of Nb-doped TiO_2 with 10 at% Nb a) treated at 700 °C in 150 ml/min NH_3 and b) post-treated in syn. air.

9 Curriculum Vitae

Bastian Mei

Ruhr-University Bochum
Department of Chemistry and Biochemistry
Bochum, 44780

Phone: 0049-(0)234-32-22341
Fax: 0049-(0)-32-15114
Email: Bastian.Mei@rub.de
Homepage: www.techem.rub.de/

Education

Ph.D. Chemistry, Ruhr-University Bochum, 2009 - present.
Supervisor: Prof. Dr. Martin Muhler
Title: "Heterogeneous photoelectrochemistry and photocatalysis of TiO_2-based nanomaterials: Towards photocatalytic CO_2 reduction."

M.Sc. Chemistry, Ruhr-University Bochum, July 2009.
Supervisor: Prof. Dr. Martin Muhler
Title: "Spectroscopic characterization of niobium-doped titania for fuel cell applications."

B.Sc. Chemistry, Ruhr-University Bochum, March 2008.

Research Experience

Ruhr-University Bochum, Department of Chemistry and Biochemistry, Bochum
PhD studies, August 2009 - present.

University of Twente, Netherlands
Visiting Student, May 2012.

Dalian Institute of Chemical Physics, China
DAAD Exchange Programm, September - December 2010.

Cardiff University, Cardiff Catalysis Institute,Wales, GB
Erasmus Internship, October 2007 - January 2008.

Research Interests

Solar fuels; photoelectrochemical hydrogen production, photocatalytic CO_2 reduction.

TiO_2-based single-site and bulk photocatalysts

Characterization techniques: UV-Vis spectroscopy, Raman spectroscopy, XRD and ultra-high vacuum technologies including UPS and XPS.

Research

Peer-Reviewed Journal Articles

B. Mei, H. Byford, M. Bledowski, L. Wang, J. Strunk, M. Muhler, R. Beranek, *Solar Energy Materials and Solar Cells*, 2013, accepted.

F. E. Oropeza, **B. Mei**, I. Sinev, M. Muhler, J. Strunk, *Applied Catalysis B: Environmental*, 2013, accepted.

J. Schartner, J. Güldenhaupt, **B. Mei**, M. Rögner, M. Muhler, K. Gerwert, C. Kötting, *Journal American Chemical Society*, 2013, **135**, 4079.

W. Busser, **B. Mei**, M. Muhler, *ChemSusChem*, 2012, **5**, 2200.

A. Ramakrishnan, S. Neubert, **B. Mei**, J. Strunk, L. Wang, M. Bledowski, M. Muhler, R. Beranek, *Chemical Communication*, 2012, **48**, 8556.

B. Mei, A. Becerikli, A. Pougin, D. Heeskens, I. Sinev, W. Grünert, M. Muhler, J. Strunk, *Journal of Physical Chemistry C*, 2012, **116**, 14318.

B. Mei, M. D. Sanchez, T. Reinecke, S. Kaluza, W. Xia, M. Muhler., *Journal of Materials Chemistry*, 2011, **21**, 11781.

D. Schäfer, C. Madare, A. Savan, M. D. Sanchez, **B. Mei**, W. Xia, M. Muhler, A. Ludwig, W. Schuhmann, *Analytical Chemistry*, 2011, **83**, 1916.

W. Xia, **B. Mei**, M. D. Sanchez, J. Strunk, M. Muhler, *Journal of Nanoscience and Nanotechnology*, 2011, **11**, 8152.

C. Jin, M. Holz, W. Xia, **B. Mei**, S. Kundu, M. Muhler, *Electrochemical Society Transactions*, 2009, **25**, 763.

Papers Under Review

B. Mei, A. Pougin, M. Muhler, J. Strunk, submitted to *Journal of Catalysis*.

E. Ventosa, **B. Mei**, W. Xia, M. Muhler, W. Schuhmann, submitted to *ChemSusChem*.

S. Neubert, A. Ramakrishnan, **B. Mei**, et al., submitted to *ACS Catalysis*.

Work in Progress

B. Mei, et al., "Effects of Au and ZnO on the structure and photocatalytic activity of TiO$_x$/SBA-15 materials".

E. Ventosa, W. Xia, **B. Mei**, et al., "Ammonia annealed TiO2 as negative material in Li-ion batteries: N-doping or oxygen deficiency?".

Conference Presentations

"Improvement of TiO$_x$/SBA-15 for photocatalytic applications by the addition of ZnO and Au." **B. Mei**, et al. International Conference on Catalysis in Munich, July 1-6, 2012. Poster Presentation

"Effect of Nb doping on TiO$_2$ and TiO$_2$-polyheptazine hybrid materials in wavelength and potential-dependent photocurrent measurements." **B. Mei**, et al. 243$^{\text{rd}}$ Spring Meeting of the American Chemical Society in San Diego, CA, March 25-29, 2012. Oral Presentation

"CO2 adsorption of potential photocatalysts for CO$_2$ reduction." **B. Mei**, et al. EuropaCat X, Glasgow, August 2011. Poster Presentation

"The synthesis and characterization of NbO$_x$/TiO$_2$ nano composites by spray drying: an efficient and scalable method." **B. Mei**, et al. Annual Meeting of the German Catalysis Society, Weimar, March 16-18, 2011. Poster Presentation

Activities

Member of the GDCh (German society of chemistry), Member of the Ruhr-University Research School (June 2010 present), Organization of the JCF Spring Symposium 2009 & EYCN Satellite Event, Speaker of the Young Chemists Bochum (2010 - 2011).
Interests include running marathon, swimming, reading, soccer and traveling.

Last updated: May 10, 2013